DEPARTAMENTO DE ASTROFISICA

Universidad de La Laguna

Radiative Transfer in Molecular Lines. Astrophysical Applications

Memoria que presenta
D. Andrés Asensio Ramos
para optar al grado de
Doctor en Ciencias Físicas.

INSTITUTO Đ ASTROFISICA Đ CANARIAS
July 2004

Examination date: 2004 July 2
Thesis supervisors: Drs. Javier Trujillo Bueno (IAC) and José Cernicharo Quintanilla (DAMIR-CSIC)

ISBN: 84-689-7166-9
Depósito legal: TF-178/2006
Some of the figures included in this document have been already published in *Nature* and *The Astrophysical Journal*.

Agradecimientos

En primer lugar quiero expresar mi más sincero agradecimiento por todo el apoyo que he recibido de mi director de tesis, Javier Trujillo Bueno, tanto a nivel profesional y científico como personal. Ha sido una experiencia realmente inolvidable haber trabajado con un gran científico, junto al cual he podido llevar a buen puerto el trabajo intensivo de cuatro años. Deseo agradecer también el apoyo que mi co-director de tesis, Pepe Cernicharo, me ha dado. La distancia geográfica entre nosotros ha impedido que pudiéramos llevar a cabo un mayor número de colaboraciones, pero las que hemos podido iniciar han sido de interés para mi pues me han motivado a aprender también sobre otros problemas de investigación en astrofísica molecular. Asimismo, deseo agradecer al Instituto de Astrofísica de Canarias (IAC) el haberme concedido una beca de Astrofísico Residente para la realización de la tesis doctoral.

Remontándome a hace bastantes años, me es grato recordar que mis primeros pasos en física solar vinieron de la mano de Valentín Martínez Pillet durante una beca de verano trabajando en el telescopio Newton del Observatorio del Teide. Asimismo, la colaboración con Ángel Alonso durante el último año de carrera me ayudó a iniciarme en los detalles de la investigación en otro campo de la astrofísica. Ya durante el período de trabajo en la tesis, me resultó especialmente reconfortante la relación científica mantenida con Michele Bianda, Mats Carlsson, Manolo Collados, Jorge Sánchez Almeida y Han Uitenbroek, con quienes hemos realizado algunas colaboraciones puntuales que también he intentado dejar reflejadas en esta tesis. Por último, los buenos momentos que pasé en Madrid, Caltech y Hawaii fueron mejores gracias a mis compañeros del Departamento de Astrofísica Molecular e Infrarroja de Madrid.

De forma muy especial agradezco a todos los compañeros de fatiga del IAC por todos los buenos momentos que hemos pasado juntos, tanto en la cafetería como fuera de ella. Nuestro grupo ha ido creciendo con el tiempo, por lo que prefiero no nombrarlos uno a uno. Seguro que me olvidaría de alguien y no me lo perdonaría.

Por último, la mayor muestra de agradecimiento es para mi familia, que siempre ha estado ahí para apoyarme, tanto en los momentos buenos como en los malos: mi madre, Rosana; mi padre, Andrés; y mis hermanos, Raúl y María. Para terminar, a Marian, la última en llegar, pero que se ha convertido en fundamental para mí.

Summary

This thesis presents the development of a variety of methods and techniques for solving radiative transfer problems in molecular lines, and their application to some research problems in molecular astrophysics. For example, we investigate the formation of rotational water lines in the giant molecular complex SgrB2, the vibro-rotational lines of CO in the circumstellar envelope of the VY CMa supergiant, the enigma of the "cool clouds" in the solar atmosphere and the Zeeman and Hanle effects in solar molecular lines.

Our first aim has been to develop an efficient radiative transfer code for molecular lines in spherically symmetric atmospheres accounting for macroscopic velocity fields and without assuming Local Thermodynamic Equilibrium (LTE). In order to solve this type of radiative transfer problems, it is first necessary to obtain the molecular number concentrations at each point within the stellar atmosphere model under consideration. To this end, we have developed a computer code which allows to obtain the molecular abundances via the instantaneous chemical equilibrium approximation. However, since in many astrophysical situations the dynamical timescales are shorter than the molecular formation and destruction timescales, we have also developed a computer program which allows us to obtain the time variation of the molecular concentrations via the numerical solution of the chemical evolution equations. This type of equations must be based on a sufficiently realistic reaction network for each particular problem under investigation. We have applied these developments to investigate several key problems in solar physics, like the enigma of the cool gas in the solar chromosphere or the possible role of photodissociations for setting the CH abundance in the G-band bright points, which are thought to be associated with spatially unresolved and intense magnetic flux concentrations in the solar photosphere.

In this thesis we also show how the fastest iterative methods for the solution of multilevel radiative transfer problems can be generalized to spherical symmetry, for both atomic and molecular lines. In particular, we describe the generalization of the accelerated Λ-iteration (ALI) method (based on Jacobi's method) and the iterative methods developed by Trujillo Bueno & Fabiani Bendicho (1995) (based on the Gauss-Seidel and SOR schemes). We show that the excellent convergence properties of such methods are maintained when going to spherical geometry. The method based on the Gauss-Seidel scheme is 4 times

faster than ALI, while the SOR method represents an improvement of an order of magnitude in the convergence rate. The convergence rate is very high, with a computing time per iteration that is very similar to that of the Λ-iteration method, and without requiring neither the construction nor the inversion of any large matrix.

The non-LTE computer program that we have developed via the implementation of such radiative transfer methods constitutes a very powerful tool for a variety of applications in molecular astrophysics, including the particularly difficult problem of radiative transfer in maser lines. For example, it has allowed us to calculate the excitation state of the rotational energy levels of H_2O in the giant molecular complex SgrB2, including the modeling of the emergent hot water spectrum. In addition, we have also investigated the formation of the fundamental vibration-rotation band of CO in the circumstellar envelope of VY CMa.

A significant part of this thesis focuses on the investigation of the spectropolarimetric properties of molecular lines, with the aim of developing new tools for empirical investigations on solar and stellar magnetism. To this end, we have investigated the polarization signals that the Zeeman effect and scattering processes induce in molecular lines. We present a very general method for accounting for the effect of a magnetic field on the rotational levels of diatomic molecules, which is based on the numerical diagonalization of the effective Hamiltonian.

Concerning the molecular Zeeman effect, we have first investigated the physical origin of anomalous polarization profiles observed in sunspots, showing that they are produced by infrared lines of CN, which show a very particular Zeeman pattern. In order to extract useful empirical information from this type of spectropolarimetric observations we have developed an inversion code of molecular Stokes profiles induced by the Zeeman effect, which allows us to infer the stratification of the kinetic temperature, density and magnetic field vector in strongly magnetized regions of the solar atmosphere. We have also investigated in great detail the circular polarization spectrum produced by CH in the G-band, and show novel observations which corroborate our theoretical predictions. In addition, we have detected for the first time polarization signals produced by the Zeeman effect in FeH lines in sunspots, pointing out their potential interest for empirical explorations in solar and stellar magnetism.

Finally, we have investigated the linear polarization signals produced by

scattering processes in MgH, C_2 and CN lines, which have been discovered recently via spectropolarimetric observations of the solar limb spectrum. We have performed an exhaustive analysis of the properties of all the molecular bands which produce sizable linear polarization signals. Applying the quantum theory of polarization, we investigate how anisotropic pumping processes induce population imbalances and quantum interferences in the molecular energy levels (i.e., atomic level polarization), and how weak magnetic fields modify such atomic level polarization (and the emergent linear polarization!) via the Hanle effect. We show that a rigorous interpretation of the observed polarization in molecular lines requires to abandon the use of one-dimensional models of the solar atmosphere and to carry out detailed investigations by using three-dimensional hydrodynamical models which describe the inhomogeneity and dynamic nature of the solar photosphere. Taking into account the different sensitivity to the Hanle effect of the observed C_2 lines, we have been able to put some constraints on the turbulent magnetic field distribution in the granular regions, showing that the magnetic fields in such regions have to be very weak.

Resumen

Esta tesis presenta el desarrollo de una serie de herramientas de transporte radiativo para líneas moleculares y su aplicación a diversos problemas de interés astrofísico: la formación de las líneas rotacionales de agua en el complejo molecular gigante SgrB2, la formación de las líneas vibro-rotacionales de CO en la envoltura circunestelar de la supergigante VY CMa, la investigación de la formación de las líneas de CO en la atmósfera solar y la investigación de las señales espectropolarimétricas producidas por especies moleculares en la atmósfera solar.

Nuestro primer objetivo ha consistido en el desarrollo de un código de transporte radiativo para líneas moleculares en atmósferas con geometría esférica y campos de velocidad macroscópicos. Para resolver tales problemas de transporte radiativo, es necesario obtener las abundancias moleculares en cada punto de la atmósfera. Para ello, paralelamente hemos desarrollado un código que permite obtener las abundancias moleculares suponiendo la aproximación de equilibrio químico instantáneo. Como muchas veces las escalas de tiempo dinámicas son más cortas que los tiempos de formación de moléculas, hemos desarrollado también un código que permite obtener la variación en el tiempo de las abundancias moleculares resolviendo las ecuaciones de evolución que surgen al describir una red de reacciones adecuada para cada problema. Hemos aplicado estos códigos para investigar problemas como el enigma del CO en la atmósfera solar o la importancia de la fotodisociación en el establecimiento de la abundancia de CH en los puntos brillantes observados en la banda G.

Mostramos en esta tesis cómo generalizar a geometría esférica los métodos iterativos más rápidos de solución de problemas de transporte radiativo. En particular, mostramos la generalización de los métodos basados en la iteración Λ acelerada (basada en el esquema de Jacobi) y los métodos iterativos desarrollados por Trujillo Bueno & Fabiani Bendicho (1995), los cuales están basados en la iteración Gauss-Seidel y SOR. Mostramos que las propiedades de convergencia de tales métodos en atmósferas plano-paralelas se mantienen en geometría esférica. El método basado en la iteración Gauss-Seidel es hasta 4 veces más rápido que la iteración Λ acelerada, mientras que SOR representa hasta un orden de magnitud de mejora en el ritmo de convergencia. La tasa de convergencia es muy alta, con un tiempo de cómputo por iteración semejante al de la iteración Λ y no requieren ni la construcción ni la inversión de ninguna gran

matriz.

Una parte significative de esta tesis se centra en la investigación de las propiedades espectro-polarimétricas de las líneas moleculares. Hemos investigado las señales de polarización producidas por el efecto Zeeman o por procesos de dispersión incluyendo el efecto Hanle. Presentamos un método muy general de calcular el efecto de un campo magnético sobre los niveles rotacionales de las moléculas diatómicas mediante la diagonalización numérica del Hamiltoniano efectivo.

En lo que concierne a las señales de polarización en líneas moleculares producidas por el efecto Zeeman, hemos descubierto e investigado perfiles anómalos producidos por líneas infrarrojas de CN y hemos desarrollado un código de inversión de líneas moleculares que permite obtener información sobre las condiciones termodinámicas y magnéticas de las zonas magnetizadas en la atmósfera solar. Hemos investigado en detalle el espectro de polarización circular producido por la molécula de CH en la banda G y hemos realizado observaciones corroborando las predicciones teóricas. Por último, hemos observado por primera vez las señales de polarización producidas por líneas de FeH en manchas solares.

Finalmente, hemos investigado con gran detalle las señales de polarización lineal producidas por las líneas de MgH, C_2 y CN cuando se observan cerca del limbo solar. Realizamos en esta tesis un estudio exhaustivo de las propiedades de las bandas moleculares que producen señal de polarización lineal. Mediante la aplicación de la teoría cuántica de la polarización, investigamos la polarización atómica en los niveles moleculares y su variación por la presencia de un campo magnético a través del efecto Hanle. Ilustramos que la señal de polarización por dispersión en las líneas es modificada por la presencia de un campo magnético. Mostramos que una interpretación rigurosa de la polarización por dispersión observada en las líneas moleculares requiere abandonar el uso de modelos unidimensionales de la atmósfera solar y hacer investigaciones detalladas en modelos hidrodinámicos tridimensionales que describan la inhomogeneidad de la fotosfera solar. Teniendo en cuenta la diferente sensibilidad al campo magnético que tienen las líneas de C_2 observadas, hemos sido capaces de poner algunas restricciones a las distribuciones de campo magnético turbulento en las zonas granulares, constatando que los campos en tales zonas de la superficie solar deben ser muy débiles.

Index

1

Introduction

In 1926, Sir Arthur Eddington affirmed that "only atoms are physics, molecules are chemistry", advising in this way his astronomy colleagues of not wasting their time trying to find molecular species in the Universe. Curiously, only a decade after, Dunham & Adams (1937a, 1937b) detected several spectral lines in the wavelength range between 3900 and 4300 Å which remained unidentified until several later works demonstrated that these lines were produced by CH in the interstellar medium. It is the well-known electronic transition of CH, known nowadays as the G-band. Other lines were assigned to CH^+. This discovery suddenly changed the ideas about the Universe, since the existence of molecular species was considered to be restricted to the Earth. After the discovery of the CH lines, molecular astrophysics became one of the most exciting and prolific branches of modern astrophysics.

Even more striking was the detection of rotational CN lines among its lowest energy levels. The rotational temperatures of such transitions were very close to 2.3 K and independent of the line-of-sight. CN has a very high dipolar moment and collisions barely affect the excitation state of the rotational levels. On the contrary, the excitation state of the rotational lines are mainly driven by the radiation field illuminating the molecule, being almost in equilibrium with this field. Therefore, this result suggested the presence of an isotropic radiation field at a temperature of $\sim$2.3 K. This result, considered at this moment of quite limited interest for people like the Nobel laureate Herzberg, was confirmed

twenty-five years later when the Cosmic Background Radiation (CMB) was discovered by Penzias & Wilson (1965). It became then obvious that the results obtained from the CN lines are produced by the radiative excitation due to the remnant black-body radiation after the Big Bang.

The optical observations at that time did not lead to any other detection of molecular species in the Universe. The discovery of new molecular species had to await the development of the first radiotelescopes. The new spectral region opened up by these telescopes produced a huge amount of new information. The rotational transitions of many molecules were expected to be situated in the radio spectral range and the presence of many molecular species was confirmed, even by the first low-sensitivity telescopes. In the sixties, Weinreb et al. (1963) discovered the presence of OH. Some years later, H_2O and NH_3 was discovered by Knowles et al. (1969) and Cheung et al. (1969), respectively, while H_2CO (formaldehyde) was discovered by Palmer et al. (1969).

During the seventies, and thanks to the expansion of the wavelength range covered by the receivers in the radiotelescopes, other molecules could be detected. Wilson et al. (1970) observed a very strong emission at 2.6 mm towards the Orion nebula which was assigned to the J=1-0 rotational transition of CO. In fact, this molecule is one of the most widely used molecular diagnostics. Other detected species were CS, HCN, CH_3OH and HCO^+. The study of the cold Universe could then be accomplished. The observed molecular lines allowed the exploration of the physical conditions in different astronomical objects by using different molecular species. The symbiosis with molecular spectroscopy turned out to be fundamental. Many of the molecular species were very difficult to produce in the laboratory due to the special conditions of low density and high radiation field present in the interstellar medium. Therefore, the frequencies of the transitions and the molecular properties were unknown. At that time, the astrophysical objects selected for the observations of molecular species immediately transformed into molecular spectroscopy laboratories where new species were found and which had to be recognized by their spectral lines.

All these steps led to a new branch in Astrophysics known as Molecular Astrochemistry. Its main aim is to answer the question of how molecular species are formed in such low density and highly irradiated environments and to obtain information on the physical properties of the medium.

Additional important advances in Molecular Astrophysics were feasible thanks to the launch of the Infrared Space Observatory (ISO) satellite. The two spec-

trometers onboard ISO, the Short Wavelength Spectrometer (SWS) and the Long Wavelength Spectrometer (LWS) have been used to detect several molecular species and to show that some molecular species are found in many different systems. The detection of CH_3 (Feuchtgruber et al. 2000), an important precursor in the development of the hydrocarbons chemistry, the detection of hydrogen fluoride HF (Neufeld et al. 1997), or the striking detection of benzene in the envelope of an evolved star (Cernicharo et al. 2001) can be considered as milestones of ISO. Future IR and sub-millimeter satellites like Herschel[1] and ground-based interferometers like ALMA[2] will expand our knowledge of the molecular species present in the Universe. As an example, a list of the molecular species that have been discovered in the interstellar and circumstellar medium is shown in Table 1.1

Interestingly, molecular species are also present in the solar atmosphere, which is a sufficiently dense and cool medium to allow the efficient formation of molecules. The majority of the molecules found in the solar atmospheric plasma are diatomic, although in the cooler sunspots, even water has been detected (see, e.g., Wallace et al. (1995)).

This Thesis focuses on some key problems in the field of molecular astrophysics, with emphasis on developing the radiative transfer tools that will be needed to scientifically exploit the future observations we will be able to obtain with Herschel, ALMA, Gran Telescopio Canarias[3] (GTC), GREGOR[4] and the Advanced Technology Solar Telescope[5] (ATST). In addition, by using the Sun as a unique molecular physics laboratory, this Thesis aims also at making a significant contribution to the emerging field of molecular spectropolarimetry.

Molecular lines contain key information on the physical properties of the cool regions of the Universe. For this reason, it is of crucial importance be able to model the observed spectral line radiation. Molecules are found in the outer parts of the stellar envelopes of evolved stars and in the interstellar medium. Therefore, they are usually immersed in strong radiation fields, coming from the lower parts of the atmospheres of evolved stars or the strong UV field present in the interstellar medium produced by the ionizing photons of young and massive

[1] `http://www.esa.int/science/herschel`
[2] `http://www.eso.org/projects/alma`
[3] `http://www.gtc.iac.es`
[4] `http://gregor.kis.uni-freiburg.de/`
[5] `http://atst.nso.edu`

Table 1.1: List of interstellar and circumstellar molecules detected up to 2003.

Diatomic molecules
AlF, AlCl, C_2, CH, CH^+, CN, CO, CO^+, CP, CS, SiC, HCl, H_2, KCl
NH, NO, NS, NaCl, OH, PN, SO, SO^+, SiN, SiO, SiS, HF, SH, HD, FeO
Triatomic molecules
C_3, C_2H, C_2O, C_2S, CH_2, HCN, HCO, HCO^+, HCS, HOC^+, H_2O
H_2S, HNC, HNO, MgCN, MgNC, N_2H^+, N_2O, NaCN, OCS, SO_2, c-SiC_2
CO_2, NH_2, H_3^+, SiCN, AlNC, H_2D^+, SiH_2?, KCN?
Molecules with four atoms
c-C_3H, l-C_3H, C_3N, C_3O, C_3O, C_2H_2, CH_2D^+, HCCN, $HCNH^+$
HNCO, HNCS, $HOCO^+$, H_2CO, H_2CN, H_2CS, H_3O^+, NH_3, SiC_3
Molecules with five atoms
C_5, C_4H, C_4Si, l-C_3H_2, c-C_3H_2, CH_2CN, CH_4, HC_3N, HC_2NC
HCOOH, H_2CHN, H_2C_2O, H_2NCN, HNC_3, HNC_3, SiH_4, H_2COH^+
Molecules with six atoms
C_5H, C_5O, C_2H_4, CH_3CN, CH_3NC, CH_3OH, CH_3SH, HC_3NH^+
HC_2CHO, $HCONH_2$m l-H_2C_4, C_5N, C_4H_2, C_6^-?, C_5S?
Molecules with seven atoms
C_6H, CH_2CHCN, CH_3C_2H, HC_5N, $HCOCH_3$, NH_2CH_3, c-C_2H_4O, C_7^-
Molecules with eight atoms
CH_3C_3N, $HCOOCH_3$, CH_3COOH, C_7H, H_2C_6, CH_2OHCHO, C_8^-?, l-HC_6H
Molecules with nine atoms
CH_3C_4H, CH_3CH_2CN, $(CH_3)_2O$ CH_3CH_2OH, HC_7N, C_8H, C_9^-?
Molecules with ten atoms
CH_3C_5N, $(CH_3)_2CO$, NH_2CH_2COOH
Molecules with more than ten atoms
HC_9N, C_6H_6, $HC_{11}N$

stars. This radiation field excites the molecular levels driving them far from thermodynamic equilibrium. In order to infer correctly the physical properties of the astrophysical plasma under consideration, it is crucial to take into account that the lines are typically formed outside LTE conditions. The most efficient numerical methods developed for the solution of radiative transfer problems in stellar physics have recently started to be applied to the case of radiative transfer problems in molecular lines (see Asensio Ramos et al. 2001; and more references therein). Previous schemes of solution were based on Montecarlo methods, which suffer from some well-known problems like statistical noise. One of the conclusions of a recent workshop which took place in Leiden was the development of a set of tests for the easy testing of new numerical codes for the solution of radiative transfer in molecular lines. In a recent paper (van Zadelhoff et al. 2002), a comparison between 8 different codes is done, being only 3 based on the Montecarlo scheme. This shows that the techniques used in stellar astrophysics are quickly been introduced in the field of molecular astrophysics. As we will show in Chapter 4 of this Thesis, the fastest numerical methods developed so far (see Trujillo Bueno & Fabiani Bendicho 1995) can be applied to radiative transfer problems in molecular lines.

An example of a research field in which molecular astrophysics could play a fundamental role is in the determination of chemical abundances in metal poor stars. One of the interesting problems which could be investigated with the RT tools presented in this Thesis is the "enigma" of the oxygen over-abundance in metal poor stars (Asplund et al. 2004). This is crucial for the determination of the age of many astrophysical objects like the globular clusters by means of their oxygen enrichment. The oxygen abundances obtained with several different tracers are not in good agreement (see, e.g., Asplund & García Pérez 2001). Among these tracers, we have the OH lines in the UV. Two fundamental problems arise, which are intrinsic to the technique used for obtaining the chemical abundances. This technique is based on a comparison between spectroscopic observations and synthetic spectra obtained in different atmospheric models. The chosen atmospheric models, typically one-dimensional and in radiative equilibrium, and the approximation employed to obtain the molecular abundances, may crucially influence the emergent spectrum. With the recent development of realistic three-dimensional simulations (see Stein & Nordlund 2000; Asplund et al. 2000), the situation for the calculation of atomic abundances has changed and many of the results have to be revised. As an example, the iron abundance

in the solar atmosphere has been recently revised (Shchukina & Trujillo Bueno 2001) using NLTE synthesis in three-dimensional hydrodynamical models of solar surface convection including the effect of the radiation transfer in the energy budget equation. For the first time, these authors found that NLTE spectral synthesis in Asplund et al.'s (2000) 3D hydrodynamical model of the solar atmosphere yields the meteoritic iron abundance. The success of such three-dimensional hydrodynamical simulations has been extended to the calculation of the abundance of other species (Asplund et al. 2003; Asplund 2004). With such 3D atmospheric models, it is now of possible interest to investigate the impact of non-LTE and chemical non-equilibrium effects when obtaining molecular abundances.

We have developed the tools needed for investigating this and other type of problems. The most important obstacles are the enormous lack of reliable molecular data and the need of computing resources. The first problem has a difficult solution in view of the amount of available molecular data and the speed at which new data is generated. Particularly urgent is the need of state-to-state collisional rates for molecular lines. There are some calculations of collisional rates for the ground levels of some molecules, which are of interest in very cold media. However, collisional rates for excited vibrational states and between different electronic states are not known. Even an approximate estimation of such collisional rates would be of enormous help for accounting for non-LTE effects in molecular lines. The second problem is much more related to technology and efforts in parallelization of non-LTE codes (see, e.g., Höflich 2003; Baron et al. 2003).

The first problem we have tackled in this Thesis as an application of our chemical evolution codes is the study of the temporal evolution of the carbon monoxide abundance in the solar atmosphere. The objective of this investigation was the resolution of the "enigma" emerged 30 years ago when Noyes & Hall (1972) inferred very low brightness temperature from their discovery of strong ro-vibrational CO lines at 4.7 μm observed close to the edge of the solar disk. It was then suggested by Ayres (1981) that the low chromosphere might not be hot at all but could instead be permeated by CO-cooled "clouds" at altitudes between 500 and 1000 km above continuum optical depth unity. This led to controversy (Kalkofen 2001; Ayres 2002; Avrett 2003) because other diagnostics had suggested the existence of a uniformly hot chromosphere with a minimum temperature of about 4400 K near 500 km and a temperature rise

above this temperature-minimum region. Over the last few years, it has become increasingly evident that for understanding the thermal structure of the solar chromosphere we need a rigorous investigation of the CO formation and destruction timescales in the solar atmospheric plasma (Uitenbroek 2000a, 2000b; Ayres & Rabin 1996; Avrett et al. 1996; Asensio Ramos & Trujillo Bueno 2003a; Avrett 2003). To this end, in this Thesis we have carried out an exhaustive comparative study between the CO abundances obtained assuming instantaneous chemical equilibrium and that obtained by following the chemical evolution in the one-dimensional hydrodynamical models of the solar atmosphere of Carlsson & Stein (1995). These models show the generation of acoustic wave trains which propagate upwards in the atmosphere until transforming into shocks. As shown in Chapter 3, we have calculated the time evolution of the CO abundance thanks to reaction databases which are widely used in combustion mechanisms (Konnov 2000). These processes cover better the kind of reactions present in the solar atmosphere than the reaction databases used in the investigation of interstellar chemistry.

It is of interest to point out that our chemical evolution codes can also be used to investigate the formation processes of complex molecules. The exact chemical mechanisms which produce such molecules with more than 10 atoms is not correctly known. Actually, very complex molecules are found in the interstellar medium. One of the most striking has been the detection of benzene C_6H_6 in circumstellar envelopes (Cernicharo et al. 2001).

Chapter 4 describes in detail the computer code developed for the solution of radiative transfer problems in molecular astrophysics assuming spherical geometry. We generalize the fast iterative methods developed by Trujillo Bueno & Fabiani Bendicho (1995) to spherical geometry with macroscopic velocity fields. We show that the fundamental properties of the iterative methods based on the Gauss-Seidel and Successive Overrelaxation schemes are maintained when spherical geometry is considered. We show two application of the computer code. The first one concerns the formation of pure rotation water spectral lines in a hot shell of the molecular complex SgrB2 and the second one concerns the formation of CO vibration-rotation lines in the envelope of the red supergiant VY CMa.

The study of atomic and/or molecular lines allows us to obtain information about the physical properties of the medium the radiation is coming from. In addition to its intensity and frequency, light is characterized by its state of

polarization. Spectropolarimetry provides an incredible amount of information about phenomena in which a break of the spherical symmetry occurs in the astrophysical system in which the spectral lines are being formed. We may have stellar geometrical asymmetries induced by the presence of another companion star in the case of a binary star, global anisotropies in the radiation field of non-resolved stars, local anisotropies in the radiation field in the Sun, the presence of magnetic fields, etc. All these phenomena produce recognizable features in the polarization state of the observed light. If the study of such polarization phenomena is tackled within the framework of the quantum theory of polarization (Landi Degl'Innocenti 1983), we can obtain reliable information about the physical properties in a variety of astrophysical objects (see Trujillo Bueno 2003a).

The polarization state of the light can be quantified by using the Stokes parameters (Born & Wolf 1980; Landi Degl'Innocenti 2002). As shown in Fig. 1.1, I is the light intensity, Q is the intensity difference between vertical and horizontal linear polarization, U the intensity difference between linear polarization at $+45^\circ$ and -45°, while V is the intensity difference between right-handed and left-handed circular polarization. Observationally, Stokes parameters can be easily obtained when working on the radio spectral domain since the detectors are directly sensitive to the polarization state of the light. In the case of shorter wavelengths, the technique is much more complicated and it relies on modulation schemes (Keller 2002). In the special case of solar physics, the present instrumentation is very sophisticated. Nowadays, very sensitive polarimeters based on several modulation schemes have been developed which allow us to measure the Stokes parameters from the infrared to the ultraviolet (TIP, ASP, ZIMPOL, etc.). Such sensitive polarimeters allow the detailed investigation of physical processes which produce very weak signatures in the polarization state of the light (see the proceedings of the Solar Polarization 3 workshop edited by Trujillo Bueno & Sánchez Almeida). In this way, the topology and strength of solar magnetic fields can be inferred via the physical interpretation of spectropolarimetric observations. The application of spectropolarimetry to night-time astronomy is currently in expansion thanks to the construction of several polarimeters: the MuSiCoS échelle spectro-polarimeter for the 2-m Bernard Lyot Télescope at Pic du Midi, the Semel's visitor polarimeter on the UCL Echelle Spectrograph of the 3.9-m Anglo-Australian Telescope or the future ESPaDOnS polarimeter mounted on the Canada-France-Hawaii Telescope

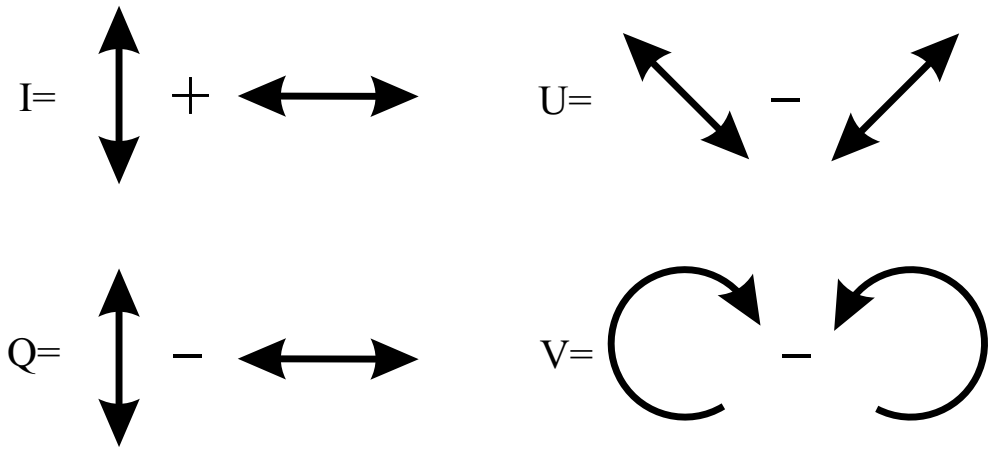

Figure 1.1: Operative definition of the Stokes profiles. Adapted from Landi Degl'Innocenti (2002).

(CFHT, Donati 2003). These polarimeters are being used or will be used for the investigation of magnetic fields in magnetic stars (see the proceedings of the above-mentioned Solar Polarization 3 workshop 2003).

An important part of this Thesis focuses on the investigation of polarization signals produced by molecular lines. Similar to what happens with the atomic case, the coupling between the different angular momenta in the molecule with the external magnetic field produces a magnetic moment and a precession of the total angular momentum around the magnetic field vector. This is molecular Zeeman effect. The influence of the magnetic field on the level structure of the molecules produces an observable effect on the polarization state of the light emitted or absorbed by the molecule. The investigation of the Zeeman effect in molecules is much more complex than in atoms, even for the simplest coupling cases. This is produced by the presence of the rotation of the molecule, which produces an additional angular momentum (Herzberg 1950; Landau & Lifshitz 1982; Judd 1975). Schadee (1978) developed formulas for the calculation of the splittings and strengths of the Zeeman components for electronic doublet states. Recently, Berdyugina & Solanki (2002) extended Schadee's formulation to electronic states of arbitrary multiplicity. We have developed in Chapter 5 a computer program which allows us to obtain the splittings and strengths of the

Zeeman components for any transition between two arbitrary rotational levels of arbitrary electronic states in a diatomic molecule. Our approach is capable of treating the inclusion of any refinement in the quantum description of the molecular motion by only adding the corresponding contribution to the total molecular hamiltonian. The calculation of the hamiltonian matrix elements is carried out by taking advantage of the powerful tools of Racah algebra (Brink & Satchler 1968; Judd 1975; Brown & Carrington 2003).

The observation of spectral line polarization in cold and magnetized regions on the solar surface (sunspots) gives us information about the magnetic field in these regions. In Chapter 6 we show that molecules usually show anomalous polarization profiles which can be explained via the different strengths of the angular momenta couplings. Some of the rotational levels of several electronic states in diatomic molecules present strong interactions with nearby levels. This produces a transition from the Zeeman regime to the Paschen-Back regime, often for rather low magnetic field strengths. The observed Stokes profiles for some molecular species are very anomalous. This is the case of the CN lines we have observed with TIP in the near infrared, as will be shown in Chapter 6. Apart from their diagnostic capabilities in solar physics, recently the molecular Zeeman effect is being used for obtaining information about magnetic fields in stars with very strong magnetic fields. Such strong fields are thought to produce very cold spots in the surface of the stars and molecules constitute one of the few observable tracers of the physical conditions in these regions (see, e.g., Berdyugina et al. 2001; Valenti & Jonhs-Krull 2001)

A serious problem is the blending of molecular lines with important atomic lines used for diagnostic purposes. We know that molecular bands are characterized by a huge amount of lines produced by their rotational structure. Therefore, it is quite probable that a molecular line is blended with an atomic line. It turns out necessary to include huge numbers of both atomic and molecular lines in our spectral synthesis codes to obtain correct information about the physical properties of the atmosphere when comparing with observations. If the molecular line is magnetically sensitive, the influence of the blend on the polarization state has to be included in the forward modeling. This analysis of the physical properties of the stellar atmosphere is usually accomplished with the aid of inversion codes (see, e.g., Ruiz Cobo & del Toro Iniesta 1992). In Chapter 6 of this Thesis we will develop an LTE inversion code which allows to include atomic and/or molecular lines in the forward modeling. We will show

the applicability of our inversion code to obtain information about the thermodynamic and magnetic structure of the umbra of sunspots by using only OH and CN lines. Ideally, one should include a suitable set of spectral lines which can trace the physical properties at different heights.

An extra novel subject we have considered in this Thesis is scattering polarization in molecular lines. Chapter 7 presents a very detailed and systematic investigation of the polarization signals produced by scattering processes in several molecular lines. When one observes the second solar spectrum of the Sun (the linearly polarized spectrum close to the solar limb) many conspicuous signals corresponding to molecular lines appear, generated by the scattering of radiation (Stenflo & Keller 1997; Gandorfer 2000). Such a polarization signal is modified by the presence of a magnetic field, which is known as the Hanle effect (Trujillo Bueno 2001). Contrary to what happens with the polarization of many atomic species, which strongly vary along the solar magnetic activity cycle, molecular lines always show the same amplitude in the linear polarization signals. Recently, is has been concluded by Berdyugina et al. (2002) that this apparent insensitivity of the molecular lines to the magnetic field is due to the very low effective Landé factors of the molecular lines. However, Landi Degl'Innocenti (2003) and Trujillo Bueno (2003b) have pointed out that the magnetic sensitivity of the scattering polarization depends on both the individual Landé factors of the levels of the transitions and on the lifetimes of the energy levels. In fact, the critical Hanle fields of molecular lines are of the same order of magnitude as those of atomic lines. Therefore, it is to be expected that molecular lines are affected by magnetic fields of the same strength as atomic lines. We will show in Chapter 7that this sensitivity to the Hanle effect is found for fields of the order of 10 G, and that the apparent insensitivity of the molecular lines has to be assigned to another physical effect (see Trujillo Bueno 2003b). We will show in detail that this behavior may be explained when taking into account that the molecules which generate the linear polarization signals are formed in a three-dimensional medium. When obtaining the molecular abundances in such 3D models, we find that they are larger in the upflowing material than in the downflowing plasma, at least in the regions where the molecular lines are "formed". We explain the apparent insensitivity of the molecular lines to the magnetic field. Additionally, we show how to obtain information about the distribution of weak magnetic fields in the "quiet" solar photosphere.

Finally, in Chapter 8 we summarize the main conclusions of this Thesis.

2

Molecular Spectroscopy of Diatomic Molecules

This chapter will give a brief but complete introduction to the details of molecular spectroscopy. Such an introduction is fundamental for a complete understanding of the rest of the Thesis. We will start with a brief introduction of the molecular motions. We will continue by describing in detail the vibrational and rotational motions in diatomic molecules, continuing with a description of the molecular electronic states. The coupling between electronic and rotational motions is treated in Section §2.5. We will finish this chapter by considering molecular transitions and their respective selection rules.

2.1 Introduction

When two or more atoms link together to form a molecule, they constitute a system which is much more complex than an isolated atom. A way to handle such a complex system is to use the *Born-Oppenheimer* approximation, which consists on treating the motion of the nuclei and that of the electrons in a separate way (Brown & Carrington 2003). The big mass difference between the electrons and the nuclei make the latter move much slower than the electrons do and so this approximation leads to extremely good results. When the nuclei move, electrons can adiabatically adapt to the new nuclear positions before the

nuclei change their position in the space. Therefore, they feel some kind of equivalent potential which depends only on the internuclear distance and the particular electronic state.

A molecule can produce three types of transitions: *rotational* transitions (they involve the rotation of the molecule as a whole), *vibrational* transitions (they involve vibrations of the nuclei around an equilibrium position) and *electronic* transitions (there is a change on the structure of the electronic cloud surrounding the molecule). The last type is also present in atoms, while the first two are exclusive of molecules. Although these transitions usually occur simultaneously (for example, when a molecule suffers a vibrational transition, the energy excess usually produces a change in the rotational state), under the Born-Oppenheimer approximation, we can consider the energy states of the electrons and those of the nuclei separately and so their corresponding transitions.

In order to get an insight of the magnitudes we are dealing with for each molecular motion, we can argue on the basis of the following order of magnitude calculation (Estalella & Anglada 1999). Assuming a typical molecular size ($a \simeq 1$ Å), a typical molecular mass ($M \simeq 10 m_p$, where m_p is the proton mass) and the mass of the electron m_e, the following can be found:

- **Electronic transitions.** Due to the uncertainty principle, $\Delta p \Delta x \simeq pa \simeq \hbar$ for an electron. Δp and Δx are the uncertainties in the determination of the velocity or momentum and position of the electron. Therefore, its momentum will be $p \simeq \hbar/a$. Since its energy is $E = p^2/2m_e$, the electronic energy level separation will be of the order of

$$E_{\rm el} \simeq \frac{\hbar^2}{m_e a^2}. \tag{2.1}$$

  For the typical values we have given, $E_{\rm el} \simeq 1.2 \times 10^{-11}$ erg $= 7.5$ eV, which corresponds to a frequency $\nu_{\rm el} = E_{\rm el}/h = 1.8 \times 10^{15}$ Hz. This frequency is in the UV ($\lambda_{\rm el} \simeq 1700$ Å). Therefore, we expect the electronic transitions to be in the visible or UV region of the spectrum.

- **Vibrational transitions.** For the stable molecules, the internuclear potential have a minimum at a given value of the separation among the nuclei. We can approximate this vibration around this minimum with the

model of a harmonic oscillator with angular frequency ω and amplitude $\xi \ll a$. The oscillator energy is $E_{\rm vib} \simeq \frac{1}{2}M\omega^2\xi^2$. We can make a very rough estimation of ω by assuming that, in the limit $\xi \simeq a$, we should have an energy of the order of the electronic energy:

$$\frac{1}{2}M\omega^2 a^2 \simeq \frac{\hbar^2}{m_e a^2} \Rightarrow \omega \simeq \left(\frac{\hbar^2}{m_e M a^4}\right)^{1/2}. \tag{2.2}$$

Therefore

$$E_{\rm vib} \simeq \hbar\omega \simeq \left(\frac{m_e}{M}\right)^{1/2} \frac{\hbar^2}{m_e a^2} \simeq \left(\frac{m_e}{M}\right)^{1/2} E_{\rm el}. \tag{2.3}$$

For the typical values we have given, $E_{\rm vib} \simeq 8.9 \times 10^{-14}$ erg $= 0.06$ eV, which corresponds to a frequency $\nu_{\rm vib} = E_{\rm vib}/h = 1.3 \times 10^{13}$ Hz. This frequency falls in the IR range of the spectrum ($\lambda_{\rm vib} \simeq 23$ μm).

- **Rotational transitions.** The molecular angular momentum is quantized and is therefore a multiple of $\hbar$. For the lowest rotational levels, it will be $J = I\omega \simeq \hbar$, where $I \simeq Ma^2$ is the moment of inertia of the molecule. The rotational energy will be:

$$E_{\rm rot} \simeq \frac{1}{2}I\omega^2 \simeq \frac{\hbar^2}{Ma^2} \simeq \left(\frac{m_e}{M}\right) E_{\rm el}. \tag{2.4}$$

For the typical values, $E_{\rm rot} \simeq 6.5 \times 10^{-16}$ erg $= 4 \times 10^{-4}$ eV, which corresponds to a frequency $\nu_{\rm rot} = E_{\rm rot}/h = 9.8 \times 10^{10}$ Hz. This frequency falls in the radio range of the spectrum ($\lambda_{\rm rot} \simeq 3.1$ mm).

In the Born-Oppenheimer approximation, these energies are approximately additive, so $E = E_{\rm el} + E_{\rm vib} + E_{\rm rot}$. As we have seen, the contribution of each motion relative to the total energy is approximately in the proportion:

$$E_{\rm el} : E_{\rm vib} : E_{\rm rot} = 1 : \left(\frac{m_e}{M}\right)^{1/2} : \left(\frac{m_e}{M}\right). \tag{2.5}$$

Now we will treat in a more rigorous way all the three types of motion in a diatomic molecule.

2.2 Principal features of the rotation and vibration in diatomic molecules

As we have seen in the previous section, molecules can have nuclear motions that are not present in atoms. In this section we present two simple models which help to understand the vibrational and rotational spectra of diatomic molecules.

2.2.1 Rotational states: the rigid rotator

The simplest model for a rotating molecule is that of a rigid rotator. Let's assume that the molecule is composed of two point-like masses m_1 and m_2 situated at a distance r from each other and joined by a massless rigid rod. In so doing, we neglect, on the one hand, the finite extent of both atoms; on the other, the fact that the atoms are not rigidly bound one to the other, since the distance r can vary under the influence of rotation. Obviously, such a simple model can be reduced to the rotation of a single mass point of mass equal to the reduced mass μ of the system at a fixed distance r from the rotation axis. In order to determine the energy levels of such a rigid rotator, the Schrödinger equation has to be solved, obtaining the following expression of the discrete values of the energy given by (Herzberg 1950):

$$E(J) = \frac{h^2 J(J+1)}{8\pi^2 I}, \tag{2.6}$$

where I is the moment of inertia of the molecule, h is the Planck's constant and J is the *rotational quantum number*, which can take integral values 0, 1, 2, ... Since only discrete energy and angular momenta values are possible, it follows that only certain rotational frequencies are possible due to the transition between an upper level with J_u and a lower level with J_ℓ. The wavenumber ω of the emitted or absorbed photon is:

$$\omega = \frac{E(J_u)}{hc} - \frac{E(J_\ell)}{hc}, \tag{2.7}$$

where $E(J_u)$ and $E(J_\ell)$ are the upper and lower rotational energies, respectively, while c is the speed of light. In molecular spectroscopy, it is usual to define the

rotational term as the energy in units of cm^{-1}:

$$F(J) = \frac{E}{hc} = \frac{hJ(J+1)}{8\pi^2 cI} = BJ(J+1), \tag{2.8}$$

where B is called the *rotational constant*. The selection rule for these pure rotational transitions can be obtained from the evaluation of the matrix elements of the electric dipole moment, giving $\Delta J = \pm 1$. With this selection rule, the wavenumber of the emitted or absorbed lines of the rigid rotator can be found by:

$$\omega = F(J_\ell + 1) - F(J_\ell) = 2B(J_\ell + 1) \qquad J = 0, 1, 2, \ldots \tag{2.9}$$

Therefore, the spectrum of the rigid rotator consists of a series of equidistant lines, the first of these ($J_\ell = 0$) lies at $2B$ and their separation is also $2B$.

2.2.2 Vibrational states: the harmonic oscillator

The simplest model for describing the vibration of diatomic molecules is that each atom oscillates moving toward or away from the other atom in a simple harmonic motion. Such a movement can be reduced to the motion of a single mass (the reduced mass μ) around an equilibrium position r_e. In this situation, the effective potential energy under which the single mass moves can be written as $V(r) = \frac{1}{2}k(r - r_e)^2$, where k is the *force constant*. Solving the Schrödinger equation for this potential energy, it is found that there are solutions only for those values of the energy which obey (Herzberg 1950):

$$E(v) = \frac{h}{2\pi}\sqrt{\frac{k}{\mu}}\left(v + \frac{1}{2}\right), \tag{2.10}$$

where v is the *vibrational quantum number*, which can take only integral values (v=0,1,2,...). It should be noted that even in the lowest vibration level (v=0), some energy remains. This remnant is called the *zero-point energy*. The wavenumber of a vibrational transition can be written as:

$$\omega = \frac{E(v_u)}{hc} - \frac{E(v_\ell)}{hc} = G(v_u) - G(v_\ell) = \omega_e\left(v_u + \frac{1}{2}\right) - \omega_e\left(v_\ell + \frac{1}{2}\right), \tag{2.11}$$

where v_u and v_ℓ are the upper and lower level vibrational quantum numbers, G is the vibrational term in cm^{-1} and ω_e is a constant. By evaluation of the

matrix elements of the electric dipole moment, we can see that the selection rule for the vibrational quantum number is $\Delta v = \pm 1$. Therefore, the wavenumber of the emitted or absorbed lines of the harmonic oscillator can be found by:

$$\omega = G(v_\ell + 1) - G(v_\ell) = \omega_e. \tag{2.12}$$

In this very simple model, all vibrational transitions overlap at the same frequency.

2.3 Refinements on the structure of the rotation and vibration in diatomic molecules

The models presented so far are idealizations of the motion of diatomic molecules. Although they give a first order representation of the spectrum of diatomic molecules, a refinement is needed in general for interpreting the observed molecular spectra. In this section, we will improve the level of description of the rotation and vibration of the molecules by introducing higher order effects.

2.3.1 Anharmonic oscillator

A harmonic oscillator is characterized by a parabolic potential energy. The potential energy, and therefore the restoring force, increases indefinitely with increasing distance from the equilibrium position. However, when both nuclei are very distant, this force must go to zero, and therefore the potential energy reaches a constant value. We show in Fig. 2.1 the potential curve for the ground electronic level of H_2, showing that the parabola is a good approximation in the zone of the minimum (the equilibrium point of the molecule), while it is unsuitable for the rest of the curve. Higher order terms can be included in the definition of the potential energy, giving rise to better approximations of the motion of the diatomic molecule. The most obvious anharmonic potential energy is (see Herzberg 1950):

$$V(r) = f(r - r_e)^2 - g(r - r_e)^3, \tag{2.13}$$

where f and g are constants such that $g \ll f$. When one solves the Schrödinger equation with such a potential energy (possibly including higher powers of $(r -$

r_e)), the term values are modified as follows:

$$G(v) = \omega_e \left(v + \frac{1}{2}\right) - \omega_e x_e \left(v + \frac{1}{2}\right)^2 + \omega_e y_e \left(v + \frac{1}{2}\right)^3, \tag{2.14}$$

where $\omega_e x_e \ll \omega_e$ and $\omega_e y_e \ll \omega_e x_e$ are vibrational constants. The selection rule $\Delta v = \pm 1$ holds, but due to the inclusion of the anharmonic terms in the potential energy, transitions with $\Delta v = \pm 2, \pm 3, \ldots$ can also appear, although with a rapidly decreasing intensity. The inclusion of this anharmonic terms produces a shift in the position of the lines for different values of v_ℓ, contrary to what happened with the model of the harmonic oscillator.

Other representations for the potential energy curve are available, being the Morse potential one of the most widely used (Herzberg 1950). This potential is given by:

$$V_{\text{Morse}}(r) = D_e \left(1 - e^{-\beta(r - r_e)}\right)^2, \tag{2.15}$$

where D_e is the dissociation energy referred to the minimum of the curve and β is a constant. In this case, the term values can be obtained with:

$$G(v) = \beta \sqrt{\frac{D_e h}{2\pi^2 c \mu}} \left(v + \frac{1}{2}\right) - \frac{h\beta^2}{8\pi^2 c \mu} \left(v + \frac{1}{2}\right)^2, \tag{2.16}$$

without any higher power of $(v + 1/2)$.

2.3.2 Non-rigid rotator

Thus far we have treated the vibrational and the rotational motions independently. However, it is quite obvious that the molecule cannot be a rigid rotator when it is allowed to perform vibrations around the equilibrium distance. Therefore, a better model to represent the rotational motion of the molecule would be that of a non-rigid rotator in which we have two masses which are connected by a massless spring, instead of a massless rigid bar. In this system, and due to the action of the centrifugal force, the internuclear distance changes with rotation. Therefore, the moment of inertia of the molecule depends now on the rotational energy (and therefore on the rotational quantum number J), and thus on the rotational constant B. When the Schrödinger equation is

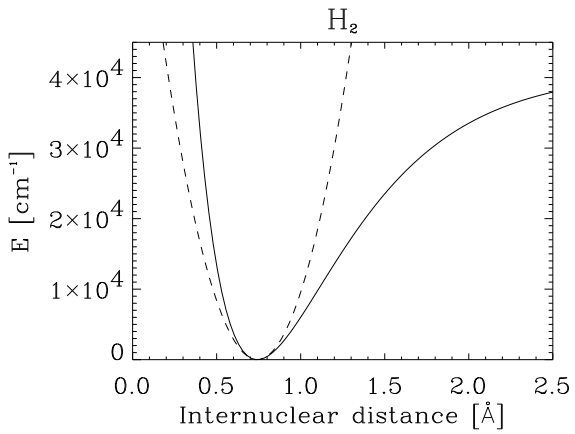

Figure 2.1: Potential energy curve for H_2 (solid line) using ω_e=4395.2 cm^{-1}, $\omega_e x_e$=117.99 cm^{-1} and r_e=0.7416 Å with the parabolic approximation (dashed line) which is valid for internuclear distances close to the equilibrium distance r_e (from Herzberg 1950).

solved with this improvement, one obtains the rotational terms of the non-rigid rotator, which can be written as (Herzberg 1950):

$$F(J) = BJ(J+1) - DJ^2(J+1)^2, \tag{2.17}$$

where $D \ll B$ is the rotational constant due to the centrifugal distortion. The selection rule obtained for a rotator ($\Delta J = \pm 1$) is valid independently of wether or not the rotator is rigid. Therefore, it can also be applied for the case of the non-rigid rotator to obtain the pure rotational spectrum. However, and because $D \ll B$, it is usually a good approximation to consider diatomic molecules as rigid rotators.

2.3.3 Vibrating rotator

We have considered the vibrational and rotational motions separately. However, it is obvious that both motions take place simultaneously. Furthermore, vibrations affect the rotational motion of the molecule. Therefore, we will consider the model of a vibrating rotator as the most refined model of the nuclear motion of a diatomic molecule. During vibrations, the internuclear distance, and

consequently, the moment of inertia and the rotational constants, are changing. After quite involved quantum mechanical calculations, one ends up with a formula for the rotational terms equal to Eq. (2.17) in which the rotational constants depend on the vibrational quantum numbers (Herzberg 1950):

$$B_v = B_e - \alpha_e \left(v + \frac{1}{2} \right) + \dots \tag{2.18}$$

$$D_v = D_e + \beta_e \left(v + \frac{1}{2} \right) + \dots , \tag{2.19}$$

where B_e and D_e are the rotational constants which correspond to the equilibrium distance r_e, while $\alpha_e \ll B_e$ and $\beta_e \ll D_e$ are constants which account for the variation of the internuclear distance during the vibration.

By taking into account the interaction between vibration and rotation, and using the fact that under the Born-Oppenheimer approximation the total energy is obtained by addition of the rotational and vibrational energies, it is possible to obtain the formula for the term values of a vibrating rotator (Herzberg 1950):

$$\begin{aligned} T = G(v) + F_v(J) &= \omega_e \left(v + \frac{1}{2} \right) - \omega_e x_e \left(v + \frac{1}{2} \right)^2 + \omega_e y_e \left(v + \frac{1}{2} \right)^3 + \dots \\ &+ B_v J(J+1) - D_v J^2 (J+1)^2 + \dots , \end{aligned} \tag{2.20}$$

where we have included the possibility of adding higher order distortions to the vibrational and rotational energies.

The selection rules $\Delta v = 0, \pm 1, \pm 2, \dots$ and $\Delta J = \pm 1$ are used to recover the vibro-rotational spectrum of a diatomic molecule. The selection rule $\Delta v = 0$ represents the pure-rotational spectrum. The wavenumber of the vibrational transitions between an upper vibrational level (v_u) and a lower vibrational level (v_ℓ) can be obtained, neglecting the small correction term for D_v, by substitution in Eq. (2.20):

$$\begin{aligned} \omega_R &= \omega_0 + 2B_v^u + (3B_v^u - B_v^\ell) J + (B_v^u - B_v^\ell) J^2 \qquad J = 0, 1, 2, \dots \\ \omega_P &= \omega_0 - (B_v^u + B_v^\ell) J + (B_v^u - B_v^\ell) J^2 \qquad J = 1, 2, 3, \dots , \end{aligned} \tag{2.21}$$

where we have explicitly indicated the rotational constants of the upper and lower vibrational levels, and $\omega_0 = G(v_u) - G(v_\ell)$ is the wavenumber of the

pure vibrational transition without taking into account the rotational structure. These two formulae represent two series of lines with $\Delta J = J_u - J_\ell = +1$ and $\Delta J = -1$, which are called the *R and P branches*, respectively. Both formulas can be also represented with a single one, namely:

$$\omega = \omega_0 + (B_v^u + B_v^\ell)m + (B_v^u - B_v^\ell)m^2, \tag{2.22}$$

where m is an integer taking values 1, 2, ... for the R branch (i.e., $m = J+1$) and the values -1, -2, ... for the P branch (i.e., $m = -J$). Note that, depending on the values of the rotational constants, one of the parabolas have a maximum value on the range of $J \geq 0$. If $B_v^u < B_v^\ell$ (the internuclear distance is greater in the upper state than in the lower), this maximum is placed on the R branch (if the condition $B_v^\ell \leq 3B_v^u$ is fulfilled), while it is in the P branch if $B_v^u > B_v^\ell$ (the internuclear distance is greater in the lower level than in the upper). The vertex of the parabolas are, therefore:

$$\begin{aligned} J^R_{\text{vertex}} &= -\frac{3B_v^u - B_v^\ell}{2\,(B_v^u - B_v^\ell)} \\ J^P_{\text{vertex}} &= \frac{B_v^u + B_v^\ell}{2\,(B_v^u - B_v^\ell)} \end{aligned} \tag{2.23}$$

All these calculations have been performed assuming that the molecule can be considered as a simple rotator; i.e., that there is only one nonzero moment of inertia and that the one about the axis joining both atoms is zero. However, the electron cloud around the atoms produce a non-zero moment of inertia about this axis. Therefore, a better model to represent a diatomic molecule would be that of a symmetric top. If we consider the vibro-rotational spectrum of a symmetric top, we find that the R and P branches can be obtained with the same formulae as for a simple rotator (Eq. 2.21), and the transitions $\Delta J = 0$ are now permitted by the selection rules. This $\Delta J = 0$ transition form the Q *branch* whose wavenumbers can be obtained with

$$\omega_Q = \omega_0 + (B_v^u - B_v^\ell)J + (B_v^u - B_v^\ell)J^2 \qquad J = 1, 2, 3, \ldots \tag{2.24}$$

Because α_e is very small, the J dependence of Eq. (2.24) is very weak, and the Q branch is characterized by having all the rotational transitions very close to ω_0.

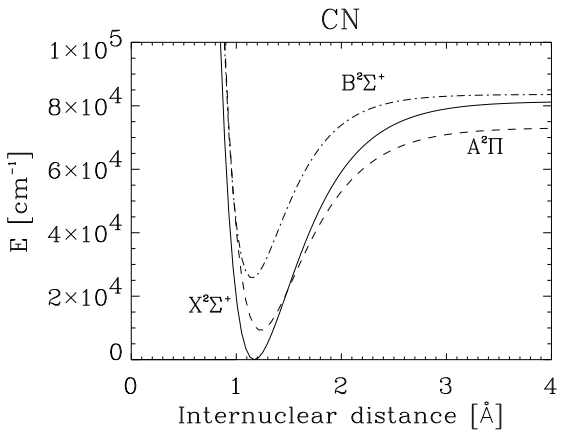

Figure 2.2: Potential energy curves for the lowest energy electronic states of CN. These curves have been obtained using the Morse potential with the r_e, β and D_e values for each electronic level.

2.4 Electronic states

The band spectra observed in the visible and the ultraviolet cannot be understood with vibrational and/or rotational motions. The frequencies of the transitions are too large in comparison with rotational or vibrational frequencies. On the other hand, the band structure does not have the well-defined simplicity of the vibration-rotation transitions. As pointed out in Section 2.1, the spectra observed in these spectral regions are produced by transitions between electronic states. The atomic nuclei in a molecule are held together by the electrons (the nuclei alone would repel each other). Depending on the orbitals in which the electrons are, we expect different electronic states of the molecule. An example can be found in Fig. 2.2 for the CN molecule, where we show the potential curves for the lowest three electronic states.

2.4.1 Orbital angular momentum

The motion of the electrons in an atom takes place in a spherically symmetric force field. As a consequence, the electronic orbital angular momentum **L** is a constant of the motion if the effect of the spin is small or neglected. In a

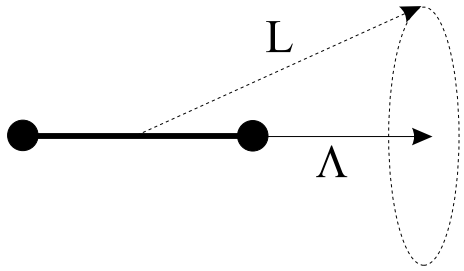

Figure 2.3: Precession of the orbital angular momentum **L** about the internuclear axis.

diatomic molecule, this symmetry is transformed into an *axial symmetry* about the internuclear axis. As a consequence, only the projection of the orbital angular momentum about the internuclear axis is a constant of motion. As illustrated in Fig. 2.3, the angular momentum **L** precesses about the internuclear axis maintaining the value of its projection on the internuclear axis (M_L). As usual, M_L can take the values

$$M_L = L, L-1, L-2, \ldots, -L. \tag{2.25}$$

Because M_L is a constant of motion, it is more appropriate to classify the electronic states of a molecule according to the value of M_L instead of **L** itself. In the electric field produced by the electronic cloud on the non-rotating molecule, reversing the directions of motion of all electrons does not change the energy of the system, while M_L is transformed into $-M_L$. Therefore, only the absolute value of M_L is important. Following standard notation, we write:

$$\Lambda = |M_L|, \tag{2.26}$$

which can take the following values:

$$\Lambda = 0, 1, 2, \ldots, L. \tag{2.27}$$

Similar to what happens in atomic spectroscopy, the electronic states $\Lambda = 0, 1, 2, 3, \ldots$ are indicated with the capital Greek letters $\Sigma, \Pi, \Delta, \Phi, \ldots$. Due to the inclusion of the absolute value in the definition of Λ, states with $\Lambda \geq 1$ are doubly degenerated (i.e., the $\Pi, \Delta, \Phi, \ldots$ states are degenerated, while Σ are not).

2.4.2 Spin

Just as for atoms, the spins of the individual electrons of both atoms form a resultant total spin **S**. If $\Lambda \neq 0$, the orbital motion of the electrons generates a magnetic field along the internuclear axis which produces a precession of **S** about the internuclear axis. The projection of the total spin on the internuclear axis is a constant of the motion and is designated as Σ, whose possible $2S+1$ allowed values are

$$\Sigma = S, S-1, S-2, \ldots, -S. \tag{2.28}$$

2.4.3 Total electronic angular momentum. Multiplets.

The total electronic angular momentum about the internuclear axis (denoted by $\mathbf{\Omega}$) is obtained by adding $\mathbf{\Lambda}$ and $\mathbf{\Sigma}$. Therefore, we define the quantum number for the total angular momentum along the internuclear axis by

$$\Omega = |\Lambda + \Sigma|. \tag{2.29}$$

If $\Lambda \neq 0$, there are $2S+1$ possible values of $\Lambda+\Sigma$. As a result of the interaction of **S** with the magnetic field produced by $\mathbf{\Lambda}$ on the internuclear axis, the levels with different value of $\Lambda + \Sigma$ have different energy. This multiplet splitting produces $2S+1$ components for each value of Λ. On the other hand, if $\Lambda = 0$, no coupling is possible and the Σ states are non-degenerate. The *multiplicity* of the electronic state is given by $2S+1$, in a similar fashion as in atomic physics.

Concerning the notation of the multiplets, the value of the multiplicity is added as a left superscript to Λ and the value of $\Lambda + \Sigma$ is added as a right subscript to Λ. Therefore, a term with $\Lambda = 3$ and $S = 2$ has the components: ${}^5\Phi_5$, ${}^5\Phi_4$, ${}^5\Phi_3$, ${}^5\Phi_2$ and ${}^5\Phi_1$. Additionally, it is usual to include a letter in front of the term name to give a fast idea of the energy ordering of the electronic levels. The fundamental level is labeled as X and the excited levels are labeled using $A, B, C, \ldots, a, b, c, \ldots$ in increasing order of energy, except for some exceptions. As an example, the energy levels of CH in increasing order of energy are $X\,{}^2\Pi$, $a\,{}^4\Sigma^-$, $A\,{}^2\Delta$, $B\,{}^2\Sigma^-$, etc. while those of OH are $X\,{}^2\Pi$, $A\,{}^2\Sigma^+$, $B\,{}^2\Sigma^+$, etc. (see Huber & Herzberg 2003 for other molecules). The superscripts + and − indicate the parity of the level and will be discussed in section §2.5.3.

2.5 Coupling of rotation and electronic motion

The interaction between the vibrational and electronic motions are taken into account by calculating the vibrational levels in a potential energy curve that depends on the electronic state under consideration. This potential energy represents the dependence of the electronic energy on the internuclear distance. The mutual interaction between vibration and rotation has been considered in §2.3.3. However, we have to consider the interaction between the rotational and electronic motions and indicate which are the quantum numbers that describe the molecular energies.

2.5.1 Hund's coupling cases

All the angular momentum of the molecule (electronic orbital $\mathbf{\Lambda}$, spin angular momentum $\mathbf{\Sigma}$ and rotational angular momentum $\mathbf{R}$) form a resultant total angular momentum which is designated by $\mathbf{J}$. If $\mathbf{\Lambda} = \mathbf{\Sigma} = 0$, $\mathbf{J}$ directly represents the rotational angular momentum, and the formulas of the simple rotator can be straightforwardly applied. For the rest of cases, we have to distinguish between different modes of coupling.

- **Hund's case (a).** We assume that the rotational motion is weakly interacting with the spin and orbital motions, while the electronic motion is strongly coupled to the internuclear axis. Therefore, $\mathbf{\Omega}$ is well defined and, together with the rotational angular momentum $\mathbf{R}$, form the total angular momentum $\mathbf{J}$. The vector diagram is shown in Fig. 2.4. In Hund's case (a) coupling, the orbital angular momentum $\mathbf{L}$ and the spin $\mathbf{S}$ precess about the internuclear axis, while $\mathbf{R}$ and $\mathbf{\Omega}$ nutate about the total angular momentum $\mathbf{J}$, which remains constant in magnitude and direction. An extra assumption is that the precession of $\mathbf{L}$ and $\mathbf{S}$ is much faster than the nutation of $\mathbf{\Omega}$ and $\mathbf{R}$.

  Given that $\mathbf{\Omega}$ is the projection of $\mathbf{J}$ over the internuclear axis (because $\mathbf{R}$ is perpendicular to the internuclear axis), the latter cannot be smaller than its projection, so:

  $$J = \Omega, \Omega + 1, \Omega + 2, \ldots \tag{2.30}$$

  Except for the missing levels with $J < \Omega$, the energy of the rotational levels are given by the formulas of the vibrating rotator.

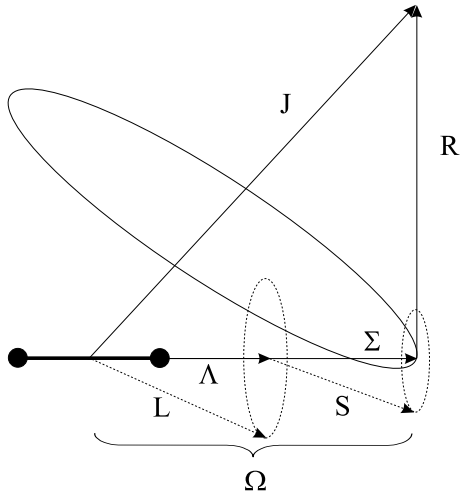

Figure 2.4: Vector diagram for Hund's case (a). The nutation of the internuclear axis is indicated with the solid-line ellipse. The much more rapid precessions of the **L** and **S** vectors about the internuclear axis are indicated by dotted-line ellipses After Herzberg (1950).

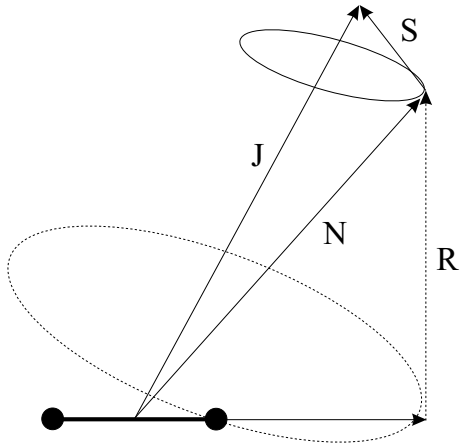

Figure 2.5: Vector diagram for Hund's case (b). The nutation of the internuclear axis (represented with the dotted-line ellipse) is much faster than the precession of **N** and **S** about **J** (represented with the solid-line ellipse).

- **Hund's case (b).** The total electronic orbital angular momentum is strongly coupled to the internuclear axis (Λ is still a good quantum number) while the spin is very weakly coupled to the internuclear axis. Therefore, $\mathbf{\Omega}$ is not defined. $\mathbf{\Lambda}$ and the rotational angular momentum $\mathbf{R}$ form a resultant $\mathbf{N}$ (the total angular momentum apart from spin), which can take the values

$$N = \Lambda, \Lambda + 1, \Lambda + 2, \ldots \tag{2.31}$$

  Care must be taken with the notation, because some authors (e.g. Herzberg 1950) use K instead of N. If $\Lambda = 0$ and $S \neq 0$, the spin is totally uncoupled from the internuclear axis and the electronic state always belongs to case (b) (i.e., the $^2\Sigma$, $^3\Sigma$, ... states). The angular momenta $\mathbf{N}$ and $\mathbf{S}$ form a resultant $\mathbf{J}$, the total angular momentum including spin, whose possible values are, according to the rules of angular momentum addition:

$$J = N + S, N + S - 1, N + S - 2, \ldots, |N - S|. \tag{2.32}$$

  The vector diagram can be seen in Fig. 2.5. In general, except when $N < S$, each level with a given value of N is composed of $2S + 1$ components characterized by a different value of J. The molecular rotation produces a very slight magnetic moment in the direction of $\mathbf{N}$, causing a small coupling of $\mathbf{S}$ and $\mathbf{N}$. This coupling produces a slight splitting of the levels with the same J and different value of N, which increases as N increases. This is the well-known spin-rotation coupling. Each of these components is given an integral value i=1, 2, 3,..., starting from the maximum value of J. For example, a molecule with spin $S = 1/2$ has components with $J = N + 1/2$ and $J = N - 1/2$, which are given the indices 1 and 2, respectively. A molecule with spin $S = 1$ has components with $J = N + 1$, $J = N$ and $J = N - 1$, which are given the indices 1, 2, and 3, respectively.

- **Hund's case (c).** In this case, the interaction between the electronic orbital angular momentum $\mathbf{L}$ and the spin $\mathbf{S}$ is stronger than the interaction with the internuclear axis. Therefore, Λ and Σ are not well defined. $\mathbf{L}$ and $\mathbf{S}$ form a resultant $\mathbf{J_e}$ which is then coupled to the internuclear axis giving rise to the component $\mathbf{\Omega}$. This electronic angular momentum is added to the rotational angular momentum $\mathbf{R}$ forming the total angular

momentum **J**. The rotational energy values are given by the same formulas as for case (a). For a schematic representation of the vector diagram, refer to Herzberg (1950).

- **Hund's case (d).** In this case, the orbital angular momentum **L** is strongly coupled to the rotational angular momentum **R**, forming the total angular momentum apart from spin (**N**) by angular momentum addition. Therefore, the values of N are:

$$N = R + L, R + L - 1, R + L - 2, \ldots, |R - L|. \tag{2.33}$$

  This resultant angular momentum **N** and the spin **S** form the total angular momentum **J**. Usually, the coupling between **N** and **S** is so weak that it is enough to consider only **N** as the total angular momentum. The vector diagram can be found on Herzberg (1950).

- **Hund's case (e).** As in Hund's case (c), we assume that **L** and **S** are strongly coupled, forming the resultant $\mathbf{J_e}$. However, this total electronic angular momentum couples to the rotational angular momentum **R** instead of with the internuclear axis, to give the total angular momentum **J**. Refer to Herzberg (1950) for the vector diagram.

Almost all the electronic states can be correctly studied assuming that case (a) or case (b) represent the coupling of angular momenta in the molecule. However, as we will see in the next section, there are some situations in which the molecule is in a coupling case intermediate between both cases.

2.5.2 Uncoupling phenomena

Hund's coupling cases are limiting cases. The relative strength of the couplings change when the rotation is increased, and a transition from one case to other occurs. Although some molecules can be correctly described with the limiting Hund's cases, intermediate cases are many times needed. In what follows we describe some of the uncoupling phenomena typically found.

- **Λ-doubling**. In Hund's cases (a) and (b) the interaction between the rotation and the electronic orbital angular momentum **L** has been neglected. We have seen that levels with $\Lambda \neq 0$ are doubly degenerate in the case

of zero rotation. However, when rotation is taken into account, the **L**-**R** interaction leads to a splitting into two components for each value of J. Although observable, this splitting is usually very small, only arriving to a few cm^{-1} for large values of J. The splitting is relatively the largest for terms with the smallest Ω.

- **Spin doubling**. While Σ states always belong to case (b), Π, Δ,... states usually belong to intermediate cases between (a) and (b). For these states, case (a) is usually a good approximation for no rotation or small rotation. However, as J increases, the rotational velocity increases and can become comparable with the precession of **S** about the internuclear axis. If the rotational velocity is increased further, the influence of the rotation dominates and the rotational angular momentum **R** couples with the projection of the orbital angular momentum $\mathbf{\Lambda}$ forming a resultant **N**. Then, the spin couples with **N** and forms the total angular momentum **J**. Therefore, we effectively have a transition from case (a) to case (b) when rotation increases, which is called spin-uncoupling.

  As we have seen, for small rotation the angular momentum **N** is not defined, since **S** is coupled to the internuclear axis. However, we can formally assign N values to the levels by direct extension to low rotation of the numbering used for high rotation. Molecules in the high rotation limit ($J \gg 1$) are usually very well described by the Hund's case (b) coupling, independently of the electronic state we are dealing with.

2.5.3 Parity

In the classification of the electronic states, it is of fundamental importance to specify the parity of the eigenfunctions under an inversion of the electronic and nuclear coordinates with respect to the center of mass of the molecule. If the eigenfunction of the state changes its sign under this inversion, the state is odd, while it is even if it does not change under this inversion. As we will show in Section §2.6, the importance of the parity of the energy is related to the existence of selection rules which have to be fulfilled in a molecular transition.

For a molecule without spin, the parity is given by the factor $p(-1)^J$, where J is the total angular momentum of the molecule, while $p = \pm 1$ is a factor which accounts for the parity of the electronic eigenfunctions under a reflection

under any plane passing through both nuclei. For a non-degenerate state (Σ state), we have a Σ^+ state ($p = 1$) if the eigenfunction does not change its sign, while we have a Σ^- state ($p = -1$) if the eigenfunction changes its sign. For states with $\Lambda \neq 0$, we have seen that electronic levels are degenerate for the two possible values of M_L. Each of the components, which are non-degenerate when rotation increases (Λ-doubling) has a definite parity (each one has a value of p).

There have been many attempts to define the parity of a rotational level. The labeling suggested by Brown et al. (1975) has become successful. It includes the effect of the spin into the definition of the parity. Levels are labeled as "e" or "f" according to the following scheme:

- Molecules with semi-integer value of J (semi-integer spin):
  - e levels have parity $(-1)^{J-1/2}$
  - f levels have parity $-(-1)^{J-1/2}$
- Molecules with integer value of J (integer spin):
  - e levels have parity $(-1)^J$
  - f levels have parity $-(-1)^J$

For the case of a molecule in which both nuclei have the same charge, the field in which the electrons move has, in addition to the symmetry axis, a center of symmetry. Therefore, the electronic eigenfunctions remain unchanged or have a sign change under a reflection on this center of symmetry. This symmetry property is indicated by adding a subscript g (even) or u (odd) to the term symbol (from the german "*gerade*" and "*ungerade*"). Therefore, we have Σ_u, Σ_g, Π_u, Π_g, ... levels. The spin has no influence on this symmetry property and therefore the components of a given multiplet term are either all even (g) or all odd (u).

We point out that the distinction between even and odd states under the reflection about the center of symmetry is independent of wether the molecule is homonuclear or not, provided the charge of both atoms is the same. Even for heteronuclear molecules, this distinction approximately holds when the charge of the atoms is very similar. This is the case of molecules like CN.

2.6 Selection rules

The quantum numbers introduced before for the description of the coupling affect the observed molecular spectra through the selection rules. As usual, the electric dipole selection rules are obtained by evaluation of the matrix elements $\mathbf{R_{ul}} = \langle\psi_u|\mathbf{M}|\psi_l\rangle$, where $\mathbf{M}$ is the electric dipole moment and ψ_u and ψ_l are the eigenfunctions of the upper and lower levels of the transition, respectively.

We distinguish between the selection rules that hold generally and those which hold only for some of the Hund's coupling cases.

2.6.1 General selection rules

For any atomic or molecular system, the selection rule for the quantum number J of the total angular momentum is

$$\Delta J = 0, \pm 1, \tag{2.34}$$

with the restriction that a $J = 0 \rightarrow J = 0$ radiative transition cannot take place. Together with this selection rule, parity selection rules hold quite generally, allowing only transitions in which there is a change in the parity of the levels:

$$+ \leftrightarrow -, \quad + \nleftrightarrow +, \quad - \nleftrightarrow -. \tag{2.35}$$

This selection rule for electric dipole transitions can be written as follows with the parity defined as in Brown et al. (1975):

$$\begin{aligned} &e \leftrightarrow f \text{ for } \Delta J = 0 \\ &e \leftrightarrow e \text{ and } f \leftrightarrow f \text{ for } \Delta J = \pm 1. \end{aligned} \tag{2.36}$$

2.6.2 Selection rules for Hund's cases (a) and (b)

Besides the general selection rules, there are some selection rules which hold only in Hund's cases (a) and (b). Since these two coupling cases are by far the most frequent, these selection rules have a quite general significance. As we have seen, the quantum number Λ is defined for both Hund cases, and the selection rule is:

$$\Delta\Lambda = 0, \pm 1, \tag{2.37}$$

so $\Sigma - \Sigma$, $\Sigma - \Pi$, $\Pi - \Pi$, ... transitions are allowed, while $\Sigma - \Delta$, $\Sigma - \Phi$, $\Pi - \Phi$, ... are forbidden. This selection rule is equivalent to the M_L selection rule for atoms in an electric or magnetic field.

The total spin **S** is well defined for both cases, and the selection rule for the associated quantum number is the same as for atoms, namely:

$$\Delta S = 0. \tag{2.38}$$

This means that we can only have transitions between states of the same multiplicity.

2.6.3 Selection rules for Hund's case (a)

The quantum number Σ corresponding to the projection of the total electronic spin on the internuclear axis is well defined in Hund's case (a). The selection rule for this quantum number is:

$$\Delta\Sigma = 0. \tag{2.39}$$

Therefore, if both states belong to case (a), transitions like ${}^2\Pi_{1/2} - {}^2\Pi_{1/2}$ and ${}^2\Pi_{3/2} - {}^2\Pi_{3/2}$ are allowed, while transitions like ${}^2\Pi_{3/2} - {}^2\Pi_{1/2}$ are forbidden.

The quantum number Ω of the projection of the total electronic angular momentum on the internuclear axis has the selection rule:

$$\Delta\Omega = 0, \pm 1. \tag{2.40}$$

This selection rule adds nothing new as long as the selection rules given by Eqs. (2.37) and (2.39) hold. However, this selection rule holds even in case that Λ and/or Σ loose their meaning, while Ω is still a good quantum number, as it happens in case (c).

If $\Omega = 0$ for both electronic states of a transition, $\Delta J = 0$ transitions are forbidden, and only $\Delta J = \pm 1$ holds. As a consequence, no Q branch appears for these transitions, like the ${}^3\Pi_0 - {}^3\Pi_0$ component of a ${}^3\Pi - {}^3\Pi$ transition.

2.6.4 Selection rules for Hund's case (b)

The quantum number N for the total angular momentum apart from the spin is well defined in case (b). If both states belong to case (b), the following selection rule holds:

$$\Delta N = 0, \pm 1, \tag{2.41}$$

with the restriction that $\Delta N = 0$ is forbidden for $\Sigma - \Sigma$ transitions.

2.6.5 General cases

The special selection rules just discussed hold if both states of a transition belong to one and the same coupling case. In the general case in which one state belongs to one coupling case and the other state to other, these selection rules lose their validity and there remain only the selection rules which hold for both cases simultaneously. Therefore, the number of branches allowed in such transitions is much greater.

As a result of the spin uncoupling, it often happens that both states approach case (b) for large rotations, while usually belonging to case (a) for small rotation. Therefore, the selection rules which hold change when rotation is increased.

2.7 Nomenclature of the transitions

In designating a given electronic transition, the upper state is always written first and then the lower. For example, $^1\Pi - ^1\Sigma$ means a transition between an upper level $^1\Pi$ and a lower level $^1\Sigma$. Sometimes, an arrow explicitly indicates if the transition is in emission ($^1\Pi \rightarrow ^1\Sigma$) or in absorption ($^1\Pi \leftarrow ^1\Sigma$).

Concerning the notation of an individual rotational transition, the convention of calling P branch to that with $\Delta J = J_u - J_\ell = -1$, R branch to that with $\Delta J = 1$ and Q branch to that with $\Delta J = 0$ holds. Due to the spin of the molecule, each of the rotational levels with a quantum number J are splitted into $2S + 1$ levels due to the interaction of the spin and the rotation. As mentioned above, each of these levels if labeled by an integer value i=1,2,3,... starting with $J = N + S$ and finishing with $J = |N - S|$. Although the rotational quantum number N is not well defined, it is useful to retain it in order to label the rotational levels. The spin-rotation index of the upper and lower level of a transition is appended as two subscripts to the P, Q or R. If both subscripts are the same, they are collapsed into only one for simplicity (i.e., R_{12}, $R_{22} \equiv R_2$, ...). If we take into account which is the variation of N during a transition, we can divide them into:

- *Principal branches*: they fulfill $\Delta J = \Delta N$. Thus, the upper and lower spin-rotation index have to be the same. They are usually the strongest

transitions in a given branch. As an example, for a molecule with $S = 1/2$, we have the P_1, P_2, R_1, R_2, Q_1 and Q_2 rotational lines. The Einstein coefficient of these transitions are comparable to the electronic transitions in atoms (although usually a bit smaller) .

- *Satellite branches*: they fulfill $\Delta J \neq \Delta N$. Thus, the upper and lower spin-rotation index have to be different. They are usually the weakest transitions in a given branch, although if the electronic state is not well reproduced in Hund's case (b), this conclusion may change. The Einstein coefficient of these transitions are usually some orders of magnitude lower than transitions belonging to the principal branches. As an example, for a molecule with $S = 1/2$, we have the P_{12} ($\Delta N = -2$), P_{21} ($\Delta N = 0$), R_{12} ($\Delta N = 0$), R_{21} ($\Delta N = 2$), Q_{12} ($\Delta N = -1$) and Q_{21} ($\Delta N = 1$) rotational lines. The transitions with $|\Delta N| \geq 2$ are forbidden from electric dipole selection rules under Hund's case (b) coupling. However, since molecules are sometimes not well described by pure Hund's cases, these transition are not strictly forbidden. Their Einstein coefficients are many orders of magnitude lower than the lines of the main branches or even those of the satellite branches.

As an example, a schematic representation of a transition between doublet states in case (b) is shown in Fig. 2.6, where each individual rotational transition is labeled, differentiating between lines from the principal branch and those from the satellite branch.

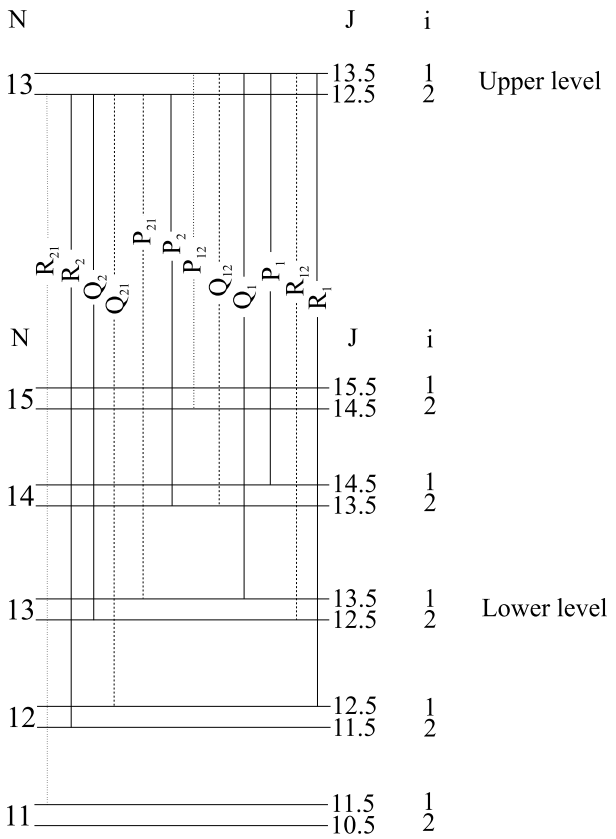

Figure 2.6: Energy diagram for a transition between two doublet states which are described under Hund's case (b) coupling. Each level is labeled by its quantum numbers N and J, indicating also the spin-coupling index i. High enough N values are selected in order to be sure that case (b) is more or less correct. All the possible transitions between a single upper rotational level are also indicated with their corresponding notation. The solid lines are those from the principal branch while the dashed lines are those from the satellite branch. The two lines marked with dotted lines are those with $\Delta N = \pm 2$, which are not permitted. After Herzberg 1950.

2.8 Résumé of molecular spectroscopy

We present in this section a brief summary of molecular spectroscopy in which we summarize all the properties presented in the chapter.

Type of angular momentum	Operator	Quantum numbers	
		Total	Projection
Electronic orbital	$\mathbf{L}$	L	$\mathbf{\Lambda} = 0, 1, 2, \ldots, L$
Electronic spin	$\mathbf{S}$	S	$\mathbf{\Sigma} = S, S-1, \ldots, -S$
Rotational	$\mathbf{R}$	R	$\cdots$
Total	$\mathbf{J} = \mathbf{R} + \mathbf{L} + \mathbf{S}$	J	$\mathbf{\Omega} = \lvert\mathbf{\Lambda} + \mathbf{\Sigma}\rvert$
Total apart from spin	$\mathbf{N} = \mathbf{R} + \mathbf{L}$	N	$\mathbf{\Lambda}$

Table 2.1: The angular momenta involved in Hund's coupling cases.

Hund's case	Case (a)	Case (b)
Good quantum numbers	Λ, S, J, Σ ($\Omega = \Lambda + \Sigma$)	Λ, S, J, N
Degeneracy (non-rotating)	$\begin{cases} 2 & \text{if } \Lambda \neq 0 \\ 1 & \text{if } \Lambda = 0 \end{cases}$	$\begin{cases} 2(2S+1) & \text{if } \Lambda \neq 0 \\ 2S+1 & \text{if } \Lambda = 0 \end{cases}$
Degeneracy (rotating)	$\begin{cases} 2 & \text{if } \Lambda \neq 0 \\ 1 & \text{if } \Lambda = 0 \end{cases}$	$\begin{cases} 2 & \text{if } \Lambda \neq 0 \\ 1 & \text{if } \Lambda = 0 \end{cases}$
Values of J	$\Omega, \Omega+1, \Omega+2, \ldots$	$N+S, N+S-1, \ldots, \lvert N-S\rvert$
Values of N	Not defined	$\Lambda, \Lambda+1, \ldots$

Table 2.2: Brief description of Hund's cases properties.

Value of the spin	Parity
Semi-integer	$\begin{cases} e \text{ levels have parity} (-1)^{J-1/2} \\ f \text{ levels have parity} -(-1)^{J-1/2} \end{cases}$
Integer	$\begin{cases} e \text{ levels have parity} (-1)^{J} \\ f \text{ levels have parity} -(-1)^{J} \end{cases}$

Table 2.3: Parity of the rotational levels.

Type of selection rule	Selection rule
Parity	$+ \leftrightarrow -, \quad + \nleftrightarrow +, \quad - \nleftrightarrow -$ or $\begin{cases} e \leftrightarrow f \text{ for } \Delta J = 0 \\ e \leftrightarrow e \text{ and } f \leftrightarrow f \text{ for } \Delta J = \pm 1 \end{cases}$
General	$\Delta J = 0, \pm 1$ (except $J = 0 \rightarrow J = 0$)
Case (a) + Case (b)	$\Delta \Lambda = 0, \pm 1$ $\Delta S = 0$
Case (a)	$\Delta \Sigma = 0$ $\Delta \Omega = 0, \pm 1$
Case (b)	$\Delta N = 0, \pm 1$

Table 2.4: Selection rules of rotational transitions.

3

Non-equilibrium chemistry in stellar atmospheres

In this chapter, we show how molecular abundances can be obtained, either assuming instantaneous chemical equilibrium or solving the full chemical evolution problem. We present the details of both schemes, including basic equations, implementation details, simple applications to the solar atmosphere, etc. We present in Section §3.3 an investigation of the relaxation times of molecular formation in the solar atmosphere. This serves as a background for understanding the results obtained in Section §3.5.1 in which we study in detail the time evolution of the CO abundance in the 1D hydrodynamical simulations of Carlsson & Stein (1997) and the effect of the finite reaction times in the emerging CO spectrum. Finally, we investigate in detail in Section §3.5.5 the molecular formation in the 3D hydrodynamical simulations of Asplund et al. (2000).

3.1 Instantaneous chemical equilibrium

Molecules are usually found in highly dynamic systems (e.g., the solar atmosphere, winds of AGB stars, ...) and their formation is influenced by the time variation of the physical conditions in the medium. However, when the dynamical timescales are much slower than the timescales of molecular formation, the approximation of Instantaneous Chemical Equilibrium (ICE) can be used

with extremely good results. Under the ICE approximation, molecules are assumed to be formed instantaneously and their abundances depend on just the local temperature and density. Another consequence of this assumption is that the specific reaction mechanisms that create and destroy a given molecule is irrelevant and only the molecule and its constituents are important. In spite of the great simplification, the ICE approximation holds in many astrophysical situations (Russell 1934, Tsuji 1964, Tsuji 1973, McCabe et al. 1979, etc.).

3.1.1 Basic equations

Consider three elements A, B and C which stick together to form the molecule $A_aB_bC_c$, in which a, b and c are the stoichiometric coefficients indicating the number of times an element is present in the molecule. Because the explicit reactions which form the molecule are irrelevant under the ICE approximation, it is enough to consider the following dissociative process for the formation of the molecule $A_aB_bC_c$:

$$A_aB_bC_c \Leftrightarrow aA + bB + cC. \tag{3.1}$$

This reaction is characterized by its dissociative reaction constant or equilibrium constant. It is given by the ratio between the product of the partial pressures of the individual elements and the partial pressure of the molecule:

$$K_p(T) = \frac{P_A^a P_B^b P_C^c}{P_{ABC}}, \tag{3.2}$$

being $K_p(T)$ a function of the temperature and P_i the partial pressure of the species i. For example, the equilibrium constant for the dissociation of CO and H_2 is given by

$$K_p^{CO}(T) = \frac{P_C P_O}{P_{CO}}, \qquad K_p^{H_2}(T) = \frac{P_H^2}{P_{H_2}}. \tag{3.3}$$

The partial pressure is related to the number density n_i of a given species by the usual ideal gas equation:

$$P_i = n_i kT, \tag{3.4}$$

where k is the Boltzmann constant and T the local temperature. This partial pressure is the pressure species i would yield if it were occupying all the volume.

The sum of all the partial pressures amounts the total pressure in the medium. Therefore, considering the case of an atmosphere with hydrogen and helium as the only components, the total pressure is given by:

$$P_T = P_H + P_{H^+} + P_{H^-} + P_{H_2} + P_{He} + P_{e^-}. \tag{3.5}$$

Following the same line of reasoning, one can consider the ionization equilibria for the atomic species:

$$\begin{aligned} A &\Leftrightarrow A^+ + e^- \\ A + e^- &\Leftrightarrow A^-, \end{aligned} \tag{3.6}$$

with their corresponding equilibrium constants:

$$K_{A^+}(T) = \frac{P_{A^+} P_{e^-}}{P_A} \qquad\qquad K_{A^-}(T) = \frac{P_{A^-}}{P_A P_{e^-}}. \tag{3.7}$$

We now define the *fictitious pressure* $P(i)$ as the pressure produced by element i if all the gas were in the neutral form of the atomic species i. In general, it is usual to give the partial pressures of all the atomic species in terms of the fictitious pressure of hydrogen $P(H)$. The coefficient relating one and the other is the abundance of each element with respect to hydrogen, $A(i)$, so $P(i) = A(i)P(H)$. The abundance of each atomic species depends on the metallicity of the star we are considering. For the solar case, we have selected the standard solar abundances given by Grevesse (1984).

Under ICE conditions, the number of atoms and molecules are obtained by solving the conservation of mass and the chemical equilibrium conditions given by Eq. (3.2). The conservation of mass establishes that the sum of the partial pressures of all the species containing a given atomic element (taking into account the stoichiometry) equals the fictitious pressure of the given element:

$$P(i) = P_i + P_{i^+} + P_{i^-} + \sum_k \omega_k^i P_k, \tag{3.8}$$

where P_i, P_{i^+} and P_{i^-} are the partial pressure of the neutral element i, and the ionized elements i^+ and i^-, respectively, while P_k is the partial pressure of molecule k which has species i in its composition. ω_k^i is the stoichiometric coefficient which indicates the number of times element i appears in molecule k.

The sum is extended over all the molecules in which the element i takes part. The previous equation can be rewritten with the aid of Eqs. (3.2) and (3.7):

$$P(i) = P_i + K_{i^+}\frac{P_i}{P_{e^-}} + K_{i^-}P_iP_{e^-} + \sum_k \omega_k^i \frac{P_i^{\omega_k^i}P_j^{\omega_k^j}\cdots P_l^{\omega_k^l}}{K_p^{(k)}(T)}, \qquad (3.9)$$

where i, j, ..., l are the atomic species composing molecule k, $\omega_k^i + \omega_k^j + \ldots + \omega_k^l = n_k$ is the number of atoms of molecule k and $K_p^{(k)}(T)$ is its equilibrium constant. Charged molecules can be easily included by taking into account its dissociation and the ionization equilibrium, simultaneously. Consider the dissociation equilibrium of a ionized diatomic molecule. The only thing to take into account is that when a charged molecule dissociates, the atomic element which remains ionized is the one with the lowest ionization potential:

$$AB^+ \Leftrightarrow A^+ + B, \qquad (3.10)$$

so that $D_0(A) < D_0(B)$. Therefore, using Eq. (3.2) and Eq. (3.7) we can calculate the partial pressure of the ionized molecule:

$$K_p(T) = \frac{P_{A^+}P_B}{P_{AB^+}} = \frac{K_{A^+}(T)}{P_{e^-}}\frac{P_AP_B}{P_{AB^+}}, \qquad (3.11)$$

We can write an equation like Eq. (3.9) for each of the N atomic species included in the calculation. Therefore, once the molecular and ionization equilibrium constants are known, we have a set of N non-linear algebraic equations which depend on the local temperature and density. The ICE approximation is intrinsically local since it depends only on the local values of the temperature and density. Therefore, for calculating the molecular number densities in a model atmosphere, we have to solve the algebraic system of equations for each point in the atmosphere. Once the partial pressures for all the atomic species are known, we can calculate the ensuing atomic number densities by using Eq. (3.4). The molecular number densities are calculated by solving for their partial pressures in Eq. (3.2), using the equilibrium constant appropriate for each molecule.

3.1.2 Equilibrium constants

As we have seen, the problem of obtaining the atomic and molecular number densities is completely defined once the temperature and the total density (or

pressure) is known. However, we also need to know the value of the equilibrium constant for each temperature. Consider the dissociative equilibrium given by Eq. (3.1). The value of the equilibrium constant can be obtained with the aid of the partition function of the molecule and of the individual atomic components, their respective masses and the dissociation energy D_0 (see, e.g., Tejero Ordoñez & Cernicharo 1991 for detailed information on how the equilibrium constants can be calculated). The expression is given by (Tejero Ordoñez & Cernicharo 1991 and references therein):

$$K_p(T) = (kT)^{NA-1} \left(\frac{2\pi kT}{h^2}\right)^{3(NA-1)/2} \left(\frac{m_A^a m_B^b m_C^c}{m_{ABC}}\right)^{3/2} \left(\frac{\phi_A^a \phi_B^b \phi_C^c}{\phi_{ABC}}\right) e^{-D_0/kT}, \tag{3.12}$$

where m_i is the mass of atomic or molecular species i, $NA = a + b + c$ is the number of atoms present in the molecule, ϕ_i is the partition function of species i. h and k stand for the Planck and Boltzmann constants, respectively. This is nothing but the law of mass action. The partition function of the atomic and molecular species are calculated with the usual formula:

$$\phi = \sum_j g_j e^{-E_j/kT}, \tag{3.13}$$

where g_j is the degeneracy of level j and E_j its energy. Ideally, the sum has to be extended over all the energy levels of the species. However, due to the difficulty of accounting for all the energy levels, the most complete available set of energy levels must be used. For molecules, the partition function has to include the contribution from the electronic, vibrational and rotational levels. Since this summation cannot be performed each time an ICE calculations is being performed, several works have been aimed at building tables with polynomial fits to the partition functions (Russell 1934, Tsuji 1971, Sauval & Tatum 1984, Tejero Ordoñez & Cernicharo 1991). If we substitute the values of the constants in the *mks* unit system, and take logarithms in Eq. (3.12), we end up with the following formula:

$$\begin{aligned} \log K_p(T) &= 3.41405(NA-1) + \frac{5}{2}(NA-1)\log T + \frac{3}{2}\log\frac{M_A^a M_B^b M_C^c}{M_{ABC}} + \\ &\quad \log\frac{\phi_A^a \phi_B^b \phi_C^c}{\phi_{ABC}} - 5039.9\frac{D_0}{T}, \end{aligned} \tag{3.14}$$

where $M_{ABC} = aM_A + bM_B + cM_C$ is the molecular weight and M_i is the atomic weight of each species. The dissociation energy is now given in eV. This expression gives the equilibrium constant for a given temperature in terms of the partition function and the masses of the molecule and its constituents and the molecular dissociation energy. The accuracy in the equilibrium constant is now given by the accuracy one can obtain for the partition function and the dissociation energy (either measured or calculated using quantum-mechanical methods). The equilibrium constant can be transformed to the *cgs* unit system by noting that:

$$\log K_p^{cgs}(T) = \log K_p^{mks}(T) + NA. \tag{3.15}$$

From direct inspection of Eq. (3.12), we can see that the equilibrium constant strongly depends on the dissociation energy. Therefore, from the combination of Eqs. (3.12), (3.4) and (3.2) it is expected that the molecular number density is proportional to $e^{D_0/kT}$. For this reason, molecules with a higher dissociation energy are more abundant than molecules with a lower dissociation energy. This is correct only approximately because the non-linearities of the system of equations can lead to molecules with lower dissociation energy to be more abundant than molecules with a higher dissociation energy.

Several authors have published compilations of equilibrium constants in the form of polynomial fits. Let us briefly summarize the available data:

- Russell (1934). This is one of the first works in which an extensive calculation of the equilibrium constants are obtained. A compilation of the molecular constants is done for about thirty molecules and used for the interpretation of the molecular bands in the Sun and other stars with different chemical composition. It was shown in this work that many of the molecular bands which had been observed in the stars at that time could be interpreted based on the theory of dissociative equilibrium, as stated in the previous sections. The small set of molecules included in the calculations led to incorrect results as shown in later works, but it represents the first serious attempt to apply the theory of dissociative equilibrium to the interpretation of molecular bands.

- Tsuji (1971). This much recent work is considered as a classical reference. A set of 44 molecules composed of H, C, N and O are included, obtaining the molecular abundances for a range of temperatures and total gas

pressures, corresponding to stars of different spectral types. The most updated molecular data was used and one of the most important results was the demonstration that polyatomic molecules like CH_4, C_2H_2, NH_3, CH_2, ... are important for some physical conditions. However, these special physical conditions are not typical in stars like the Sun, except perhaps in the colder regions like sunspots.

- Sauval & Tatum (1984) This work is considered one of the most exhaustive calculations of partition functions and equilibrium constants. The molecular data is obtained for 300 diatomic molecules of astrophysical interest and for the relevant atoms for a temperature range from 1000 to 9000 K. Almost all the molecular spectroscopic data is obtained from Huber & Herzberg (1979) in order to lead to a homogeneous set of data.

- Tejero Ordoñez & Cernicharo (1991) This work represent one of the biggest compilations of molecular data for 240 molecules. Spectroscopic data for 128 diatomic molecules and equilibrium constants for 240 diatomic and polyatomic molecules are obtained based on the determination of the partition function by summation of Eq. (3.13). The electronic energy levels and the vibrational and rotational constants are those obtained from the compilation of molecular data from different sources. In this thesis we have made use of the equilibrium constants and partition functions of this work which are complete enough and represents a totally self-consistent work. The molecular data is given as the coefficients of a polynomial fit to the partition function and equilibrium constants.

3.1.3 Numerical method

We have developed a computer program which solves the non-linear system of equation given by Eq. (3.9). To this end, we have applied a Newton-Raphson method for the solution of nonlinear equations (Press et al. 1986). We will briefly sketch the basis of this method. The system of equations given by Eq. (3.9) can be rewritten as:

$$F_i(P_1, P_2, \ldots, P_N) = 0 \qquad i = 1, 2, \ldots, N, \tag{3.16}$$

where N is the number of included atomic species, while the N unknowns P_i are the partial pressures of the atomic elements. We denote by $\mathbf{P}$ the entire vector

of unknowns P_i and by $\mathbf{F}$ the entire vector of functions F_i. In the neighborhood of $\mathbf{P}$, each of the functions F_i can be expanded in Taylor series:

$$F_i(\mathbf{P}+\delta\mathbf{P}) = F_i(\mathbf{P}) + \sum_{j=1}^{N} \frac{\partial F_i}{\partial P_j}\delta P_j + O(\delta\mathbf{P}^2), \tag{3.17}$$

where $\delta\mathbf{P}$ is a correction to the partial pressure vector. The matrix of partial derivatives appearing in the previous equation is the *Jacobian* matrix $\mathbf{J}$, defined as:

$$J_{ij} = \frac{\partial F_i}{\partial P_j}. \tag{3.18}$$

One has to take into account that this Jacobian matrix can be calculated analytically by calculating the partial derivatives of Eq. (3.9). The previous Eq. (3.17) can be written in matrix notation as:

$$\mathbf{F}(\mathbf{P}+\delta\mathbf{P}) = \mathbf{F}(\mathbf{P}) + \mathbf{J}\cdot\delta\mathbf{P} + O(\delta\mathbf{P}^2). \tag{3.19}$$

If we now neglect terms of order $\delta\mathbf{P}^2$ and higher and assume that the perturbed vector of partial pressures is the solution to the system of equations –that is, we set $\mathbf{F}(\mathbf{P}+\delta\mathbf{P}) = 0$– we end up with a set of linear equations for the corrections:

$$\mathbf{J}\cdot\delta\mathbf{P} = -\mathbf{F}. \tag{3.20}$$

Since we have neglected terms of order two and higher, the new estimation $\mathbf{P}_{\rm new} = \mathbf{P}_{\rm old} + \delta\mathbf{P}$ is not the exact solution to the nonlinear system and the procedure must be iterated to convergence.

3.1.4 Molecular abundances in the solar atmosphere

In order to give an idea of the molecular abundances in different regions of the solar atmospheric plasma, we have solved the ICE problem at all the heights of various solar models. We have chosen the FAL-C model (Fontenla et al. 1993) as representative of the magnetic network of the most quiet regions of the Sun, the COOL-C (Ayres et al. 1986) model as representative of the inter-network regions and a granular and intergranular models from the 3D hydrodynamical simulations of Asplund et al. (2000). The temperature profiles of the four models are shown in Fig. 3.1. Note that the granular and intergranular models

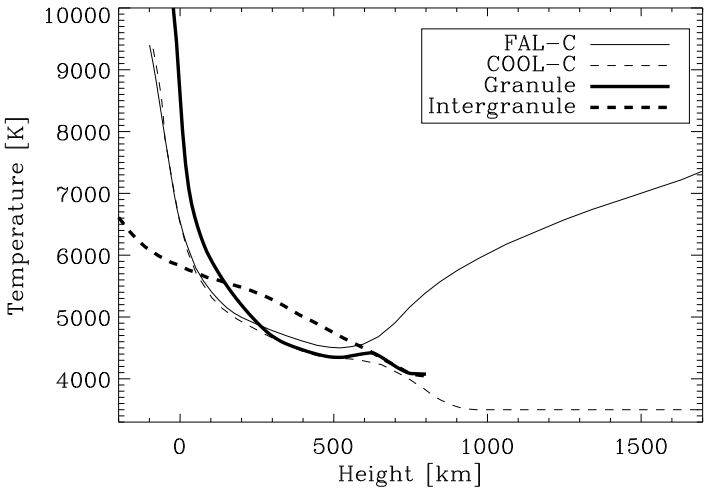

Figure 3.1: Temperature stratification of the FAL-C, COOL-C, granular and intergranular models. Note that the upper boundary for the granular and intergranular models is placed at 800 km because this simulation did only include photospheric regions.

arrive only to 800 km above the visible solar "surface" (defined as the position of continuum optical depth unity at 5000 Å at vertical incidence) because the 3D simulation only included photospheric regions. On the other hand, FAL-C and COOL-C semi-empirical models do include a chromospheric region since they were constructed to fit observed spectral features which are generated in the chromosphere. We now discuss some of the properties of the molecular abundances shown in Fig. 3.2, which we have calculated in each atmospheric model:

- **FAL-C**. The upper left panel of Fig. 3.2 shows the molecular abundances relative to the hydrogen abundance for the FAL-C quiet Sun model. We can see that the molecular abundances of all the species considered have a peak below ∼500 km, which is the atmospheric height where the model has its temperature minimum. The most abundant molecule is H_2 due to the high abundance of atomic hydrogen. The second most abundant molecule is CO. This results in part by its extremely high dissociation

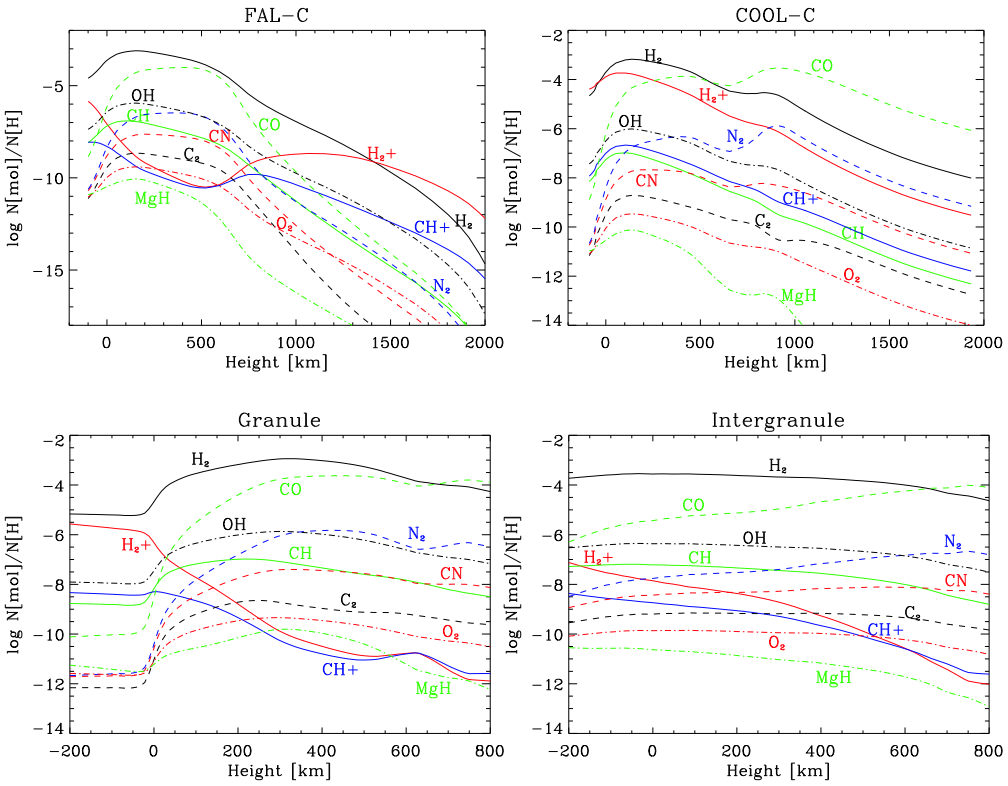

Figure 3.2: Molecular abundances relative to the total hydrogen abundance for the semi-empirical models FAL-C and COOL-C and two models taken from the 3D hydrodynamical simulations of Asplund et al. (2000) representative of a granule and an intergranule.

potential of 11.23 eV which makes this molecule quite difficult to dissociate at the typical temperatures in the solar photosphere. However, in this log-linear plot we see that the abundance of all the molecules fall above 500 km following an almost linear trend. This is caused by the exponential decrease of the density in the solar atmosphere. Consequently, there is a decrease in the number of collisions and, therefore, a decrease in the number density of the molecular species. Furthermore, the exponential decrease is accompanied by a rise in the kinetic temperature (the chromospheric temperature rise) which plays also a role in decreasing the

molecular abundances by its effect on the equilibrium constant. However, the physical conditions in these regions are favorable for the formation of ionized species like H_2^+ and CH^+ which can even become more important than the molecular hydrogen itself.

- **COOL-C**. The molecular abundances in this semi-empirical model are shown in the upper right panel of Fig. 3.2. This model atmosphere presents a higher relative abundance because the COOL-C model is colder than FAL-C. The COOL-C model has an almost constant temperature above 1000 km and, therefore, the fall of the molecular abundances above 1000 km is essentially produced by the decrease in the density due to the exponential stratification. Although below 600 km the most abundant molecule is H_2, above this height the most abundant molecule is CO, reaching a peak at $\sim$900 km.

- **Granular model**. As seen in Fig. 3.1, the granular plasma is very hot deep in the photosphere. As a consequence, the molecular abundances in this region are quite low. The molecular abundances are shown in the lower left panel of Fig. 3.2. H_2 and H_2^+ become the most abundant molecules, although still 5 orders of magnitude lower than atomic hydrogen. CO only becomes dominant above $\sim$700 km while deeper inside it is 5 orders of magnitude lower than molecular hydrogen. Since temperature and density are monotonically decreasing with height in the atmosphere, the formation of ionized molecular species is not favored and its abundance rapidly decreases when going outwards.

- **Intergranular model**. The temperature stratification in the intergranular gas is much less steeper than in the granular plasma and this behavior is transferred to the stratification of molecular abundances. CO becomes the most important molecule above $\sim$650 km, while H_2 is the most important below this height. The behavior of the ionized species is similar to what happens in the granule, although their abundance in the deeper regions is much lower due to the lower temperature. The molecular abundances are shown in the lower right panel of Fig. 3.2.

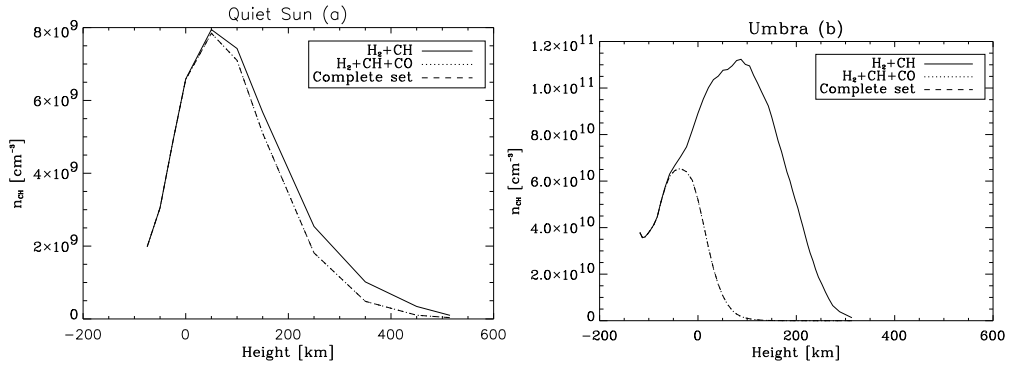

Figure 3.3: CH abundance obtained when considering different sets of molecules to solve the chemical equilibrium equations: H_2 and CH (*solid lines*), H_2, CO and CH (*dotted lines*), and up to 12 molecular species, including H_2, CO and CH (*dashed line*). The latter can be regarded as the exact solution. In the quiet Sun model (see panel (a)), even considering the sole formation of CH gives reasonable values. This approximation clearly breaks down in umbrae (see panel b). In this case, however, including just H_2 and CO renders good results. Note that the dashed and the dotted lines are overlapped and they cannot be distinguished graphically.

3.1.5 Completeness

The size N of the system of equations depends only on the number of atomic species included in the problem. The number of molecular species does not increase the size, but adds more terms in each Eq. (3.16). The larger the number of molecular species included, the more realistic the result would be. The number of species included (atomic and molecular) is one of the most important parameters, together with the value of the equilibrium constants. One decides the number of molecular species included in the model according to the problem under investigation. It is a compromise between the realism of the calculation and the time to solve the problem. The list of molecules for which we have equilibrium constants are formed by combinations of 21 atomic species. Therefore, we have decided to always maintain the size of the system to 21×21 (the maximum size) and the free parameter is the number of molecular species included. If a given atomic species is not entering in the formation of any molecular species, we only solve its ionization equilibrium.

We have applied our ICE code to calculate molecular number densities for

many molecules in the solar atmosphere. We have even included molecules which, although having low abundances, show conspicuous signals in the solar spectrum (either the non-polarized or the polarized spectrum). Therefore, we will discuss the number of molecular species needed for molecules with high abundance and those with low abundance.

High abundance molecules

If we are interested in one of the most abundant molecules in the solar environment, it is enough to include only a restricted subset of the molecular species in our database. The formation of the less abundant molecules negligibly affects the formation of the more abundant ones, which are mainly driven by the rest of more abundant molecules and the atomic species.

As an example, we will discuss the formation of CH in the solar atmosphere. Except in the umbrae of sunspots, most of the photospheric plasma in the quiet Sun is in the form of atoms. We have verified that a restricted subset containing CH, CO, H_2, H_2^+, C_2, N_2, O_2, CN, NH, NO, OH and H_2O is complete enough for a reliable calculation of the number density of CH molecules. However, for the calculation of the CH abundance, this subset can be reduced further by including simply H_2, CO and CH. This gives correct results because H_2 and CO are usually the most abundant molecules. Almost all the hydrogen that is not in atomic form is in the form of molecular hydrogen and the rest is taken by the formation of CH (the rest of molecules containing hydrogen, even if they are more abundant than CH, do not influence the formation of CH since the hydrogen used in these molecules is negligible with respect to the most abundant H_2). On the other hand, almost all the oxygen and carbon not in atomic form is in the form of CO, and the rest is taken by CH (similarly to what happens with hydrogen, the rest of molecules containing hydrogen do not influence the formation of CH). Therefore, the reduced set of equations given by Eq. (3.9) can be written as:

$$\begin{aligned} P(H) &= P_H + \frac{P_C P_H}{K_{CH}} + 2\frac{P_H^2}{K_{H_2}} \\ A_C P(H) &= P_C + \frac{P_C P_O}{K_{CO}} + \frac{P_C P_H}{K_{CH}} \\ A_O P(H) &= P_O + \frac{P_C P_O}{K_{CO}}, \end{aligned} \tag{3.21}$$

which can be even solved analytically. In order to show the effect of the number of molecular species included in the system, we have solved the ICE equations in two different photospheric models: the quiet Sun model VAL-C of Vernazza et al. (1981) and the umbra model of Collados et al. (1994). We have done calculations for the following cases:

1. CH and H_2;
2. CH, CO and H_2;
3. CH, CO, H_2, H_2^+, C_2, N_2, O_2, CN, NH, NO, OH and H_2O,

where the third case is supposed to represent the exact solution. The general behavior is very well illustrated in Fig. 3.3, where we have indicated as *complete set* that obtained from case 3. The number of CH molecules corresponding to cases 2 and 3 differ by less than 0.01 % in the quiet Sun (Fig. 3.3a). Even if the formation of CO is neglected (case 1), the errors are smaller than 10 % (see Fig. 3.3a). We have verified that the approximation corresponding to cases 1 and 2 works even better in hotter models, like models of network and plage regions. However, sunspot umbrae are different. Here the CO exhausts the carbon available to create CH, and its formation must be considered (Fig. 3.3b). The approximation in case 2 still holds within 1 %.

Therefore, it is shown that for very abundant molecules, smaller subsets of the total database can be used without obtaining a very big difference in the calculated molecular number densities. However, things might change for other molecules, even if its abundance is supposed to be high. Therefore, it turns out necessary to study in detail each case if one is interested in speeding up the calculations by reducing the numerical work. On the other hand, we think that the actual computing power is high enough to permit the solution of the ICE problem with the full molecular database without many problems except in selected situations in which poor convergence is obtained in the Newton-Raphson scheme. This poor convergence can be produced by initializing the scheme very far from the final solution. In this situation, the assumptions made on the Newton-Raphson method are broken (see Eq. 3.19) and the method does not converge. However, more powerful numerical schemes are available which converge to the correct solution even if the initialization is far from the solution (see Press et al. 1986 for a description of such global methods).

Low abundance molecules

When one is interested in the abundance of trace molecules, a very careful selection of molecular species has to be done. Since the numerical methods for the solution of the ICE problem are very fast, we think it is worth including the whole database of molecular species. The system turns out to be extremely non-linear, but the solution is usually obtained in less than 10 iterations.

3.2 Formulation of the chemical evolution problem

3.2.1 Basic equations

The mechanisms responsible for the formation or destruction of a molecule are of no importance under the ICE approximation. However, this assumption is only valid when the equilibrium situation has been reached. In any other case, the formation and destruction paths and their timescales are of crucial importance.

When the timescales in which the physical conditions change in a gas are smaller than the time to reach the molecular equilibrium abundances, it is fundamental to consider all the reactions which create and destroy a given species and solve the full chemical evolution (CE) problem. The change in time of the abundance of a given species i can be modeled with the following set of nonlinear ordinary differential equations (e.g., Bennett 1988):

$$\begin{aligned}\frac{dn_i}{dt} = &\sum_A \sum_B \sum_C k_{ABC} n_A n_B n_C + \sum_A \sum_B k_{AB} n_A n_B \\ &+ \sum_A k_A n_A - \sum_A \sum_B k_{ABi} n_A n_B n_i \\ &- \sum_A k_{Ai} n_A n_i - k_i n_i .\end{aligned} \tag{3.22}$$

We have classified the set of reactions according to the number of species which have to collide to let the reaction take place:

- **Three-body reactions**. The reactions are of the type A + B + C → *products*. They are included in the model by means of the first and the fourth terms in Eq. (3.22). They correspond to reactions which

create and destroy species i from the reaction of other three components, respectively. They are characterized by the reaction rates k_{ABC} in units of $cm^6\ s^{-1}$ whose value is usually extremely small. They typically give a negligible contribution to the total rate of variation of the abundance of species i for low density media. On the other hand, for relatively high density media like the solar photospheric plasma these reactions become extremely important. For example, the catalytic formation of hydrogen by the three body reaction H+H+H $\rightarrow$ H_2+H has a rate of $\sim 10^{-30}$ cm^6 s^{-1}. However, the typical hydrogen densities in the solar photosphere are of the order of 10^{15}-10^{17} cm^{-3} and the rate of formation of H_2 turns out to be of the order of 10^{15}-10^{21} cm^{-3} s^{-1}.

- **Two-body reactions**. The reactions are of the form $A + B \rightarrow products$. They are included in the model by means of the second and fifth terms in Eq. (3.22). They correspond to reactions which create and destroy species i from the reaction of other two components, respectively. They are characterized by the reaction rates k_{AB} in units of $cm^3\ s^{-1}$ and typically represent the most important reactions in almost all the media in which chemical reactions take place.

- **One-body reactions**. The reactions are of the form $A \rightarrow products$. They usually represent photodissociation or photoionization in which the species is dissociated by photons of energy greater than the dissociation potential (this is only valid for molecular species because atomic species cannot dissociate) or ionized by photons higher than the ionization potential (valid both for atomic or molecular species). Therefore, these reactions are often written as $A + h\nu \rightarrow products$, where we have explicitly indicated the necessity of a radiation field for the reaction to take place. This dependence on the radiation field present in the medium is implicitly taken into account in the reaction rate k_A in units of s^{-1}. The model includes these reactions by means of the third and sixth terms in Eq. (3.22), corresponding to reactions which create and destroy species i, respectively.

Once the physical conditions, the set of species included in the model, and the reaction rates of the reactions which take place among them are known, the system of equations given by Eq. (3.22) is completely defined. This set of

nonlinear differential equations represents a very *stiff* problem because of the different variables and rates having disparate ranges of variation. A suitable method that can cope with this stiffness has to be used. We employ an algorithm based on the backward differentiation formula which can assure stability (see e.g. Gear 1971) and allow to use time steps high enough to obtain the solution for very long evolution times.

3.2.2 Initial conditions

In order to solve the set of first order differential equations (3.22) we need the initial conditions for all the unknowns. There are two obvious options depending on the study we want to perform:

- **Zero molecular abundance**. This means that we set the number density of all the molecular species to zero and all the atomic number densities proportional to the hydrogen abundance, where the proportionality is given by the abundance of every atomic species relative to hydrogen. For chemical studies in the solar atmosphere, we have selected the atomic abundances given by Grevesse (1984). For metal-poor or metal-rich environments, these abundances can be changed accordingly. This type of initial condition can be used to verify the formation time of the molecular species at given heights of different atmospheric models.

- **ICE**. This means that the initial number densities are obtained assuming the ICE approximation.

The chosen initial condition should be in accordance with the problem under investigation. In order to be conservative, we consider that initializing with the abundances given by the ICE approximation is a good option in general. This approach is better for regions of high density and temperature since the equilibrium abundances are rapidly obtained. On the contrary, the zero molecular abundance option may be of application for regions where extreme shocks have just passed and molecules have been efficiently destroyed.

3.2.3 Reaction databases

In order to get reliable results out of Eqs. (3.22), it is desirable to include all the reactions that can produce or destroy a given species. Incompleteness in the

reaction database will produce differences between the molecular abundances obtained in the ICE approximation and those obtained by solving the chemical evolution equations until reaching the equilibrium solution. Time-dependent chemistry has been extensively used in the interstellar medium (ISM) (e.g., van Dishoeck & Blake 1998), typically including only two-body reactions, photoionization and photodissociation by the interstellar UV radiation field as the set of fundamental processes. This approximation is justified owing to the low densities present in the ISM that make three-body reactions extremely rare. There are some databases with reactions oriented towards interstellar chemistry. This is the case of the UMIST[1] astrochemistry database (Le Teuff et al. 2000) which was recently updated to include 4113 gas-phase reactions important for interstellar and circumstellar chemistry among 396 species involving the 12 elements H, He, C, N, O, Na, Mg, Si, P, S, Cl and Fe. This database includes two- and one-body gas-phase reactions, but lack from the important three-body reactions. Therefore, this database does not contain the full set of reactions needed for solar-like stars.

For our problem, it is better to use a chemical reaction database oriented towards the description of combustion reactions Konnov (2000)[2]. This database contains reactions mechanisms which take place in the Earth environment in a combustion process. Therefore, they are useful for high density media at high temperature (conditions compatible with the solar atmosphere ones). Contrarily, this database lacks from some reactions present in the UMIST database which are important in the solar environment. The final database we are using is a combination of combustion and interstellar reaction databases. Our database contains 1950 reactions between species involving H, He, C, N and O.

Common sense suggests that the higher the temperature, the faster a given chemical reaction takes place. Quantitatively this relationship between the rate a reaction proceeds and its temperature is determined by the Arrhenius equation:

$$k(T) = Ae^{-E_a/\mathcal{R}T}, \tag{3.23}$$

where $\mathcal{R} = 8.314\times10^7$ erg K^{-1} is the universal gas constant, equivalent to $\mathcal{R} = kN_A$, where k is the Boltzmann constant and N_A is Avogadro's number. E_a is the activation energy of the reaction, i.e. the amount of energy required

[1] `http://saturn.ma.umist.ac.uk:8000/~tjm/rate/rate.html`

[2] `http://homepages.vub.ac.be/~akonnov/`

to ensure that a reaction happens. This energy is necessary because there is usually a potential barrier between the reactants and the products, even when the products are more stable than the reactants. A is assumed to be a constant in the Arrhenius equation, although usually depends on the temperature. We will model this temperature dependence as a power-law. Therefore, the final expression for the reaction rate we will use is:

$$k(T) = k_0 T^{\beta} e^{-\gamma/T}, \tag{3.24}$$

where $\gamma = E_a/kN_A$. As we have said, reactions take place by the collision of the reactants with an energy higher than the activation energy. The higher the temperatures, the higher the probability that two molecules will collide. This higher collision rate results in a higher kinetic energy, which results in collisions with enough kinetic energy to surpass the activation energy of the reaction. This intuitive idea is represented in the Arrhenius equation by the exponential term, which increases as the temperature increases. For example, consider the reaction $2NO_2 \rightarrow 2NO + O_2$ with a reaction rate of 10^{-10} s^{-1} at 300 K and an activation energy of 111 kJ mol^{-1}. The ratio between the reaction rate at two temperature can be obtained by the expression:

$$\frac{k(T_1)}{k(T_2)} = \left(\frac{T_1}{T_2}\right)^{\beta} e^{-\gamma\left(\frac{1}{T_1}-\frac{1}{T_2}\right)}. \tag{3.25}$$

If we assume that $\beta = 0$, the rate reaction at 273 K is $k(273\text{ K}) = 1.23\times10^{-2}$ $k(300\text{ K})$. Therefore, a reduction of a factor of 80 is obtained in the reaction rate by a small reduction of 27 K in the temperature. It is clear that the temperature is a crucial factor in determining how fast the chemistry is. In a very crude first-order approximation, we can assume that chemical reactions take place the faster the higher the temperature is by neglecting the completely nonlinear character of the chemical evolution equations. However, this very crude approximation is often only correct for very abundant species like CO, whose time evolution abundance barely depends on the rest of species and only on the atomic carbon and oxygen abundances.

3.2.4 Photodissociation

We have pointed out that one-body reactions are photodissociations and photoionizations produced by the radiation field present in the medium where the

reactions are taking place. If this radiation field has a strong contribution in the UV region, one-body reactions can become important and affect the chemistry. Photodissociation plays a dominant role in the chemistry of diffuse interstellar clouds and in the outer parts of dense clouds (Bates & Spitzer 1951). It has been realized that cosmic-ray induced photons can significantly affect the chemistry inside dense clouds (Prasad & Tarafdar 1982, Sternberg et al. 1987). Finally, it can be also important for the outer parts of the circumstellar envelopes (Goldreich & Scoville 1976).

The mean photodissociation rate for a given molecular species can be written as:

$$k_{\rm photo} = \frac{4\pi}{hc} \int_{\lambda_{\rm H}}^{\lambda_{\rm dis}} \lambda J_\lambda \sigma(\lambda) d\lambda. \tag{3.26}$$

J_λ stands for the mean intensity in the medium, $\sigma(\lambda)$ corresponds to the cross section for the photodissociation processes and c and h are the speed of light and the Planck constant, respectively. The integral is extended from the Lyman limit $\lambda_{\rm H}$ at 912 Å to the molecular dissociation potential in wavelength units $\lambda_{\rm dis}$. Bluer photons than 912 Å are efficiently absorbed by neutral hydrogen to produce H^+ by photoionization. Photons with larger wavelengths than the molecular dissociation potential $\lambda_{\rm dis}$ cannot dissociate the molecule and only produce excitations to the high energy electronic-vibration-rotation levels. This effect is already taken into account in the dissociation cross section and so the upper limit of the integral can be formally extended to infinity since $\sigma(\lambda)$ falls off below the dissociation wavelength.

Although photodissociation is usually referred to as a relatively simple process, it can proceed in various ways. The process is the responsible for the dependence on wavelength of the dissociation cross section $\sigma(\lambda)$. A discussion about all these mechanisms can be found in van Dishoeck (1987a). We briefly summarize the possible mechanisms for a diatomic molecule:

- Direct photodissociation: the molecule, initially in a vibrational state of a bound electronic state (state with a stable potential well) absorbs a photon and jumps to a repulsive state (state without a stable potential well) and dissociates. The cross section is a continuous function of λ and its shape reflects that of the vibrational wave function of the lower state.

- Indirect photodissociation: the molecule, initially in a vibrational state

of a bound electronic state absorbs a photon and jumps to another vibrational level of an excited electronic state which subsequently interacts with another repulsive state and the molecule dissociates. The cross section depends on whether the symmetry of the repulsive state is the same or different as the excited bound state. If it is the same, $\sigma(\lambda)$ may consist of a continuous background with superposed resonances. If it is different, the cross section consists of a series of discrete peaks, broadened by the predissociation process.

- Spontaneous radiative dissociation: the molecule, initially in a vibrational state of a bound electronic state absorbs a photon and jumps to another vibrational level of an excited electronic state. Then, a radiative transition can occur to a lower lying repulsive state, producing the dissociation. The cross section consists in this case of a series of sharp peaks situated at the wavelength of the transitions whose widths are determined by the natural radiative lifetimes of the levels.

We have applied the chemical evolution equations to investigating the importance of photodissociation in the solar photosphere for the establishment of the CH abundance. In order to take into account the possible photodissociation of CH, we need the photodissociation rates of the CH molecule in the solar environment. The dissociation potential of CH is 3.47 eV (3575 Å in wavelength units) and it dissociates mainly through indirect photodissociation. CH photodissociation rates have been computed for the interstellar medium (van Dishoeck 1987b), where the UV radiation field responsible for the dissociation is much lower than in the Sun (Draine 1978). Therefore, because these rates are of no use for the solar case, we have calculated the photodissociation rate using Eq. (3.26). Kurucz et al. (1987) tabulate the CH photodissociation cross sections for a discrete set of temperatures. We used them to integrate Eq. (3.26) under the assumption that J_λ is given by the local Planck function. We have selected four combinations of T and n_H characteristic of the solar photosphere physical conditions. The photodissociation rates are shown in Table 3.1.

The table also contains the mean lifetime of a CH molecule owing to photodissociation, defined as the inverse of the photodissociation rate $\bar{t}_{\rm photo} = 1/k_{\rm photo}$. Some of these lifetimes are fairly small (2×10^{-4} s), indicating that it could be an efficient process in the solar chemistry. However, these numbers are not enough to conclude whether the photodissociation is important or not since

Table 3.1: Value of the photodissociation rates for the CH molecule for the limiting physical conditions in the solar photosphere.

T (K)	$k_{\rm photo}$ (s^{-1})	$\bar{t}$ (s)	n_H (cm^{-3})	$r_{\rm photo}$
4400	1.65×10^{2}	6.1×10^{-3}	2.7×10^{15}	4.8×10^{-4}
4400	1.65×10^{2}	6.1×10^{-3}	1.2×10^{17}	1.1×10^{-5}
6520	4.05×10^{3}	2.5×10^{-4}	2.7×10^{15}	1.2×10^{-2}
6520	4.05×10^{3}	2.5×10^{-4}	1.2×10^{17}	2.6×10^{-4}

one has to take into account all possible branches producing and destroying CH. Such a simple molecule results from dissociation of more complicated molecules and can be easily generated in several reaction paths where very efficient two- or three-body reactions are present.

In order to solve the chemical evolution problem, we have adopted a set of 110 neutral-neutral reactions involving the following species: H, C, O, N, He, CH, CO, H_2, OH, NH, CN, N_2, NO, O_2, HO_2, H_2O and H_2O_2. The reaction rates have been obtained from the reaction database for combustion mechanisms of Konnov (2000). Although reactions involving ions should be included for comprehensiveness, our assumption is reasonable considering that the main atoms involved in the CH formation (H, C and O) remain neutral under typical photospheric conditions. The photodissociation of CH is included in the set of reactions by using the rates obtained from Eq. (3.26). The solutions are initialized assuming that no molecular species are present in the medium and everything is in atomic form. Hydrogen densities for the typical photospheric conditions are chosen (see Table 3.1). The rest of atomic species are taken according to standard solar abundances (Grevesse 1984). We have checked that the set of reactions included in our chemical evolution code for the solution of this problem are adequate since the most important species approach ICE abundances when the solutions become stationary. Small differences and differences in other minor molecules are to be expected because of the incompleteness of the database. In Fig. 3.4a we show the equilibrium abundances of H_2, CO and CH in the quiet Sun VAL-C model. The CH abundance has a peak at the bottom of the photosphere where the temperature and density conditions allow an efficient formation. Its abundance is largest at around 50 km and it

goes away where the CO formation peaks. Interestingly, since the dissociation potential of H_2 is 4.47 eV (Herzberg 1950), its abundance peak is in a position similar to that of CH, while the CO peak is at ∼250 km due to the higher dissociation potential.

We have also explored which processes produce CH in the photosphere. First we investigate the importance of photodissociation as compared to the rest of the destruction mechanisms. We define the parameter $r_{\rm photo}$ as the ratio between the number of photodissociations of species i and the total number of destructions of this species:

$$r_{\rm photo} = k_{\rm photo} \Bigg/ \left(\sum_A \sum_B k_{ABi} n_A n_B - \sum_A k_{Ai} n_A - k_i \right). \tag{3.27}$$

This ratio in equilibrium (actually we present the ratio after 10^2 s) is listed in Table 3.1. Note that $r_{\rm photo} < 2\%$, even in the worst-case scenario. This clearly indicates that photodissociation is of secondary importance for destroying CH in the Sun. The conclusion is based on photodissociation rates that assume the radiation field to be Planckian at the local temperature. We would have reached the same conclusion using a more realistic radiation field to evaluate $k_{\rm photo}$. For example, even if J_λ were 10 times the local Planck function, photodissociation would still be negligible.

Fig. 3.4b shows the time evolution of the abundances of the most important molecular species at the bottom of the photosphere. The analysis of the different destruction rates indicates that, in all cases, CH is predominantly destroyed by collisions with neutral hydrogen that yield molecular hydrogen, namely:

$$\mathrm{CH + H \rightarrow C + H_2}. \tag{3.28}$$

We have also inspected the creation rates, i.e. the positive terms in Eq. (3.22). The CH is produced via the reverse reaction of Eq. (3.28), i.e.,

$$\mathrm{C + H_2 \rightarrow CH + H}. \tag{3.29}$$

The direct reaction between the CH constituents (C + H → CH) is ∼2 orders of magnitude slower. The tight link between CH and H_2 is made clear in Fig. (3.4b), where the CH curve closely follows the curve of H_2. In particular, both reach the equilibrium abundance within 10^{-5} s. This timescale depends very

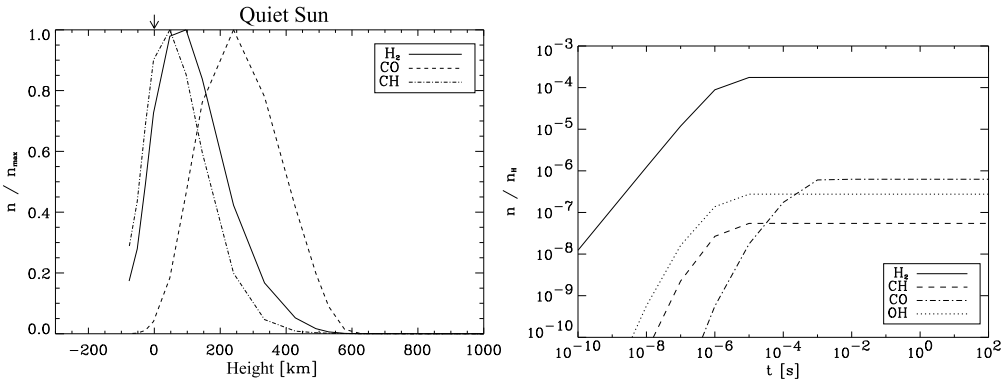

Figure 3.4: Abundance of the main diatomic molecules in the quiet Sun VAL-C model atmosphere (left panel) an the temporal evolution for the case T=6500 K and n_H=1.7×10^{17} cm^{-3} (right panel). The variation with height of each species is normalized to its maximum value: 3.4×10^{13} cm^{-3} for H_2, 2.4×10^{12} cm^{-3} for CO and 7.2×10^{9} cm^{-3} for CH. Note that the CH peaks deep down in the atmosphere, just 50 km above continuum optical depth unity at 5000 Å in normal incidence. The integration of the chemical evolution equations has been initialized with no molecules. The (thermodynamic) equilibrium CH abundance is reached within 10^{-5} s, a timescale primarily set by the reactions that produce and destroy H_2. Photodissociation seems to play a minor role in determining the CH abundance, and so its exact rate does not modify these curves. All abundances n are referred to the abundance of atomic hydrogen n_H.

much on the densities and temperatures in the atmosphere, but it is extremely short and always below 10^{-4} s for the typical photospheric atmospheric conditions. Due to its intrinsic high abundance, the time needed for CO to reach its equilibrium abundance is ∼2 orders of magnitude larger.

3.3 Relaxation times

Consider that we have a medium at a given temperature T and hydrogen density $n_{\rm H}$. We initialize the chemical evolution calculation without molecular species (only atomic species are present at $t = 0$ s). Let the system evolve until reaching the equilibrium abundances which, if the set of reactions and the species included are complete enough, will be similar to the abundance obtained using directly the ICE approximation. Next we introduce a perturbation in the physical conditions and we calculate the time to reach the new equilibrium situation, compatible with the new physical conditions. We will call this

timescale the *relaxation time*. In order to be able to get some information from these relaxation times, we will assume that the perturbations are small enough to consider that the performed analysis is in the linear regime ($|\Delta T|/T \ll 1$, $|\Delta n_{\rm H}|/n_{\rm H} \ll 1$). We have selected a granular and an intergranular model from the three-dimensional hydrodynamical simulations of the solar surface convection of Asplund et al. (2000). In Fig. 3.5 we show the temperature profile for both models, noting that, while the granular model is hotter in the deep regions of the photosphere, it turns out to be cooler above ∼250 km. These models are very realistic up to heights around 400-500 km. For comparison, we have made the calculations in the FAL-C and COOL-C semi-empirical models. In Fig. 3.6 we plot the molecular abundance relative to the abundance at $t = 0$ for some selected species at some atmospheric heights. These calculations have been obtained by performing a 1% relative decrease in the temperature. It is clear from the figure that almost all the species increase their abundance after the perturbation, once the new equilibrium situation is reached. This can be understood since molecular equilibrium constants usually decrease when the temperature increases (see Eq. 3.14). If the atomic partial pressures remain constant, the molecular partial pressure increases following Eq. (3.2). It is interesting to take into account that the relaxation time for the regions above 600 km in the COOL-C model are very high, produced by the low temperatures and densities in these regions.

The time evolution of the molecular abundances seems to be quite simple for some molecules like CO following a smooth step function. On the other hand, it becomes complicated for the majority of the molecules shown in the plots, with episodes in which the abundance is increasing and others in which it is decreasing. However, one thing that is clear in the plots is that the time to reach equilibrium increases when going to higher heights. This is produced by the fall in the temperature and the hydrogen density in both the granule and the intergranular material when going to higher regions. Both the temperature and hydrogen density fall produce a lower rate of collisions which result in slower reactions. However, the time to reach equilibrium at all the heights is below 10 s. Although this analysis is linear, we can make an order-of-magnitude study of what is going to happen
with the molecular abundances in the deep regions on the solar atmosphere.

The quite simple time variation of the CO abundance can be explained using the following model, which resembles the investigation performed by Ayres &

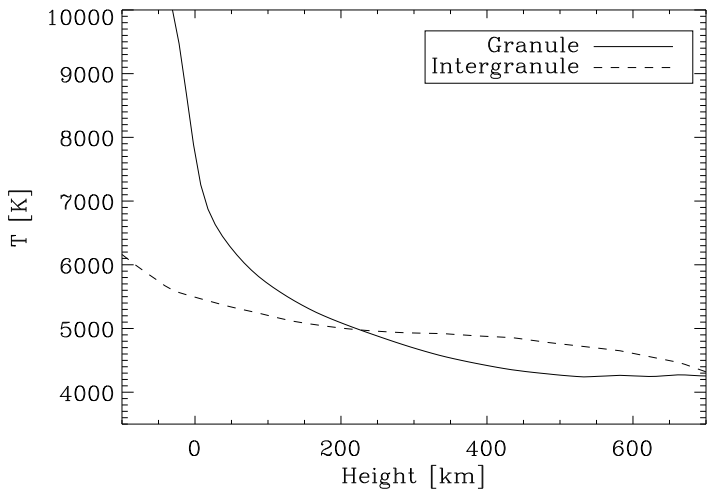

Figure 3.5: Temperature profile of the chosen representative granular and intergranular models of Asplund et al. (2000) hydrodynamical simulations. Note that, while the granule is hotter in the inner regions of the atmosphere, it turns out to be cooler for heights above ∼250 km.

Rabin (1996). Since CO is one of the most abundant molecules in the solar environment, we can first assume that its formation and destruction depends only on its abundance and the abundance of the constituents in atomic form. Therefore, the equilibrium we have to solve is given by:

$$\begin{aligned} \mathrm{C} + \mathrm{O} &\xrightarrow{K_{\mathrm{CO}}} \mathrm{CO} \\ \mathrm{CO} &\xrightarrow{K'_{\mathrm{CO}}} \mathrm{C} + \mathrm{O}, \end{aligned} \tag{3.30}$$

where K_{CO} and K'_{CO} are the reaction rate for the formation of CO by neutral association of its constituents and the reaction rate for the dissociation of CO, respectively. The differential equation which governs the time variation of n_{CO} can be written as:

$$\frac{dn_{\mathrm{CO}}}{dt} = K_{\mathrm{CO}} n_{\mathrm{C}} n_{\mathrm{O}} - K'_{\mathrm{CO}} n_{\mathrm{CO}}. \tag{3.31}$$

If we assume that the atomic abundances are constant, we can solve this equa-

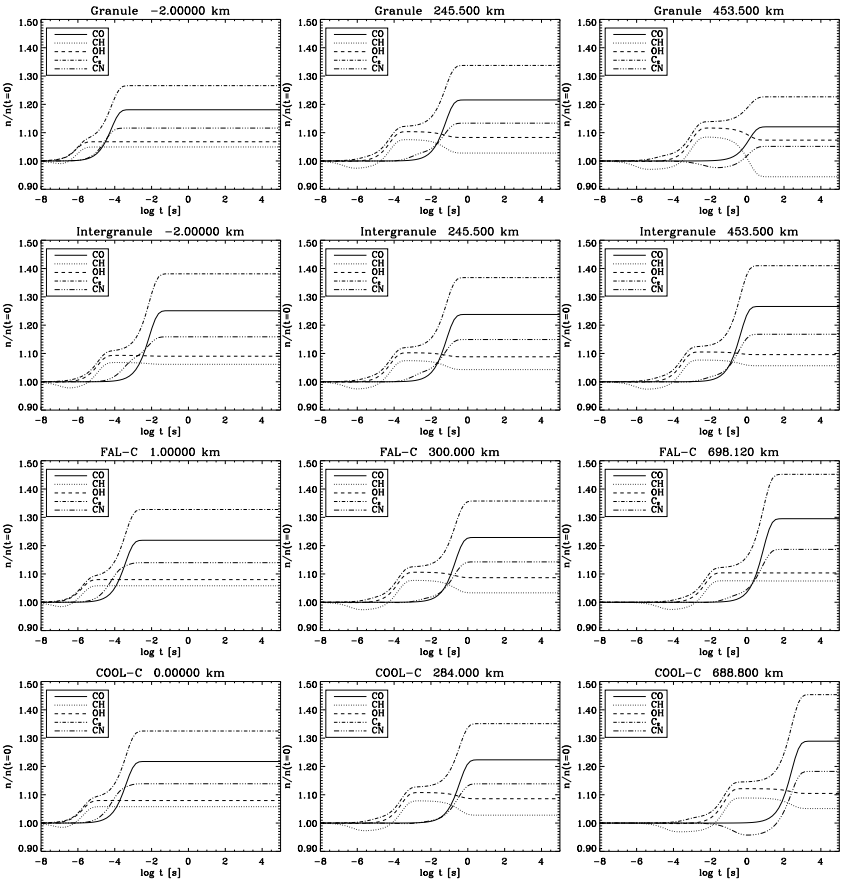

Figure 3.6: Time evolution of the molecular number densities for some selected molecules at some heights of the granular and intergranular models and the semi-empirical models FAL-C and COOL-C. At $t = 0$ s, a reduction of 1% in the temperature has been performed and the evolution until reaching the new equilibrium abundance has been obtained. Note the simple behavior of the CO abundance, while the rest of molecules have a complicated evolution showing the extremely non-linear character of the chemical evolution problem. All the molecules reach their new equilibrium concentrations in less than 10 s, except for the points at ∼700 km in both semi-empirical models. Since the granular and intergranular models represent only the photospheric conditions of the solar atmosphere, no high relaxation times are found.

tion and obtain the CO abundance for each time t:

$$n_{\rm CO}(t) = n_{\rm CO}(\infty) + [n_{\rm CO}(0) - n_{\rm CO}(\infty)]\, e^{-K'_{\rm CO}t}, \tag{3.32}$$

where $n_{\rm CO}(0)$ is the starting CO abundance and $n_{\rm CO}(\infty)$ is the CO abundance for $t \to \infty$, i.e. the CO equilibrium abundance for the given physical conditions. This equilibrium abundance is given by:

$$n_{\rm CO}(\infty) = \frac{n_{\rm C} n_{\rm O} K_{\rm CO}}{K'_{\rm CO}}. \tag{3.33}$$

Note the resemblance of this equation with Eq. (3.2), which states that the equilibrium constant can be obtained from the reaction rates for this extremely simple model by the relation:

$$K_p^{\rm CO}(T) = kT \frac{K'_{\rm CO}}{K_{\rm CO}} \tag{3.34}$$

The simplicity of the model let us define a timescale for the approach to chemical equilibrium, which will be referred to as the relaxation time, which is given here by:

$$\tau_{\rm relax} = \frac{1}{K'_{\rm CO}}. \tag{3.35}$$

Although the direct association of C and O to form CO is the most simple reaction one can assume, CO is more efficiently formed through other faster reaction paths. A similar simple behavior can be obtained if we consider that the reactions which efficiently form CO are (refer to Ayres & Rabin 1996 for a discussion about the CO formation reactions):

$$\begin{aligned} {\rm C} + {\rm OH} &\xrightarrow{K_1} {\rm CO} + {\rm H} \\ {\rm CO} + {\rm H} &\xrightarrow{K_2} {\rm OH} + {\rm C}. \end{aligned} \tag{3.36}$$

As a first approximation, we can assume that OH is formed much more faster than CO and so its abundance can be considered constant during the time interval in which the CO abundance is changing. This fact is reinforced by the chemical evolution calculations, as can be seen in Fig. 3.6. We see that OH

has almost reached its equilibrium abundance when CO starts to change from its value at $t = 0$. The evolution equation can be written as:

$$\frac{dn_{\rm CO}}{dt} = K_1 n_{\rm C} n_{\rm OH} - K_2 n_{\rm CO} n_{\rm H}. \tag{3.37}$$

Consider now the following simplifying conditions: the hydrogen abundance is constant; the OH abundance can be written in terms of the hydrogen abundance as $n_{\rm OH} \approx A_{\rm OH} n_{\rm H}$ (where $A_{\rm OH}$ is the OH abundance relative to hydrogen), and the carbon abundance is given by the number density of atomic carbon itself minus the number density of carbon in the form of CO, so that $n_{\rm C} \approx A_{\rm C} n_{\rm H} - n_{\rm CO}$ (where $A_{\rm C}$ is the carbon abundance relative to hydrogen). The first assumption introduces a very small error since the hydrogen abundance is barely affected by the presence of molecular species unless the temperature is extremely small (note from Fig. 3.2 that the most abundant molecule is at most 3 orders of magnitude less abundant than hydrogen). The second assumption can be considered since OH reaches its equilibrium abundances much faster than CO. The third assumption is applicable because almost all the carbon not in atomic form is in the form of CO. Therefore, the previous equation can be rewritten as:

$$\frac{dn_{\rm CO}}{dt} = K_1 \left(A_{\rm C} n_{\rm H} - n_{\rm CO}\right) n_{\rm OH} - K_2 n_{\rm CO} n_{\rm H}, \tag{3.38}$$

which is an equation quite similar to Eq. (3.31) and whose solution can be written as Eq. (3.32) below, but where:

$$n_{\rm CO}(\infty) = \frac{K_1 A_{\rm OH} A_{\rm C} n_{\rm H}}{K_1 A_{\rm OH} + K_2}, \tag{3.39}$$

$$\tau_{\rm relax} = \frac{1}{\left(K_1 A_{\rm OH} + K_2\right) n_{\rm H}}. \tag{3.40}$$

These calculations show that, if the behavior of the abundance of a molecule can be written in a simple way like we have done with CO, its evolution can be characterized by a timescale which depends on the main reactions which create and destroy the molecule and by its abundance in equilibrium (which also depend on the main reactions). Note that it is not correct to define timescales to both the formation or destruction processes, but there is only one global timescale which involves both processes. This is the reason why, even in the

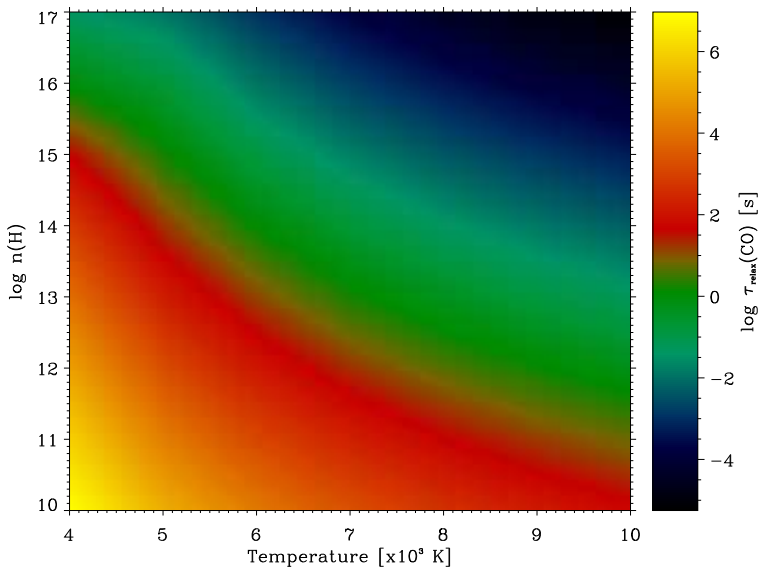

Figure 3.7: CO abundance relaxation time for a set of physical conditions ranging from 4000 to 10000 K and from 10^{10} to 10^{17} cm^{-3} for the hydrogen number density. Note that there is a variation of more than 10 orders of magnitude for different physical conditions which can be found in the solar atmosphere. This plot shows that the relaxation time increases when the temperature and hydrogen density are reduced, while it decreases when the temperature and density are increased.

most simple example, one cannot make an idea of how fast a chemical reaction is going to take place by only taking into account the rate of the individual reaction. However, when the whole system of differential equations which describe the chemical evolution problem is solved, many non-linearities arise for most of the molecules which makes a simple relaxation time investigation impossible.

The linear analysis of the CO abundance evolution shows that CO is mainly driven by itself in a way similar to Eq. (3.31). Therefore, we can perform a fit of the evolution with a functional form like:

$$n_{\rm CO}(t) = n_{\rm CO}(\infty) + [n_{\rm CO}(0) - n_{\rm CO}(\infty)]\, e^{-t/\tau_{\rm relax}}, \tag{3.41}$$

and obtain the relaxation time $\tau_{\rm relax}$. Since this linear analysis is correct for CO, we have calculated the relaxation time to perturbations in the temperature for a range of temperatures and hydrogen densities. The results are shown in Fig.

3.7. The general trend in this plot is that, *for a given density, the relaxation time is the larger the cooler the medium where the temperature perturbation is introduced*. Similarly, *for a given temperature of the unperturbed medium, the relaxation time increases rapidly with decreasing density*. Short relaxation times are typical of high-temperature and high-density media (e.g. $t_{\rm relax} \approx 0.006$ s for $n_{\rm H} = 10^{16}\,{\rm cm}^{-3}$ and $T = 6000$ K), while long relaxation times are characteristic of low-temperature and low-density situations (e.g. $t_{\rm relax} \approx 400$ s for $n_{\rm H} = 10^{14}\,{\rm cm}^{-3}$ and $T = 4000$ K). In the solar atmosphere, one would find a broad range of relaxation times at a fixed height due to the dynamic atmosphere which results in density and temperature fluctuations which are continually changing the atmospheric conditions. Obviously, the situation is highly non-linear and the relaxation time concept, although useful, loses its meaning in the real Sun. Therefore, any firm conclusion needs to be achieved via detailed numerical simulations. This is the only possible solution for the rest of species which do not behave in the simple way as CO.

3.4 LTE synthesis for molecular lines

In order to investigate whether the ICE approximation or the full chemical evolution is valid for each environment, we have to compare our calculations with observables. Since we cannot directly measure the molecular abundances in the solar atmosphere, we have to calculate the effect of the differences between the ICE approximation and the chemical evolution results on the spectral lines emerging from the solar photosphere. Once the abundance of a given molecule is known for each depth point in the atmosphere, the line absorption due to molecular transitions can be evaluated. Given an energy level in the molecule, its population in LTE follows from the Boltzmann equation:

$$n_{evJ} = N_{\rm mol} \frac{g_{evJ}}{U(T)} \exp[-E_{evJ}/kT], \tag{3.42}$$

where the quantum numbers e, v and J denote the electronic level (including the parity of the level), the vibrational level inside each electronic level and rotational level within each vibrational level, respectively. The other symbols have the usual meaning: g_{evJ} is the degeneracy of the level (although we have included the v dependence of the degeneracy, it only depends on the electronic and rotational quantum numbers), E_{evJ} is the energy of the level and $U(T)$ is

the total partition function of the molecule. The temperature dependence of the total partition function has been tabulated as polynomial fits (see Sauval & Tatum 1984, Tejero Ordoñez & Cernicharo 1991). These partition functions were calculated using the available molecular data. In case refined molecular data is obtained, these polynomial fits must be revised.

Consider a molecular transition between a lower level l and an upper level u. The line opacity assuming LTE is obtained from (Mihalas 1978):

$$\chi_l^{\rm LTE}(\nu) = \frac{h\nu}{4\pi}\phi_\nu\big(n_l^* B_{lu} - n_u^* B_{ul}\big) = \frac{h\nu}{4\pi} n_l^* B_{lu}\phi_\nu\Big(1 - e^{-h\nu/kT}\Big), \tag{3.43}$$

where n_u^* and n_l^* are the LTE populations of the upper and lower level of the transition, respectively, ν is the frequency of the transition in s^{-1}, B_{lu} is the absorption Einstein coefficient, ϕ_ν is the line profile and $e^{-h\nu/kT}$ is the stimulated emission correction. The line profile is normalized to have unit area $\int d\nu\phi_\nu = 1$. Is is usual to tabulate f in the linelists, so we can rewrite the previous expression by using the oscillator strength f. Making use of the relation between the Einstein coefficients and knowing that the oscillator strength and the spontaneous emission Einstein coefficient A_{ul} are related through

$$g_l f = \frac{m_e c}{8\pi^2 e^2}\lambda^2 g_u A_{ul}, \tag{3.44}$$

where e, m_e, g_i and λ are the electron charge, electron mass, degeneracy of level i and wavelength of the transition, respectively, we can finally rewrite the line opacity as:

$$\chi_l^{\rm LTE}(\nu) = \frac{\pi e^2}{m_e c}\frac{N_{\rm mol}}{U(T)} g f e^{-E_{evJ}^{low}/kT}\Big(1 - e^{-h\nu/kT}\Big)\phi_\nu, \tag{3.45}$$

Since many lines are usually contributing to the opacity at a given frequency, we can calculate the total line opacity contribution at a given frequency by summing over all these lines:

$$\chi_l(\nu) = \sum_i \chi_{l_i}^{\rm LTE}(\nu), \tag{3.46}$$

The individual line profile ϕ_ν is chosen to be a Voigt function with a damping parameter a.

3.5 Non-equilibrium CO chemistry in the solar atmosphere

3.5.1 Introduction

Thirty years ago Noyes & Hall (1972) inferred very low brightness temperatures ($T \approx 3700$ K) from their discovery of strong rovibrational CO lines at 4.7 μm observed close to the edge of the solar disk. Several years later, after such surprising observational results had been confirmed by Ayres & Testerman (1981), it was suggested that the low chromosphere might not be hot at all but could instead be permeated by CO-cooled 'clouds' at altitudes between 500 and 1000 kilometers above continuum optical depth unity (Ayres 1981). This led to controversy because other (UV and submillimeter) diagnostics had suggested the existence of a uniformly hot chromosphere with a minimum temperature of about 4400 K near 500 km and a temperature rise above this temperature-minimum region. The controversy over the existence of cool gas in the low chromosphere continues today (see Kalkofen 2001, Ayres 2002, Avrett 2003), after the publication of an abundance of literature on the subject with theoretical investigations concluding that the CO lines have LTE source functions (Ayres & Wiedemann 1989; Uitenbroek 2000a) and with new observations showing off-limb CO emission protruding hundreds of kilometers into the chromosphere (Solanki et al. 1994; Clark et al. 1995), but also with the discovery that far-UV chromospheric lines observed on the solar disk always remain in emission at all positions and times (Carlsson et al. 1997).

Over the last few years, it has become increasingly evident that the next crucial step towards a better understanding of the enigmatic thermal structure of the solar chromosphere is to carefully investigate the reliability of the assumption of instantaneous chemical equilibrium (ICE), which is currently used for calculating the molecular number densities in stellar atmospheres (see, in particular, Uitenbroek 2000a, 2000b; see also Ayres & Rabin 1996; Avrett et al. 1996; Asensio Ramos & Trujillo Bueno 2003a; Avrett 2003). Actually, both observations and simulations indicate that the solar chromosphere is a highly inhomogeneous and dynamic region of low density plasma whose thermal, dynamic and magnetic properties we need to decipher for unlocking new discoveries. If the ICE approximation turns out to be adequate for modeling the strongest CO lines close to the edge of the solar disk, then the available CO observations would really be indicating the existence of cool gas in the solar

chromosphere. Otherwise, a natural resolution of the current chromospheric temperature discrepancy could perhaps emerge if the CO concentration turns out to be sufficiently lower than would be expected on the basis of chemical equilibrium.

3.5.2 Formulation of the problem

Our strategy consists in performing chemical evolution calculations in the radiation hydrodynamical simulations of solar chromospheric dynamics described by Carlsson & Stein (1997, 2002), which do not include CO cooling in the energy equation. Therefore, at each time step of the hydrodynamical simulation, we have fixed the ensuing thermodynamic conditions and calculated the corresponding CO number density by following the chemical evolution starting from the molecular concentrations of the previous time step.

Two key ingredients have to be taken into account: the number of chemical species and the reaction rates for all possible reactions. Concerning the number of species, after a careful investigation, we found that at least the following set of 13 species, which includes the most abundant diatomic molecules, is needed: H, C, O, N, He, CH, CO, H_2, OH, NH, N_2, NO and CN. We have verified that the inclusion of ionic species does not significantly affect the CO concentration for the typical atmospheric conditions encountered at heights $h \leq 1000$ km, although they should be ideally taken into account for very strong shocks capable of producing sizable changes in the degree of ionization. Concerning the reactions rates, we have used the reaction database created for the study of combustion mechanisms (Konnov 2000) which seems to be appropriate for the physical conditions in the solar atmospheric plasma. We have also investigated the possible influence of CO photodissociations, which are one-body reactions. They are mainly produced by discrete photon absorptions at wavelengths between the Lyman cutoff (912 Å) and the dissociation threshold (1120 Å). By using the photodissociation rates of Mamon et al. (1988), we have verified, in a similar way as done in the study of the photodissociation of CH, that the contribution of photodissociation processes to the total CO concentration is negligible for the radiation field in the solar atmosphere. In fact, the CO dissociation energy is very large (11.07 eV), thus making it very difficult to break up the molecules into their constituents by interactions with solar atmospheric photons. This possibility is even reduced when *self-shielding* (absorption of photons by CO

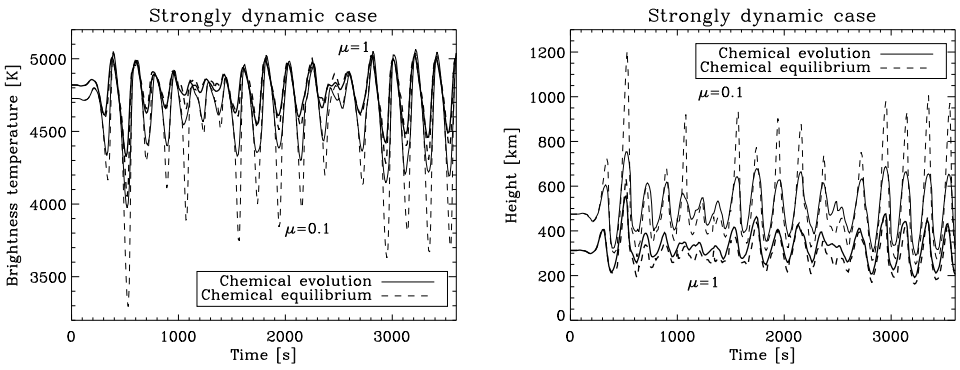

Figure 3.8: Temporal variation of the brightness temperature in the core of the strong 3-2 R14 line (*left*) and of the height of line-core optical depth unity (*right*) for the strongly dynamic case and for two observing angles: disk center (μ=1, *heavy lines*) and close to the solar limb (μ=0.1, *light lines*), where $\mu = \cos\theta$ (with θ the angle between the solar radius vector through the observed point and the line of sight.

which avoid these photons to photodissociate other CO molecules) is taken into account.

3.5.3 Numerical simulations in the 1D hydrodynamical models

We used two time-series of snapshots from the above-mentioned radiation hydrodynamical simulations, each one lasting about 3600 seconds and showing the upward propagation of acoustic wave trains growing in amplitude with height until eventually producing shocks. The first one corresponds to a relatively strong photospheric disturbance showing well-developed cool phases and pronounced hot zones at chromospheric heights (see Carlsson & Stein 1997). The strongest dynamic cycle of this simulation produces a peak-to-peak line-core brightness temperature of 1000 K, concerning the strong 3-2 R14 CO-line synthesized at disk center with the ICE approximation. However, the brightness temperature variations in most of the cycles of this simulation are 400 K approximately, which is similar to the observed values found by Uitenbroek et al. (1994) under excellent seeing conditions, but larger than those inferred from the temperature histograms in Ayres & Rabin (1996). We shall refer to this as

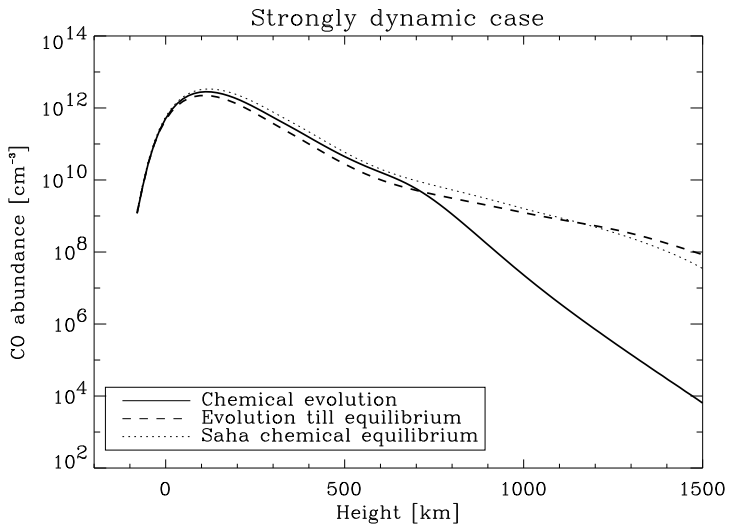

Figure 3.9: *Solid line*: Height variation of the time-averaged CO concentration obtained from the chemical evolution calculation in the strongly dynamic simulation case. *Dashed line*: Time-averaged CO concentration corresponding to the ICE approximation, but calculating the CO number densities of the atmospheric models associated to each time step by using the same chemical evolution code until reaching the ensuing equilibrium concentrations. *Dotted line*: Time-averaged CO concentration corresponding to the ICE approximation, but calculating the CO concentrations directly from the Saha chemical equilibrium equations. A comparison of the dashed and dotted lines illustrates the reliability of the chosen database for the chemical evolution calculations. In any case, in order to be fully consistent with our comparisons, all ICE results refer to "evolution until equilibrium" calculations

the strongly dynamic case.[3] The second simulation corresponds to a much less intense photospheric disturbance (see Carlsson & Stein 2002), which for strong CO lines synthesized at disk center produces a peak-to-peak line-core brightness temperature fluctuation which is always smaller than 400 K. We shall refer to this as the weakly dynamic case.

Starting from the molecular concentration given by the ICE approximation, we have followed the chemical evolution in order to obtain the temporal vari-

[3]This is similar to that used by Uitenbroek (2000a) and Ayres (2002) in their ICE modeling, although they considered only a segment of 190 s corresponding to the most dynamic cycle of the full simulation.

ation of the CO number density ($N_{\rm CO}$) at each height in the simulated solar atmosphere. As expected, the CO concentration is anticorrelated with the local temperature variations, yielding relatively low $N_{\rm CO}$ values in the hot phases and relatively high $N_{\rm CO}$ values in the cool phases. However, the amplitude of the local $N_{\rm CO}$ fluctuation is smaller than that given by the ICE approximation. In relatively low density regions characteristic of the outer atmospheric layers (e.g. around $h = 1000$ km) the ICE approximation does a fairly good job during the hot phases, but it overestimates the CO number density during the cool phases. In contrast, in relatively high density regions characteristic of photospheric layers (e.g. around $h = 400$ km) the ICE approximation underestimates the $N_{\rm CO}$ values during the hot phases. Thus, the CO abundance does not react instantaneously to the changes in the temperature because of the finite reaction rates.

Fig. 3.8 refers to the strongly dynamic case. The left panel shows the temporal variation in the brightness temperatures of the line-core emergent intensities at $\mu = 1$ and $\mu = 0.1$ in the strong 3-2 R14 CO-line. The right panel gives the ensuing fluctuations of the atmospheric height where the line-core optical depth is unity, which we use as an indicator of the 'representative height' where the CO line-core radiation originates. As seen in the figure, the ICE approximation does a sufficiently good job concerning the synthesis of the emergent CO spectrum at the solar disk center ($\mu = 1$), but it largely underestimates the line-core emergent intensities at $\mu = 0.1$ during the cool phases, producing brightness temperatures that are typically 500 K *lower* than those computed with the non-equilibrium CO concentration. Clearly, this is because during the cool phases the ICE approximation overestimates the 'heights of line formation' by about 300 km, concerning the synthesis of strong CO lines at $\mu = 0.1$ in the strongly dynamic simulation case. This happens because during the cool phases of the hydrodynamical simulations the CO number density in the outer atmospheric regions is smaller than what is stipulated by the ICE approximation, resulting in decreased CO opacity in the solar chromosphere. Interestingly, in the weakly dynamic case which has smaller kinetic temperature fluctuations (but still larger than the fluctuations of observed brightness temperatures!) the ICE approximation does a much better job even at $\mu = 0.1$.

Fig. 3.9 contrasts the time-averaged CO concentration obtained assuming ICE at each time step of the strongly dynamic simulation case with that resulting from the chemical evolution. Note that the ICE approximation leads

to a significant overabundance of CO in the outer layers of the atmosphere (i.e. above 700 km). Thus, the CO number density can be relatively low in such outer layers, in spite of the fact that the temporally averaged temperature of the Carlsson & Stein (1997) simulations decreases outwards and does not show any chromospheric temperature rise. As expected from the previously reported results, the ICE approximation does a sufficiently good job concerning the modeling of the temporally-averaged CO spectrum at the solar disk center ($\mu = 1$). In contrast, the emergent CO spectrum computed close to the edge of the solar disk (i.e. at $\mu = 0.1$) shows significantly *stronger* CO-lines when the ICE approximation is used, especially concerning strong CO lines like the 3-2 R14 one, for which the line-core brightness temperature is about 100 K *lower* than that obtained using the non-equilibrium CO number densities.

Finally, we turn our attention to the modeling issue of the off-limb CO emissions, which we have carried out by solving the radiative transfer equation in spherical coordinates at each time step of the hydrodynamical simulation[4]. The off-limb distances where (time-averaged) CO emission has been observed depend on the line (see Ayres 2002, for a summary of the available off-limb observational results): the off-limb emission extension of strong lines like the 3-2 R14 line lies between 0.55" and 0.7" above the 4.7 μm continuum limb, while weaker lines like the 7-6 R68 line extend to $\sim$0.4". Fig. 3.10 refers to the strongly dynamic case. It shows that the atmospheric region where we can have a significant off-limb emission is extremely large when the ICE approximation is used, i.e. much larger than when the spectral synthesis is carried out using the non-equilibrium CO number densities. The dashed and solid lines show the corresponding height variation of the temporally-averaged off-limb emission at the core of the strong 3-2 R14 CO-line. They show that the non-equilibrium CO chemistry improves the agreement with the available off-limb observations. First, as seen in Fig. 3.10, the ICE approximation predicts that appreciable emission in the 3-2 R14 line should continue to relatively large off-limb distances, while partial eclipse measurements by Clark et al. (1995)

[4]This is a suitable strategy for contrasting ICE and non-ICE results, as done also in Fig. 3.8 concerning the on-disk spectral syntheses at $\mu = 0.1$. It is however clear that a truly realistic modeling of the available observations should take into account not only the finite spectral resolution and seeing effects, but also the geometrical foreshortening effect resulting from the fact that the solar chromosphere is a highly inhomogeneous medium in which the raypath goes through many different structures.

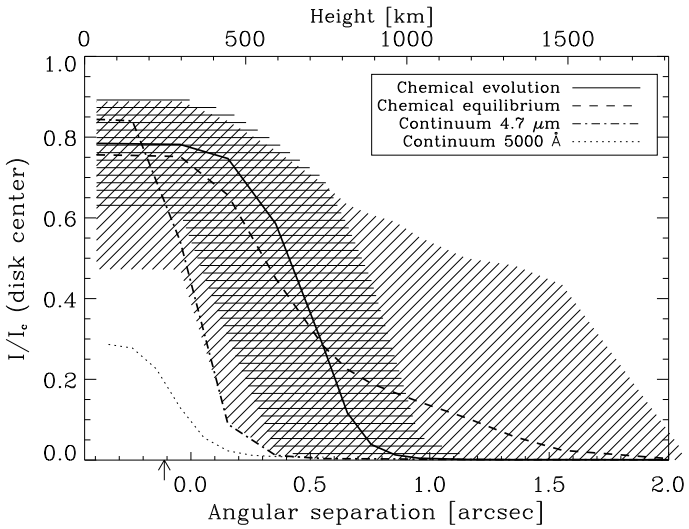

Figure 3.10: *Diagonal shading* indicates the relatively large atmospheric region where the ICE approximation predicts off-limb emission in the core of the 3-2 R14 CO-line, while the *horizontal shading* shows that corresponding to the chemical evolution calculation. The figure also shows the calculated limb profiles for the continua at 4.7 μm and 5000 Å. The zero level of the angular separation scale refers to the 4.7 μm continuum edge calculated as the 50% point in the intensity drop, as normalized to the ensuing continuum intensity at disk center. The arrow indicates the continuum edge for the optical continuum. At each angular distance, the vertical extensions of the shadings indicate the amplitude of the temporal variation of the line-core CO-emission. The dashed and solid lines give the corresponding temporally averaged off-limb emissions. The upper horizontal axis gives the height in the atmosphere, $z = 0$ km being the location of continuum optical depth unity at 5000 Å for a disk center observation (i.e., the usual depth scale in solar models). Note that at low altitude locations, where the IR continuum dashed-dotted curve lies above the (temporally-averaged) dashed and solid curves, the synthesized CO line turns into an absorption line for the ICE and non-equilibrium cases, respectively.

show a rapid disappearance of CO emission at heights above 700 km, which is more in line with our chemical evolution calculations. Second, as can also be inferred from Fig. 3.10, the representative off-limb emission extension where the normalized intensity falls to 50% of the on-disk value is larger when the non-equilibrium CO concentration is used, which helps to improve the agreement with the observations of translimb emission extensions, although they still seem

to be below the most recently observed values (see Ayres 2002).

3.5.4 Conclusions of our 1D simulations

Our results indicate that the CO line radiation observed close to the edge of the solar disk comes from atmospheric heights not greater than ∼700 km, and that the gas in these regions of the low chromosphere must be much cooler than indicated by the cool phases of the Carlsson & Stein (1997) hydrodynamical simulations. Lower temperatures will probably increase the relaxation times needed to reach the molecular equilibrium concentrations. In a next step forward, we will investigate what happens when the hydrodynamical simulations themselves are carried out taking the CO cooling into account, in a way consistent with the non-equilibrium evolution of the molecular number densities.

3.5.5 Results in 3D hydrodynamical models

Our conclusion that the ICE approximation is suitable for modeling the CO spectrum at the solar disk center may be found surprising, given that Uitenbroek (2000b) found that the spatially averaged line cores of weak CO lines synthesized in the three-dimensional (3D) hydrodynamical model of Stein & Nordlund (1989) are overly dark compared to the observed ATMOS spectrum described by Farmer et al. (1989). As an example, the strong 3-2 R14 line brightness temperature is ∼300 K lower than the observed brightness temperature. while the brightness temperature of the weak line 7-6 R68 is ∼500 K lower than the observed brightness temperature. The conclusion reached by Uitenbroek (2000b) was that either the model was too cold in the CO line-formation region, which would mean that the granulation simulation overestimated radiative cooling in these layers or that the CO lines were forming too far outward because CO concentrations were overestimated in the calculations assuming the ICE approximation. However, we have shown that the ICE approximation is suitable for modeling the CO spectrum at $\mu = 1$ in the 1D models of Carlsson & Stein (1997).

As we have pointed out, more improved 3D hydrodynamical models are available (Asplund et al. 2000) and we are interested in verifying whether this new simulation is suitable for interpreting the spatially averaged CO solar spectrum. To this end we have used a snapshot of this 3D radiation hydrody-

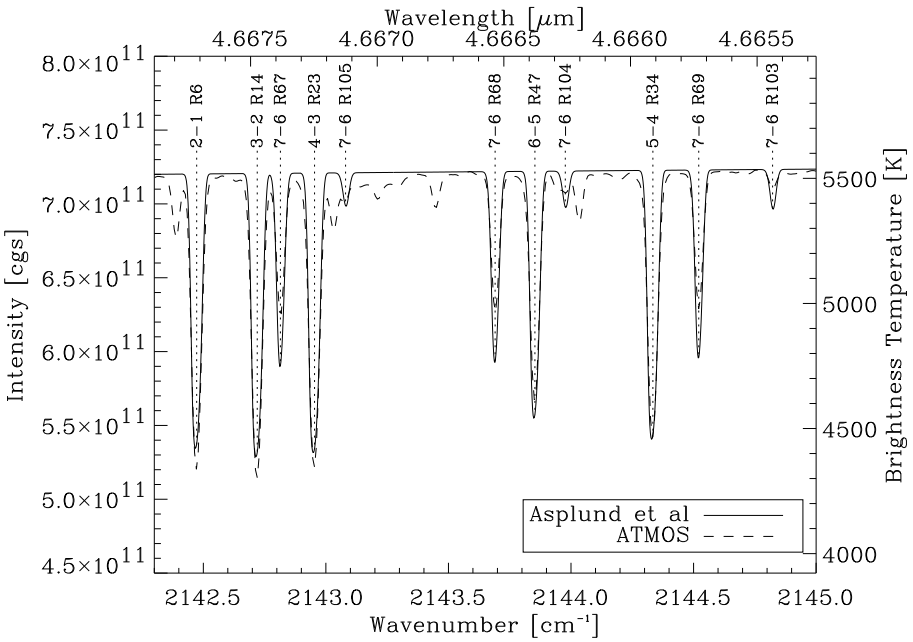

Figure 3.11: *Solid line*: CO spectrum synthesized at disk center (μ=1) in the model of Asplund et al. (2000) and averaged over all the surface of the simulation box. *Dashed line*: CO spectrum observed by the ATMOS mission. Note the good agreement between the observation and the synthesis in the width and the depth of most CO lines.

namical simulation of the solar photosphere. These time-dependent simulations are similar to those of Stein & Nordlund (1989) but with the improvement of having been performed in a grid with better spatial resolution and using a more realistic equation of state. The original grid of the hydrodynamic simulation has 200×200×82 grid points covering the physical dimension corresponding to 6×6×3.8 Mm, of which 1 Mm is located above continuum optical depth unity. The original snapshots were interpolated to a coarser grid of 50×50×82 points in order to facilitate the RT calculations. It is interesting to note that these simulations have been successful in reproducing the spatially averaged iron spectrum by detailed NLTE calculations (see Shchukina & Trujillo Bueno 2001).

We have carried out LTE synthesis of some CO lines in the region 2142.4-2145 cm^{-1} where strong and weak CO lines are present (see Fig. 3.11 for line

identifications). We have not included in the synthesis the extremely weak ^{13}CO lines which are formed very close to where the continuum at this wavelength is formed. They can be recognized as the lines appearing in the ATMOS spectrum and not in the synthetic one. Since we are performing LTE synthesis at disk center, we can construct 50×50 one-dimensional atmospheric models, each one giving the variation with height of the relevant physical quantities (temperature, density, macroscopic velocity, etc.) and perform spectral synthesis using one-dimensional formal solvers.

The LTE opacities have been calculated according to Eqs. (3.45) and (3.46) assuming that the CO molecular number density is correctly given by the ICE approximation. The oscillator strengths of the $X^1\Sigma^+$ ground state lines of CO were taken from Goorvitch (1994) and the partition function was taken from Tejero Ordoñez & Cernicharo (1991). We have verified that the partition function of CO obtained from the available tabulations (Tejero Ordoñez & Cernicharo 1991; Sauval & Tatum 1984; Kurucz 1985) are extremely similar. The background continuum opacities were calculated using the same opacity package used by Shchukina & Trujillo Bueno (2001). In Fig. 3.11 we have plotted the synthesized spectrum averaged over the 50×50 points of the simulation together with the observed ATMOS spectrum. Note that the agreement between both spectra is fairly good. The width of the lines is correctly reproduced taking into account only the macroscopic motions of the simulations without the necessity of including an ad-hoc fitting parameter like macro and microturbulent velocities. The emergent profiles are obtained after averaging the 2500 spectra obtained for each point of the simulation, which have a variety of Doppler shifts due to the macroscopic motions present in the simulation. Interestingly, the depth of the strong lines is very well reproduced while that of the weak lines are slightly overestimated. The fit to the observed CO lines obtained with this simulations is much better than that obtained by Uitenbroek (2000b) with the previous simulations by Stein & Nordlund (1989). Although the strong CO lines are originated close to the upper boundary of the hydrodynamical simulations, it is striking that the synthesized line is so close to the observed one, suggesting that the simulation at these altitudes is not so incorrect, as one would perhaps expect because of the neglect of CO cooling, thus suggesting that the "cool clouds" are mainly caused by hydrodynamical processes instead of CO cooling.

Fig. 3.12 shows the temperature distribution in a vertical cut on the sim-

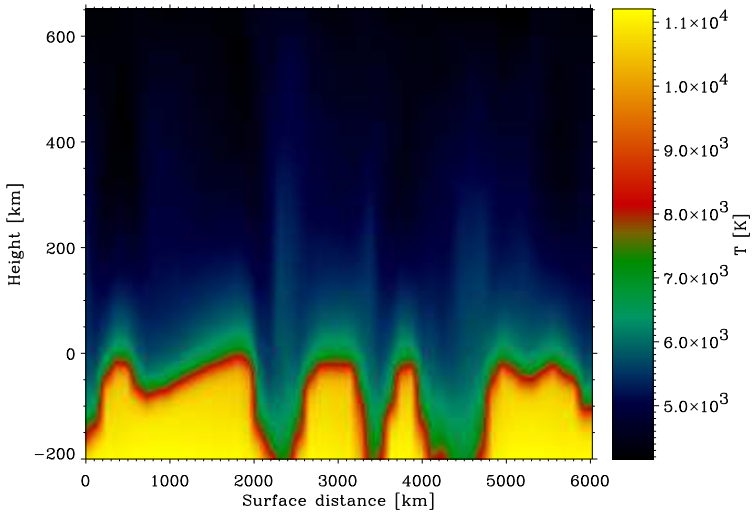

Figure 3.12: Temperature in a vertical cut of the 3D box of the simulation by Asplund et al. (2000) at position Y=5. Note the abrupt descent in the temperature in regions above h=0 km. We can find a ∼4000 K reduction in temperature in less than ∼50 km.

ulation box of the Asplund et al. (2000) 3D hydrodynamical models. Material rises through the upflow regions corresponding to bright granules in optical continuum images and returns through the downflow regions corresponding to dark intergranules in optical continuum images. When flowing upwards, the material rapidly expands to compensate for the drastic decrease of density in the regions above the photosphere. This expansion leads to cooling, while the material is heated by compression when returning through the downflows. This effect is seen in the Fig. 3.12 as the bright plumes (heated material) above the intergranular regions.

In Fig. 3.13 we show the CO abundance obtained assuming the ICE approximation for a cut in the three-dimensional box of the simulation. Note that there is a change in six orders of magnitude in the abundance from the bottom of the photosphere and the upper regions. Note also that the CO abundance changes very steeply close to z=0 km, where there is a change of ∼3 orders of magnitude in less than 50 km. This region is probably produced by the fall in a factor of 2 of the temperature in these models which is produced at

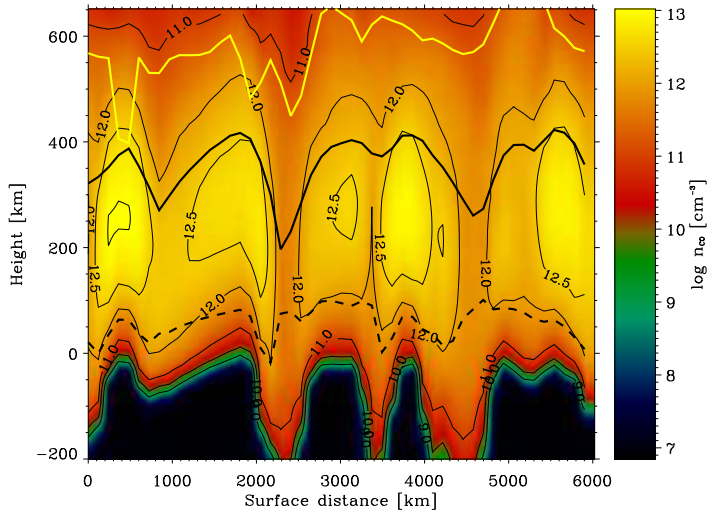

Figure 3.13: CO abundance in a vertical cut of the 3D box of the simulation at position Y=5. We have plotted the logarithm of the CO abundance obtained assuming the ICE approximation. Note that there is 6 orders of magnitude difference between the CO abundance at the bottom of the photosphere and in the upper region. We have also shown as a contour plot the regions where different logarithmic CO abundances are obtained. For knowing the region of formation of the CO lines we have marked the surfaces of optical depth unity in vertical incidence as thick lines for the strong 3-2 R14 line (yellow line), the weak 7-6 R67 line (black solid line) and the local continuum (black dashed line). Note that these surfaces approximately follow the spatial variations of the CO abundance.

regions close to z=0 km, as can be seen from Fig. 3.12. A simple calculation reinforces this assumption. Assume that the atomic carbon and oxygen density are almost constant in this small region of ∼50 km. The previous assumption is close to the reality since the hydrogen density does change very smoothly in this region and the atomic carbon abundance is much larger than the CO abundance. Therefore, we can use Eqs. (3.2) and (3.4) to write:

$$n_{\rm CO} = \frac{n_{\rm C} n_{\rm O}}{K_p(T)} kT. \tag{3.47}$$

A glance at the definition of the equilibrium constant given by Eq. (3.12) let us state that one of the most important terms in defining the actual value of

$K_p(T)$ is the exponential factor depending on the dissociation potential. Neglecting the temperature dependence of the partition function in the definition of $K_p(T)$, we can calculate the ratio between the CO abundance at two different temperatures:

$$r = \frac{n_{\rm CO}(T_1)}{n_{\rm CO}(T_2)} = \left(\frac{T_2}{T_1}\right)^3 \exp\left[\frac{D_0}{k}\left(\frac{1}{T_2} - \frac{1}{T_1}\right)\right]. \tag{3.48}$$

If we select now T_1=7000 K and T_2=11000 K, we get $r \sim$3100, which is in good accordance with the difference observed in Fig. 3.13.

This link between the temperature and the CO abundance is also demonstrated in another effect. The expansion cooling produced above the upflow regions leads to CO concentrations 3-4 times higher than over the downflow regions at the same height. Therefore, the line formation region for weak lines is higher for the granular regions (at least for vertical incidence) than for the intergranular regions. To demonstrate this effect, we also show in this figure the surfaces of optical depth unity at vertical incidence at the core of the strong 3-2 R14 and the weak 7-6 R67 lines and the local continuum. It is interesting to note that, since the continuum opacity at this wavelength is dominated by H^- and H free-free processes (see Uitenbroek 2000b), the curve of optical depth unity for the local continuum closely follow the contours of temperature as seen in Fig. 3.12. Note that the average height of the region of formation of the weak line is ∼350 km, while that of the strong line is ∼600 km.

In Fig. 3.14 we show the brightness temperature T_B of the core of the strong 3-2 R14 line and the weak 7-6 R67 line. This brightness temperature is taken at the wavelength where the line profile has its minimum and therefore correspond to different wavelength positions at each spatial point due to the Doppler shifts produced by the macroscopic motions of the plasma. Note that the core brightness temperature of the strong line is as low as 3500 K for some points in the surface while the weak line has minimum temperatures of ∼4000 K. Concerning the highest brightness temperatures, the upper limit for the strong line is at ∼5500 K while that for the weak line is ∼5800 K. The correlation between the brightness temperature of the weak line and the separation between granules and intergranules is higher than for the strong line. This can be understood because the formation zone of the weak line is closer to the continuum formation zone. The continuum is formed close to the $h = 0$ region. Therefore, the contrast obtained in the weak line for the granulation is higher than for the

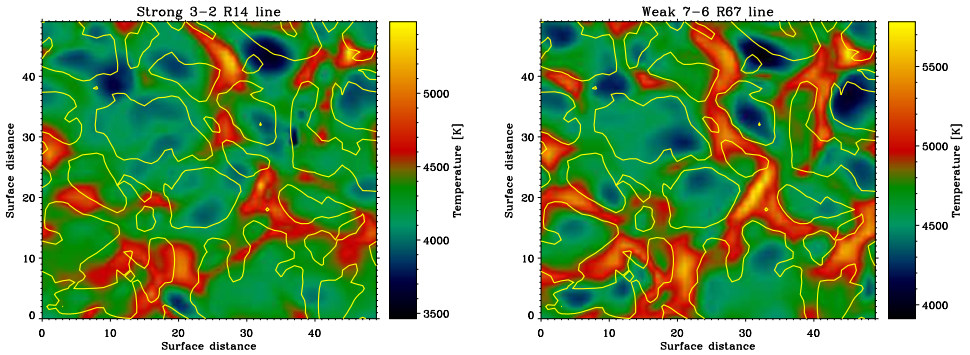

Figure 3.14: Brightness temperature at the core of the strong 3-2 R14 line (left panel) and at the weak 7-6 R67 line (left panel) for every point in the Asplund et al. (2000) 3D snapshot model of the solar photosphere. We have also plotted the contours of $v_z = 0$ km s^{-1} at $h = 0$ km, which can give an idea of the spatial position of the granules (with upward macroscopic motions at the bottom of the photosphere) and the intergranules (with downward macroscopic motions at the bottom of the photosphere).

strong line. This behavior qualitatively reproduces the observations of Uitenbroek (2000b) which shows a higher contrast of the granulation for the weak line than for the strong one.

We have performed a statistical study of the brightness temperature of the strong and weak lines. The histograms are shown in Fig. 3.15. The plot shows the number of times a given temperature with a binsize of 40 K appears in the synthetic spectrum. Note that the histogram of T_B is shifted to lower temperature for the strong line than for the weak line. As seen in Fig. 3.14, we do not find T_B lower than 3500 K for the strong line and lower than 4000 K for the weak line. Concerning the highest T_B, we find that the limit is at 5000 K for the strong line and at 5500 K for the weak one. Since we have not normalized the histograms we can verify that the peak of the strong line distribution is more populated than that for the weak line, which has a more spread distribution. We have tried to fit these histograms with a gaussian distribution although there is a clear overpopulation of high temperature lines. The reason for this overpopulation could be produced by the perhaps small number of points (only 2500 points are used) or could be physically real. However, we do not see any clear reason why to obtain a gaussian distribution for the temperatures of

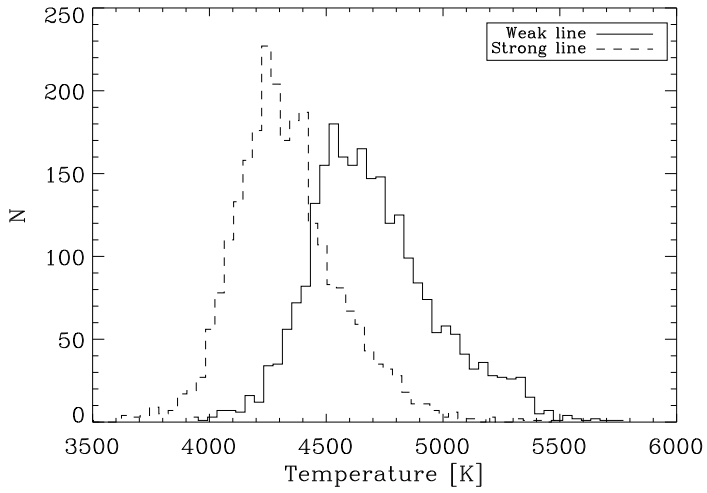

Figure 3.15: Histograms of the brightness temperature at the core of the strong 3-2 R14 and the weak 7-6 R67 lines. The peak of each distributions is close to the average brightness temperature obtained in Fig. 3.11, although the distributions are slightly shifted to higher temperatures. The width of the distributions is too high if they are compared with the amplitude of variation of the brightness temperature in movies taken with low spectral resolution (Ayres & Rabin 1996).

the core of the lines unless the temperature distribution is completely random. Furthermore, the brightness temperature is not a linear function of the kinetic temperature, so that, even if the distribution of kinetic temperature is gaussian, the distribution of brightness temperature may be not gaussian. The fitted gaussian is of the form:

$$N = A \exp\left[\frac{-(T-T_0)^2}{2\sigma^2}\right], \tag{3.49}$$

where the important quantity is the width of the gaussian given by σ. We have tabulated the data of the fit in Table 3.2, where we have calculated the FWHM=$\sqrt{8\ln 2}\sigma$ for comparison with existing data. Note that these histograms have been calculated assuming that we have a resolution of 120 km (equivalent to 0.″165), while almost all the observations concerning spec-

Table 3.2: Parameters inferred from the fit of a gaussian to the histograms obtained from the simulations of Asplund et al. (2000). The functional form is given by Eq. (3.49).

Line	A	T_0	σ [K]	FWHM [K]
3-2 R14	196.73	4296.85	193.956	456.73
7-6 R67	161.91	4646.52	235.092	553.60

troscopy of the CO lines have spatial resolutions worst than $1''$ (see e.g. Ayres & Rabin 1996, Uitenbroek 2000b). Therefore, we should degrade our synthetic data to be able to compare with the observations. The problem is that we would end up with very few points (the number of points would be reduced in a factor $(0.165)^{-2} \sim 6^2$) which does not allow performing reliable statistical studies.

Similar histograms of the temperature of a strong and weak lines have been obtained by Ayres & Rabin (1996) based on a movie of ∼1 hour taken close to disk center. The inferred histograms are very close to gaussians with rms widths of 75 K for the strong 3-2 R14 line and 44 K for the weak 7-6 R68 one. Although these results are the histograms of a movie, we think that our 3D snapshot calculations could be representative of the distribution of brightness temperatures in the whole 3D simulation.

A similar observational study was performed by Uitenbroek (2000b), who plotted the brightness temperatures of the 3-2 R14 strong line versus that for the 7-6 R68 weak line. There is a correlation between them, but it is rather loose with considerable local variation. However, the amplitude of variation of the brightness temperature of the strong line is around ∼450 K for the nonmagnetic regions, while the amplitude for the weak line is ∼200 K. These variations are centered around ∼4400 K and ∼4900 K for the strong and weak lines, respectively. These observations are not directly comparable to ours, since they were made at μ=0.5 while our synthesis are at $\mu = 1$.

3.6 Conclusion

We have presented in this chapter two computer codes for the calculation of the molecular abundances under different assumptions: the first one assumes

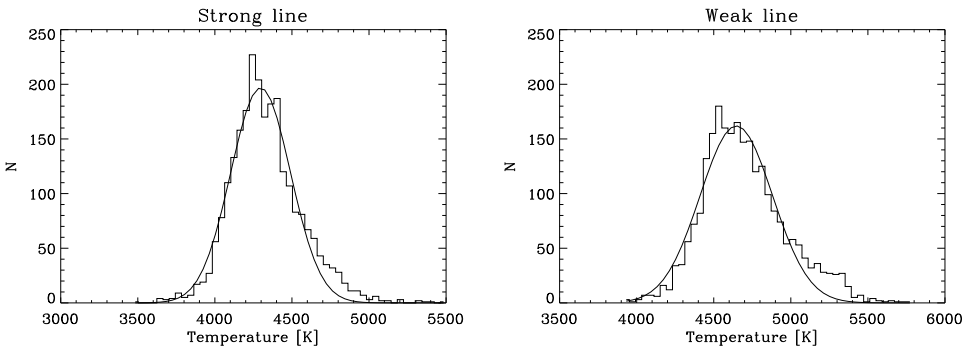

Figure 3.16: Gaussian fits to the brightness temperature in the core of the strong and weak lines of CO. Note that the gaussian fit does not reproduce the overpopulation of high temperatures. Note also that the width of the variation of the weak line is higher than that for the strong line, which is not in accordance with the observations.

that the molecular abundances are obtained instantaneously and the second one assumes that molecules are formed via chemical reactions with finite reaction times. We have shown details about their implementations and we have used them to investigate molecular formation in the solar atmosphere.

Relaxation times have been calculated for CO and other diatomic species in the solar atmosphere by using different atmospheric models. The conclusion is that, *for a given density, the relaxation time is the larger the cooler the medium where the temperature perturbation is introduced*. Similarly, *for a given temperature of the unperturbed medium, the relaxation time increases rapidly with decreasing density*.

We have performed calculations of the evolution on time of the CO abundance in the 1D hydrodynamical simulations of the solar atmosphere of Carlsson & Stein (1997) and the effect this non-equilibrium abundance has on the emerging spectrum. Recalling the conclusions possed on Section §3.5.4, our results indicate that the CO line radiation observed close to the edge of the solar disk comes from atmospheric heights not greater than ∼700 km, and that the gas in these regions of the low chromosphere must be much cooler than indicated by the cool phases of the Carlsson & Stein (1997) hydrodynamical simulations. Lower temperatures will probably increase the relaxation times needed to reach the molecular equilibrium concentrations. In a next step forward, we will in-

vestigate what happens when the hydrodynamical simulations themselves are carried out taking the CO cooling into account, in a way consistent with the non-equilibrium evolution of the molecular number densities.

Since the 1D simulations show that CO lines are almost not affected by non-equilibrium chemical effects, we have investigated the CO line formation in the 3D hydrodynamical simulations of Asplund et al. (2000). We have found an improved agreement between the CO lines observed by the ATMOS mission and the synthesis in this snapshot, in comparison with the previous results obtained by Uitenbroek (2000b). The agreement between synthesis and observation for the strong CO lines is quite good, while that for the weak CO lines is worse. Since no CO cooling is included in the simulations, this suggests that the "cool clouds" are mainly caused by hydrodynamical processes instead of by CO cooling. The lack of agreement for the weak lines suggests that non-equilibrium chemical effects are taking place in these deep regions of the 3D simulations. We are now working on verifying this possibility.

4

Non-LTE Radiative Transfer in Molecular Lines assuming Spherical Geometry

This chapter is devoted to the development of a computer code for the solution of radiative transfer problems in molecular astrophysics assuming spherical geometry. We formulate the non-LTE radiative transfer problem in general and we particularize to the plane-parallel and spherical geometries. We describe how the radiative transfer equation can be efficiently solved in spherical geometry by means of the short-characteristics formal solver. We stress the non-linear and non-local character of the non-LTE problem, thus introducing the iterative methods as the solution techniques for such a problem.

Section §4.3 introduces the iterative methods which have been developed in spherical geometry. We describe their fundamental properties and how they can be efficiently implemented for the solution of non-LTE problems in spherical geometry. Finally, in Section §4.4 we introduce a commonly used approximation which neglects the non-local character of the non-LTE problem. We investigate the range of applicability and investigate which are the effects of using this approximation in situations where the applicability conditions are not fulfilled.

The previous iterative methods are applied to two simple problems in order to obtain their convergence properties. We verify that the good convergence

properties of the methods based on the Gauss-Seidel and Successive Overrelaxation schemes are maintained when solving problems in spherical geometry. We then apply these methods to the solution of two real astrophysical problems: the formation of pure rotation water spectral lines in a hot shell of the molecular complex SgrB2 in the Galactic Center and the formation of CO vibration-rotation lines in the envelope of the red supergiant VY CMa.

4.1 Basic equations

The standard multilevel radiative transfer problem requires the joint solution of the radiative transfer (RT) equation which describes the radiation field and the kinetic equations (KE) for the atomic or molecular level populations which describe the excitation state (see, e.g., Mihalas 1978). The numerical solution of the problem requires to discretize the model atmosphere in NP points.

The physical properties of the atmosphere are assumed to be known at such $i = 1, 2, \ldots, \mathrm{NP}$ points. The RT problem consists on obtaining the population n_j of each of the $j = 1, 2, \ldots, \mathrm{NL}$ levels included in the atomic/molecular model that are consistent with the radiation field within the stellar atmosphere. This radiation field has contributions from possible background sources and from the radiative transitions in the given atomic/molecular model.

In the field of stellar atmosphere modeling, it is usual to make the assumption of statistical equilibrium. This assumption is supported by the comparison of the dynamical timescales and the radiative timescales. The radiative timescale for obtaining the atomic/molecular level populations that are consistent with the radiation field are usually much smaller than the dynamical timescales (except for some isolated cases like supernovae explosions). This way, the equilibrium between the radiation field and the matter is reached almost instantaneously in comparison with the macroscopic motions. Therefore, we can assume that the atmosphere is instantaneously static (although taking into account the Doppler shifts due to the velocities) when calculating the level populations. To this end, we formulate the rate equations for each level i at each spatial point as:

$$\frac{dn_i}{dt} = \frac{\partial n_i}{\partial t} + \mathbf{v} \cdot \nabla n_i = \sum_{j \neq i} n_j P_{ji} - n_i \sum_{j \neq i} P_{ij} = 0, \tag{4.1}$$

where the statistical equilibrium has been assumed. In this equation, n_j is the population of level j in the atomic or molecular model and the P_{ij} are the transition rates in s^{-1} between level i and j. Two different processes contribute to this transition rate: the collisions between the model atom/molecule and external abundant species induce collisional transitions between levels i and j with a rate which is defined as C_{ij}; on the other hand, the radiative processes, denoted as R_{ij} produce transitions between energy levels following the selection rules applicable in each case. The total transition rate can then be written as $P_{ij} = C_{ij} + R_{ij}$. Note that one of the previous equations can be obtained from the summation of the rest, so that the previous set is not linearly independent. Since an independent equation is needed in order to close the system, one of the equations is replaced by the particle conservation law. This law states that the sum of the population of all the energy levels must be equal to the total abundance of the species ($n_{\rm total}$):

$$\sum_i n_i = n_{\rm total}. \tag{4.2}$$

Formally speaking, the system of equations given by Eqs. (4.1) together with Eq. (4.2) can be written in matrix form as:

$$\mathbf{A} \cdot \mathbf{n} = \mathbf{f}, \tag{4.3}$$

where $\mathbf{A}$ is a matrix of size NL×NL whose matrix elements contain the transition rates P_{ij} (except for one of the rows which contains only 1 due to the conservation law), $\mathbf{f}$ is a vector of length NL with zeros except for the $n_{\rm total}$ of the conservation law, and $\mathbf{n}$ is a vector containing the population of each level. The result of grouping all the sets of equations similar to Eq. (4.3) together for all the NP points in the atmosphere can be symbolically represented by means of the system (see Socas-Navarro & Trujillo Bueno 1997):

$$\mathbf{L} \cdot \mathbf{n} = \mathbf{f}, \tag{4.4}$$

where $\mathbf{f}$ is now a known vector of size NP×NL, $\mathbf{n}$ is a vector of the same length with the level populations of the NL levels for the NP points and $\mathbf{L}$ is a *block-diagonal* matrix such that each of the NP blocks of size NL×NL is given by the matrix $\mathbf{A}$ of Eq. (4.3).

The collisional rates C_{ij} are assumed to be known once the local physical conditions of the atmosphere are given. On the other hand, the radiative rates R_{ij} depend on the radiation field present in the atmosphere:

$$\begin{aligned} R_{ij} &= B_{ij}\bar{J}_{ij} \qquad i<j \\ R_{ji} &= B_{ji}\bar{J}_{ji} + A_{ji} \qquad i<j, \end{aligned} \tag{4.5}$$

where B_{ij} and B_{ji} are the Einstein coefficients for stimulated emission and absorption, respectively, A_{ji} is the Einstein coefficient for spontaneous emission and $\bar{J}_{ij}$ ($\bar{J}_{ji}$) is the mean frequency-averaged intensity weighted by the absorption (emission) profile. Since we assume *complete frequency redistribution* (CRD), $\bar{J}_{ij} = \bar{J}_{ji}$, which is given by:

$$\bar{J}_{ij} = \frac{1}{4\pi}\int d\mathbf{\Omega}\int d\nu\phi_{ij}(\nu,\mathbf{\Omega})I_{\nu\mathbf{\Omega}}, \tag{4.6}$$

where ϕ_{ij} and $I_{\nu\mathbf{\Omega}}$ are, respectively, the normalized line profile and the specific intensity at frequency ν and direction $\mathbf{\Omega}$. We have explicitly indicated the direction dependence in the line profile to account for directional Doppler shifts due to macroscopic velocity fields in the medium. The integration has to be carried out for the full 4π solid angle subtended by the sphere and for the frequency range of the transition. The specific intensity is governed by the radiative transfer equation:

$$\frac{d}{ds}I_{\nu\mathbf{\Omega}} = \chi_{\nu\mathbf{\Omega}}\left(S_{\nu\mathbf{\Omega}} - I_{\nu\mathbf{\Omega}}\right). \tag{4.7}$$

which describes the variation of the specific intensity at frequency ν along a ray of direction $\mathbf{\Omega}$, being $\chi_{\nu\mathbf{\Omega}}$ and $S_{\nu\mathbf{\Omega}}$ the opacity and the source function, respectively, and s the geometrical distance along the ray (see, e.g., Mihalas 1978). The opacity describes how the photons are absorbed when being transported in the atmosphere, while the source function describes the generation of new photons in the atmosphere. Therefore, the RT equation is nothing but a conservation law for the specific intensity where we take into account the sinks and sources of radiation. This equation can be formally solved if we know the variation of the opacity and the source function along the ray. Once the atmosphere is discretized, the specific intensity and the mean intensity can be

written formally as:

$$\begin{aligned} \mathbf{I}_{\nu\mathbf{\Omega}} &= \mathbf{\Lambda}_{\nu\mathbf{\Omega}}\left[\mathbf{S}_{\nu}\right] + \mathbf{T}_{\nu,\mathbf{\Omega}} \\ \bar{\mathbf{J}}_{\mathbf{ij}} &= \bar{\mathbf{\Lambda}}\left[\mathbf{S}_{\mathbf{ij}}\right] + \mathbf{T}, \end{aligned} \tag{4.8}$$

where $\mathbf{T}_{\nu\mathbf{\Omega}}$ is a term which accounts for the contribution of the boundary conditions to the intensity at a given point and $\mathbf{\Lambda}_{\nu\mathbf{\Omega}}$ gives the response of the radiation field to perturbations in the source function.

The opacity and the source function have two main contributions coming from the background continuum and from the atomic/molecular model transitions. We will assume that the continuum opacity coming from the background species can be obtained once the physical conditions at each spatial point are known. This contribution includes, for example, the free-free and bound-free absorption processes in hydrogen, the background molecular species which are treated in LTE, opacity due to metals, absorption due to interstellar dust, etc. The contribution due to the active atomic/molecular model transitions can be obtained in terms of the population of the upper and lower levels. Therefore, the opacity at a given frequency for a bound-bound transition between a lower level l and an upper level u taking into account the background opacity can be calculated using the expression (see, e.g., Mihalas 1978):

$$\chi_{\nu\mathbf{\Omega}} = \frac{h\nu}{4\pi}\phi_{\nu\mathbf{\Omega}}\left(n_l B_{lu} - n_u B_{ul}\right) + \chi_c(\nu). \tag{4.9}$$

The positive term accounts for the direct absorption from the lower to the upper level and the negative term accounts for the stimulated emission from the upper to the lower level. It is usual to include this term as a negative absorption although it effectively represents an emission. As mentioned above, we have also assumed that the emission line profile is equal to the absorption line profile. We have also explicitly included the continuum opacity χ_c which can be calculated from the physical conditions. The emissivity is given by:

$$\epsilon_{\nu\mathbf{\Omega}} = \frac{h\nu}{4\pi}\phi_{\nu\mathbf{\Omega}} n_u A_{lu} + \epsilon_c(\nu), \tag{4.10}$$

which takes into account the spontaneous emission from the upper to the lower level. ϵ_c is the continuum emissivity which is also assumed to be known from the physical conditions. In some astrophysical systems, the continuum emissivity can be very important at the infrared wavelengths since dust can be an

extremely efficient emitter (this is the case of dusty circumstellar envelopes). The source function can be obtained from Eq. (4.9) and (4.10) with the usual definition:

$$S_{\nu\mathbf{\Omega}} = \frac{\epsilon_{\nu\mathbf{\Omega}}}{\chi_{\nu\mathbf{\Omega}}}. \tag{4.11}$$

The previous definitions have made clear that, unless the value of $\bar{J}_{ij}$ is known, the system of Eqs. (4.3) is not linear, because the radiative rates R_{ij} depend on the population through its dependence on the mean intensity, and this intensity is governed by the radiative transfer equation, whose terms (opacity and source function) depend on the level populations themselves. This *nonlinear* character of the RT problem makes it necessary to solve it by means of an iterative scheme. Moreover, the RT equation couples different zones of the atmosphere, so making the specific intensity a *nonlocal* function of the emitting and absorbing conditions throughout the medium. This nonlinear and nonlocal character of the whole non-LTE RT problem implies that its solution is a very difficult task, and many efforts have been made in developing fast and reliable solution methods (see Trujillo Bueno & Fabiani Bendicho 1995 and more references therein).

4.2 Formal Solution in Spherical Symmetry

The kinetic Eqs. (4.1) can be easily solved at each point in the atmosphere independently once the radiation field is known. The level populations turn out to be geometry dependent because of the dependence on the medium's radiation field. The solution of the RT equation has to be done accounting for enough information about the angular variation of the radiation field at each point in order to calculate the mean intensity as the angular average of the specific intensity. Any symmetry present in the problem should ideally be used to reduce the angular information needed for calculating $\bar{J}$.

4.2.1 Plane-parallel geometry

The most used geometry is that of a plane-parallel atmosphere. Let L be the physical size of the atmosphere and R the total radius of the star. When $L/R \ll 1$, we consider that the curvature of the atmosphere is so small that we can assume it to be plane-parallel. We also consider that the physical conditions

vary only along the vertical direction z. In the plane-parallel case, the RT Eq. (4.7) can be written as:

$$\frac{d}{\mu d\tau_\nu} I(z,\mu,\nu) = I(z,\mu,\nu) - S(z,\mu,\nu), \tag{4.12}$$

where we have defined the optical depth $d\tau_\nu = -\chi_\nu dz$, z being the vertical coordinate in the atmosphere and $\mu = \cos\theta$ is the cosine of the angle between the vertical and the ray. On the other hand, the mean intensity for a given transition between levels i and j is:

$$\bar{J}_{ij} = \frac{1}{2}\int_{-1}^{1} d\mu \int d\nu \phi_{ij}(\nu,\mu) I(z,\mu,\nu). \tag{4.13}$$

We have explicitly indicated the μ dependence of the line profile to account for macroscopic velocities in the material. Many numerical methods have been proposed to solve the linear first order differential equation (4.12). We will describe below the *short-characteristics* method which is very efficient and precise in solving this equation.

4.2.2 Spherical geometry

Consider now an atmosphere with $L/R \sim 1$. The curvature makes it necessary to include the sphericity effects on the problem. Assume that the physical conditions vary only along the radial direction. When the distance element ds is expressed in spherical coordinates, one then obtains the corresponding RT equation:

$$\mu \frac{\partial I_\nu(r,\mu)}{\partial r} + \frac{\left(1-\mu^2\right)}{r}\frac{\partial I_\nu(r,\mu)}{\partial \mu} = \eta_\nu(r,\mu) - \chi_\nu(r,\mu) I_\nu(r,\mu), \tag{4.14}$$

where r is the radial coordinate, and μ is the cosine of the angle between the radial direction and the ray. Note that the RT equation is not an ordinary differential equation (ODE) but a partial differential equation (PDE) which accounts for the curvature effects of the media. As can be seen from Eqs. (4.9) and (4.10), the angular dependence of the opacity and emissivity comes from the angular dependence of the line profile, which can be Doppler shifted by macroscopic velocity fields.

4.2.3 Boundary conditions

In order to solve Eq. (4.14), we discretize the spherical atmosphere in N_r radial shells parameterized by their radius r_i, where $i = 1 \ldots N_r$. We note that $i = 1$ and $i = N_r$ refer to the internal and external boundaries, respectively, where the incident intensity is assumed to be known. Therefore, $r_1 = R_c$ is the radius of the internal core (considered as the surface where the internal boundary condition is given) and $r_{N_r} = R_a$ is the radius of the atmosphere (considered as the surface where the external boundary condition is given). The usual external boundary condition is to assume that there is no incident radiation. In some situations it is necessary to include an external source of radiation which can affect the radiation field inside the astrophysical system under consideration. This is the case of a cold molecular cloud in which the Cosmic Microwave Background Radiation (CMBR) has to be included because it produces an important excitation of the lowest energy levels of some molecules. Another case would be coronal radiation which may affect the excitation properties of some atomic species in the chromosphere of magnetically active stars like the Sun. Concerning the internal boundary condition, its value depends also on the type of object one is modeling. We can assume no incident radiation for a molecular cloud in free-fall, the usual diffusion approximation or even the photospheric stellar spectrum for a central star embedded in a circumstellar envelope. The star's radiation can be even diluted by the presence of absorbing material or by the geometric dilution. Schematic representations of the three possible internal boundary conditions are shown in Fig. 4.1

Instead of solving the full partial differential equation (4.14) by appropriate standard numerical methods, one can always reduce a PDE to a set of ODEs once the characteristics curves of the equation are found. We parameterize these curves with the variable t so that the intensity along these curves can be found by requiring $I_\nu(r, \mu) = I_\nu(r(t), \mu(t))$, so that:

$$\frac{dI}{dt} = \frac{\partial I}{\partial r}\frac{\partial r}{\partial t} + \frac{\partial I}{\partial \mu}\frac{\partial \mu}{\partial t}. \tag{4.15}$$

By comparison with Eq. (4.14), we find:

$$\begin{aligned} \frac{\partial r}{\partial t} &= \mu \\ \frac{\partial \mu}{\partial t} &= \frac{1-\mu^2}{r}. \end{aligned} \tag{4.16}$$

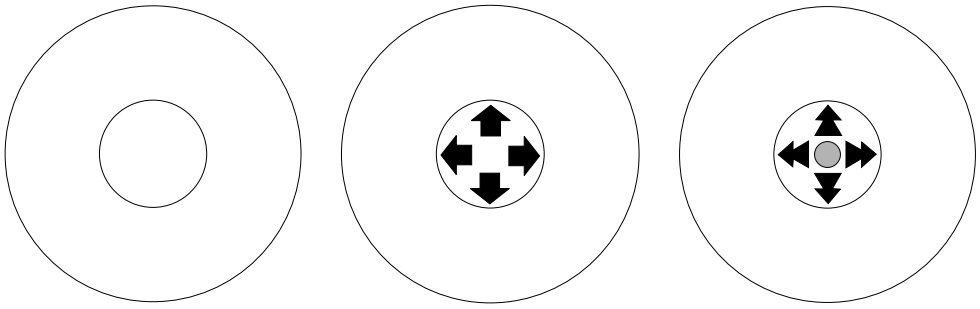

Figure 4.1: Schematic representations of the three possible *internal* boundary conditions. The left panel shows the case without incident radiation from the central point, the middle panel shows the case in which the boundary condition is constant and given, e.g., by the diffusion approximation, while the right panel shows the case in which there is a central star whose radiation is being diluted, either geometrically or by absorption.

The solution to the previous set of equations are straight lines with a constant value of μ and with $r(t) \propto t$, i.e. rays with a constant inclination which are limited by their intersection with the boundary surfaces. The scheme can be found in the left panel of Figure 4.2. A more suitable representation can be found in the right panel of the same figure. This representation makes use of the symmetry properties of the atmosphere and the characteristics are straight lines parallel to the central ray (the ray which is perfectly radial) and parameterized by its distance to this central ray (the so-called impact parameter p_j). We choose these impact parameters to be equal to the radius of the different N_r shells, so each characteristics is tangent to a shell. In order to correctly sample the central core, this set is augmented by some rays which intersect the central core (N_c), so the total number of characteristics is $N_p = N_r + N_c$ (see, e.g., Mihalas 1978). Therefore,

$$p_j = \frac{r_1}{N_c} j \qquad \text{for} \qquad j \leq N_c, \tag{4.17}$$

$$p_j = r_{j-N_c} \qquad \text{for} \qquad j > N_c. \tag{4.18}$$

The final geometry used to solve the RT equation is that shown in the right panel of Fig. 4.2. The intersections between each characteristics and the radial shells define a grid, parameterized by its depth z. The relation between these quantities is straightforwardly obtained from geometrical considerations, thus

$z(r, p_i) = \left(r^2 - p_i^2\right)^{1/2}$. Therefore, we have made a transformation of variables from (r, μ) to (p, z) which are geometrically equivalent but simpler to use in this situation (Mihalas 1978). We have only plotted one quadrant of the whole atmosphere due to the symmetry properties. Since we have stated that the physical conditions are only dependent on the radial direction and not on the angular direction, any position on each shell is equivalent. This leads to a considerable saving in the total computing time. The only drawback is that additional boundary conditions have to be included. We apply a reflection boundary conditions at $z = 0$ and consider the points with the same value of $|p_j|$ as equivalent.

4.2.4 Angular information

Consider a ray parameterized by its constant value of the impact parameter p_i. The RT equation describing the variation of the specific intensity along this ray can be written as:

$$\pm \frac{\partial I^{\pm}(z, p_i, \nu)}{\partial z} = \eta(z, p_i \nu) - \chi(z, p_i, \nu) I^{\pm}(z, p_i, \nu), \tag{4.19}$$

because these straight lines are the characteristics. The + and − signs refer, respectively, to radiation flowing toward and away from the external observer. This equation can then be reduced to one equivalent to Eq. (4.12) by defining the optical depth as $d\tau_\nu(z, p_i) = -\chi_\nu(p_i, z)dz$, i.e., by using a different optical depth mesh for every characteristics. Solving the previous equation along each characteristics, one can get the value of the intensity at each intersection. Since the value of the impact parameter and the angle μ are related by the geometrical relation $\mu(r, p) = \left(r^2 - p_i^2\right)^{1/2} / r$, the knowledge of the intensity at the intersections between the characteristics and the shells is equivalent to the knowledge of the angular distribution of the specific intensity. The previous technique is only possible when the physical conditions depend only on the radial distance, and not on the angle. This way, the mean intensity can be calculated by choosing an appropriate numerical quadrature. Eq. (4.13) has been numerically integrated using a trapezoidal rule because the number and particular values of the μ angles depend on the chosen shell (note that each shell is intersected by a different number of characteristics curves and at different z positions). This makes impossible to use a Gaussian quadrature.

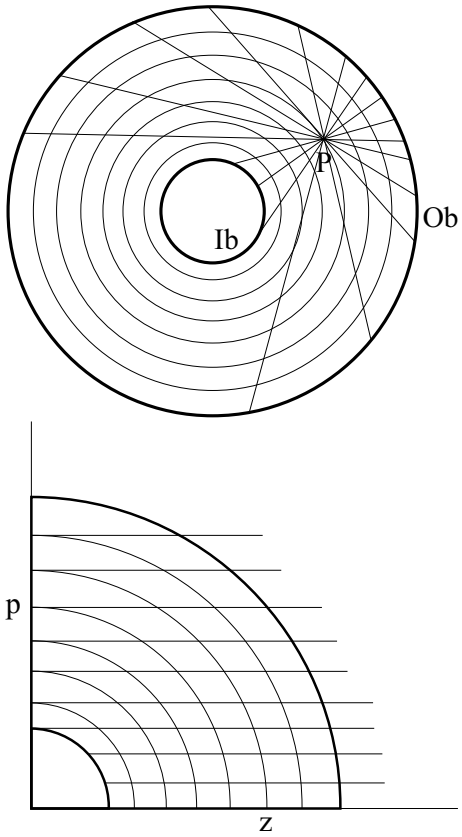

Figure 4.2: Schematic representations of the geometry used in the RT problem. The left panel shows the contribution of all the rays to the mean intensity at shell P. "Ob" stands for *Outer boundary* and "Ib" for *Inner boundary*. The right panel shows the chosen reduced geometry which takes advantage of the symmetry properties of the problem.

4.2.5 Formal solution

In order to solve the RT equation in spherical geometry, we solve each of the equivalent plane–parallel problems with the *short–characteristics* (SC) method (see Kunasz & Auer 1988). It is the same formal solver used by Trujillo Bueno & Fabiani Bendicho (1995) for cartesian geometries. As shown below, it facilitates the efficient implementation of the fast iterative methods developed by Trujillo Bueno & Fabiani Bendicho (1995) and provides a good precision with a reduced

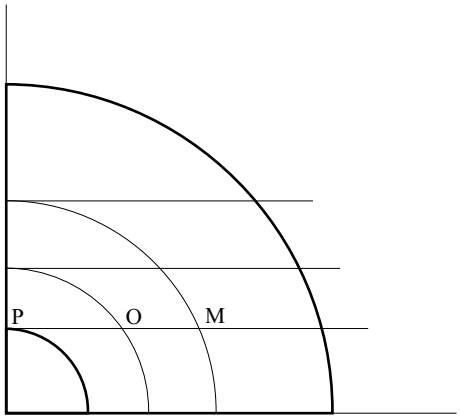

Figure 4.3: Schematic representation of how the short-characteristics formal solver is applied for solving the RT equation for spherical symmetry. We have indicated points M, O and P which are used in the parabolic SC method.

computational time. In fact, it scales linearly with the number of points in the atmosphere.

The SC method can be obtained by assuming that the source function varies as a polynomial between a given number of points along the ray propagating in the stellar atmosphere. Therefore, the RT equation can be integrated very easily. We will use the following scheme in our codes. Consider three points, the *upwind* point M, point O and the *downwind* point P, where the value of the source function are known a priori. Assume that we know the intensity at point M and we want to calculate its value at O. If we assume that the source function varies parabolically between M, O and P, we can integrate analytically the radiative transfer equation and obtain the following formula:

$$I_O = I_M e^{-\Delta\tau_{MO}} + \Psi_M S_M + \Psi_O S_O + \Psi_P S_P, \tag{4.20}$$

where I_M is the intensity at the *upwind* point M. The quantities $\{\Psi_i, i = M, O, P\}$ are functions of the optical distances between the upwind point M and the given point O ($\Delta\tau_{MO}$) and between the given point O and the downwind point P ($\Delta\tau_{OP}$), while $\{S_i, i = M, O, P\}$ are the values of the source function at points M, O and P, respectively. We can build a similar formula assuming that the source function varies linearly between points M and O, so

that the last term in Eq. (4.20) disappears and Ψ_M and Ψ_0 will only depend on $\Delta\tau_{MO}$.

The parabolic short-characteristics formula has been used in all our calculations for obtaining the required accuracy, although the linear formula has to be used in the boundaries because a downwind point cannot be defined. Although useful, it is better to use the linear formula only in these selected points due to its intrinsic lack of precision.

4.2.6 Computational cost

The previous way of obtaining the angular information of the radiation field (described in detail in Mihalas 1978) involves an increase in the time needed to carry out the solution of the RT equation in spherical symmetry with respect to the plane–parallel case. Consider a plane-parallel atmosphere with N_r shells and let N_q be the number of angles chosen for the numerical calculation of the mean intensity. The number of points in the atmosphere in which the specific intensity has to be calculated is:

$$N_{\rm pp} = N_q N_r. \tag{4.21}$$

In the case of a spherically symmetric atmosphere, we can calculate the number of points by summing all the points in all the characteristics:

$$N_{\rm spher} = \sum_{i=1}^{N_c} N_r + \sum_{i=N_c+1}^{N_r+N_c-1} (N_r + N_c - i) = \frac{N_r^2}{2} + \left(N_c - \frac{1}{2}\right) N_r. \tag{4.22}$$

The increase factor between a formal solution for the spherically symmetric case and the plane-parallel case is:

$$f = \frac{N_{\rm spher}}{N_{\rm pp}} = \frac{N_r + 2N_c - 1}{2N_q}. \tag{4.23}$$

For typical cases in which $N_q = 3$, $N_r = 40$ and $N_c = 6$ we have $f = 8.5$, that is, each formal solution takes around an order of magnitude more computing time in the spherical case than in the plane-parallel case.

4.3 Iterative methods

The nonlinear character of the system of equations given by Eq. (4.3) makes it necessary to apply iterative methods. The main idea of an iterative method for the solution of a nonlinear problem is to start from an estimation of the solution and then to perform successive corrections to this estimation until the final solution is found. Iterative methods for multilevel transfer problems obey the same structure. Consider the iterative solution of Eq. (4.3) at each one of the NP spatial points. We start from an estimate $\mathbf{n}^{\rm old}$ of the atomic or molecular level populations at this point. If this estimate is not the exact solution of the problem, there exists a nonzero residual

$$\mathbf{r} = \mathbf{f} - \mathbf{A}^{\rm old} \cdot \mathbf{n}^{\rm old} \neq \mathbf{0}. \tag{4.24}$$

We have explicitly indicated that the system matrix $\mathbf{A}^{\rm old}$ depends on the previous estimation of the populations $\mathbf{n}^{\rm old}$. This matrix is built, for every point in the atmosphere, by using the appropriate collisional rates and the radiative rates given by Eq. (4.5). The objective is to find the correction $\delta\mathbf{n}$ such that the estimation:

$$\mathbf{n}^{\rm new} = \mathbf{n}^{\rm old} + \delta\mathbf{n} \tag{4.25}$$

gives a zero residual and, therefore,

$$\mathbf{A}^{\rm new} \cdot \delta\mathbf{n} = \mathbf{f} - \mathbf{A}^{\rm new} \cdot \mathbf{n}^{\rm old}. \tag{4.26}$$

Note that this equation cannot be directly solved because it is still nonlinear and similar to the original Eq. (4.3), hence it is impossible to solve the problem in one step. It is much more efficient to perform approximate corrections instead of the exact correction and arrive to the solution iteratively.

The different iterative methods applied to the solution of radiative transfer problems differ in the way one manages to build a linear system in order to get *approximate* corrections to the level populations. The scheme one chooses to carry out this linearization is crucial to end up with a fast iterative method which additionally accounts for all the radiative couplings in the atomic or molecular system (see Trujillo Bueno & Fabiani Bendicho 1995; Socas-Navarro & Trujillo Bueno 1997). We now briefly describe each of the methods developed so far.

4.3.1 The Λ-iteration Method

This method is the most direct and simple one. It consists on solving Eq. (4.26) by calculating the system matrix at each point in the atmosphere using the populations from the previous iterative step, $\mathbf{n}^{\rm old}$. Therefore, the corrections to the estimation of the population can be obtained from:

$$\mathbf{A}^{\rm old} \cdot \delta\mathbf{n} = \mathbf{r} \tag{4.27}$$

Therefore, the value of the mean intensity $\bar{J}_{ij}$ at each spatial point is obtained by solving the RT equation using the $\mathbf{n}^{\rm old}$ values of the populations at this point. At each iterative step the nonlinear system is transformed into a linear one, which can be solved easily to obtain the approximate corrections to the populations. This procedure is iterated until convergence. Although very simple and easy to code, this method has a main drawback, which is its very poor convergence rate. This is due to the fact that this method is equivalent to assuming that the field does not react to the perturbations in the populations (see Socas-Navarro & Trujillo Bueno 1997), which is a very unrealistic approximation. Due to the this assumption, the information is transferred in the atmosphere one photon mean free path per iteration. Hence, if the medium is optically thick, it takes many iterations to radiatively connect all the points in the atmosphere. However, it is still useful for optically thin problems (see, e.g. Uitenbroek 2000b, Dickel & Auer 1994, Bernes 1979, etc.).

4.3.2 The Accelerated Λ-iteration Method (ALI)

Description of the scheme

ALI is a clever modification to the Λ-iteration method which implies a much better convergence behavior (Cannon 1973; Olson, Auer, & Buchler 1986). There are several methods to achieve the linearity in the system matrix in the ALI method. The most powerful ones are linearization (Auer & Mihalas 1969; Scharmer & Carlsson 1985) and preconditioning (Rybicki & Hummer 1991, 1992) schemes. Socas-Navarro & Trujillo Bueno (1997) showed that both schemes are almost equivalent, although the preconditioning scheme leads to a more stable behavior of the iterative scheme. The preconditioning scheme is nowadays the most used due to its simplicity and good performance. It is usually referred to as the Multilevel-ALI (MALI). This method is based on

two strategies: the *operator splitting formula* that Cannon (1973) introduced into the RT literature and the preconditioning scheme. The operator splitting strategy rewrites the formal solution of the RT equation given by Eq. (4.8) as:

$$\mathbf{I}_{\nu\mathbf{\Omega}} = \mathbf{\Lambda}^*_{\nu\mathbf{\Omega}}[\mathbf{S}_\nu]^{new} + (\mathbf{\Lambda}_{\nu\mathbf{\Omega}} - \mathbf{\Lambda}^*_{\nu\mathbf{\Omega}})\,[\mathbf{S}_\nu]^{old} + \mathbf{F}_{\nu\mathbf{\Omega}}, \tag{4.28}$$

where $\mathbf{\Lambda}^*_{\nu\mathbf{\Omega}}$ is an approximation to the full operator $\mathbf{\Lambda}_{\nu\mathbf{\Omega}}$. Note that the $\mathbf{\Lambda}^*$ and $\mathbf{\Lambda}$ operators are dependent on the "old" populations. The approximate operator is usually chosen to be the diagonal of the full operator because it is easy to obtain and its inversion is trivial. The preconditioning strategy consists on the evaluation of some selected quantities of the iterative process using the populations from the previous iterative step, which allows to achieve linearity. The main advantage of this preconditioning approach is that we can achieve linearity in the system but we maintain the essential information on the radiative coupling. The resulting iterative scheme is equivalent to Eq. (4.27), but now the system matrix $\mathbf{A}^{\rm old}$ is obtained, for each spatial point, with some small modifications (see Rybicki & Hummer 1991 for details), which does take into account the response of the radiation field to the source function perturbations (Socas-Navarro & Trujillo Bueno 1997):

$$\mathbf{A}^{\rm old}_{\rm MALI} \cdot \delta\mathbf{n} = \mathbf{r}. \tag{4.29}$$

Since the value of $\bar{J}_{ij}$ is obtained from the value of the populations $\mathbf{n}^{\rm old}$, the system becomes linear and can be easily solved in order to get the approximate corrections for the populations at each iterative step. The only difference with the Λ-iteration scheme lies on the way the matrix for each spatial point is obtained, which includes the calculation of the approximate $\mathbf{\Lambda}^*_{\nu\mathbf{\Omega}}$ operator. When this approximate operator is equal to the diagonal of the full operator $\mathbf{\Lambda}_{\nu\mathbf{\Omega}}$, the computational time per iteration is equivalent to the Λ-iteration scheme. When this procedure is iterated until convergence, we obtain a much better convergence rate than the Λ-iteration scheme.

The MALI scheme in spherical geometry

In this section we describe how the previous MALI scheme can be implemented in spherical symmetry. The following notes are applicable to the Λ-iteration scheme since the calculation of the mean intensity has to be carried out in both

schemes. For solving the non-LTE problem, we need to evaluate the system matrix $\mathbf{A}^{\rm old}_{\rm MALI}$ at each spatial point. In order to calculate this matrix, we need to calculate the mean intensity in each transition $\bar{J}_{ij}$ and the approximate operator $\mathbf{\Lambda}^*$. With the SC formal solver scheme, this operator can be efficiently obtained (see Olson & Kunasz 1987, Auer & Paletou 1994). The following steps describe how the mean intensity and the diagonal of the full $\mathbf{\Lambda}$ operator can be efficiently obtained in spherical symmetry:

1 *Incoming part.* We start the integration of the RT equation along each characteristics from the outer boundary surface using the appropriate boundary condition. If the outer boundary condition has a dependence with the angle μ, then each characteristics will have a different boundary condition $I(R,\mu)$. The intensity is then propagated inwards using repeatedly the formal solution given by the parabolic short-characteristics Eq. (4.20). This process is carried out in each characteristics until reaching the inner boundary surface for the N_c rays which intersect the core or until reaching the surface $z=0$ for the N_r rays which do not intersect the core. At this moment, we have enough information to obtain the angular dependence of the incoming radiation field and obtain, using a numerical quadrature, its contribution to the mean intensity using Eq. (4.13):

$$\bar{J}_{ij}({\rm in}, r_i) = \frac{1}{2}\int_{-1}^{0} d\mu \int d\nu \phi_\nu I(r_i,\mu), \tag{4.30}$$

where we have explicitly indicated that it is the contribution to the mean intensity of the incoming radiation. Similarly, we calculate the contribution of the incoming radiation to the approximate operator. Since this operator is diagonal, it represents the response of the mean intensity to a unit pulse perturbation in a given point O. Therefore:

$$\Lambda^*_{ij}({\rm in}, r_i) = \frac{1}{2}\int_{-1}^{0} d\mu \int d\nu \phi_\nu \Psi_O, \tag{4.31}$$

where Ψ_O is the coefficient which enters the short-characteristics formula (4.20).

2 *Outgoing part.* We apply the boundary condition for all the rays (the inner boundary condition for the rays which intersect the core and the

reflection condition to those which do not intersect the core) and continue integrating the RT equation along the characteristics until reaching the external boundary surface. The contribution of the outgoing radiation field to the mean intensity can be obtained by:

$$\bar{J}_{ij}(\mathrm{out}, r_i) = \frac{1}{2}\int_0^1 d\mu \int d\nu \phi_\nu I(r_i, \mu), \tag{4.32}$$

and similarly for the approximate operator.

When this process is done for all the spectral lines in the model, the mean intensity $\bar{J}_{ij}$ and the diagonal of the $\mathbf{\Lambda}$ operator is obtained at each spatial point. We can then build the system matrix $\mathbf{A}^{\mathrm{old}}_{\mathrm{MALI}}$ for each point and obtain the approximate corrections to the populations. Note that such a matrix can be obtained independently for each spatial point once the value of the mean intensity is known.

Parallelization

Finally, let's comment something about the possibilities of parallelization of the previous schemes. Note that in MALI, the formal solution of the RT equation and the level population correction process are totally uncoupled. This allows an immediate parallelization scheme which separates the solution of the RT equation along each characteristic in different processing units. The ideal case would be that in which we have $N_r + N_c$ processors, one for solving the RT equation along each characteristics. Each processor has to carry out the solution for all the line frequencies included in the model to take advantage of the vectorization properties of the modern processors and compilers, although the formal solution can be performed frequency by frequency. Once the radiation field is known, the population correction can be performed for all the shells simultaneously.

4.3.3 The Multilevel Gauss–Seidel Method (MUGA)

Description of the scheme

This method was developed by Trujillo Bueno & Fabiani Bendicho (1995). Section 2.1 in the paper by Fabiani Bendicho, Trujillo Bueno, & Auer (1997) gives

a suitable summary of its application to the multilevel problem in cartesian coordinates. Although maintaining a computational time per iteration comparable to MALI, it has a much better convergence behavior. For MALI, the system matrix $\mathbf{A}^{\rm old}$ is built, for each spatial point, from the populations of the previous iteration. We have used an approximate $\mathbf{\Lambda}^*$ operator which is the diagonal of the full $\mathbf{\Lambda}$ operator. The key idea of the Gauss–Seidel based methods is that one can obtain the convergence rate of an upper or lower triangular (and therefore non-linear) approximate $\mathbf{\Lambda}^*$ operator without the necessity of neither building nor inverting this triangular operator. To this end, once the radiation field is known at the atmospheric point being considered, the population correction can be made directly using Eq. (4.29). Then, if these new populations are taken into account when calculating the radiation field at the next spatial point, the resulting scheme turns out to be equivalent to a Gauss-Seidel scheme, which has a much better convergence rate. The ordering in which the radiation field is calculated now turns out to be crucial, as we will see below.

Iterative scheme in spherical geometry

Trujillo Bueno & Fabiani Bendicho (1995) developed a novel RT method based on GS iterations and showed how to implement it efficiently for the plane–parallel case. The short-characteristics formal solver is suitable for achieving an efficient solution of the non-LTE RT problem using the Gauss-Seidel iterative scheme. We describe below how it can be implemented in spherical geometry. The idea is first to consider the contribution to the radiation field of the *incoming* rays, i.e., of those rays which enter the atmosphere from above the outer boundary. When this contribution has been calculated, we consider the propagation of the *outgoing* rays and we calculate the population corrections point by point consecutively. To facilitate the description, we divide each iteration in these two main steps:

1 *Incoming part.* The formal integration of the RT equation along each characteristics of constant impact parameter p_j is started at the outer boundary. This process is schematized in the upper left panel of Fig. 4.4. Note that the intensity can be propagated simultaneously along all the characteristics because they are independent. The integration along each ray is done using Eq. (4.20), calculating the intensity at each shell i until

the ray intersects the central core (if its impact parameter obeys $p_j < R_c$) or arrives tangent to the shell which fulfills $p_j = r_i$. Once the incoming intensity at every intersection point between the shells and the whole set of characteristics is known, the contribution to the mean intensity of the incoming rays ($\mu < 0$) can be calculated by integrating Eq. (4.30) using the above-mentioned trapezoidal numerical quadrature.

2 *Outgoing part.* When the contribution to $\bar{J}_{ij}$ from the incoming radiation is known for every shell, the boundary condition at the inner core can be applied to get the contribution of the outgoing radiation to the mean intensity, thus allowing us to write the linear system of Eqs. (4.29) and solving it to get the population correction at the inner core. The schematic representation of this step is shown in the upper right panel of Fig. 4.4. With these improved level populations, one can propagate the intensity outwards until the shell r_2 and get the mean intensity at this shell ($\bar{J}_{ij}^{\text{old\&new}}$), which then allows us to write again the linear system of Eqs. (4.29). The procedure is repeated until arriving to the outer boundary. This subsequent process is schematized in the lower left and right panels of Fig. 4.4. The "old&new" label of the mean intensity is used to clearly show that the value of the mean intensity $\bar{J}_{ij}$ at shell n is obtained by using the new population at the shells with $r < r_n$, contrarily to what happens in the Jacobi–based methods, where the mean intensity is calculated by using the "old" population estimation. Consequently, the final system to be solved at each shell is:

$$\mathbf{A}_{\text{GS}}^{\text{old\&new}} \delta\mathbf{n} = \mathbf{r}, \tag{4.33}$$

where the coefficients of $\mathbf{A}_{\text{GS}}^{\text{old\&new}}$ are calculated at each spatial point independently as explained above.

In the plane–parallel case all the rays have both boundary conditions (the outer and the inner) because all the rays intersect both surfaces. However, in the spherically symmetric case only the rays with $p_j < R_c$ intersect the inner boundary surface, while the rest of the rays cross the whole atmosphere (see Fig. 4.4).

As explained in detail by Trujillo Bueno & Fabiani Bendicho (1995) for the plane–parallel case, the previous scheme will only give a full Gauss-Seidel

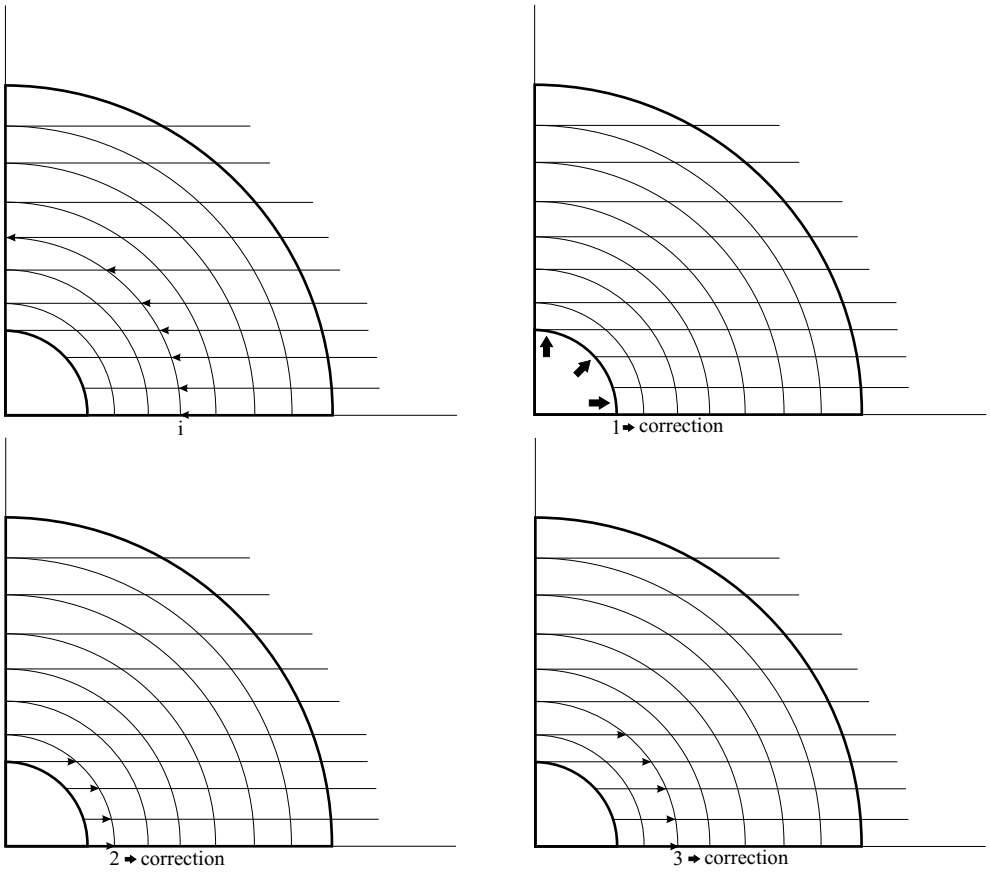

Figure 4.4: Schematic representation of the Gauss-Seidel iterative scheme in all its phases.

iteration if the linear short-characteristics formal solver is used. Since we are using the parabolic short-characteristics formal solver, two corrections have to be performed in order to obtain a true GS iteration. They are graphically schematized in Figure 4.5.

a) The first one, represented in the left panel, affects the incoming radiation field after the population correction is performed. Since the parabolic short-characteristics formal solver has been used, the radiation field at point $i+1$ depends on the absorption and emission properties of points i,

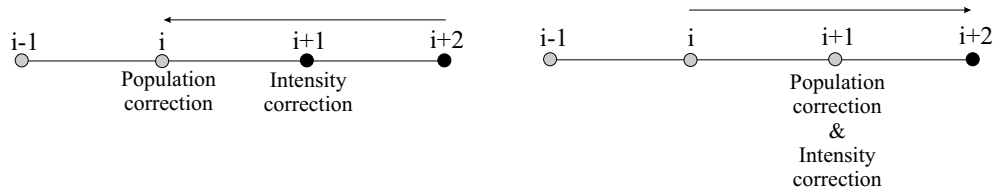

Figure 4.5: Corrections needed for obtaining a true Gauss-Seidel iteration. The left panel shows the corrections to the incoming radiation field at point $i+1$ due to the population correction at point i. The right panel shows the corrections to the outgoing radiation field at point $i+1$ due to the population correction at point $i+1$.

$i+1$ and $i+2$. The incoming radiation field at $i+1$ was calculated using the "old" populations at point i. Since we have now a new estimation of the populations at point i, we have to correct the incoming radiation field as indicated in the plot. We indicate in grey those points for which we have a "new" estimation of the populations, while those with the "old" populations are marked in black. The intensity at point $i+1$ for the characteristics with impact parameter p_j was calculated according to the formula:

$$\begin{aligned} I^{\rm old}_{i+1}({\rm in},p_j) &= I_{i+2}({\rm in},p_j)e^{-\Delta\tau_{i+2,i+1}} + \Psi_{i+2}S^{\rm old}_{i+2}(p_j) + \Psi_{i+1}S^{\rm old}_{i+1}(p_j) \\ &+ \Psi_i S^{\rm old}_i(p_j), \end{aligned} \tag{4.34}$$

which has to be replaced with:

$$\begin{aligned} I^{\rm new}_{i+1}({\rm in},p_j) &= I_{i+2}({\rm in},p_j)e^{-\Delta\tau_{i+2,i+1}} + \Psi_{i+2}S^{\rm old}_{i+2}(p_j) + \Psi_{i+1}S^{\rm old}_{i+1}(p_j) \\ &+ \Psi_i S^{\rm new}_i(p_j) = \\ &= I^{\rm old}_{i+1}({\rm in},p_j) + \Psi_i\left[S^{\rm new}_i(p_j) - S^{\rm old}_i(p_j)\right], \end{aligned} \tag{4.35}$$

since the populations at point i has just been corrected. This correction in the specific intensity is performed in each characteristics and affects the mean intensity as:

$$\bar{J}^{\rm new}_{ij}({\rm in},r_{i+1}) = \bar{J}^{\rm old}_{ij}({\rm in},r_{i+1}) + \frac{1}{2}\int_{-1}^{0} d\mu \int d\nu\phi_\nu\Psi_i\left[S^{\rm new}_i(p_j) - S^{\rm old}_i(p_j)\right], \tag{4.36}$$

where the relation between p_j and μ has to be used.

b) The second correction, represented in the right panel of the figure, is necessary once a new estimation of the populations is available for point $i+1$. Since the outgoing radiation field at point $i+1$ has been obtained with the "old" populations at this point, they have to be corrected in order to obtain the correct behavior of the outgoing radiation field. Therefore, the emerging intensity at point $i+1$, which has been obtained using:

$$\begin{aligned} I_{i+1}^{\rm old}({\rm out},p_j) &= I_i({\rm out},p_j)e^{-\Delta\tau_{i,i+1}} + \Psi_i S_i^{\rm new}(p_j) + \Psi_{i+1}S_{i+1}^{\rm old}(p_j) \\ &+ \Psi_{i+2}S_{i+2}^{\rm old}(p_j), \end{aligned} \tag{4.37}$$

has to be replaced by:

$$\begin{aligned} I_{i+1}^{\rm new}({\rm out},p_j) &= I_i({\rm out},p_j)e^{-\Delta\tau_{i,i+1}} + \Psi_i S_i^{\rm new}(p_j) + \Psi_{i+1}S_{i+1}^{\rm new}(p_j) \\ &+ \Psi_{i+2}S_{i+2}^{\rm old}(p_j) = \\ &= I_{i+1}^{\rm old}({\rm out},p_j) + \Psi_{i+1}\left[S_{i+1}^{\rm new}(p_j) - S_{i+1}^{\rm old}(p_j)\right], \end{aligned} \tag{4.38}$$

since now the populations at point $i+1$ have been corrected. The mean intensity is changed similarly to Eq. (4.36).

These corrections are applied consecutively when obtaining the outgoing radiation field until reaching the outer boundary surface.

Summarizing, when these two corrections are applied to the iterative scheme, a true Gauss-Seidel iteration is obtained once the radiation field is propagated from the outer to the inner boundary, and again to the outer one. A very exhaustive explanation of these corrections for the case of plane–parallel atmospheres can be found in Trujillo Bueno & Fabiani Bendicho (1995). The differences between their scheme and ours lies in the slightly different treatment of the solution of the RT equation along its characteristics.

The previous scheme leads to convergence rates a factor of 2 faster than those obtained with the MALI scheme. This increase in the convergence rate resides in the fact that the convergence rate of this RT method is equivalent to that of an operator splitting method based on a triangular approximate $\mathbf{\Lambda}^*$ operator, which contains much more information about the radiative couplings between all the points in the atmosphere than the diagonal approximate $\mathbf{\Lambda}^*$ operator. *The main advantage of the proposed GS-based iterative scheme is that neither the construction nor the inversion of this triangular operator has to be*

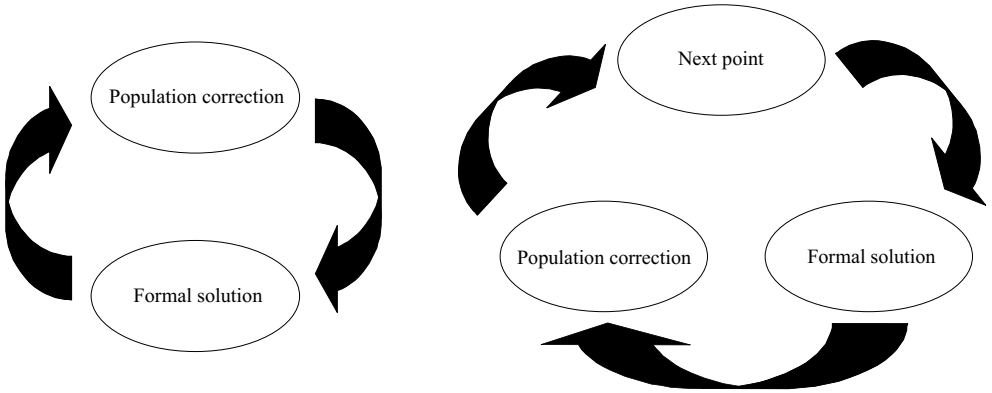

Figure 4.6: Schematic difference between the Jacobi and the Gauss-Seidel iterative schemes. The Jacobi or MALI scheme consists on calculating the radiation field for all the points and then the population correction is carried out. On the other hand, in the Gauss-Seidel or MUGA scheme, once the radiation field is known at the spatial point under consideration, the population correction is carried out and then we move to the next point in the atmosphere taking into account the previously corrected populations.

performed. The main disadvantage is that the two previous corrections have to applied to every point in the atmosphere in order to end up with a true GS scheme. These corrections might take an appreciable amount of computational time. Since they are produced by the use of the parabolic short-characteristics, it should be desirable to use a formal solver of the same precision of parabolic SC but which does not suffer from these problems. The first option would be to use linear SC but they do not present enough accuracy to obtain the correct result in typical non-LTE RT problems. The second option would be to use non-centered parabolic SC, but it is known to be unstable when used in iterative schemes. We are now investigating other options in which only information on the points M and O are used (and possible other previous points) like the parabolic or cubic Bezier splines (Auer 2003). The problem is again that non-centered operations have to be used which may lead to instabilities.

As pointed out by Trujillo Bueno & Fabiani Bendicho (1995) and Trujillo Bueno (2003c), the increase in convergence rate can be even increased to a factor of 4 if the previous correction scheme is applied, not only when the field is being propagated outwards, but also when the field is propagated inwards. The scheme is now slightly more complicated but can be perfectly obtained. The

resulting iterative scheme is similar to one in which both the upper triangular and lower triangular approximate $\mathbf{\Lambda}^*$ operators are involved, the first one when the incoming radiation field is being calculated and the second one when the outgoing radiation field is being calculated.

Parallelization

The case of the parallelization of the MUGA scheme turns out to be more difficult than for the MALI case since the formal solution and the correction scheme are coupled. The parallelization philosophy would be similar to that of MALI, i.e., to assign each processing unit to performing the formal solution of the RT equation along each characteristic. A barrier on the execution has to be put at each shell when calculating the outgoing radiation field in order to recover all the angular information for each shell. One of the processors recovers all this information and calculates the correction to the populations at each shell. Another communication has to be performed to carry out the needed corrections. At this point, the new populations are broadcasted to all the processing units and they advance the formal solution of the RT equation to the next shell, where the very same process is executed. Note that each processing unit has to solve the RT equation for all the frequencies of the lines included in the problem at the same time. The option of performing the formal solution frequency by frequency which was available in the MALI scheme cannot be applied here since we need the full spectral structure of the radiation field inside the iterative scheme. Schematic representations of the MALI and MUGA schemes can be found in Fig. 4.6.

4.3.4 The Multilevel SOR Method (MUSOR)

The Successive Overrelaxation method (SOR) has been also introduced for the solution of the non-LTE RT problem by Trujillo Bueno & Fabiani Bendicho (1995). It is highly inspired in the Gauss–Seidel scheme and in fact it can be considered as an improvement of their GS scheme. The solution process is exactly the same and the only difference lies on the level population correction. In the SOR method, a parameter ω is introduced to overcorrect the population, thus allowing for some kind of anticipation of the future corrections. This

scheme can be written as

$$\begin{aligned} \mathbf{A}_{\rm GS}^{\rm old\&new} \cdot \delta\mathbf{n}^* &= \mathbf{r} \\ \mathbf{n}^{\rm new} &= \mathbf{n}^{\rm old} + \omega\delta\mathbf{n}^*, \end{aligned} \tag{4.39}$$

where the ω parameter has a value between 1 and 2 to produce the overcorrection. We see that this scheme consists on applying the GS correction and multiplying the population correction by a constant in the range $[1, 2]$. Note that the GS scheme is a particular case of the SOR scheme. There exists an optimum value for this parameter which minimizes the number of iterations, although it cannot be known *a priori*. However, some methods are available to automatically estimate the optimum value of this parameter ω (see Hageman & Young 1981) and it has been shown by Trujillo Bueno & Fabiani Bendicho (1995) that they can be applied to the RT problem with great success. The optimum value can be obtained with the aid of the formula:

$$\omega_{opt} = \frac{2}{1 + \sqrt{1 - \frac{R_c(itr+1)}{R_c(itr)}}} \qquad itr \gg 1, \tag{4.40}$$

where $R_c(itr)$ is the *maximum relative change* at iteration itr, defined as

$$R_c(itr) = \max \left| \frac{\mathbf{n}(\mathrm{itr}) - \mathbf{n}(\mathrm{itr}-1)}{\mathbf{n}(\mathrm{itr})} \right|. \tag{4.41}$$

The reason for the previous formulas can be found on Trujillo Bueno & Fabiani Bendicho (1995) and references therein but it is related to the fact that $R_c(itr+1)/R_c(itr)$ becomes a very good estimation of the spectral radius ρ of the iteration when $itr \gg 1$. This is produced because, after the first possible oscillatory behavior of the maximum relative change, we enter a regime in which $R_c(itr) \propto \rho^{itr}$.

4.3.5 Computational time

A fundamental consideration of any iterative method is to know how the total computational time scales with the number of spatial grid points, rays, frequencies and radiative transitions in the atomic or molecular model. We have seen that the number of spatial grid points in which the specific intensity has to

be known is larger in the spherically symmetric case than in the plane-parallel case. Consider $N_{\rm atm}$ to be the number of points in the atmosphere where the specific intensity has to be calculated, which can be obtained using Eq. (4.21) or (4.22). Note that this includes the dependence on the number of rays for the angular quadratures. Let N_ν be the number of frequencies at which the RT equation has to be solved, $N_{\rm iter}$ be the number of iterations needed for reaching the desired precision and $T_{\rm cpu}$ be the computational time per iteration. With the short-characteristics method, the computational time scales linearly with the number of spatial grid points in the atmosphere, the number of frequency points and the number of iterations, so that:

$$T_{\rm cpu} \propto N_\nu N_{\rm atm} N_{\rm iter}. \tag{4.42}$$

The dependence of the total computational time on the number of points in the atmosphere scales as $N_{\rm atm}^2$ for MALI, as $N_{\rm atm}^2/2$ for MUGA and as $\sqrt{N_{\rm atm}}N_{\rm atm}/2$ for MUSOR (Trujillo Bueno & Fabiani Bendicho 1995). This is a direct consequence of the different number of iterations which have to be performed for obtaining convergence in each of the methods. It is of the order of $N_{\rm atm}$ for MALI, $N_{\rm atm}/2$ for MUGA and $\sqrt{N_{\rm atm}}$ for MUSOR, as will be shown later on.

4.4 LVG approximation

This approximation was first introduced by Sobolev (1958, 1960) for the treatment of the highly nonlinear RT problem and later refined by other authors (Castor 1970, Lucy 1971). It assumes that there is a *large velocity gradient* (LVG) in the atmosphere, which leads to the simplification of the whole problem. When a large velocity gradient is present, the Doppler shifts suffered by the spectral lines at each position due to the macroscopic motions are very high, thus points which are geometrically very close can be radiatively uncoupled. Therefore, a photon generated at a given point can only be absorbed in the vicinity of this point. If it manages to escape from this region, then it will escape until reaching the exterior boundary because the rest of points in the atmosphere have line absorptions profiles which are Doppler shifted. The immediate consequence of the previous assumption is that the non-locality of the RT problem is lost and we can avoid any radiative coupling between different

zones of the atmosphere. The problem then becomes completely local and the radiation field can be calculated easily. Although the non-local character of the problem has been avoided, its non-linear character still remains since the statistical equilibrium equations depend non-linearly on the populations themselves through the radiative rates.

This method is usually applied to problems where the approximation is not valid because it is relatively easy to code and much more faster than the full non-local code. To identify which kind of problems can be solved with this approximation one has to define the domain of validity of the approximation. The presence of a macroscopic velocity field produces a shift in the observed frequency of a transition between levels i and j due to the Doppler effect. For velocities much smaller than the speed of light, we can write the shifted frequency as:

$$\nu_{ij} = \nu_0 \left(1 - \frac{\vec{n} \cdot \vec{v}(r)}{c}\right), \tag{4.43}$$

where ν_0 is the rest frequency of the transition between levels i and j, $\vec{n}$ is a vector in the direction of the line of sight (LOS), $\vec{v}(r)$ is the velocity field in the source and c is the speed of light. $v_l = \vec{n} \cdot \vec{v}(r)$ is the projection of the velocity vector on the direction of the LOS. When we move along the LOS, we can obtain the variation of the shifted frequency by differentiating the previous expression with respect to a distance l which measures the distance along the LOS, obtaining:

$$\delta\nu_{ij} = \frac{\nu_0}{c} \left|\frac{dv_l}{dl}\right| \delta l, \tag{4.44}$$

being δl an elementary distance along the line of sight and dv_l/dl the velocity gradient. With the help of this expression, one can define a length unit L, called the *Sobolev length*:

$$L = \frac{c\delta\nu_{ij}}{\nu_0 \left|\frac{dv_l}{dl}\right|}, \tag{4.45}$$

which represents the typical distance between two points x and $x + L$ along the LOS needed for obtaining a considerable Doppler shift in the line profile so that the profiles at both points have a negligible overlap. For the case of a Doppler

profile, $\delta\nu_{ij} = \nu_0 v_{th}/c$, and the Sobolev length can be written as:

$$L = \frac{c\delta\nu_{ij}}{\nu_0 \left|\frac{dv_l}{dl}\right|} = \frac{v_{\rm th}}{\left|\frac{dv_l}{dl}\right|}. \tag{4.46}$$

Consider now R to be the typical distance in the medium where the physical conditions change. Therefore, we can estimate the velocity gradient as $|dv_l/dl| \approx v_0/R$, where v_0 is a typical velocity in the medium. The ratio between the Sobolev length and the typical scale of the medium then depends on the ratio between the thermal and the typical velocities in the medium, $L/R \approx v_{\rm th}/v_0$. Therefore, the Sobolev approximation turns out to be valid for $R \gg L$, since the typical velocities in the medium are larger than the thermal velocities. This way, the possible resonance regions around a point x are relatively sharp and radiative coupling is only possible in the surroundings of x. Another possibility in which the LVG approximation turns out to be valid is that in which we have an optically thin atmosphere. In this case, a photon generated in any zone can escape from the atmosphere with a very small probability of absorption and the problem then becomes completely local.

The complete derivation of the LVG equations is out of the scope of this thesis so that we will only write the final results (see Castor 1970, Lucy 1971 for more details). The LVG approximation leads to a very simple formula for obtaining the mean intensity at a given point which depends only on local quantities:

$$\bar{J}(r) = [1 - \beta(r)]\, S(r) + \beta_\star(r) I_\star + \beta_{\rm bg}(r) I_{\rm bg}(T_{\rm bg}). \tag{4.47}$$

In this expression, $S(r)$ is the source function at the radial distance r, $I_\star$ is the radiation coming from the star or, equivalently, the radiation at the inner boundary surface, while $I_{\rm bg}(T_{\rm bg})$ is the cosmic background radiation field (given by a blackbody at the background temperature $T_{\rm bg}$) or, equivalently, the radiation at the outer boundary surface. Note that the Sobolev or LVG approximation directly gives an expression for the mean intensity without the necessity of calculating the specific intensity itself. The angular quadrature is

transferred to the β functions, which are the escape probabilities, defined as:

$$\begin{aligned} \beta(r) &= \int_0^1 d\mu \frac{1-e^{-\tau(r,\mu)}}{\tau(r,\mu)} \\ \beta_\star(r) &= \int_{\mu_c}^1 d\mu \frac{1-e^{-\tau(r,\mu)}}{\tau(r,\mu)} \\ \beta_{\rm bg}(r) &= \beta(r). \end{aligned} \tag{4.48}$$

The escape probability $\beta(r)$ gives the probability that a photon, generated at the radial distance r, escapes from its neighborhood without suffering any absorption or scattering. The probability $\beta_\star(r)$ is the probability that a photon, generated at r, escapes from its neighborhood and strikes the core. Finally, the probability $\beta_{\rm bg}(r)$ is the probability that a photon, generated at r, escapes from its neighborhood and strike the outer boundary surface. Since the definition is equivalent to $\beta(r)$, they have the same functional form.

The optical depth $\tau(r,\mu)$ is defined in the Sobolev theory (see Castor 1970) as:

$$\tau(r,\mu) = \frac{\chi_l(r) c}{\nu_{ij}} \frac{1}{\frac{v(r)}{r}\left[1+\mu^2\left(\frac{d\ln v(r)}{d\ln r}-1\right)\right]}, \tag{4.49}$$

where $\chi_l(r)$ is the line opacity while $d\ln v(r)/d\ln r$ is the logarithmic derivative of the velocity field, which can be written in terms of the velocity field itself and its gradient as $d\ln v(r)/d\ln r = r/v(r)\cdot dv(r)/dr$. Once the atmosphere is correctly sampled with N_r shells in the radial direction, the $\beta(r)$ function can be numerically calculated. We have calculated this function with a 24 points gaussian quadrature, which provides a very high accuracy. For the calculation of the escape probability $\beta_\star(r)$, one should note that $\mu_c = \left(1-R_\star^2/r^2\right)^{1/2}$ is the angle subtended by the star from a point arbitrarily far from the star. Therefore, the integral can be calculated explicitly using another gaussian quadrature for the new interval or one can assume, for simplicity, that $\beta_\star(r) \approx \omega\beta(r)$, where $\omega \approx (1-\mu_c)/2$ is a dilution factor. This assumption simplifies the calculation to obtaining only one integral, leading to a faster algorithm.

4.5 Illustrative examples

This section is aimed at testing the correct behavior of the code we have developed and at demonstrating the convergence properties of the novel iterative

schemes on which it is based on. Later on, we will show some applications to more complicated problems in which complex molecular models are used. Three indicators have been chosen to describe the behavior of the convergence properties. The first one is the *maximum relative change*, which is defined by Eq. (4.41). This quantity typically shows a monotonically decreasing behavior which stabilizes when the computer precision has been reached. This is only an indicator that the process is convergent, that is, the corrections $\delta\mathbf{n}$ become smaller when the iteration number increases.

However,this is not an indicator of the final precision which can be reached with the selected grid. To account for this, we have employed the *true error*, which is defined as:

$$T_e(itr) = \max \left| \frac{\mathbf{n}(\mathrm{itr}) - \mathbf{n}}{\mathbf{n}} \right|, \tag{4.50}$$

where $\mathbf{n}$ is the exact solution of the problem. As pointed out by Auer, Fabiani Bendicho, & Trujillo Bueno (1994), although there is no analytic solution (this is the situation in the majority of the RT problems), for the purpose of evaluating $T_e(itr)$ this exact solution can be taken as the one obtained in a very fine grid after iterating to convergence. Of course, the previous definition of the true error makes it impossible to calculate it while the iterative process is being carried out. One would need to perform a previous run of the same problem with a grid finer than the one chosen for solving the RT problem. However, the behavior of T_e is much more interesting than R_c since it becomes constant once the maximum precision the used grid can give is reached. It can be used then as a very efficient stopping criterion. One can continue the iterative process until a very small maximum relative change is obtained but the maximum precision of the grid may have been reached many iterations before. Therefore, as shown by Auer, Fabiani Bendicho, & Trujillo Bueno (1994) it is of no use to continue the iterative process above the point in which T_e becomes constant. We will see some examples of that later on.

The last indicator we will use is the *convergence error*, which is defined as:

$$C_e(itr) = \max \left| \frac{\mathbf{n}(\mathrm{itr}) - \mathbf{n}(\infty)}{\mathbf{n}(\infty)} \right|, \tag{4.51}$$

where $\mathbf{n}(\infty)$ is the solution obtained in the same grid chosen for solving the problem but when $itr \to \infty$. Note that this solution is not the "exact" solution, but the solution at a given resolution level given by the grid being used.

Although the final solution at the grid under consideration is not known a priori, it is possible to obtain an estimation of the value of the convergence error (see Auer, Fabiani Bendicho, & Trujillo Bueno 1994) by using the formula:

$$C_e(itr) \approx R_c(itr)\frac{\rho}{1-\rho}, \tag{4.52}$$

where $\rho = R_c(itr+1)/R_c(itr)$ is an estimation of the spectral radius of the problem, i.e. the maximum eigenvalue of the iteration matrix. Note that, even if $R_c(itr)$ is very small, if $\rho \approx 1$, we will have a large convergence error. As an example, assume a slowly convergent iterative scheme which leads to a spectral radius of $\rho \approx 0.98$ and assume that the maximum relative change is 0.1 %. The convergence error would be ~ 5 %, a factor of $\sim$50 higher. Since both R_c and ρ can be obtained during the iterative process, we will use Eq. 4.52 as a reliable stopping criterion.

We now turn to present some simplified model problems which are of interest to illustrate the convergence properties of the developed methods. They will be presented following an increasing order of complexity.

4.5.1 Quasi plane-parallel case

In order to show the convergence properties of these methods in spherical symmetry, we have selected the simple problem treated by Avrett & Loeser (1987), which concerns a simplified three-level hydrogen atom without continuum in an isothermal semi-infinite medium with T=5000 K. The atmosphere is $\sim$1500 km thick and the radius of the internal core is 6.95×10^{10} cm. This may be considered as an isothermal representation of the solar atmosphere in spherical geometry. The collisional rates among the three levels of the model atom are considered as constant. All the relevant information is shown in Table 4.1.

Transition	A_{ul} [s^{-1}]	ΔE [cm^{-1}]	C_{ul} [cm^3 s^{-1}]
2–1	4.68×10^8	82333.3	10^5
3–1	5.54×10^7	97666.7	10^5
3–2	4.39×10^7	15333.3	10^5

Table 4.1: Transitions in the 3-level hydrogen model atom.

We define the curvature q of a given atmosphere as the ratio between its

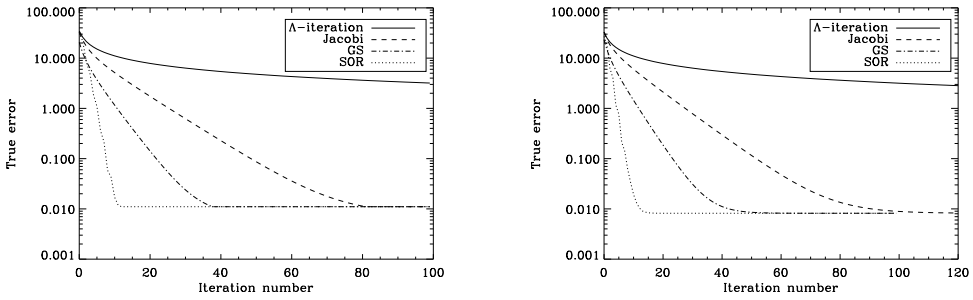

Figure 4.7: Convergence properties of the iterative methods showing the evolution of the true error versus the iteration number. The left panel shows the results for the quasi plane–parallel case using the spherical geometry code while the right panel shows the same result but using the plane–parallel code.

extension ΔR and the radius of the star R:

$$q = \frac{\Delta R}{R}, \tag{4.53}$$

so that the RT problem must be solved using the spherically symmetric geometry when $q \gtrsim 1$ and may be solved using the plane–parallel geometry when $q \ll 1$. The case under study here has $\Delta R = 1500$ km and R=6.95×10^{10} cm, so that $q \approx 0.002$ and may be solved using the plane–parallel approximation without any problem unless one is interested in the emerging profiles which are obtained in extreme-limb or even off-limb observations. However, we have solved the problem using both geometric approximations in order to investigate the reliability of our non-LTE RT code in spherical geometry.

The non-LTE problem has been solved with the four available methods: Λ-iteration, MALI (based on the Jacobi iterative scheme), MUGA (based on the Gauss-Seidel iterative scheme) and MUSOR (based on the SOR iterative scheme). The MALI and MUGA options of our RT computer program have been used with and without acceleration techniques. In the left panel of Fig. 4.7 we show the convergence behavior of all of them for the spherical case. The exact solution has been obtained by iterating until full convergence in a grid with 150 radial shells with a grid step of Δr =10 km, sampling the ∼1500 km thick atmosphere. The problem is then solved using a coarser grid which only has 80 radial shells (thus Δr = 19 km). Note that the true error which

can be reached in this grid is approximately 1 %. The Λ-iteration method, although converging, is not capable of finding the solution in a suitable number of iterations. Since this is a problem with optical depth $\tau > 1000$, we would need around 1000 iterations to radiatively connect all the points in the atmosphere using the Λ-iteration method. When the other methods have achieved the maximum precision that the chosen grid can give, the true error of the Λ-iteration iterative method is still well above 100 %.

On the other hand, the method based on the Jacobi iterative scheme reaches total convergence in a suitable number of iterations. It is interesting to see the behavior of the generalization of the GS and SOR based methods (MUGA and MUSOR) to spherical geometry. The method based on the GS iterative scheme reaches the total convergence in half the number of iterations required by the MUGA scheme, which leads to approximately half the total computational time, since the computational time per iteration is approximately the same in both methods. Finally, the convergence rate for the SOR method is much better than for the GS method, which is a direct consequence of the anticipation of future corrections feature. As can be seen from Eq. (4.39), the time per iteration is virtually the same for SOR and for GS, so that the reduction in the number of iterations implies a similar reduction factor in the total computational time. This improvement can make it possible to obtain the solution with more complicated model atoms or molecules than what it was possible up to now.

Let $T_{\rm Jac}$ and $T_{\rm GS}$ be the time per iteration for the Jacobi and GS schemes, respectively. Therefore, $\mathcal{W} = T_{\rm GS}/T_{\rm Jac} \gtrsim 1$ takes into account the increase in the computational time per iteration between both methods. The GS method appears to converge in $\mathcal{W}N/2$ iterations (where N is the number of iterations needed by the Jacobi method to reach convergence in the grid) and the SOR method in $\sqrt{\mathcal{W}N}$. Usually, $\mathcal{W}$ is of the order of 1.3-1.5 and depends on how complex the model atom or molecule is. Since it should be ideal to have $\mathcal{W} = 1$, we are working on investigating the application of different formal solvers which do not suffer from the problem the parabolic short-characteristics have.

The convergence behavior when the problem is solved using the plane-parallel approximation is plotted in the right panel of Fig. 4.7. It is interesting to note that, due to the low curvature radius of the atmosphere, both results are very similar, with a reduction in the total computational time for the GS and SOR methods which are comparable. However, the total computational

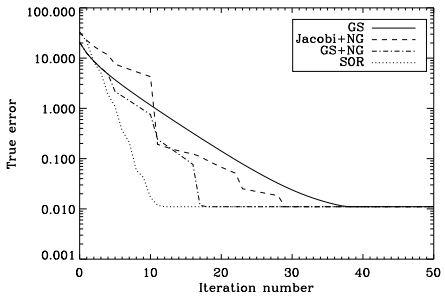

Figure 4.8: Convergence properties of the various iterative methods showing the effect of including Ng acceleration. Note that, even when the MALI and MUGA schemes are applied with acceleration techniques, the MUSOR scheme converges faster.

time results much higher for the spherically symmetric case due to the large number of formal solutions performed along the characteristics.

In order to highly improve the convergence behavior of these methods, powerful acceleration techniques may be applied (see Auer 1987, 1991). One of the most widely applied acceleration techniques is the one developed by Ng (1974), which has been included here in the Jacobi-based and the GS-based methods. The convergence properties are shown in Fig. 4.8 in comparison with the SOR method.

One of the main problems of these techniques is that the acceleration in the convergence process, that is, the reduction on the number of iterations highly depend on the step the acceleration is turned on and on the number of iterations between successive acceleration steps. We have verified that the acceleration cannot be turned on very soon to obtain a remarkable reduction. On the other hand, the starting of the acceleration cannot be delayed much, since the iterative methods may have obtained the desired level of convergence. One of the main drawbacks is that every acceleration technique requires an additional memory storage and and extra computing time per iteration, which does not apply to the SOR method. However, some tests with more complicated atomic/molecular models show that the SOR method with the optimal ω–parameter may sometimes lead to instabilities in the convergence process. The SOR overcorrections may be too big so that the method may become unstable. This behavior is specially critical when population inversions are found.

Transition	A_{ul} [s^{-1}]	ΔE [cm^{-1}]	C_{ul} [$cm^3\ s^{-1}$]
5–1	1.40×10^8	25433.3	5.1×10^4
4–1	1.40×10^8	25200.0	5.1×10^4
5–3	7.20×10^6	11700.0	1.4×10^5
5–2	8.10×10^5	11766.7	1.6×10^4
4–2	7.80×10^6	11533.3	1.6×10^5
3–1	–	13733.3	8.2×10^3
2–1	–	13666.7	8.2×10^3
5–4	–	233.3	4.8×10^6
3–2	–	66.7	1.0×10^7
4–3	–	11466.7	1.0×10^3

Table 4.2: Transitions in the 5-level Ca II model atom. Lines with no value of A_{ul} are pure collisional transitions.

In this case, it is a better option to use an iterative method which produces a smooth convergence (e.g., MALI or MUGA) so that the population corrections turn out to be small, even being necessary to use the Λ-iteration in the most delicate problems (e.g., maser transitions).

By examining Fig. 4.8, one can see that the SOR method is always better than the rest of the methods, even when acceleration schemes are used. On the other hand, one must note that the convergence behavior for the SOR calculation shown in this figure has been obtained using the optimum value of the SOR parameter ($\omega_{\rm opt}$). However, this is not the case in practical situations so that the number of iterations for the SOR method is somewhat larger. The value of this parameter can be obtained by using Eq. (4.40) during the iterative process, which always requires to "loose" a few iterations.

4.5.2 Spherical case

The previous problem served as a first test for the spherical geometry generalization of the methods developed by Trujillo Bueno & Fabiani Bendicho (1995). Let us consider now a problem which is very similar to the previous one, but having a more extended atmosphere. The core radius is still 6.95×10^{10} cm, but the total thickness of the atmosphere is now increased to 6.3×10^6 km, which implies a curvature of $q\sim9$. With this q–value, sphericity effects have a great

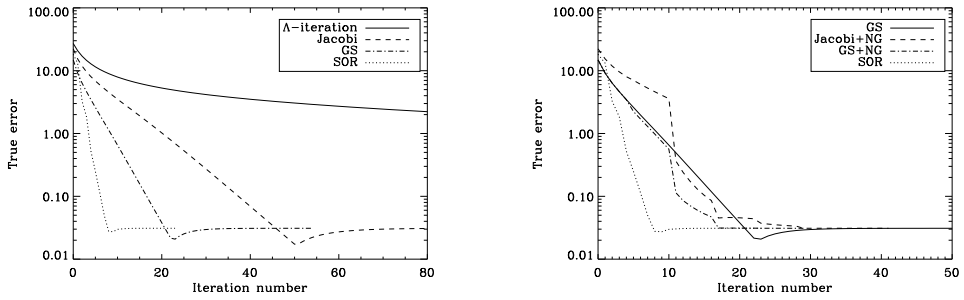

Figure 4.9: Convergence properties of the various iterative methods showing the true error versus the iteration number. The left panel shows the results for the pure iterative methods, while the right panel shows what happens when applying acceleration techniques to the methods based on Jacobi and GS.

influence in the final result because there are now directions in the atmosphere where the photons can escape more easily. The temperature of the atmosphere is still T=5000 K. We have chosen a slightly more complicated model representing a simplified 5–level Ca II model atom with constant collisional rates. The relevant information about this model atom can be found in Table 4.2. The optical thickness of the atmosphere is well beyond 10^6 in every transition, so the problem converges extremely slow when using the Λ-iteration method.

In order to use the true error as indicative of the convergence properties, the fully converged solution has been obtained in an atmosphere sampled at 300 radial shells. The atmosphere is now ~ 4000 times more extended. Therefore, in order to obtain a reasonable precision, the number of radial shells have to be greater than in the quasi plane–parallel case of the previous section. In the left panel of Fig. 4.9 we show the true error for the four iterative schemes studied in this thesis. The calculations have been performed using a grid of only 150 radial shells. The convergence behavior is very similar to the previous case, but the true error is 3 % due to the larger distance between grid points. As expected, the Λ-iteration method does not reach convergence in a suitable number of iterations, although it is a converging scheme. When the rest of methods have reached the 3 % precision of the grid, the true error is still higher than 100 %. On the other hand, the convergence properties of the rest of methods closely resembles that of the previous calculation. Following a procedure similar than

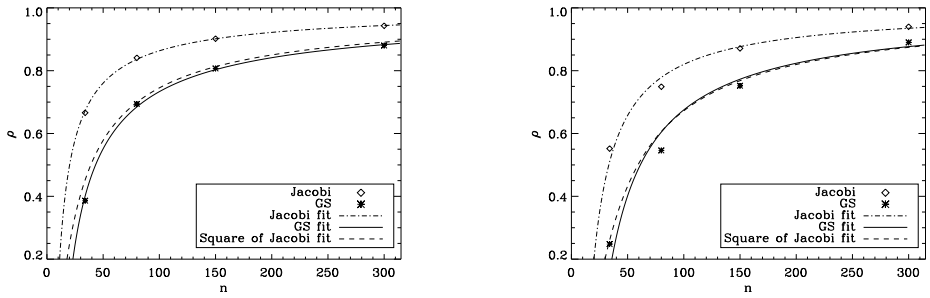

Figure 4.10: Spectral radius of the different iterative schemes versus the number of points in the atmosphere for the quasi plane–parallel case in the left panel and for the spherical case in the right panel. Both calculations have been carried out using our spherical formal solvers.

for the previous test, the GS methods reaches convergence in $\mathcal{W}N/2$ iterations and the SOR method in $\sqrt{\mathcal{W}N}$. Therefore, the good convergence properties of the SOR method studied in Trujillo Bueno & Fabiani Bendicho (1995) for cartesian coordinates appear to be similar when going to spherical symmetry. Therefore, these iterative schemes are very efficient methods to solve non-LTE RT problems in spherical symmetry. We have applied the Ng's acceleration technique. The results are shown in the right panel of Fig. 4.9. Note that the SOR method with the optimum ω–parameter is still the best in comparison with the accelerated versions of the rest of methods. Note also that the accelerated version of the GS method gives a substantial improvement in the total computational time with respect to the Jacobi–based methods.

In order to investigate the dependence of the convergence properties of these iterative methods on the number of points in a spatial grid of *fixed* dimensions, we show in Fig. 4.10 the value of the spectral radius ρ of the iterative scheme versus the number of grid points. We show $R_c(itr+1)/R_c(itr)$ for itr$\gg$1, for both the Jacobi and the Gauss–Seidel based iterative schemes. Following Trujillo Bueno & Fabiani Bendicho (1995), we have fitted a functional form to the variation of the spectral radius with the number of points in the grid:

$$\rho = 1 - \frac{a}{n^b}, \tag{4.54}$$

where ρ is the spectral radius of the iteration, n is the number of spatial grid points and a and b are two free parameters. In Trujillo Bueno & Fabiani

Bendicho (1995), n is the number of grid points per decade in optical depth while we are using directly the number of grid points. This is because our grid is built with the points equidistant in geometrical distance. Trujillo Bueno & Fabiani Bendicho (1995) have shown that this formula gives a very good representation of how the spectral radius varies with the fineness of the grid. Similarly, we have verified that the same applies to our case as can be seen in Fig. 4.10, although n is not defined in the same manner. This simple formula for the spectral radius relation can be used to estimate the number of iterations one would require to solve the RT problem for any other grid.

For completeness, we have also shown the curve which results from squaring the fit of the Jacobi–based method. Note that it fits very well the curve of the Gauss–Seidel method, showing that the maximum eigenvalue of the iteration operator for the GS method is approximately the square of that of Jacobi's method. This is the reason why the GS method is around two times faster than Jacobi's method.

These figures clearly show one of the main drawbacks of all these operator splitting methods. They suffer from a deterioration of the convergence properties when the spatial resolution of the grid is refined. In the limit of an infinitely fine grid, all these methods will converge infinitely slow, as can be seen from Fig. 4.10. The limit value of the spectral radius for $n \to \infty$ is $\rho \to 1$. This intrinsic "deficiency" can be circumvented by using more powerful techniques like the *multigrid* method. Steiner (1991) first applied this technique to linear radiative transfer problems, while Fabiani Bendicho, Trujillo Bueno, & Auer (1997) developed the generalization of the multigrid method to the full non-linear radiative transfer multilevel problem. This method does not suffer from this deterioration and rapidly converges irrespective of the grid resolution. Furthermore, their convergence rate is much faster than the previous methods and is of the order $O(n)$. The following table summarizes the dependence of the computational work W on the number of grid points for the previous methods:

- Jacobi-based methods $\rightarrow W \sim n^2$
- GS-based methods $\rightarrow W \sim n^2/2$
- GS-up-down-based methods $\rightarrow W \sim n^2/4$
- SOR method $\rightarrow W \sim n\sqrt{n}$

- Multigrid $\rightarrow W \sim n$

4.5.3 Population inversion

We have shown the convergence properties of the iterative methods when dealing with simple atomic/molecular models which present relatively large energy differences between the levels. It is instructive to consider now the case of a molecular model in which the energy levels are so close in energy that they all have comparable populations and the phenomenon of population inversion can occur. The previous examples have shown the ability of the selected iterative methods for drastically reducing the number of iterations necessary to solve RT problems. The following example shows the ability of these fast iterative methods for dealing with typical molecular models which present difficulties in the convergence due to the appearance of population inversions. Consider a transition between an upper level u and a lower level l. There is a population inversion in this transition when:

$$n_l B_{lu} - n_u B_{ul} < 0, \tag{4.55}$$

where n_u and n_l are the populations of the levels and B_{lu} and B_{ul} are the absorption and stimulated emission Einstein coefficients. Under these circumstances, the line opacity becomes negative as can be seen from Eq. (4.9) because the stimulated emission term becomes more important than the pure absorption term. Using the relation between the Einstein coefficients, the previous condition can be rewritten as

$$\frac{n_u}{n_l} > \frac{g_u}{g_l}, \tag{4.56}$$

where g_u and g_l are the statistical weights of the upper and lower levels, respectively. Therefore, if the ratio between the upper level population and the lower level population is higher than the ratio of their statistical weights, the line opacity becomes negative. The previous condition cannot hold in LTE, so it can only be obtained under non-LTE conditions. When the total opacity becomes negative, that is, when the line opacity becomes negative and larger in absolute value than the background opacity, the optical depth $\Delta\tau$ of the transition becomes negative. Since the specific intensity attenuates as $e^{-\Delta\tau}$, the population inversion produces an exponential increase of the specific intensity, thus producing a *maser*. This is the very same process produced in a standard

laser. The population inversion is produced by the thermodynamical conditions and the radiation field present in the plasma. An energy conservation reasoning leads to the conclusion that the radiation in the zone where a maser appears must be beamed thus reducing the solid angle. From a phenomenological point of view, the radiation is beamed in the direction where the macroscopic velocity field in the atmosphere maintains the necessary resonance to produce the maser. There is a wide bibliography for the study of astronomical masers but Elitzur (1992, 2002) represents a useful starting point.

From the numerical point of view, the appearance of population inversions produce instabilities in the radiative transfer codes, which are mainly due to the exponential increase of the specific intensity due to the negative opacities. These numerical problems must be avoided in order to obtain the correct answer to the problem. The straightforward way to solve the previous issue is to generate additional grid points in the regions where the population inversions appear, so that the radiation transfer correctly obtains the intensity behavior. Our code does not include these grid refinement techniques. Note that when the optical distance between two grid points is $\Delta\tau = -10$, the intensity increases in a factor 2.2×10^4. For the moment our code is limited to the case of very weak masers.

As an example, we have considered the solution of the water radiative transfer problem in a hot molecular cloud. H_2O is a planar molecule with an axis of symmetry. Since its three moments of inertia are different, it is an asymmetric top with a rather complex level structure. We will only consider the fundamental vibrational level inside the fundamental electronic state. The rotational levels are labeled $J_{K_+K_-}$, where J is the total angular momentum and K_- and K_+ are its projection on two molecular axes. The selection rules are that $\Delta J = 0, \pm1$ and that K_- and K_+ must change their evenness, that is, the allowed transitions are *odd* $\leftrightarrow$*even*. The result of these selection rules is two distinct species that are radiatively uncoupled: ortho-H_2O with nuclear spin 1 and (K_-,K_+)=(odd, even) or (even, odd) and para-H_2O with nuclear spin 0 and (K_-,K_+)=(odd, odd) or (even, even). It is usual to give the value of $\tau = K_- - K_+$ instead of the individual K_- and K_+. The energy level structure of ortho-H_2O and para-H_2O obtained from Chandra et al. (1984) is shown in Fig. 4.11. Note that the lowest energy level of ortho-H_2O has no zero energy, but is situated 23.7943 cm^{-1} above the fundamental level of para-H_2O.

We show here the convergence details of one of the astrophysical problems

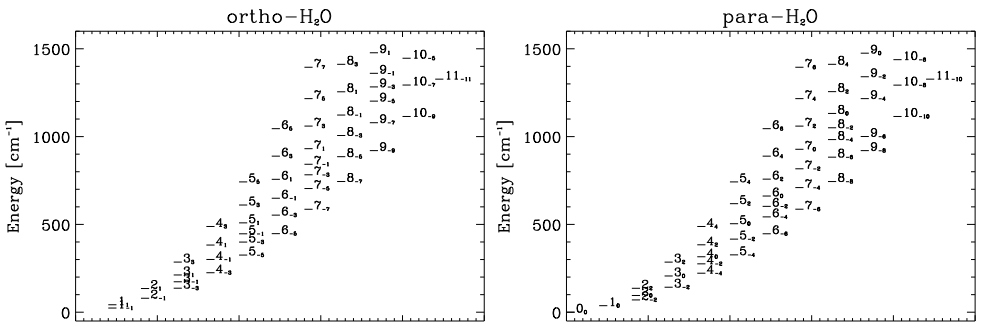

Figure 4.11: Rotational levels of ortho-H_2O and para-H_2O with energies below 1500 cm^{-1}.

discussed in Section §4.7. This problem consists on obtaining the excitation state of water in a geometrically thin but optically thick hot shell surrounding a molecular cloud. The inner surface of the shell is situated at 1.472×10^{18} cm from the symmetry center, while the outer surface is situated at 1.837×10^{18} cm. Therefore, the total angular diameter of the shell, assuming a distance of 8500 pc, is 28.9". The temperature is fixed at 500 K (although we will present results for a range of temperatures), the ortho-H_2O column density is chosen to be 1.8×10^{17} cm^{-2} while the hydrogen density is 6.4×10^{5} cm^{-3}. The microturbulent velocity in the shell is 8 km/s. The inner boundary condition has been chosen to be a grey body. A grey body is defined as a blackbody affected by a simple wavelength dependent absorption. In our case, we have used the following simple relation:

$$I_{\rm GB}(\lambda) = B_\lambda(T_c)\,(1 - e^{\tau_{\rm GB}}) \qquad\qquad \tau_{\rm GB} = \tau_{\rm ref}\left(\frac{\lambda_{\rm ref}}{\lambda}\right)^{\beta}, \qquad (4.57)$$

where $\lambda_{\rm ref}$ and $\tau_{\rm ref}$ are the reference wavelength and optical depth, respectively, and β is the spectral index of the law. In our case, we have chosen $\beta = 1$ and $\tau_{\rm ref} = 2.5$ for $\lambda_{\rm ref}$ =80 μm. T_c is the central temperature with a value of $T_c = 30$ K. The reference opacity is chosen so that the molecular hydrogen column density is $N(H_2)$ $\sim4\times10^{23}$ cm^{-2}. Note that the visual extinction in magnitudes

A_v can be expressed with the following expressions (see, e.g., Emerson 1996):

$$\begin{aligned} A_v &= 2.5 \log(e^{-\tau_{\rm vis}}) \\ A_v &= 10^{21} N({\rm H_2}), \end{aligned} \tag{4.58}$$

where $\tau_{\rm vis}$ is the opacity of the grey body at $\lambda \sim$5000 Å. From the previous two expressions, we can obtain an estimation of the reference opacity.

The molecular model includes the first 14 rotational levels of ortho- and para-H_2O, which must be solved independently. The ortho-H_2O abundance is typically three times higher than that of para-H_2O. The included levels are enough to investigate the excitation properties of water for temperatures as low as 500 K. The energy levels and Einstein coefficients have been obtained from Chandra et al. (1984), while the collisional rates stem from Green et al. (1993). The collisional rates have been obtained for collisions between H_2O and He. We have corrected them to account for collisions between H_2O and H_2, the correction factor being $\sqrt{\mu_{\rm H_2}/\mu_{\rm He}}$, where $\mu_{\rm H_2}$ and $\mu_{\rm He}$ are the reduced weight of the H_2O-H_2 and H_2O-He systems, respectively.

The reference solution to this problem has been obtained by solving it until convergence is reached in a grid with 300 points. It is then solved in two coarser grids with only 150 and 40 points in the radial direction. It is expected then that the accuracy of the solution obtained in these grids is degraded. The results are shown in Fig. 4.12. We have only shown the convergence properties of the MALI and MUGA schemes. We find that the MUSOR scheme does not converge in this case. This lack of convergence seems to be produced by the delicate behavior of the maser transitions. When the overrelaxation coefficient is applied, we produce oscillations in the populations which do not converge or converge very slowly to the correct solution.

The precision obtained with the grid containing 150 shells ($\sim$20%) is better than that obtained with the grid with only 40 shells ($\sim$45%). However, both grids are insufficient to obtain the solution with a true error below 20%. This is quite astonishing since this is the typical number of shells used to solve such kind of problems. However, we have to note that the true error gives the maximum difference between the converged solution and the "exact" solution. It may happen that the levels which we are interested in or the regions where the lines are formed may present a smaller difference with respect to this exact solution. In this situation, converging the problem in such a grid may still be

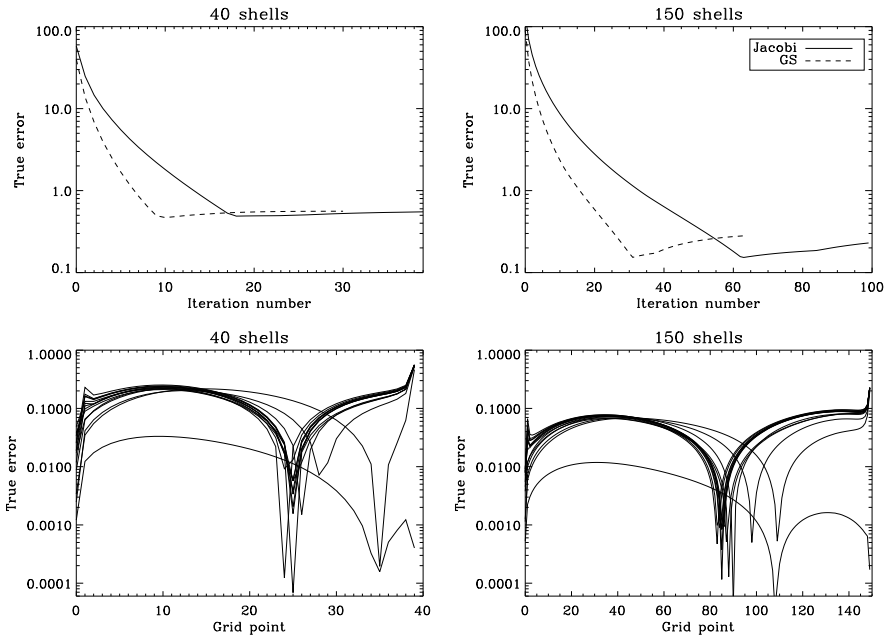

Figure 4.12: Convergence properties of the iterative methods when solving the water problem with two different radial grids. The upper panel shows the true error taking into account all the points in the atmosphere. The lower panel shows the relative difference between the converged populations and the populations obtained on the atmosphere discretized with 300 grid points versus the grid point. The inner and outer boundary conditions are at the extremes of each plot. The accuracy obtained with 150 shells is better than that obtained with only 40 although both are quite inaccurate. The time to reach the final precision is half for the scheme based on Gauss-Seidel than for that based on Jacobi.

of utility. In fact, this is what happens if we plot the relative error between the converged solution in each grid and the exact solution. We find that, when the grid of 40 shells is used, all the levels are below 20% for all the points except for the more external ones, while if we use the grid of 150 shells, all the levels are below 10% except for the more external ones. Since the spectral lines are typically formed in the inner regions of the atmosphere and not close to the outer surface, we can remove these points from the calculation of the true error since they do not significantly influence the final emergent spectrum. In view of the previous results, we can state that the results which will be shown in

Section §4.7 have an error of ∼20% since the grid with 40 points will be used.

Finally, we have to take into account that the effect of reducing the number of shells is not exactly equivalent in the spherically symmetric case and in the plane–parallel case. This reduction in the number of spatial grid points affects the number of angles available for performing the mean intensity quadrature in the spherically symmetric case. Therefore, it is expected that the degradation of the final true error is more severe in the spherical case than in the plane–parallel case when the number of points in the atmosphere is reduced.

4.6 Comparison with LVG

The LVG approximation is frequently used to obtain the excitation state of molecular energy levels in many situations of astrophysical interest since it is relatively fast. However, it is important to keep in mind the conditions under which the LVG approximation is expected to be valid. In this section we show some comparisons by solving different problems using both the LVG approximation and the full non-local problem.

4.6.1 Bad approximation

The first example is the cloud model used by Bernes (1979) to illustrate the performance of his radiative transfer code based on the Monte Carlo technique. It consists on a spherical cloud of external radius 3×10^{18} cm ($\sim$ 1 pc) and internal radius 5×10^{17} cm, with a constant temperature profile of 20 K, a constant molecular hydrogen density of 2×10^{3} cm^{-3} and a microturbulent velocity of 1 km s^{-1}. The cloud is collapsing following a linear velocity law, being v =-1 km s^{-1} at the outer surface. The problem is to find the excitation state of the first six rotational energy levels of CO. The CO abundance is taken to be constant and equal to [CO]= n(CO)/n(H$_2$) =5×10^{-5}. The low energy of these rotational levels (the highest level of the six is only at 83 K) makes it necessary to account for the influence of the CMBR radiation illuminating the outer surface of the cloud, since it has a significant impact on the excitation state in the cloud. The CMBR radiation is modeled via a blackbody radiation at 2.7 K. Although more recent collisional excitation rates for CO are available, we have decided to use the same rates used by Bernes (see Green & Thaddeus 1976) in order to be able to obtain comparable results. By substituting a linear veloc-

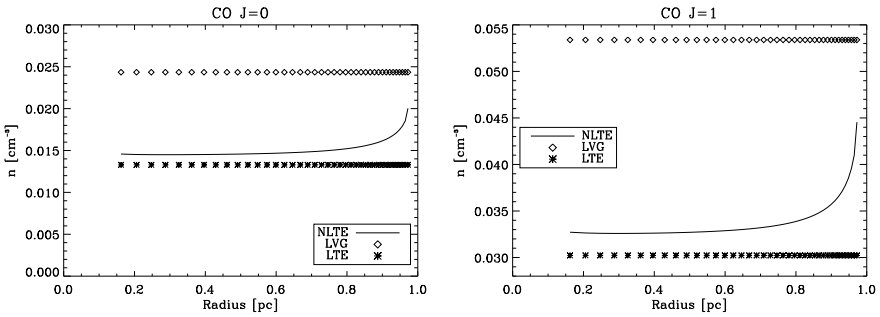

Figure 4.13: Population of the J=0 and J=1 rotational levels of CO in the cool cloud model of Bernes (1979). Note that the results given by the LTE and LVG approximations are not in agreement with the results we have obtained with the full non-LTE code.

ity field law into the Eqs. (4.48) and (4.49), one can verify that $\tau(r, \mu)$ does not depend on the angle μ, so that the escape probability can be immediately integrated. Moreover, if the physical conditions (temperature and molecular abundance) are constant throughout the medium, the escape probability does not depend on the radius. For this reason, the mean intensity given by the LVG approximation is independent of the radius for a cloud which has no illumination in the inner surface by the presence of, for example, a star being formed. Of course, this radially constant mean intensity is not physically correct since the presence of an outer surface permits the photons to escape from the cloud and the radiation field in the outer parts of the cloud tend to be weaker. Therefore, this is a situation in which radiative trapping effects are important and the full non-local radiative transfer problem has to be solved.

This effect is not correctly accounted for by the LVG approximation. This can be explained using the following reasoning. The velocity gradient in the cloud is approximately $4{\times}10^{-19}$ km s^{-1} cm^{-1}. Considering a thermal velocity of the order of the microturbulent velocity, Eq. (4.46) gives $L \approx 2.5{\times}10^{18}$ cm. Therefore, the Sobolev length is of the order of the radius of the cloud and the condition of validity of the LVG approximation $L \ll R$ is not fulfilled. In Fig. 4.13 we show the level population for the rotational levels J=0 and J=1 calculated with the LTE and LVG approximation and the exact solution obtained with the Gauss–Seidel option of our non-LTE code. The level populations are constant throughout the cloud in both the LTE and LVG approximations. The

reason for that in the LTE approximation is that the temperature is constant all over the cloud. In the LVG case, the constancy is produced by the constant temperature and the presence of a linear velocity field. On the other hand, the full non-LTE RT solution gives level populations which change with the radial distance. The populations in the inner regions of the cloud are similar to those obtained under the LTE approximation because in such regions the levels tend to become thermalized.

4.6.2 Good approximation

The following problem has been obtained from a set of test cases which became available after the workshop *Radiative Transfer in Molecular Lines* held at the Lorentz Center of Leiden University[1]. We have chosen one of these RT problems to show a situation in which the LVG approximation leads to acceptable results.

The model considers a collapsing cloud similar to that described by Shu (1977) in which the excitation state of the first 21 rotational levels of HCO^+ have to be obtained. The radiative transitions among these levels follow the selection rule $\Delta J{=}\pm 1$. The molecular abundance is very low ($n(HCO^+)/n(H_2) = 10^{-9}$), so the lines are only slightly optically thick ($\tau < 20$). The CMB radiation has to be included in order to account for all the excitation mechanisms in the cloud since the lowest rotational levels of HCO^+ have energies comparable to the temperature of the CMB. In Fig. 4.14 we show the level population throughout the atmosphere for three different rotational levels of HCO^+. We show also the results obtained using the LTE and the LVG approximations. The LTE approximation does not describe correctly the behavior of the populations. This is because radiative excitation is a very important source of pumping in the molecular model. Radiative pumping transfer population from the low energy levels to the high energy levels. This approximation gets worse when going to higher levels because the effect of the radiative pumping is larger for the higher levels of the model.

On the other hand, the LVG approximation leads to results which are in good accordance with the correct solution obtained using the methods based on the Gauss-Seidel iterative scheme. Furthermore, the LVG solution becomes closer to the exact solution for high J levels. This can be explained if the

[1] `http://www.strw.leidenuniv.nl/~radtrans`

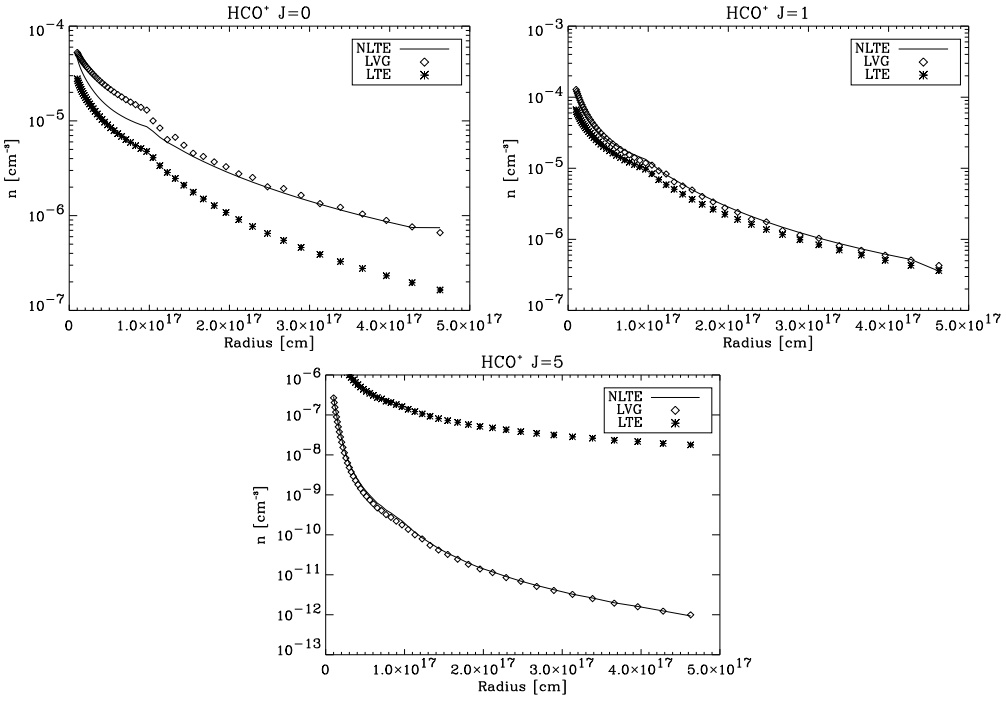

Figure 4.14: Population of the J=0 and J=1 and J=5 rotational levels of HCO^+ in the cloud model of Shu (1977). Except for the level J=0, the result given by the LVG approximation is in good agreement with that obtained using the full non-LTE code.

radiative trapping of the photons which pump these high J is less important than for the low J levels. In fact, the transitions among high J levels are optically thin and only the transitions between the lowest four rotational levels have opacities $\tau > 1$. A photon emitted in any of these optically-thin transitions will almost surely escape from the cloud without being absorbed. Therefore, the requisites for the LVG approximation to be valid are fulfilled and it gives a solution very close to the exact one.

In view of the previous results, it is important to note that the LVG approximation can be used as a technique for initializing the full non-LTE solution of a given radiative transfer problem. It cannot give the correct solution, but it usually gives a better approximation to the correct solution than the LTE approximation. In this way, the time to reach convergence with the full non-LTE

code will be significantly reduced. In fact, for some RT problems it is difficult to obtain convergence unless the initialization is done via the LVG approximation. Many of the problems concerning the convergence of H_2O models which have been investigated in the previous section and which will be investigated in the following one have been initialized using the LVG approximation. Population inversions are very easily obtained in H_2O and an approximation to this maser solution is obtained with the LVG approximation, so that the subsequent iterative scheme only makes small corrections to this solution, thus making it much more stable.

4.7 Applications to Sgr B2

4.7.1 Description of the object

Around 100 pc apart from the Galactic Center (GC) we find the giant molecular complex Sgr B2. This region appears as the most brilliant emission in the GC region when observed from the centimeter wavelengths to the far infrared. Its angular size is ∼15' which gives a diameter of ∼40 pc observed at a distance of 8.5 kpc and has a mass of $\sim 10^7$ $M_\odot$. Although it shares almost all the fundamental properties of the GC clouds, it is one of the most active formation regions of massive stars on the galaxy, with rates similar to those found on the disk star formation regions. All the star formation tracers are present in this complex: hot and dense cores (HC) where the evolution of proto-stars occurs surrounded by dust envelopes; ultra and hypercompact HII regions generated by the strong UV field produced by young massive stars; maser emission from different species like H_2O, OH, CH_3OH, SiO and H_2CO. This fragmented and clumpy medium is surrounded by a giant molecular cloud which often makes it difficult to interpret the astronomical observations.

4.7.2 Observations

Many molecular species have been identified in Sgr B2. Almost all of them present spectral features which appear in absorption. Identifications so far include: HF (Neufeld et al. 1997), H_2O (Cernicharo et al. 1997), C_3 and NH (Cernicharo et al. 2000), H_3O^+ and NH_2 (Goicochea & Cernicharo 2001) and NH_3 (Ceccarelli et al. 2002). The lines of these species have been always

found in absorption. The only molecule which shows lines in emission is OH (Goicochea & Cernicharo 2002).

In Fig. 4.15 we show the observations of ortho- and para-H_2O lines obtained with the Long-Wavelength Spectrometer (LWS) onboard the Infrared Space Observatory (ISO) in its Fabry-Perot mode. The resolution of this instrument is $R = 7500$, equivalent to $\sim$40 km s^{-1}, which allows to resolve the line profiles. The observations are shown together with the molecular model of ortho-H_2O. Note that all the lines are in absorption except for the maser transition at 183 GHz. This maser line has been observed with the 30-m telescope at Pico Veleta (Spain) (Cernicharo et al. 2004). All the lines have been shown against the LSR (local standard of rest) velocity so that the center of the lines indicate the velocity of the source. Using the 183 GHz maser which presents a narrower profile, we have obtained a velocity of 60 km s^{-1}. This shift is present in all the lines except that at 121.72 μm which appears to be a blend of HF. The lines among the lowest energy levels present quite strong absorptions, specially the $2_{12} - 1_{01}$ line at 179.5 μm which is completely saturated. Furthermore, the absorption is not situated shifted to 60 km s^{-1}, which may indicate that the absorption in this line is not coming from the same regions as the rest of lines. Since the fundamental level takes part in this transition, this line is probably absorbed by all the cold water vapor present between Sgr B2 and the Earth. This water vapor may have a velocity which is not the same as Sgr B2.

The general tendency in the observations is that the lines get weaker when going to transitions between higher energy levels. Apparently, there is an effective pumping of population only up to the lowest energy levels. The IR photons generated in the inner core due to the dust emission are not able to produce an efficient pumping to the upper levels.

We have also shown additional lines whose carrier is the isotopic water $H_2^{18}O$ (see panels at 179.527 μm and 100.983 μm in Fig. 4.15). Its abundance is much lower and their lines are extremely weak. Note that we have scaled the line in the panel at 100.983 μm in order to make the absorption visible.

4.7.3 Modeling

In Section §4.5.3, we have previously advanced the model we are going to use in section. We discuss now the reasons that led us to choose such a model. The inner regions of the cloud (which are very efficient star forming regions)

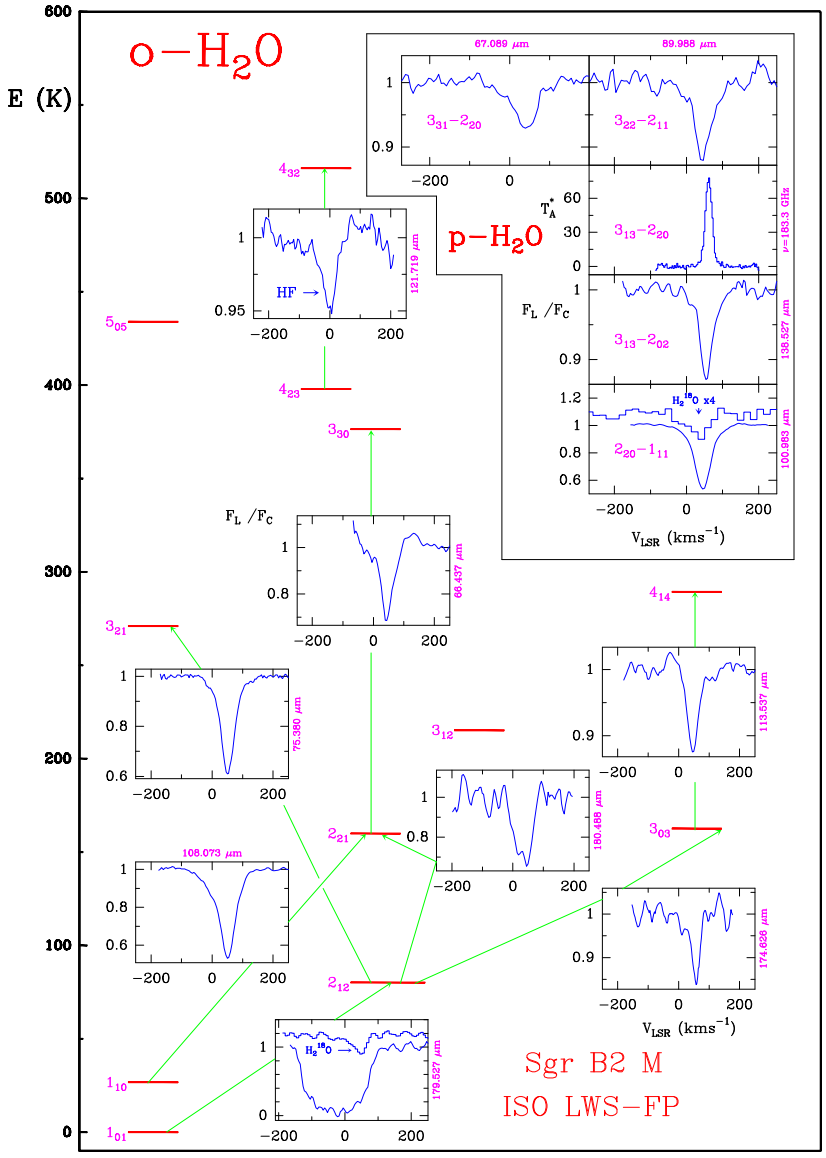

Figure 4.15: Ortho- and para-H_2O lines observed with the LWS spectrograph in its Fabry-Perot mode. We have also plotted the maser transition of para-H_2O at 183 GHz (Cernicharo et al. 2004).

are dominated by the dust radiation. Due to the large dust opacity in the inner regions, the innermost regions are completely hidden in the mid and far infrared. We can then assume that all the molecular transitions in the core are thermalized to the dust temperature. If we move out of the inner core, we find a region where molecular species are formed. However, this region is assumed to be not very thick since the strong UV field generated by the massive stars which are being formed in the environment tends to destroy the molecules.

In fact, the formation of water vapor in these clouds is not completely understood. If we assume that H_2O is formed through radiative dissociation of H_3O^+ we find that the predicted water abundance is not enough to explain the observed absorptions. Therefore, other mechanisms have to be found which can produce a significant abundance of water vapor. It has been shown recently that there exists a high amount of solid water on the surface of the dust grains (Moneti et al. 2001). This water could be transferred to the gas phase through the action of the radiation field coming from the GC or directly through the kinetic energy produced by shock fronts. These two processes are specially efficient for the formation of H_2O close to the dusty inner cores. The water present on the external regions of the clouds and the gas between us and the GC may be produced only by radiative dissociation of H_3O^+ since the action of the radiation field or the formation of shock fronts are thought to be not efficient in these weakly irradiated regions (see Goicoechea 2003).

We have to take into account that the external UV field is also very efficient in photodissociating H_2O so that the region where the water vapor lines are coming from may be quite thin. In these regions where the UV fields photodissociates H_2O there is a zone of high OH abundance which produces the absorption/emission lines observed towards Sgr B2 (Goicochea & Cernicharo 2002).

All the previous facts give us an idea of the physical dimensions and properties of the zone where the H_2O lines are being formed. As explained in Section §4.5.3, we have adopted a spherical geometry for a cloud made of two regions: an inner region consisting of a dust core with a constant temperature of $T_d = 30$ K and an opacity law with $\beta = 1$ and $\tau_{\rm ref} = 2.5$ for $\lambda_{\rm ref}$ =80 μm. This shell arrives to 1.472×10^{18} cm from the center of symmetry which gives an angular diameter of 23.5" at the distance of Sgr B2. The outer shell is between the outer surface of the inner shell and the region where the H_2O photodissociation starts to be efficient, which is situated at 1.837×10^{18} cm, giving a diameter of

28.9" for a distance of 8.5 kpc. We will solve the non-LTE RT problem in this outer thin shell. We can compare this region with the one chosen in Goicochea & Cernicharo (2002) for their modeling of OH in Sgr B2. They chose an inner core of 25", equivalent to ours and the outer surface was put at 42", equivalent to 5.3×10^{18} cm. The outer surface of the OH emission region is chosen to be much further away because OH is the product of the radiative dissociation of H_2O with the aid of the interstellar UV field. OH is then much more stable than H_2O against the UV field and it can be found at much larger distances from the center.

We take temperatures for this thin shell of only 0.12 pc between 40 K and 500 K. There are observational indications that the gas surrounding the inner dusty core may be at high kinetic temperature (Ceccarelli et al. 2002). This is the reason why we have performed calculations with temperatures as high as 500 K. The hydrogen density is varied from 5×10^3 cm^{-3} to 6.4×10^5 cm^{-3} in steps of 2. The column densities of ortho-H_2O are chosen to be 1.8×10^{16}, 9×10^{16} and 1.8×10^{17} cm^{-2}. The ratio between ortho- and para-H_2O are chosen to be 3. The turbulent velocity has been chosen to be 8 km s^{-1} in order to reproduce the observed width of the lines. The problem is solved by using a grid of 40 radial shells. We have shown in Section §4.5.3 that we could obtain a final true error below 20% for such a grid in the populations, except for those at the outer surface. However, they marginally influence the observed spectrum since the opacity at the outer regions is very small.

Concerning the numerical convergence scheme, we have used the MALI scheme without any acceleration for solving the majority of the physical situations. Since we have not done any previous run using a finer grid in order to use the true error, we have converged the models until reaching a value of the convergence error of the order of 1%. This guarantees that the minimum true error which can be obtained in the grid has been obtained. We have not made use of the fast methods based on the Gauss-Seidel iterative scheme because the water models are slightly difficult and delicate to converge. We have mentioned before that many of the levels of H_2O may produce population inversions which lead to maser transitions. The corrections to the populations calculated under the GS approach are usually very large and lead to instabilities in the code. Despite these problems, we have been able to use the MUGA scheme for solving the problem in many of the combinations of physical conditions with great success, using half of the iterations than those needed using the MALI scheme.

Moreover, it has been necessary to use a combination of the Λ-iteration followed by a transition to MALI in some of the most difficult cases in order to obtain convergence. We are currently working on trying to solve these problems using different approaches. One of them would be to limit the change on the population calculated under the MALI or MUGA schemes in order to finish up with an iterative scheme which may be used for all the problems. The first tests show that this approach may be of use, although the convergence properties of the methods is highly deteriorated.

We show in Figs. 4.16, 4.17 and 4.18 the emerging spectrum for all the models. Each line is plotted in a small box and the position of the lines are not representative of their wavelength. For each temperature we show the spectrum obtained when varying the hydrogen density. We show in the upper part of each plot the identification of each line, showing whether the line is a transition of ortho- or para-H_2O. The wavelength is also indicated in μm for the lines with wavelength below the ortho-H_2O line at 273.22 μm. The wavelength of the lines to the left of this one are indicated in GHz. This is the case of the well-known 183 GHz line of para-H_2O which very easily turns into a maser line.

The modeling shows that emission lines appear for almost all the combination of physical conditions. However, the lines below 60 μm only appear in emission for high temperature and high density cases. For temperatures between 300 K and 500 K and hydrogen densities above 2×10^4 cm^{-3}, the excitation temperature of the lines is larger than the dust temperature of the background. This way, they appear in emission with respect to the dust emission background. Since the observed H_2O lines are in absorption, it is expected that these physical conditions are not representative of those in the shell where the H_2O lines are being formed. The equivalent dust temperature at a wavelength λ can be obtained from the dust temperature T_d and the dust opacity τ_d by:

$$\begin{aligned} T_d^{\rm equiv} &= \frac{hc}{\lambda k}\left[\ln\left(1+\frac{2hc^2}{\lambda^5 B'}\right)\right]^{-1} \\ B' &= \frac{2hc^2}{\lambda^5}\left[e^{hc/\lambda k T_d}-1\right]^{-1}\left(1-e^{-\tau_d}\right). \end{aligned} \tag{4.59}$$

For wavelengths below 60 μm this optical depth correction has no effect, and the equivalent dust temperature is equal to the true dust temperature. However,

the lines situated at higher wavelengths are affected. For example, the line at 179.5 μm has an equivalent dust temperature of $\sim$26 K, 4 K lower than the true temperature of the background. This effect is important because the lines may appear in emission for lower kinetic temperature. Summarizing, *we need all the lines to have excitation temperatures lower than the equivalent dust temperature in order to see them all in absorption.*

Another conclusion from the modeling is that the predicted lines are almost insensitive to the temperature for densities below 2×10^4 cm^{-3}. Hence, the ISO data alone cannot be used to put a value on the temperature, but only an upper limit. Additional observations, perhaps in the near infrared on the vibration-rotation bands of water are needed. Other observations which may be of interest are the lines in the GHz region which may show variation with the temperature.

In order to give a graphical idea of the combination of physical conditions which give emission or absorption in some lines, we show Fig. 4.19, 4.20 and 4.21 the ratio between the flux at the line center and the continuum flux. If this ratio is larger than 1, the line is in emission. However, note that the wings of the lines are often in emission while the core is not. Therefore, when this ratio is lower than 1, the line could be producing a net emission while the core is still in absorption with respect to the background. We have plotted the ratio for the $2_{12}-1_{01}$, $3_{03}-2_{12}$, $2_{21}-1_{10}$ and $3_{30}-2_{21}$ ortho-H_2O lines, which are representative of the excitation properties of the lowest energy levels. We have also indicated with horizontal dotted lines the values of the hydrogen densities chosen for the modeling in order to make it easier the identification of the ranges in which the physical conditions give results comparable to the observations.

The general behavior is that the lines are sensitive to the physical conditions only for hydrogen densities above 4×10^4 cm^{-3}. Below this density, the variation of the core of the lines is negligible. Above this density, the emission of the lines among the lowest energy levels is increased when the temperature and the density are increased. Note that the fundamental line at 179.5 μm is almost always in absorption for these combinations of physical conditions. Note also that the variation of the ratio F_l/F_c is negligible in the zone where it is lower than 1.

Finally, it would be of great interest to verify wether an inversion code would be of any use in obtaining information from these observations.

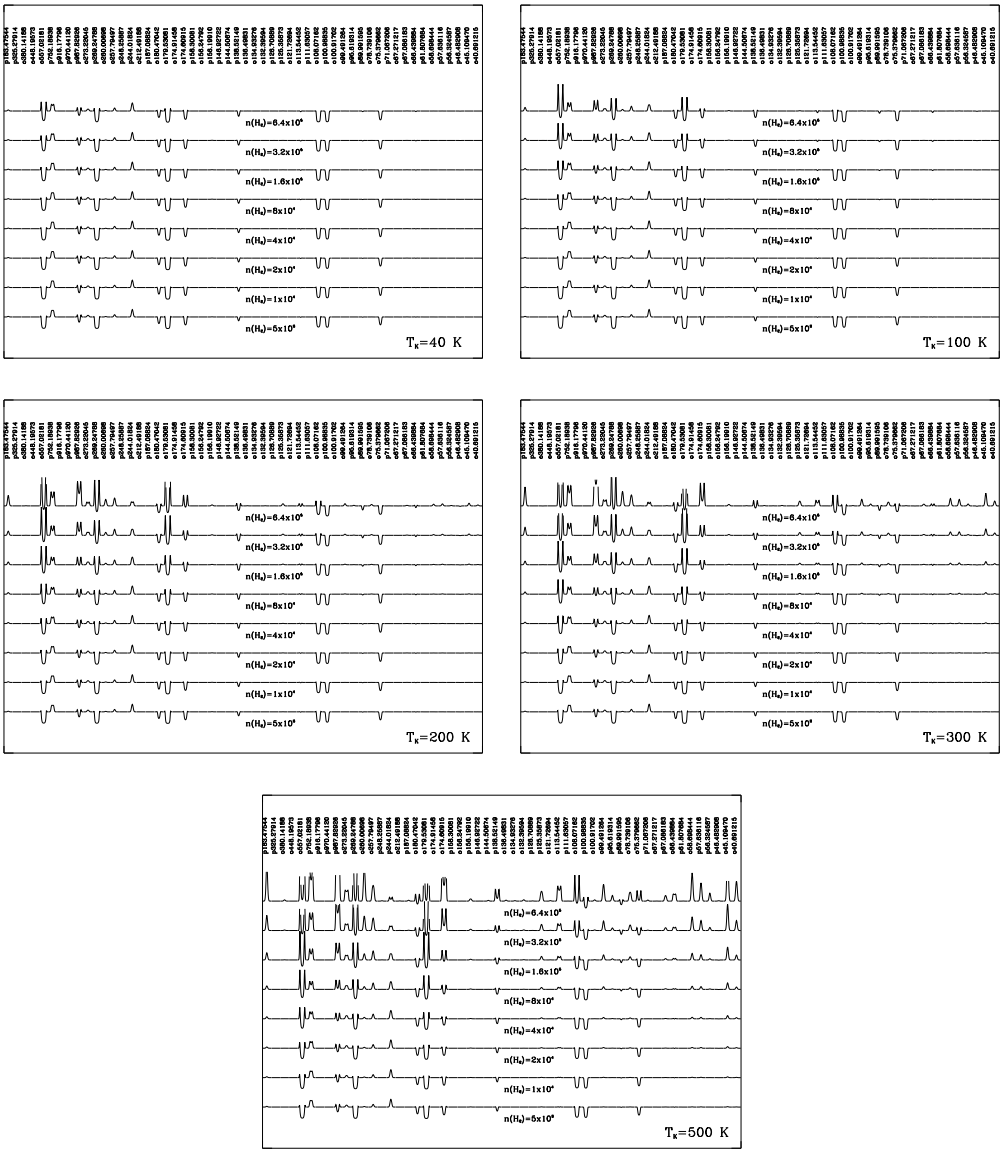

Figure 4.16: Emergent water spectrum for N(ortho-H_2O)=1.8×10^{16} cm^{-2} for the whole set of chosen temperatures and hydrogen densities. The wavelength and species of each transition are indicated. Note that the wavelengths are in μm starting from the right of the plots until arriving to the transition at 273.22 μm. The rest of the transitions are given in GHz.

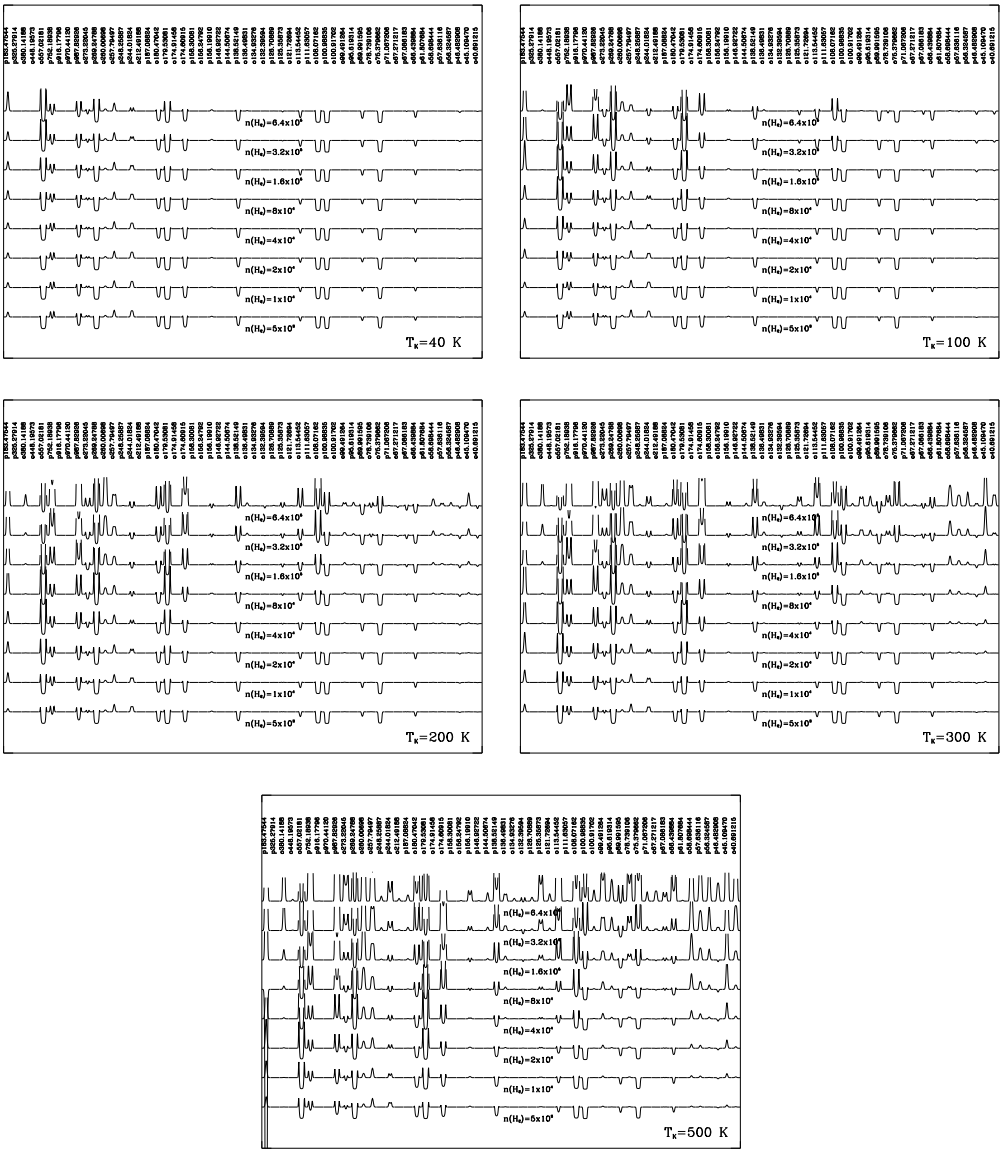

Figure 4.17: Emergent water spectrum for N(ortho-H_2O)=9×10^{16} cm^{-2} for the whole set of chosen temperatures and hydrogen densities. The wavelength and species of each transition are indicated. Note that the wavelengths are in μm starting from the right of the plots until arriving to the transition at 273.22 μm. The rest of the transitions are given in GHz.

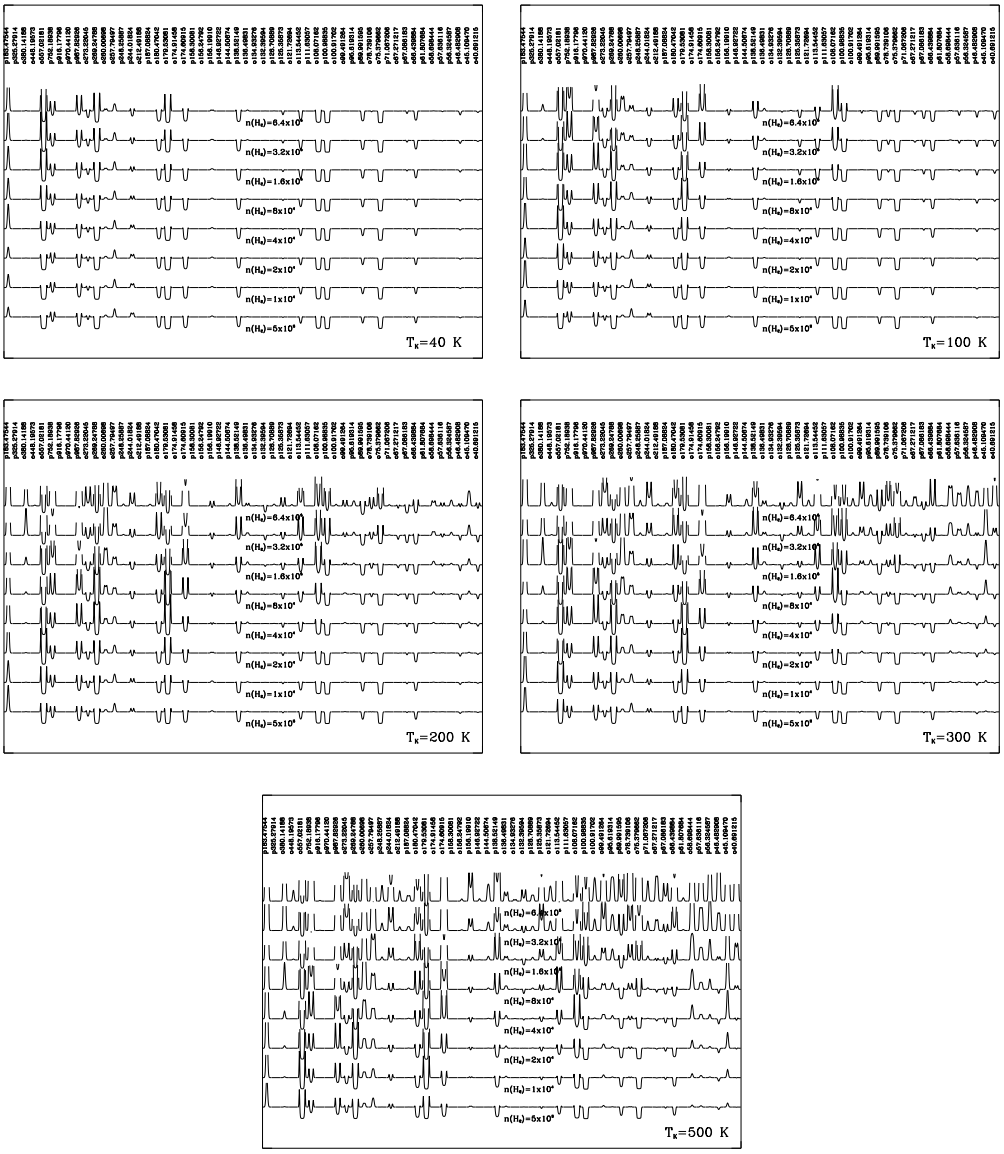

Figure 4.18: Emergent water spectrum for N(ortho-H_2O)=1.8×10^{17} cm^{-2} for the whole set of chosen temperatures and hydrogen densities. The wavelength and species of each transition are indicated. Note that the wavelengths are in μm starting from the right of the plots until arriving to the transition at 273.22 μm. The rest of the transitions are given in GHz.

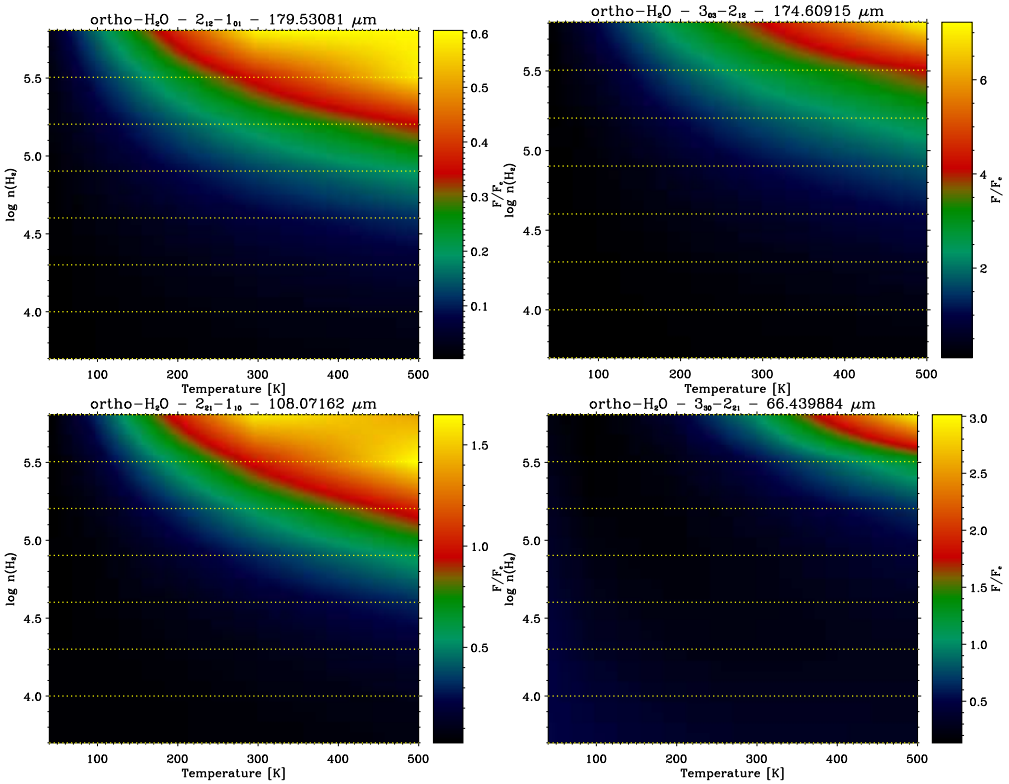

Figure 4.19: Ratio between the flux at the center of the line and at the continuum for all the combinations of kinetic temperature and hydrogen density for a column density of ortho-H_2O of $1.8{\times}10^{17}$ cm^{-2}. If this ratio is larger than 1, the line is in emission. However, note that it may be lower than 1 and the wings of the line may be in emission.

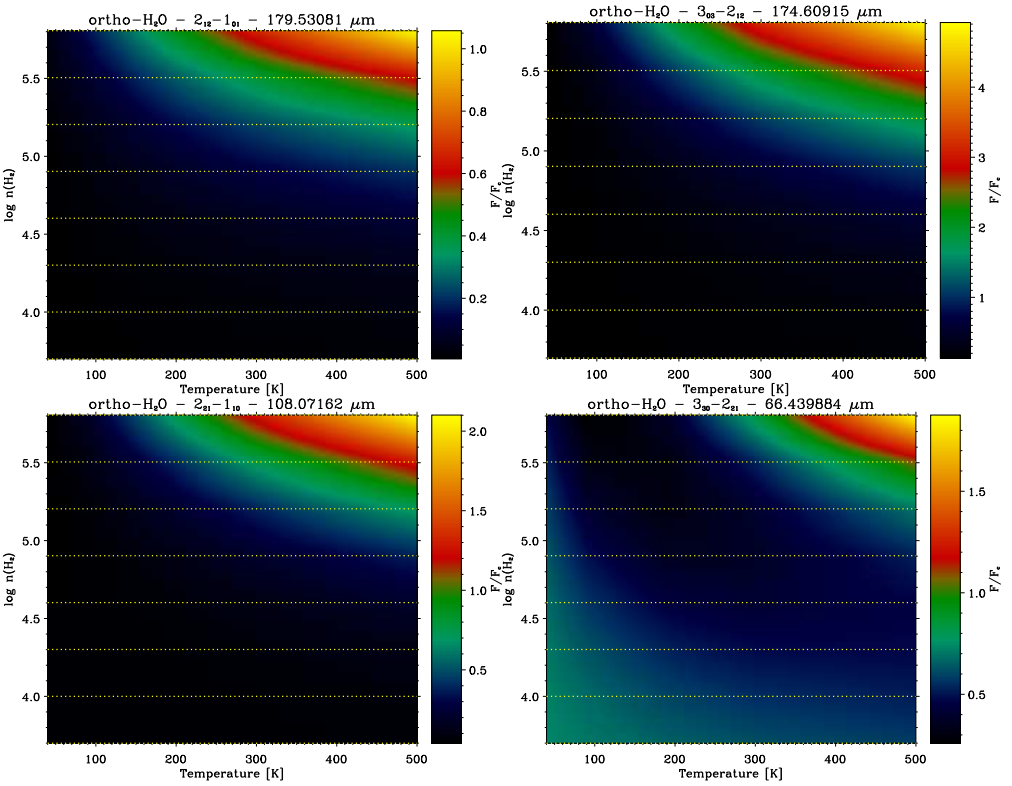

Figure 4.20: Same as Fig. 4.19 but for a column density of ortho-H_2O of 9×10^{16} cm^{-2}.

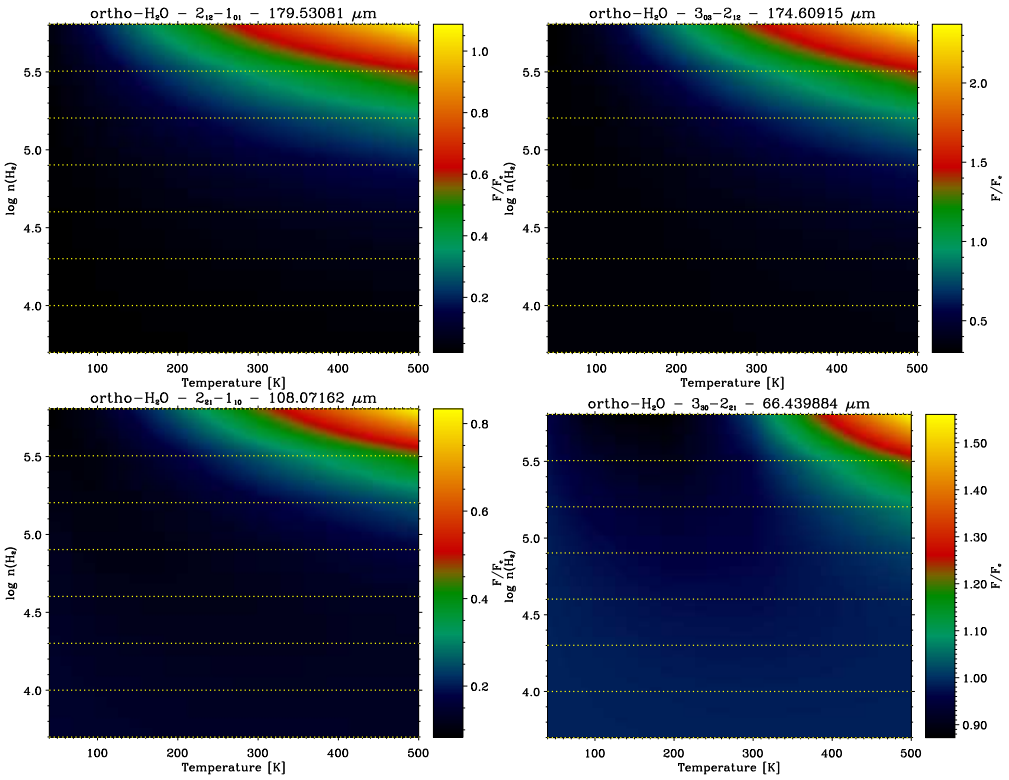

Figure 4.21: Same as Fig. 4.19 but for a column density of ortho-H_2O of $1.8{\times}10^{16}$ cm^{-2}.

4.8 Applications to VY CMa

4.8.1 Description of the object

VY CMa is a massive red supergiant star of spectral type M5 Iae quite unusual which is supposed to be in a late evolutionary stage. It is characterized by a strong maser radio emission produced by a large set of molecules (Cernicharo et al. 1993, Benson & Mutel 1992, Wu Zheng et al. 1998), high infrared emission coming from dust grains, high polarization signal in the near infrared and a large variability in the optical. Lada & Reid (1978) estimated a distance of ∼1.5 kpc by associating the star to a well-known group of molecular clouds. This distance has been confirmed by the study of the H_2O maser emission in the star's envelope (Richards et al. 1998), and it implies that VY CMa is one of the most intrinsically brilliant stars in our galaxy because its bolometric luminosity is $\sim 5\times10^5$ $L_\odot$. It is expected to have a high mass, at least ∼25 $M_\odot$ and a very low effective temperature of $T_{\rm eff} \approx 2800$ K. With these properties, an estimation of the time needed for its explosion as a supernova may be $\sim 10^4$ years (Brunish & Truran 1992). The mass loss is extraordinarily high, exceeding 10^{-4} $M_\odot$ year^{-1} (Danchi et al. 1994). Its envelope is very asymmetric (Monnier et al. 1999), which motivates us to investigate this star in detail by using polarimetric techniques once the instrumental tools become available.

4.8.2 Observations

General description

We have a complete infrared spectrum of VY CMa. The spectral region between 2.38 and 45 μm has been observed with the spectrograph Short-Wavelength Spectrometer (SWS; de Graauw et al. 1996) onboard the Infrared Space Observatory (ISO) satellite. The spectral region between 40 and 200 μm has been observed with the Long-Wavelength Spectrometer (LWS) also onboard ISO. The SWS observations were performed on the grating mode with a spectral resolution of $\lambda/\Delta\lambda$ ∼1000-2500. Additionally, three pure rotational lines of ortho-H_2O were observed in the Fabry-Perot mode of this instrument, with a resolution of $\lambda/\Delta\lambda \sim 3\times10^4$, equivalent to a resolution of ∼10 km s^{-1}. The observations between 29.5 and 45 μm have been presented by Neufeld et al. (1999) with the detection of many water vapor emission lines in the far in-

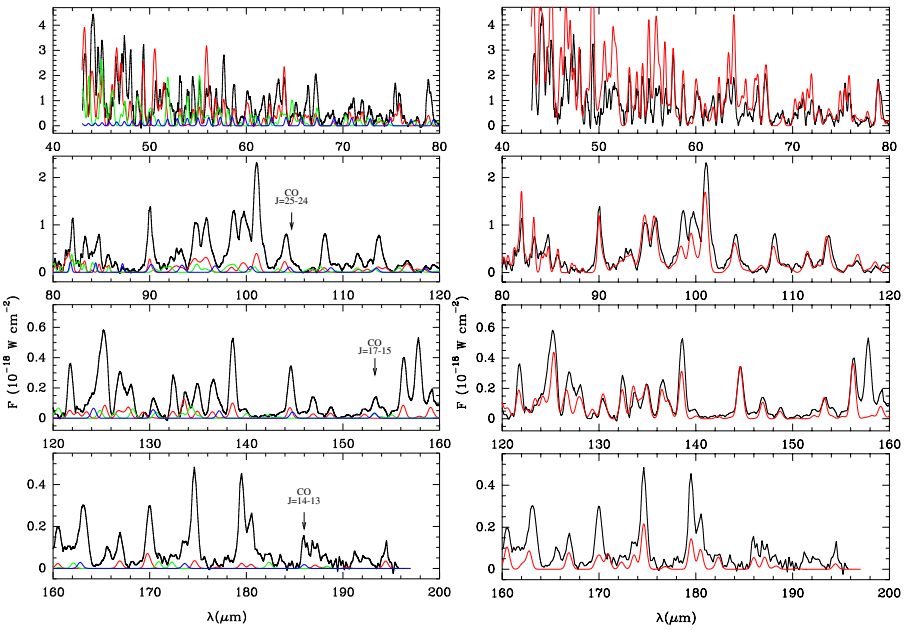

Figure 4.22: LWS spectrum of VY CMa between 40 and 200 μm. The left panel shows a comparison between the observation in black and different models including different species only for line identification purposes. Blue indicates CO lines, red indicates H_2O in the fundamental vibrational level ν=0 and green indicates H_2O in the ν_2=1 excited vibrational level. The right panel shows a fit of the spectrum using a LVG model.

frared. In the grating mode of the SWS they found at least 41 spectral features which are associated with water vapor emission in pure rotational lines, either coming from the fundamental vibrational level or from the first excited $\nu_2 = 1$ vibrational bending mode. The total luminosity in these water lines accounts for 25 $L_\odot$. Due to its high resolution, the Fabry-Perot observations of these water vapor lines show conspicuous P-Cygni profiles indicating that the lines are being formed in an expanding envelope.

We have centered our investigation on the spectral region below 30 μm, together with the far infrared observations taken with the LWS instrument. Both spectral regions trace different regions in the envelope with different physical conditions and will help us to obtain the physical conditions in the envelope.

Far infrared

We start with the identification of the spectral features in the far infrared between 40 and 200 μm. In this zone we can find pure rotational transitions of H_2O and pure rotational transitions of CO between high J levels (starting from the J=14-13). The left panel of Fig. 4.22 shows the complete LWS spectrum of VY CMa where the continuum has been extracted. All the spectral features appear in emission after the continuum substraction. We have made a comparison of this spectrum with the result obtained from a LVG code in order to identify different species. We have identified CO pure rotational lines (solid blue line), together with pure rotational lines of H_2O in its fundamental level ν=0 (solid red line) and some of the pure rotational lines of the ν_2=1 excited vibrational level of H_2O (solid green line). We also show in the figure the angular momentum J of some of the CO transitions. Note that the lines with $J \gtrsim$23–25 cannot be yet assigned to any feature in the observed spectrum thus indicating that the temperature where the CO is formed may not be very high. We will see that this characteristics is reinforced by the structure of the fundamental vibration-rotation band of CO at 4.6 μm.

Including several shells with different physical conditions, we can obtain a quite good fit to the LWS observed spectrum. The emergent spectrum has has been obtained using the LVG approximation. The fit in the region between 60 μm and 150 μm is quite satisfying as shown in the right panel of Fig. 4.22. The region below 60 μm may be affected by the presence of dust in the envelope. The excess of emission obtained in this region which cannot be reproduced with the LVG code may be due to dust absorption and re-emission mechanisms on the envelope of the star.

Near infrared

The vibration-rotation bands of many of the most conspicuous molecules in this star are located in the near infrared. We will analyze the most important feature we have found.

- CO. After the detection of some weak CO lines in the LWS spectrum, we have investigated the CO band in the near infrared at 4.6 μm. Since the fundamental electronic level of CO is $X^1\Sigma^+$ the rotational structure of the vibrational bands are extremely simple. The fundamental band

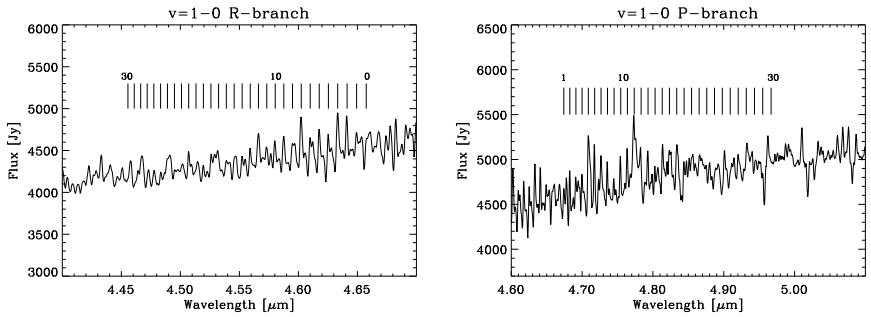

Figure 4.23: Identification of the lines of the v=1-0 vibration-rotation band of CO at 4.6 μm. The left panel shows the lines from the R branch, while the right panel shows the lines from the P branch. Note that only low J transitions allow a secure identification, while high J transitions seem to be absent.

is centered at ∼4.65 μm and is composed of a P branch which extends to larger wavelengths than the center of the band and a R branch which extends to shorter wavelengths. Since the molecule does not rotate as a rigid body, the lines of the P branch start to drift apart when the wavelength increases and those of the R branch move closer when the wavelength decreases, forming the *bandhead*. In Fig. 4.23 we show the SWS spectrum of the CO band in Janskys[2]. We have also plotted vertical lines at the position of the CO lines to facilitate an easy identification. All the lines which can be easily identified appear to be in emission. We have even detected some of the spectral features which can be associated with the lines of the v=2-1 band. Note that in accordance with what has been obtained in the far infrared, we only observe CO lines up to J ∼23-25. Additionally, we show in the right panel of Fig. 4.24 the comparison between two different modes of operation of the SWS spectrograph. The SWS01 mode has a resolution of 120 km s^{-1} and the SWS06 mode has a resolution of 300 km s^{-1}. We can verify then that both spectra look very similar giving us the idea that all the oscillations which might be interpreted as pure noise are spectral lines. In fact, almost every observed line that cannot be assigned to a CO transition can be associated to a line belonging to a water vapor band, specially for wavelengths larger than 4.9

[2] 1 Jansky is equal to 10^{-23} erg cm^{-2} s^{-1} Hz^{-1}

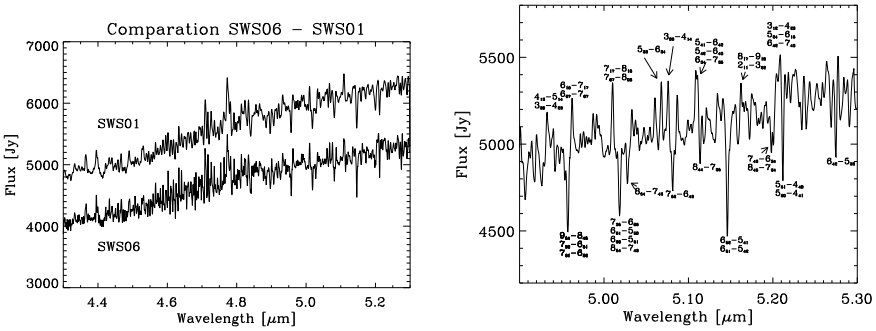

Figure 4.24: The left panel shows the difference between the observation taken with the SWS instrument in two different modes of operation with different resolutions. The right panel shows the identification of H_2O pure rotational lines in the VY CMa spectrum.

μm.

- H_2O. The CO lines disappear for wavelengths larger than 4.9 μm and quite conspicuous water vapor lines start to be observed, either in absorption or emission. In the right panel of Fig. 4.24 we show a region between 4.9 and 5.3 μm where we have identified the individual water vapor transitions. Note that almost all the lines which appear in absorption belong to the R branch, that is, those with $\Delta J = 1$, while the lines which appear in emission belong to the P branch, that is, those with $\Delta J = -1$. The same behavior appears at longer wavelengths when going closer to the center of the band. This behavior has been investigated in detail by González-Alfonso & Cernicharo (1999) and is a consequence of the radiative pumping. Although exceptions exist, the strongest transitions are those with $\Delta K_+ = \Delta K_- = \pm 1$.

4.8.3 Modeling

In order to investigate the observed bands of CO and H_2O, we have generated atmospheric models which approximately describe the physical conditions on the envelope of such a supergiant star. The radius of the star is chosen to be $R_\star = 6{\times}10^{13}$ cm and our model starts at $4{\times}10^{14}$ cm, leaving a region between

the star's surface and the zone where the formation of molecules is efficient. The model extends out to 1000 $R_\star$. The density structure of the envelope critically depends on the mass loss $\dot{M} = dM(r)/dt$ of the star since:

$$\frac{dM(r)}{dt} = 4\pi r^2 \mu n(r) V(r), \tag{4.60}$$

where $n(r)$ is the molecular hydrogen density, $V(r)$ is the velocity field and μ is the mean molecular weight obtained as:

$$\mu = \sum_i A_i m_i, \tag{4.61}$$

with A_i and m_i are the relative abundance and the mass in grams of each element, respectively, while the sum is extended over all the elements present in the medium. The typical velocity field in this kind of envelope starts from zero velocity at the stellar surface and it undergoes a fast acceleration at the point where the dust is formed R_d due to the radiation pressure and then the velocity rapidly increases until reaching the escape velocity V_∞. We model this behavior with a law like:

$$V(r) = V_\infty \left(1 - \frac{0.984 R_\star}{r}\right)^{1/2}. \tag{4.62}$$

If we assume that the mass loss is constant, we can obtain the variation of the density through the atmosphere as:

$$n(r) = \frac{C}{r^2} \frac{V_\infty}{V(r)}, \tag{4.63}$$

where

$$C \approx 3 \times 10^{37} \frac{\dot{M}_5}{V_6}. \tag{4.64}$$

$\dot{M}_5$ is the mass loss in units of 10^{-5} $M_\odot$ yr^{-1} and V_6 is the escape velocity V_∞ in units of 10^6 cm s^{-1}.

Concerning the temperature, we have decided to use a model which correctly reproduces radiative equilibrium calculations in the envelope of evolved stars

taking into account many heating and cooling mechanisms. The temperature is given as a piecewise fit:

$$\begin{aligned} T_k(r) &= 2300.0\left(\frac{1}{\bar{r}}\right)^{0.6} && \bar{r} \leq 3 \\ T_k(r) &= 1189.7\left(\frac{3}{\bar{r}}\right)^{0.7} && 3 \leq \bar{r} \leq 17 \\ T_k(r) &= 353.2\left(\frac{17}{\bar{r}}\right)^{1.3} && \bar{r} \geq 17, \end{aligned} \tag{4.65}$$

where $\bar{r} = r/R_\star$. Furthermore, the dust temperature T_d follows a law like:

$$T_d(r) = 1300\left(\frac{3}{\bar{r}}\right)^{0.6}, \tag{4.66}$$

so that the temperature at $3R_\star$ is 1300 K, 600 K at $10R_\star$ and 300 K at $40R_\star$. The CO abundance is chosen to be [CO] $= 10^{-4}$, which is of the order of magnitude of the CO abundance in an oxygen-rich envelope.

The CO energy levels and the Einstein coefficients of the radiative transitions have been obtained from the linelist of Goorvitch (1994). They tabulated the energy levels of the fundamental $X^1\Sigma^+$ electronic level of CO for the vibrational levels from $v = 0$ to $v = 20$ and rotational levels from $J = 0$ to $J = 149$. Collisional rates between individual rotational levels of different vibrational levels are not available. In fact, this state-to-state collisional rates are only available for SiO. In order to introduce in the model these collisional rates, we have made use of the analytic formulas for the SiO state-to-state collisional rates given by Langer & Watson (1984). They produced analytic fits to the collisional rates of Bieniek & Green (1983a) and Bieniek & Green (1983b). They give the collisional rates between any level J and the level $J = 0$ for every combination of vibrational quantum numbers fulfilling $\Delta v = 0, 1$. The rate between any pair of levels J_u and J_l is obtained with the aid of the Infinite Order Sudden approximation (IOS) (see Watson et al. 1980):

$$k(v_u, J_u; v_l, J_l) = \frac{E_0}{E_{J_u}} g_{J_l} \sum_l \begin{pmatrix} J_u & l & J_l \\ 0 & 0 & 0 \end{pmatrix}^2 k(v_u, 0; v_l, l), \tag{4.67}$$

where E_J is the energy of the level.

The previous collisional rates are only available for vibrational levels up to $v = 4$ which has been used as a limit in our calculations. On the other hand, they can be extrapolated to very high J with the aid of the formulas given by Langer & Watson (1984). Of course, this kind of extrapolation has to be taken with care. The model molecule we have used for obtaining the emergent spectrum in VY CMa is composed of the first 5 vibrational levels between $v = 0$ and $v = 4$ including 26 rotational levels in each vibrational level from $J = 0$ to $J = 25$. The model includes 130 levels, with 325 radiative transitions among them, including the vibration-rotational and the pure rotational transitions. Including the collisional transitions which do not have selection rules, the total amount of transitions is 4329.

In order to verify that the collisional rates are representative of the true collisional rate for CO, we have solved the problem of CO in the solar atmosphere. The CO abundance has been calculated using the ICE approximation in the semi-empirical FAL-C model. A model molecule including 40 rotational levels in each of the 5 vibrational level has been used and the problem is solved using the plane–parallel approximation. We recover the fact that both the vibrational levels and the rotational levels inside a vibrational level are in LTE in the lower part of the atmosphere below 500 km, where the CO lines are formed. This result has been obtained without the assumption that the rotational levels of CO are in LTE but solving the complete non-LTE CO problem in a semi-empirical model of the solar atmosphere.

We have made calculations of the emerging spectrum for VY CMa using different mass losses in $M_\odot$ year^{-1}, from $\log \dot{M} = -4$ to $\log \dot{M} = -9.5$, in steps of 0.5 in the logarithm scale. The problems have been solved using the MALI and MUGA schemes initialized using the LVG approximation. Assuming a thermal velocity of $\sim$1 km s^{-1} and the velocity field given by Eq. (4.62), the Sobolev length varies from 10^{14} cm in the inner regions of the envelope to 10^{18} cm in the outer parts. In view of that, the LVG approximation could perhaps be valid in the inner parts of the envelope. However, since the CO lines are optically thin in the outer parts of the envelope, the approximation may result valid in these regions too. Even though the LVG approximation may result invalid for almost all the envelope, we have used it as an initialization, giving populations which are closer to the correct solution than if we initialize in LTE. Almost all the models converged to the desired precision (maximum relative change of 10^{-3}) in less than $\sim$10 iterations, each iteration taking $\sim$75 seconds.

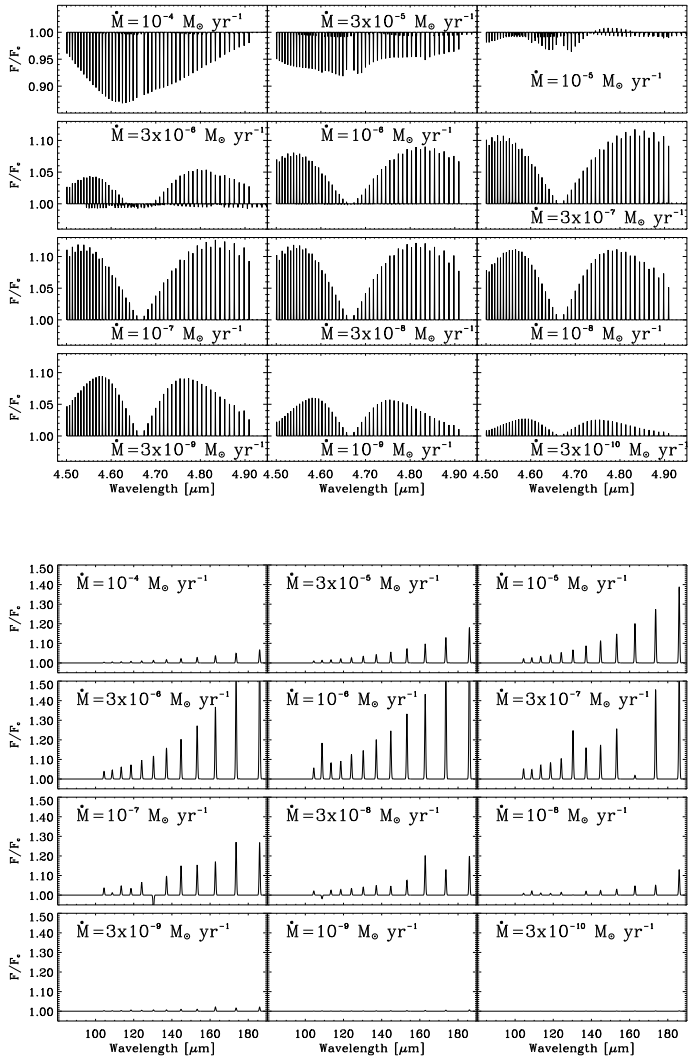

Figure 4.25: Calculated CO vibration-rotation (upper panel) and pure rotation (lower panel) bands for each of the considered mass loss values. The results for mass losses below 10^{-5} $M_\odot$ yr^{-1} are plotted in the same scale in order to show the relative differences. Note how the near-IR band suffers from a transition from absorption to emission when the mass loss is decreased.

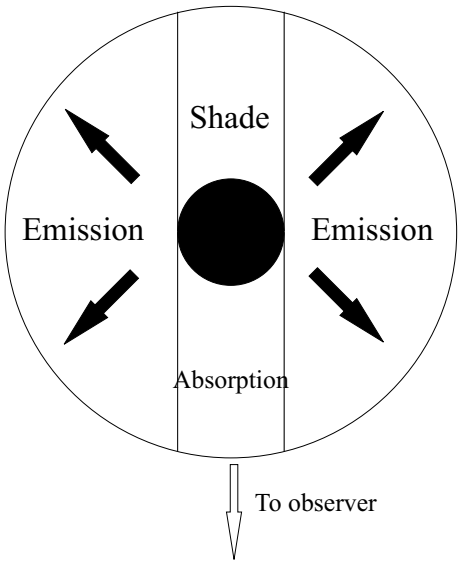

Figure 4.26: Schematic representation of a circumstellar envelope. The region between the star and the observer produces absorption, the region behind the star is completely shaded by the star's radiation and the rest of the envelope produces emission lines since no background is present.

Only the models with mass losses larger than 10^{-5} $M_\odot$ yr^{-1} needed between 10 and 20 iterations to converge.

The results are presented in Fig. 4.25. Here we have plotted the IR vibration-rotation band at 4.6 μm using the resolution of the SWS instrument together with the pure rotation lines which arise between 100 and 200 μm as observed with the grating mode of the LWS instrument.

Near IR

The P and R branches of CO are perfectly distinguished with the center of the band at 4.67 μm. The most obvious conclusion of these results is that the band turns from being in emission to being in absorption when the mass loss is incremented. This is easily understood since the CO column density proportionally increases as the mass loss increases. Three important regions can be identified in a circumstellar envelope as indicated in the scheme of Fig. 4.26. The region

between the star and the observer produces absorption of the star's radiation. We have assumed that the star emits as a blackbody but, in order to be consistent, we should have assumed that the star has a photospheric spectrum which is modified by the presence of the envelope producing absorption lines. Because the envelope is in expansion, the absorption lines are blue-shifted with respect to the rest wavelength. The region behind the star is completely shaded by the star's radiation and produces no signature in the spectrum. Finally, the rest of the envelope produces emission lines since there is no background to absorb. The expansion produces that the emission lines have a widespread distribution of velocities thus being blue-shifted, red-shifted or at the rest frequency depending on the zone they are formed.

Unless the mass loss is very high, the column densities in the circumstellar envelopes are not very high and the emission produced by these regions is not very important. The cases with low $\dot{M}$ do not produce enough opacity in the band to give a significant absorption or emission but, since the emission region is much larger, the average line profile shows the emission feature. For a higher mass loss, the CO column density increases and the emission and absorption also increases. The whole absorption region contributes to the same wavelength since the blue-shift is almost the same, thus giving a strong absorption component. On the other hand, the widespread distribution of the emission regions produces a broad emission feature which is not enough to cancel the absorption and the whole line turns out to be in absorption when the envelope is observed with the resolution of the SWS instrument.

It is difficult to compare the modeling results we have obtained with the observations of VY CMa. The observations seem to indicate that almost all the lines are in emission with respect to an underlying continuum in the P and R branches. The modeling predicts an absorption band for a value of the mass loss of VY CMa, which is supposed to be of the order or larger than 10^{-4} $M_{\odot}$ yr^{-1}. On the other hand, our RT modeling predicts a more or less smooth variation of the strength of the lines in each branch which is not observed. Contrarily, the observation shows a variation of the strength of the lines for very close lines.

The wavelength where the P and R branches have their maximum emission is related to the temperature. The observations show that the maximum emission is at $\sim$4.6 μm for the R branch and below 4.8 μm for the P branch, which is approximately equivalent to what the models predict.

Far IR

We have also presented the results obtained for the far-IR lines starting at 100 μm since no emission is found below this wavelength. The lines above 100 μm do not show an important emission, even for transitions as low as $J = 14-13$ at 186 μm. We see a behavior similar to what happens in the near-IR region but with some differences. For very low and very high mass losses, the far-IR lines are not seen, while they are conspicuous for intermediate mass losses, between 10^{-5} and 3×10^{-8} $M_\odot$ yr^{-1}. The fact that we have very weak emission lines in the far-IR as can be seen in Fig. 4.22 is compatible with a very high mass loss rate.

4.9 Conclusion

We have solved the non-LTE problem in spherical symmetry for molecular lines using fast iterative methods based on the Gauss-Seidel and Successive Overrelaxation schemes. We have presented the basic equations to solve in order to obtain the solution to the problem. The characteristics technique has been applied in order to solve the radiative transfer equation in spherical geometry. The fast iterative methods developed by Trujillo Bueno & Fabiani Bendicho (1995) have been implemented in spherical symmetry and we have verified that they lead to an increase in the convergence rate similar to that obtained for Cartesian geometries.

We have investigated in detail the convergence properties of these iterative methods with the aid of two simple problems, namely the quasi plane-parallel case and the spherical case. We have also investigated the behavior of these methods when dealing with unstable problems like maser transitions. With the aid of the developed code, we have made a comparison between the results obtained with the LVG approximation and the full non-LTE solution. We point out that the LVG approximation has to be carefully applied and only when the applicability conditions are fulfilled. We show some wrong results which may arise with the LVG approximation when these applicability conditions are not fulfilled.

Finally, we have applied the code for the solution of the non-LTE problem in two selected astrophysical situations. The first one is the excitation state of the water energy levels in a hot shell in the SgrB2 cloud in the Galactic Center. The

second one refers to the formation of the CO fundamental vibration-rotation band in the envelope of the red supergiant VY CMa.

5

Molecular Spectropolarimetry

We investigate in this chapter the Zeeman effect in diatomic molecules. We start with the definition of some important elements on angular momentum theory which will be of utility for the rest of the chapter. We introduce the Zeeman Hamiltonian and discuss the formulas for the Landé factors in some simple cases. In Section §5.3, we introduce a general description of the Zeeman effect for diatomic molecules based on an effective Hamiltonian. We give the expressions for the matrix elements of the Hamiltonian matrix and describe the diagonalization technique. In Section §5.4, we give a brief introduction to the equations which describe the phenomena of scattering polarization and its modification due to the presence of a magnetic field, the so-called Hanle effect.

5.1 Elements of Angular Momentum Theory for Diatomic Molecules

Angular momentum theory provides a robust framework for describing the complex dynamical processes going on in a molecule. As early as 1927, Hund showed how molecular kinetics could be represented by the successive coupling of the angular momenta coming from the orbital motions and the spins of the constituents particles (Hund 1926; Hund 1927; Herzberg 1950). Racah's work on tensor algebra in the 1940s has led to powerful techniques for the study of molecular spectroscopy (Racah 1942; Judd 1975). In this section, we will show

how these techniques can be applied to the calculation of the matrix elements of angular momentum operators which will be of importance for the calculation of the Zeeman effect in diatomic molecules.

The Born-Oppenheimer approximation leads to an effective separation of the energies due to the electronic, vibrational and rotational motions. The same happens with the eigenfunctions associated with each motion. We will usually work using the case (a) eigenfunctions since the eigenvalues of the angular momentum operators are very easy to obtain, thus simplifying the calculation of the matrix elements of the total Hamiltonian. The case (a) eigenfunctions can be written as (Judd 1975):

$$|\alpha\Lambda\Sigma; v; \Omega JM\rangle \equiv |\alpha\Lambda\Sigma\rangle|v\rangle|\Omega JM\rangle, \tag{5.1}$$

where we have explicitly indicated the separation of the eigenfunctions following the Born-Oppenheimer approximation. $|\alpha\Lambda\Sigma\rangle$ is the electronic eigenfunction, being α a collection of quantum numbers which indicate the electronic configuration of the molecule, Λ and Σ are the projections of the total orbital electronic angular momentum and the total spin on the internuclear axis, respectively (see Chapter 2). $|v\rangle$ is the vibrational eigenfunction which depends on the vibrational quantum number v. Finally, $|\Omega JM\rangle$ is the rotational eigenfunction which depends on the total angular momentum J, its projection on a quantization axis M (typically the axis along the magnetic field) and the quantum number $\Omega = |\Lambda + \Sigma|$.

Due to the difference in mass between the electrons and the nuclei of a molecule, it is appropriate to refer the motion of the electrons to a frame fixed to the nuclei (F') whose center is the center of mass of the molecule, rather to an external laboratory frame. The coordinates of an electron in the laboratory frame F (with its center also at the center of mass of the molecule) are (x, y, z), while the coordinates on the frame fixed to the molecule are (ξ, η, ζ). It is convenient to consider the ζ axis parallel to the internuclear axis and the z axis along the quantization axis. The angle between both frames can be represented by the three Euler angles (α, β, γ). Once the coordinates of an electron are known in one of the frames, a geometrical transformation between both frames using the Euler angles can be applied to obtain the coordinates in the other frame. As usual, once the ζ axis is fixed, there is freedom in the choice of the direction of the ξ and η axis, which results in an indetermination on the value of γ. It is usual to assign the value $\gamma = \pi/2$.

The explicit expression for the normalized rotational eigenfunction, which depends explicitly on the Euler angles, is obtained by solving the Schrödinger equation for a symmetric top and is given by (Judd 1975):

$$|\Omega JM\rangle = \sqrt{\frac{2J+1}{8\pi^2}}\mathcal{D}^J_{M\Omega}(\alpha,\beta,\gamma)^*, \tag{5.2}$$

where $\mathcal{D}$ is the rotation matrix (e.g., Edmonds 1960, Judd 1975). The representation of the rotational eigenfunctions in terms of the rotational matrices is very convenient due to some relevant properties. The conjugation property for the rotation matrices can be written as (Edmonds 1960)

$$\mathcal{D}^J_{M\Omega}(\alpha,\beta,\gamma)^* = (-1)^{M-\Omega}\mathcal{D}^J_{-M-\Omega}(\alpha,\beta,\gamma). \tag{5.3}$$

One of the most useful properties of the rotation matrices for calculating matrix elements of a given operator is the Weyl theorem of the Racah's algebra, which states that the integral of the product of rotational matrices over the Euler angles can be easily calculated as follows (Edmonds 1960):

$$\int_0^{2\pi} d\alpha \int_0^{\pi} d\gamma \int_0^{2\pi} d\beta \sin\beta\, \mathcal{D}^{J_1}_{M_1\Omega_1}(\alpha,\beta,\gamma)\mathcal{D}^{J_2}_{M_2\Omega_2}(\alpha,\beta,\gamma)\mathcal{D}^{J_3}_{M_3\Omega_3}(\alpha,\beta,\gamma) = \\ = 8\pi^2 \begin{pmatrix} J_1 & J_2 & J_3 \\ M_1 & M_2 & M_3 \end{pmatrix} \begin{pmatrix} J_1 & J_2 & J_3 \\ \Omega_1 & \Omega_2 & \Omega_3 \end{pmatrix}, \tag{5.4}$$

where the $\begin{pmatrix} \cdots \\ \cdots \end{pmatrix}$ are the 3-j symbols, which are highly symmetric representations of the Clebsch-Gordan (CG) coefficients (e.g., Edmonds 1960). Another property which can be of interest is

$$\int_0^{2\pi} d\alpha \int_0^{\pi} d\gamma \int_0^{2\pi} d\beta \sin\beta\, \mathcal{D}^{J_1}_{M_1\Omega_1}(\alpha,\beta,\gamma)^*\mathcal{D}^{J_2}_{M_2\Omega_2}(\alpha,\beta,\gamma) = \\ = \frac{8\pi^2}{2J+1}\delta_{J_1J_2}\delta_{M_1M_2}\delta_{\Omega_1\Omega_2}, \tag{5.5}$$

where δ_{ab} is the Kronecker's delta, which is 1 for $a = b$ and zero otherwise.

With the aid of the rotation matrices, it is very easy to transform vectors from one frame to another once the Euler angles between both frames are known. Let's assume that $\vec{r}$ is a vector in $\mathbb{R}^3$, whose spherical components on the laboratory frame are given by r_q, where $q = 0, \pm 1$ (see Edmonds 1960 for the

definition of the spherical components of a tensor). The spherical components of the same vector on the frame fixed to the molecule are denoted by $\bar{r}_q$. The relationship between both components can be written as:

$$r_q = \sum_{q'=0,\pm1} \bar{r}_q \mathcal{D}^1_{q'q}(-\alpha,-\beta,-\gamma) = \sum_{q'=0,\pm1} \bar{r}_q \mathcal{D}^1_{qq'}(\alpha,\beta,\gamma)^*, \tag{5.6}$$

which is of great help in the evaluation of matrix elements of some operators (e.g., the problem of calculating the energy levels for diatomic molecules). We have used the fact that the rotation to carry the molecular fixed frame to the laboratory frame is expressed by the inverse rotation $(-\alpha,-\beta,-\gamma)$.

Finally, the central theorem of angular momentum theory is the Wigner-Eckart (WE) theorem, which allows to calculate the matrix elements of any tensor operator (Edmonds 1960, Brink & Satchler 1968. The WE theorem shows up and takes full advantage of any symmetry that may be inherent in a problem. In other words, it allows us to isolate those parts of a problem that are essentially geometric in character from those which depend explicitly on the physics of the problem. The theorem establishes that, for the q component of a given tensor of order k:

$$\langle JM|T^{(k)}_q|J'M'\rangle = (-1)^{J-M} \begin{pmatrix} J & k & J' \\ -M & q & M' \end{pmatrix} \langle J\|T^{(k)}\|J'\rangle. \tag{5.7}$$

The quantity $\langle J\|T^{(k)}\|J'\rangle$ is called the reduced matrix element. It is important to recognize that it is merely a number, and the fact that it appears as a matrix element is only for notational convenience. A particularly common reduced matrix element involves an angular momentum **J** between its own eigenfunctions. Therefore:

$$\langle J\|J\|J\rangle = \sqrt{J(J+1)(2J+1)} \tag{5.8}$$

5.2 The Molecular Zeeman effect

When a diatomic molecule is in the presence of a magnetic field, the total angular momentum **J** of the molecule can have only certain orientations such that the projection of **J** on an axis along the field direction takes the $2J+1$ possible values:

$$M = J, J-1, \ldots, -J. \tag{5.9}$$

Note that, in the absence of a magnetic field, the previous condition holds for the quantization axis. If the molecule has a magnetic moment, that is, if an interaction between the field and the molecule exists, a precession of **J** takes place at the corresponding angle compatible with its projection **M**. Therefore, **J** looses its meaning as a good quantum number, and only **M** is a constant of motion. Levels with different values of M have slightly different energies if there is a coupling of the magnetic field with the total angular momentum. There are three contributions to the magnetic moment of a diatomic molecule: i) the magnetic moment associated with the orbital and spin angular momenta of the electrons, ii) the magnetic moment produced by the rotational motion of the molecule and iii) the magnetic moments associated with the nuclear spins. The first contribution is of the order of the Bohr magneton ($\mu_0 = eh/4\pi m_e c$), the second and the third are of the order of the nuclear magneton ($\mu_n = eh/4\pi m_p c$), that is, of the order of $m_p/m_e \simeq 1836$ times smaller than the first. Therefore, whenever the orbital or spin angular momenta of the electrons are different from zero (that is, all electronic states except $^1\Sigma$ states) the second and third contributions may in general be neglected.

As for atoms, the selection rule

$$\Delta M = 0, \pm 1 \tag{5.10}$$

holds for dipole radiation, where $\Delta M = 0$ gives rise to spectral line radiation polarized parallel to the field (π components) and $\Delta M = \pm 1$ to polarization perpendicular to the field (σ components), assuming observation perpendicular to the field. The transition $M = 0 \rightarrow M = 0$ is forbidden for $\Delta J = 0$. Note that the selection rule $\Delta J = 0, \pm 1$ still holds.

The Zeeman Hamiltonian for a molecule in the presence of a magnetic field assuming that the main contribution is that coming from the electronic orbital and spin angular momenta can be written as:

$$H_Z = \mu_0 \left(\vec{\mathbf{L}} + 2\vec{\mathbf{S}} \right) \cdot \vec{\mathbf{B}}, \tag{5.11}$$

where $\vec{\mathbf{B}}$ is the magnetic field vector, $\vec{\mathbf{L}}$ is the total electronic orbital angular momentum and $\vec{\mathbf{S}}$ is the total electronic spin.

5.2.1 Zeeman Effect in Hund's case (a) coupling

For simplicity, we choose the z axis of the laboratory frame as that pointing along the magnetic field vector. Because the spherical component of a vector along this z axis is the one with $q = 0$, we can reduce the Zeeman Hamiltonian to:

$$H_Z = \mu_0 \left(\vec{\mathbf{L}} + 2\vec{\mathbf{S}}\right) \cdot \vec{\mathbf{B}} = \mu_0 \left(L_0 + 2S_0\right) B, \tag{5.12}$$

where L_0 and S_0 are the components of the total electronic and spin angular momenta along the z axis, respectively. This Zeeman Hamiltonian can be transformed to use the spherical components of the vectors in the molecular fixed frame by using Eq. (5.6):

$$H_Z = \mu_0 \left(L_0 + 2S_0\right) B = \mu_0 B \sum_{q=0,\pm1} \left(\bar{L}_q + 2\bar{S}_q\right) \mathcal{D}^1_{0q}(\alpha,\beta,\gamma)^*. \tag{5.13}$$

The diagonal matrix element of the Zeeman Hamiltonian can be obtained with the use of the WE theorem (Eq. 5.7) and the property given by Eq. (5.4). Therefore, the energy difference between the magnetic and the non-magnetic case (the magnetic splitting) is obtained by (Herzberg 1950):

$$\Delta E_M = \langle \alpha\Lambda\Sigma; v; \Omega JM | H_Z | \alpha\Lambda\Sigma; v; \Omega JM \rangle = \mu_0 BM \frac{(\Lambda + 2\Sigma)(\Lambda + \Sigma)}{J(J+1)}, \tag{5.14}$$

for a given magnetic field and a given electronic state (defined by the quantum numbers) in Hund's (a) coupling case. In similarity with the atomic case, the splitting of a given level is parameterized in terms of the Landé factor g_L, defined as $\Delta E_M = \mu_0 BM g_L$. Therefore, for electronic levels which are in Hund's case (a), the Landé factor is:

$$g_L = \frac{(\Lambda + 2\Sigma)(\Lambda + \Sigma)}{J(J+1)}. \tag{5.15}$$

The maximum splitting due to the magnetic field (for $M = \pm J$) decreases inversely proportional to $J + 1$. Since the number of sublevels increases as $2J + 1$, sublevels start to be very close in energy for moderately low J. Given that the total angular momentum in a molecule is a contribution from the total electronic angular momentum and the rotational angular momentum, J is usually higher for molecules than for atoms. Therefore, the Landé factor of the

levels of the transitions which are observed are usually smaller for molecules than for atoms. Concerning the sign of the effective Landé factor, it can be shown that $g_L < 0$ provided that $-\Lambda < \Sigma < -\Lambda/2$ when $\Lambda > 0$.

The effect of the magnetic field on the observable spectrum is produced by the appearance of components for each rotational line that, for the zero-field case, have no substructure. This substructure is produced by the permitted transitions (following the selection rules) between the magnetic sublevels of each rotational level. The relative strength of each component $S_q^{JJ'}(M, M')$ can be calculated by evaluating the matrix elements of the electric dipole between the eigenfunctions of the upper and lower level of the transition and taking only the part of the matrix element which depends on the M quantum number:

$$S_q^{JJ'}(M, M') = 3 \begin{pmatrix} J' & 1 & J \\ M' & -q & -M \end{pmatrix}^2, \tag{5.16}$$

where $q = 0, \pm 1$ and $S_q^{JJ'}(M, M')$ is normalized to unity:

$$\sum_{MM'} S_q^{JJ'}(M, M') = 1. \tag{5.17}$$

5.2.2 Zeeman Effect in Hund's case (b) coupling

In this case, it is obviously more convenient to use the eigenfunctions of the Hund's coupling case (b). These eigenfunctions are labeled by the good quantum numbers of this case (Judd 1975):

$$|\alpha\Lambda; v; NSJM\rangle \equiv |\alpha\Lambda\rangle|v\rangle|NSJM\rangle. \tag{5.18}$$

If we calculate the diagonal matrix element of the Zeeman Hamiltonian, we obtain a formula similar to that obtained in case (a), but where the Landé factor is now:

$$g_L = \frac{J(J+1) + S(S+1) - N(N+1)}{J(J+1)} + \frac{\Lambda^2 \left[J(J+1) + N(N+1) - S(S+1)\right]}{2J(J+1)N(N+1)}. \tag{5.19}$$

It is clear that the Landé factor can take negative values depending on the combination of quantum numbers of the level. For example, for a doublet state

$S = 1/2$ in which J can take values $J = N \pm 1/2$, the Landé factor is positive for $J = N + 1/2$ and negative for $J = N - 1/2$ (as long as $N > \Lambda$).

The relative strength of each Zeeman component is obtained, as in case (a), by evaluating the matrix elements of the electric dipole operator and retaining the term which depends on the M quantum number. The result is again:

$$S_q^{JJ'}(M, M') = 3 \begin{pmatrix} J' & 1 & J \\ M' & -q & -M \end{pmatrix}^2, \tag{5.20}$$

where the strength is normalized to unity, as indicated in Eq. (5.17).

5.2.3 Zeeman Effect in Hund's (a)-(b) intermediate coupling for doublets

As we have seen in Section §2.5.2, a transition between Hund's cases (a) and (b) occurs when rotation increases (spin-uncoupling) because the spin uncouples from the internuclear axis and couples to the rotation. A simple Hamiltonian in this case includes the rotational Hamiltonian and the spin-orbit coupling term, together with the Zeeman Hamiltonian:

$$H = H_{\rm SO} + H_{\rm rot} + H_Z. \tag{5.21}$$

The first two terms constitute the Hamiltonian of a molecule in the intermediate state between Hund's cases (a) and (b). The strength of the spin-orbit interaction is included in the *spin-orbit constant* A which is introduced in Eq. (5.23). The last term is included as a perturbation to the first two terms. This study was done first by Hill (1929) for doublet terms. However, it was difficult to obtain analytical expressions for the strength of the Zeeman components due to Hill's choice of Hund's case (b) basis functions. Much later, Schadee (1978) repeated Hill's calculations for doublet states for arbitrary spin-orbit and spin-rotation interactions (spin-rotation is included for those states with $\Lambda = 0$ for which the spin-orbit coupling is zero), but using Hund's case (a) basis functions. The formulas for the calculation of the splittings and the strength of each of the Zeeman components are all given in Schadee (1978) and we will not reproduce them here. Since the matrix elements of the electric dipole operator are quite simple to obtain using the eigenfunctions of case (a) (given by Eq. 5.16), the strength of the Zeeman components can be obtained in a much easier way.

Recently, Berdyugina & Solanki (2002) have described the perturbation calculation of the molecular Zeeman effect for the intermediate case (a)-(b) for terms of any multiplicity. The Zeeman splittings and strengths of the components are obtained by numerical diagonalization of a 2×2 Hamiltonian.

5.3 General Description of the Zeeman Effect for Diatomic Molecules

All the cases we have described so far are simplifications of the motion of a molecule in order to obtain closed analytical formulas for the energy of the molecular levels. To give a better description of the motion of the molecule one has to include more terms in the Hamiltonian. Therefore, it turns out impossible to find out closed and simple analytical formulas for the energy levels, including the splittings and the strength of the Zeeman components. In this section, we describe the work we have done for developing a very general scheme for obtaining the splittings and strengths of the Zeeman components for a given molecular level including many of the possible couplings which can take place in a molecule. The advantage of this approach is that it allows a very accurate description of the energy levels. Furthermore, any of the terms in the Hamiltonian can be neglected to see how the energy levels are affected by its inclusion. Another important advantage is that the eigenfunctions of each molecular level are obtained self-consistently, therefore the expected value of any operator can be evaluated quite easily for each level or transition between levels.

5.3.1 Molecular Hamiltonian

Consider a diatomic molecule in a given electronic, vibrational and rotational state. We work within the framework of the Born-Oppenheimer approximation, so the rotational energy is considered as an additive energy to the electronic and vibrational energies. However, we consider the coupling between the electronic state and the rotational motion. A very general *effective Hamiltonian* for such a diatomic molecule in a magnetic field can be written as (see, e.g., Brown & Carrington 2003):

$$H_{\rm eff} = H_{\rm SO} + H_{\rm rot} + H_{\rm cd} + H_{\rm sr} + H_{\rm LD} + H_{\rm cdLD} + H_{\rm hfs} + H_{\rm cdhfs} + H_Z. \quad (5.22)$$

$H_{\rm SO}$ represents the spin-orbit coupling, $H_{\rm rot}$ and $H_{\rm cd}$ represent the rotational kinetic energy and centrifugal distortion, respectively, $H_{\rm sr}$ represents the spin-rotation interaction, $H_{\rm LD}$ and $H_{\rm cdLD}$ represent the Λ-doubling interactions and the appropriate centrifugal distortion corrections, respectively. $H_{\rm hfs}$ represents the magnetic hyperfine interactions and $H_{\rm cdhfs}$ the centrifugal distortion of the hyperfine interactions as the molecule rotates. Finally, H_Z represents the Zeeman hamiltonian which includes the coupling between the magnetic field and the rotation angular momentum, the total spin and the total angular momenta.

Each of the terms of the Hamiltonian can be written in terms of the different angular momenta of the molecule. These terms are written using the tensorial notation (see, for example, Edmonds 1960 or Brink & Satchler 1968) with a slight variation. The symbol $T^k_q(\mathbf{A})$ is used to indicate that we are referring to the q spherical component of the tensor $\mathbf{A}$ of order k on the molecular fixed frame. For the spherical component of the tensor on the laboratory frame, we will use $T^k_p(\mathbf{A})$. Since we are only dealing with the angular momenta vectors, $k = 1$ is the only value for k we will use. The explicit forms of the most important terms which are appropriate for a later calculation of the matrix elements on the Hund's case (a) basis set are as follows:

$$H_{\rm SO} = AT^1_{q=0}(\mathbf{L})T^1_{q=0}(\mathbf{S}) + \frac{1}{2}A_D\left[\mathbf{R}^2T^1_{q=0}(\mathbf{L})T^1_{q=0}(\mathbf{S}) + T^1_{q=0}(\mathbf{L})T^1_{q=0}(\mathbf{S})\mathbf{R}^2\right], \tag{5.23}$$

where A and A_D are the spin-orbit coupling constant and the centrifugal correction to A, respectively. The rotational Hamiltonian can be written as:

$$H_{\rm rot} = BT^1(\mathbf{R})\cdot T^1(\mathbf{R}) \equiv B\mathbf{R}^2, \tag{5.24}$$

where B is the rotational constant. The centrifugal distortion term can be written:

$$H_{\rm cd} = -D(\mathbf{R}^2)^2 + H(\mathbf{R}^2)^3, \tag{5.25}$$

where D and H are the quartic and sextic distortion constants. Finally, the spin-rotation Hamiltonian can be written as the dot product between the rotational angular momentum and the spin:

$$H_{\rm sr} = \gamma T^1(\mathbf{J}-\mathbf{S})\cdot T^1(\mathbf{S}), \tag{5.26}$$

where γ is the spin-rotation coupling constant. The rest of terms of the effective Hamiltonian can be obtained in the same manner. See Brown et al. (1978) and

Brown & Carrington (2003) for the exact analytical expressions for each of the terms included in the effective Hamiltonian. The eigenvalues of a linear molecule are obtained by diagonalization of the effective Hamiltonian assuming that $T^1_{q=0}(\mathbf{R}) = 0$, i.e., that there is no rotation about the internuclear axis. This leads to helpful simplification of the matrix elements of the Hamiltonian, especially those in which the rotational angular momentum $\mathbf{R}$ appears.

When the molecule is under the action of a magnetic field $\mathbf{B}$, a splitting occurs due to the precession of the total angular momentum $\mathbf{J}$ about the quantization axis (which is selected as the z axis in the laboratory frame, equivalent to the direction on the magnetic field). The effective Hamiltonian for a diatomic molecule can be written as:

$$H_{\mathrm{Z}} = g_S\mu_0 T^1(\mathbf{B})\cdot T^1(\mathbf{S}) + g_L\mu_0 T^1(\mathbf{B})\cdot T^1(\mathbf{L}) - g_r\mu_0 T^1(\mathbf{B})\cdot T^1(\mathbf{J}-\mathbf{L}-\mathbf{S}), \quad (5.27)$$

where μ_0 is the Bohr magneton, B is the magnetic field strength, g_S is the electron spin g-factor, g_L is the electron orbital g-factor and g_r is the rotational g-factor (including the nuclear and electronic contribution $g_r = g_r^{\mathrm{nuclear}} - g_r^e$). As pointed out, the last term is only relevant when the molecule is in a $^1\Sigma$ state, because then there is no contribution from the electronic motion to the Zeeman effect (e.g. the ground state of CO). More terms can be included in the Zeeman Hamiltonian which take into account several higher order corrections (anisotropic corrections to the electron spin g-factor, nuclear spin, ...). Since we have selected the z quantization axis as the field direction, the dot product between the magnetic field vector and the angular momenta give their projection over this axis. Therefore, we end up with the spherical components of the vectors along the z axis of the laboratory frame:

$$H_{\mathrm{Z}} = g_S\mu_0 B T^1_{p=0}(\mathbf{S}) + g_L\mu_0 B T^1_{p=0}(\mathbf{L}) - g_r\mu_0 B T^1_{p=0}(\mathbf{J}-\mathbf{L}-\mathbf{S}). \quad (5.28)$$

The value of the g-factors have to be determined by fitting this effective Hamiltonian to the laboratory observed molecular spectra under the presence of a magnetic field. However, it is a very good approximation to consider $g_S = 2$ and $g_L = 1$. The nuclear contribution to the rotational g-factor for a diatomic molecule formed by two nuclei A and B can be very roughly estimated by the following formula (Judd 1975):

$$g_r^{\mathrm{nuclear}} \simeq \frac{\mu_0}{\mu_n}\frac{\left(Z_A M_B^2 + Z_B M_A^2\right)}{M_A M_B\left(M_A + M_B\right)}, \quad (5.29)$$

where M_A and M_B are the masses of each nuclei in atomic mass units and Z_A and Z_B are the atomic number of each nuclei. It is usual that high order effects are important, and this estimation of $g_r^{\rm nuclear}$ is not very suitable. For example, for the OH molecule, $g_r^{\rm nuclear} \simeq 5.25 \times 10^{-4}$ while the exact value is $g_r = -6.33 \times 10^{-4}$ (Brown et al. 1978). Therefore, we see that the contribution of the electrons to the rotational g-factor is extremely important, being $g_r^e = 1.16 \times 10^{-3}$.

5.3.2 Matrix Elements

In order to obtain the energy levels of a diatomic molecule, the effective Hamiltonian matrix ($H_{\rm eff}$) has to be built and then numerically diagonalized. We have chosen to express the matrix elements of the molecular Hamiltonian in Hund's case (a) basis set because it makes it easier to calculate the effect of the various operators which appear in $H_{\rm eff}$.

The basis set of Hund's case (a) is given by Eq. (5.1). In order to calculate the matrix elements of the Hamiltonian, we express the rotational eigenfunctions with their explicit form given by Eq. (5.2) which contains the rotation matrix. The bras of the matrix elements are obtained by complex conjugation of the rotation matrices and transformed with the help of the conjugation property Eq. (5.3). All the tensors should be evaluated on the molecular fixed frame because their eigenvalues are known in case (a). If the components of a tensor on the laboratory frame appear on the Hamiltonian (as happens in the Zeeman Hamiltonian), a transformation to the molecular fixed frame is performed through Eq. (5.6). We often end up with a product of three rotation matrices for the evaluation of the matrix element, which is easily calculated using Weyl's theorem given by Eq. (5.4). Some matrix elements can be calculated with the aid of the Wigner-Eckart theorem given by Eq. (5.7). Therefore, we can give simple analytical expressions for the matrix elements of each term of the Hamiltonian [1].

[1] A rigorous explanation of the techniques for obtaining the matrix elements of the effective Hamiltonian can be found on Brown & Carrington (2003)

Spin-orbit coupling

$$\langle \Lambda S \Sigma \Omega J M | H_{\mathrm{SO}} | \Lambda S \Sigma \Omega J M \rangle = A\Lambda\Sigma + A_D \Lambda\Sigma \left[J(J+1) - \Omega^2 + S(S+1) - \Sigma^2 \right], \tag{5.30}$$

Rotational Hamiltonian

$$\begin{aligned} \langle \Lambda S \Sigma' \Omega' J M | H_{\mathrm{rot}} | \Lambda S \Sigma \Omega J M \rangle = & \\ & B \delta_{\Sigma'\Sigma} \delta_{\Omega'\Omega} \left[J(J+1) - \Omega^2 + S(S+1) - \Sigma^2 + \langle L_x^2 + L_y^2 \rangle \right] \\ & - 2B \sum_{q=\pm 1} (-1)^{J-\Omega'+S-\Sigma'} \begin{pmatrix} J & 1 & J \\ -\Omega' & q & \Omega \end{pmatrix} \begin{pmatrix} S & 1 & S \\ -\Sigma' & q & \Sigma \end{pmatrix} \\ & \times \sqrt{J(J+1)(2J+1)S(S+1)(2S+1)}. \end{aligned} \tag{5.31}$$

Centrifugal distortion of order 4 in the rotation

$$\begin{aligned} \langle \Lambda S \Sigma' \Omega' J M | H_{\mathrm{cd}}^{(4)} | \Lambda S \Sigma \Omega J M \rangle = & \\ & - D \delta_{\Sigma'\Sigma} \delta_{\Omega'\Omega} \left[J(J+1) - \Omega^2 + S(S+1) - \Sigma^2 \right]^2 \\ & + 4D \delta_{\Sigma'\Sigma} \delta_{\Omega'\Omega} \sum_{q=\pm 1} \sum_{\Omega'' \Sigma''} \begin{pmatrix} J & 1 & J \\ -\Omega & q & \Omega'' \end{pmatrix}^2 \begin{pmatrix} S & 1 & S \\ -\Sigma & q & \Sigma'' \end{pmatrix}^2 \\ & \times J(J+1)(2J+1)S(S+1)(2S+1) - 2D \sum_{q=\pm 1} (-1)^{J-\Omega'+S-\Sigma'} \\ & \times \begin{pmatrix} J & 1 & J \\ -\Omega' & q & \Omega \end{pmatrix} \begin{pmatrix} S & 1 & S \\ -\Sigma' & q & \Sigma \end{pmatrix} \\ & \times \sqrt{J(J+1)(2J+1)S(S+1)(2S+1)} \\ & \times \left[2J(J+1) - \Omega^2 - (\Omega')^2 + 2S(S+1) - \Sigma^2 - (\Sigma')^2 \right]. \end{aligned} \tag{5.32}$$

Centrifugal distortion of order 6 in the rotation

$$
\begin{aligned}
&\langle \Lambda S \Sigma' \Omega' J M | H_{\rm cd}^{(6)} | \Lambda S \Sigma \Omega J M \rangle = \\
&H \delta_{\Sigma'\Sigma} \delta_{\Omega'\Omega} \left[J(J+1) - \Omega^2 + S(S+1) - \Sigma^2 \right]^3 \\
&+ 4H \delta_{\Sigma'\Sigma} \delta_{\Omega'\Omega} \sum_{q=\pm 1} \sum_{\Omega''\Sigma''} \begin{pmatrix} J & 1 & J \\ -\Omega & q & \Omega'' \end{pmatrix}^2 \begin{pmatrix} S & 1 & S \\ -\Sigma & q & \Sigma'' \end{pmatrix}^2 \times \\
&\times J(J+1)(2J+1) S(S+1)(2S+1) \\
&\times \left[3J(J+1) - 2\Omega^2 - (\Omega'')^2 + 3S(S+1) - 2\Sigma^2 - (\Sigma'')^2 \right] \\
&- 2H \sum_{q=\pm 1} (-1)^{J-\Omega'+S-\Sigma'} \begin{pmatrix} J & 1 & J \\ -\Omega' & q & \Omega \end{pmatrix} \begin{pmatrix} S & 1 & S \\ -\Sigma' & q & \Sigma \end{pmatrix} \\
&\times \sqrt{J(J+1)(2J+1)S(S+1)(2S+1)} \Bigg[\left[J(J+1) - \Omega^2 + S(S+1) - \Sigma^2 \right]^2 \\
&+ \left[J(J+1) - (\Omega')^2 + S(S+1) - (\Sigma')^2 \right]^2 \\
&+ \left[J(J+1) - \Omega^2 + S(S+1) - \Sigma^2 \right] \left[J(J+1) - (\Omega')^2 + S(S+1) - (\Sigma')^2 \right] \\
&+ 4 \begin{pmatrix} J & 1 & J \\ -\Omega' & q & \Omega \end{pmatrix}^2 \begin{pmatrix} S & 1 & S \\ -\Sigma' & q & \Sigma \end{pmatrix}^2 J(J+1)(2J+1)S(S+1)(2S+1) \Bigg]
\end{aligned}
\tag{5.33}
$$

Spin-rotation interaction

$$
\begin{aligned}
&\langle \Lambda S \Sigma' \Omega' J M | H_{\rm sr} | \Lambda S \Sigma \Omega J M \rangle = \\
&\gamma \delta_{\Sigma'\Sigma} \delta_{\Omega'\Omega} \left[\Omega\Sigma - S(S+1) \right] + \sum_{q=\pm 1} (-1)^{J-\Omega'+S-\Sigma'} \\
&\times \begin{pmatrix} J & 1 & J \\ -\Omega' & q & \Omega \end{pmatrix} \begin{pmatrix} S & 1 & S \\ -\Sigma' & q & \Sigma \end{pmatrix} \sqrt{J(J+1)(2J+1)S(S+1)(2S+1)}
\end{aligned}
\tag{5.34}
$$

Zeeman Hamiltonian

$$\langle \Lambda S \Sigma' J' M_J \Omega' | H_Z | \Lambda S \Sigma J M_J \Omega \rangle =$$
$$\mu_B B_0 \sum_{q=0,\pm 1} (-1)^{2J'-M-\Omega'} \left[(2J'+1)(2J+1)\right]^{1/2}$$
$$\begin{pmatrix} J' & 1 & J \\ -M & 0 & M \end{pmatrix} \begin{pmatrix} J' & 1 & J \\ -\Omega' & q & \Omega \end{pmatrix} \Bigg[(g_L + g_r)\Lambda \delta_{\Sigma\Sigma'} + (g_S + g_r)(-1)^{S-\Sigma'}$$
$$\times \begin{pmatrix} S & 1 & S \\ -\Sigma' & q & \Sigma \end{pmatrix} \left[S(S+1)(2S+1)\right]^{1/2} \Bigg] - g_r \mu_B B_0 M \delta_{JJ'} \delta_{\Sigma\Sigma'} \delta_{\Omega\Omega'} \tag{5.35}$$

5.3.3 Diagonalization

We have explicitly indicated that the matrix elements are diagonal in some of the eigenvalues which are included in the case (a) eigenfunctions. For example, the spin-orbit coupling is completely diagonal in the case (a) basis set, the molecular rotation is diagonal in Λ, S, J and M, but not in Σ and Ω, while the Zeeman interaction is diagonal only in Λ, S and M (J looses its meaning as a good quantum number and only M is still a good quantum number). Our basis set is built using the following rules:

- We include eigenfunctions with the two possible values of the projection of the orbital angular momentum on the internuclear axis Λ, i.e., $\pm\Lambda$. Since we do not include any Λ-doubling interaction, the eigenvalues corresponding to both values of Λ are degenerated.
- We include eigenfunctions with the two possible values of the projection of the spin on the internuclear axis Σ, i.e., $\pm\Sigma$.
- For a given value of J, we include eigenfunctions from the level J and from the levels with surrounding values of J, i.e., $J-1$ and $J+1$. This rule is only applied when a magnetic field is present since the Zeeman Hamiltonian is the only term included in the effective Hamiltonian which is non-diagonal in the quantum number J (therefore J is no more a good quantum number). If no magnetic field is present, all the terms are diagonal in J and no coupling between levels with different value of J is possible.

- For each value of J, we include all the possible values of M from $-J$ to J. We pointed out that the Hamiltonian is always diagonal in M unless the hyperfine structure is taken into account.

The total number of eigenfunctions is obtained by summing all the possible values of the quantum numbers: 2 possible values of Λ, $2S+1$ possible values of Σ and the $2J+1$ values of M for each value of J. Therefore,

$$\mathcal{N} = 2(2S{+}1)\Big[[2J{+}1]{+}\big[2(J{+}1){+}1\big]{+}\big[2(J{-}1){+}1\big]\Big] = 6(2S{+}1)(2J{+}1) \quad (5.36)$$

As an example, the eigenfunctions we use for the calculation of the energies of a rotational level J of a $^2\Pi$ electronic state are $|1, 1/2, 1/2; 3/2, J', M\rangle$, $|1, 1/2, -1/2; 1/2, J', M\rangle$, $|-1, 1/2, -1/2; 3/2, J', M\rangle$ and $|-1, 1/2, -1/2; -3/2, J', M\rangle$. This subset of four eigenfunctions is included for each value of J' in $J' = J-1, J, J+1$ and the values of M for each value of J. The total number of eigenfunctions is $\mathcal{N} = 24J + 12$, which is quite a big number for high values of J.

With the help of these eigenfunctions, the Hamiltonian can be built. It is a $N \times N$ matrix which must be numerically diagonalized using any of the available numerical procedures (see, e.g., Press et al. 1986). The size of the matrix increases linearly with the value of J and it represents a very hard numerical work even for low values of J. However, we can use the fact that the Hamiltonian is diagonal in M to perform the diagonalizations in boxes with the same value of M. The problem is transformed from the diagonalization of the whole matrix to diagonalizing $2J+1$ submatrices of size $6(2S+1)$. For the example case of a $^2\Pi$ level, we should diagonalize $2J+1$ boxes of 12×12.

5.4 Scattering polarization and the Hanle effect

The Zeeman effect requires the presence of a magnetic field, which causes the atomic energy levels to split into different magnetic sublevels characterized by their magnetic quantum number M. The Zeeman splitting produces local sources and sinks of light polarization because of the wavelength shift between the π and σ components.

In contrast, the spectral line polarization that is induced by scattering processes in the outer layers of stellar atmospheres is directly related with the

	$\langle 3\ 3\|$	$\langle 3\ 2\|$	$\langle 3\ 1\|$	$\langle 3\ 0\|$	$\langle 3\ -1\|$	$\langle 3\ -2\|$	$\langle 3\ -3\|$	$\langle 2\ 2\|$	$\langle 2\ 1\|$	$\langle 2\ 0\|$	$\langle 2\ -1\|$	$\langle 2\ -2\|$	$\langle 1\ 1\|$	$\langle 1\ 0\|$	$\langle 1\ -1\|$
$\|3\ 3\rangle$	×	0	0	0	0	0	0	0	0	0	0	0	0	0	0
$\|3\ 2\rangle$	0	×	0	0	0	0	0	×	0	0	0	0	0	0	0
$\|3\ 1\rangle$	0	0	×	0	0	0	0	0	×	0	0	0	×	0	0
$\|3\ 0\rangle$	0	0	0	×	0	0	0	0	0	×	0	0	0	×	0
$\|3\ -1\rangle$	0	0	0	0	×	0	0	0	0	0	×	0	0	0	×
$\|3\ -2\rangle$	0	0	0	0	0	×	0	0	0	0	0	×	0	0	0
$\|3\ -3\rangle$	0	0	0	0	0	0	×	0	0	0	0	0	0	0	0
$\|2\ 2\rangle$	0	×	0	0	0	0	0	×	0	0	0	0	0	0	0
$\|2\ 1\rangle$	0	0	×	0	0	0	0	0	×	0	0	0	×	0	0
$\|2\ 0\rangle$	0	0	0	×	0	0	0	0	0	×	0	0	0	×	0
$\|2\ -1\rangle$	0	0	0	0	×	0	0	0	0	0	×	0	0	0	×
$\|2\ -2\rangle$	0	0	0	0	0	×	0	0	0	0	0	×	0	0	0
$\|1\ 1\rangle$	0	0	×	0	0	0	0	0	×	0	0	0	×	0	0
$\|1\ 0\rangle$	0	0	0	×	0	0	0	0	0	×	0	0	0	×	0
$\|1\ -1\rangle$	0	0	0	0	×	0	0	0	0	0	×	0	0	0	×

Table 5.1: Part of the Hamiltonian matrix for a level with $J = 2$ indicating with the symbol $\times$ the elements which can be non-zero. The eigenfunctions are of the form $|JM\rangle$. The basis set is ordered by the value of J and the resulting matrix is extremely non-diagonal.

	$\langle 3\ 3\|$	$\langle 3\ 2\|$	$\langle 2\ 2\|$	$\langle 3\ 1\|$	$\langle 2\ 1\|$	$\langle 1\ 1\|$	$\langle 3\ 0\|$	$\langle 2\ 0\|$	$\langle 1\ 0\|$	$\langle 3\ -1\|$	$\langle 2\ -1\|$	$\langle 1\ -1\|$	$\langle 3\ -2\|$	$\langle 2\ -2\|$	$\langle 3\ -3\|$
$\|3\ 3\rangle$	×	0	0	0	0	0	0	0	0	0	0	0	0	0	0
$\|3\ 2\rangle$	0	×	×	0	0	0	0	0	0	0	0	0	0	0	0
$\|2\ 2\rangle$	0	×	×	0	0	0	0	0	0	0	0	0	0	0	0
$\|3\ 1\rangle$	0	0	0	×	×	×	0	0	0	0	0	0	0	0	0
$\|2\ 1\rangle$	0	0	0	×	×	×	0	0	0	0	0	0	0	0	0
$\|1\ 1\rangle$	0	0	0	×	×	×	0	0	0	0	0	0	0	0	0
$\|3\ 0\rangle$	0	0	0	0	0	0	×	×	×	0	0	0	0	0	0
$\|2\ 0\rangle$	0	0	0	0	0	0	×	×	×	0	0	0	0	0	0
$\|1\ 0\rangle$	0	0	0	0	0	0	×	×	×	0	0	0	0	0	0
$\|3-1\rangle$	0	0	0	0	0	0	0	0	0	×	×	×	0	0	0
$\|2-1\rangle$	0	0	0	0	0	0	0	0	0	×	×	×	0	0	0
$\|1-1\rangle$	0	0	0	0	0	0	0	0	0	×	×	×	0	0	0
$\|3-2\rangle$	0	0	0	0	0	0	0	0	0	0	0	0	×	×	0
$\|2-2\rangle$	0	0	0	0	0	0	0	0	0	0	0	0	×	×	0
$\|3-3\rangle$	0	0	0	0	0	0	0	0	0	0	0	0	0	0	×

Table 5.2: Part of the Hamiltonian matrix for a level with $J = 2$ indicating with the symbol $\times$ the elements which can be non-zero. The basis set is ordered by the value of M and the resulting matrix is block-diagonal, therefore allowing a block diagonalization in each of the subspaces spanned by the eigenfunctions with the same value of M.

anisotropic illumination of the atoms or molecules (see the review by Trujillo Bueno 2001). Anisotropic radiation pumping produces atomic level polarization (i.e. population imbalances and quantum interferences between the sublevels of degenerate energy levels). For example, upper-level population pumping occurs when some upper state sublevels have more chance of being populated than others. On the contrary, lower level population pumping occurs when some lower state sublevels absorb light more strongly than others. As a result, an excess population tends to build up in the weakly absorbing sublevels. It is also important to note that atomic polarization can be transferred between energy levels via a process called repopulation pumping.

The presence of a magnetic field is not necessary for the operation of such optical pumping processes, which can create atomic polarization if the depolarization rates due to elastic collisions are sufficiently low. The Hanle effect (Hanle 1924; Moruzzi & Strumia 1991; Trujillo Bueno 2001) is the modification of the atomic level polarization (and of the ensuing observable Stokes parameters) caused by the action of a magnetic field such that the corresponding Zeeman splitting is comparable to the inverse lifetime of the degenerate level under consideration. For the Hanle effect to operate, the magnetic field vector must be significantly inclined with respect to the axis of symmetry of the radiation field.

A useful formula to estimate the magnetic field intensity $B_{\rm H}$ (in gauss) to which the Hanle effect can, in principle, be sensitive is

$$2\pi\nu_L g_L = 8.79\times10^6 B_{\rm H} g_L \simeq 1/t_{\rm life}, \tag{5.37}$$

where ν_L is the Larmor frequency (the frequency associated with the magnetic field), while g_L and $t_{\rm life}$ are the Landé factor and the lifetime (in seconds) of the level under consideration, respectively. As a very good approximation, the inverse of the lifetime of a level is similar to the spontaneous emission Einstein coefficient A_{ul} for the upper level of a transition and to the absorption Einstein coefficient times the radiation field ,$B_{lu}\bar{J}$, for the lower level of a transition. Therefore, for typical values of the Einstein coefficient for spontaneous emission (i.e., between 10^4-10^8 s^{-1}), we can diagnose, in principle, fields between 10^{-3} and 100 gauss, assuming g_L for the Landé factor.

5.4.1 Radiative Transfer Equation

In the polarized case, instead of the standard scalar radiative transfer equation for the specific intensity $I_\nu(\mathbf{\Omega})$, one has to solve, in general, the following *vectorial* transfer equation for the Stokes vector $\mathbf{I}_\nu(\mathbf{\Omega}) = (I, Q, U, V)^\dagger$ (where $\dagger$ means the transpose):

$$\frac{d}{ds}\begin{pmatrix} I \\ Q \\ U \\ V \end{pmatrix} = \begin{pmatrix} \epsilon_I \\ \epsilon_Q \\ \epsilon_U \\ \epsilon_V \end{pmatrix} - \begin{pmatrix} \eta_I & \eta_Q & \eta_U & \eta_V \\ \eta_Q & \eta_I & \rho_V & -\rho_U \\ \eta_U & -\rho_V & \eta_I & \rho_Q \\ \eta_V & \rho_U & -\rho_Q & \eta_I \end{pmatrix} \begin{pmatrix} I \\ Q \\ U \\ V \end{pmatrix}. \tag{5.38}$$

This equation, whose Quantum Electrodynamics (QED) derivation can be found in Landi Degl'Innocenti (1983), can be written in more compact notation as follows:

$$\frac{d}{ds}\mathbf{I} = \mathbf{j} - \mathbf{K}\mathbf{I}, \tag{5.39}$$

where s measures the geometrical distance along the ray of direction $\mathbf{\Omega}$, $\mathbf{K}$ is the absorption matrix and $\mathbf{j}$ is the emission vector. Trujillo Bueno (2003c) discusses efficient numerical methods for the formal solution of this Stokes-vector equation.

5.4.2 The rate equations for the elements of the atomic density matrix

The concept of overall population of each level of total angular momentum J is not enough to describe the excitation state of a polarized atomic or molecular system. In general, one has to use the density operator $\rho^{\rm A}$ of quantum mechanics (e.g. Fano 1957). This operator is represented in the basis of eigenfunctions of the total angular momentum as a matrix called the atomic density matrix whose $(2J+1)^2$ elements are:

$$\rho^{\rm A}_{\alpha J}(M, M') = \langle \alpha J M | \rho^{\rm A} | \alpha J M' \rangle, \tag{5.40}$$

where $\rho^{\rm A}_{\alpha J}(M, M)$ is the population of the sublevel with magnetic quantum number M, while $\rho^{\rm A}_{\alpha J}(M, M')$ represents the degree of quantum interference (or coherence) between the sublevels M and M'.

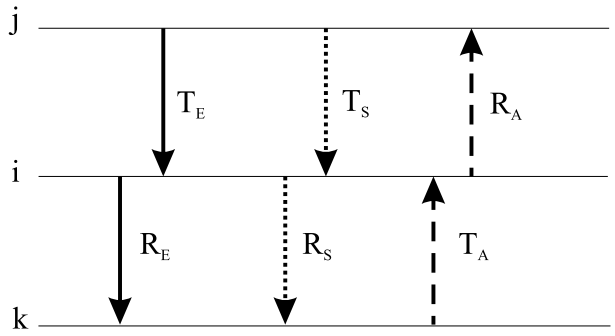

Figure 5.1: Radiative processes included in the statistical equilibrium equations of a given level i given by Eq. (5.42). j and k are generic upper and lower levels, respectively. In solid lines we represent the spontaneous emissions, in dashed lines the absorption processes and in dotted line the stimulated emission processes.

In the context of scattering polarization and the Hanle effect it is more convenient to quantify the atomic polarization of a given level by means of the spherical statistical tensor components:

$$\rho^K_Q(\alpha, J) = \sum_{MM'} (-1)^{J-M} \sqrt{2K+1} \begin{pmatrix} J & J & K \\ M & -M' & Q \end{pmatrix} \rho^{\rm A}_{\alpha J}(M, M'), \quad (5.41)$$

where the sum is extended over the possible values of M according to the value of the total angular momentum J. It is important to note that $0 \leq K \leq 2J$ and $-K \leq Q \leq K$. The ρ^K_Q with $Q = 0$ are real numbers given by linear combinations of the populations of the Zeeman sublevels. The total population of the level is quantified by $\sqrt{2J+1}\rho^0_0$, while the population imbalances among the Zeeman sublevels are quantified by ρ^K_0 (e.g. $\rho^2_0(J=1) = (N_1 - 2N_0 + N_{-1})/\sqrt{6}$). However, the ρ^K_Q elements with $Q \neq 0$ are, in general, complex numbers given by linear combinations of the coherences between the Zeeman sublevels whose magnetic quantum numbers differ by Q. Since the density operator is Hermitian, we have that for each spherical statistical tensor component ρ^K_Q with $Q > 0$, there exists another component with $Q < 0$ which fulfill $\rho^K_{-Q} = (-1)^Q [\rho^K_Q]^*$. As a matter of notation, the ρ^2_Q are usually called the alignment components while the ρ^1_Q are usually called the orientation components.

For the case of a multilevel atom without hyperfine structure and taking into account quantum coherences only between the sublevels with the same J,

the rate of change of the density matrix element $\rho^K_Q(J)$ in the magnetic field reference frame[2] reads (Landi Degl'Innocenti 1983):

$$\begin{aligned}
\frac{d}{dt}\rho^K_Q(J) &= -2\pi \mathrm{i}\nu_L g_L Q \rho^K_Q(J) + \sum_{J_l}\sum_{K_lQ_l} \rho^{K_l}_{Q_l}(J_l) T_{\mathrm{A}}(J_l; K_lQ_l \rightarrow J; KQ) \\
&+ \sum_{J_u}\sum_{K_uQ_u} \rho^{K_u}_{Q_u}(J_u) T_{\mathrm{E}}(J_u; K_uQ_u \rightarrow J; KQ) \\
&+ \sum_{J_u}\sum_{K_uQ_u} \rho^{K_u}_{Q_u}(J_u) T_{\mathrm{S}}(J_u; K_uQ_u \rightarrow J; KQ) \\
&- \sum_{K'Q'} \rho^{K'}_{Q'}(J) R_{\mathrm{A}}(J; KQ, K'Q' \rightarrow J_u) - \sum_{K'Q'} \rho^{K'}_{Q'}(J) R_{\mathrm{E}}(J; KQ, K'Q' \rightarrow J_l) \\
&- \sum_{K'Q'} \rho^{K'}_{Q'}(J) R_{\mathrm{S}}(J; KQ, K'Q' \rightarrow J_l) - D^{(K)}(J)\rho^K_Q(J).
\end{aligned}$$

This equation indicates that, in the magnetic field reference frame, the population imbalances (i.e. the ρ^K_0) are insensitive to the magnetic field, while the coherences (i.e. the ρ^K_Q with $Q \neq 0$) are changed and dephased as the magnetic field increases.

The last term of the equation is the contribution of elastic collisions to the rate of change of $\rho^K_Q(J)$ since $D^{(K)}$ is the depolarizing collisional rate for the density matrix element of rank K. This equation does not include the inelastic collisional rates (we are assuming that the problem is radiation-dominated), although, if available, they can be included (see, e.g., Manso Sainz & Trujillo Bueno 2003). A representation of the radiative rates which must be considered for obtaining the density matrix elements of a level i is shown in Fig. 5.1: transfer rates due to absorption (T_{A}), spontaneous emission (T_{E}) and stimulated emission (T_{S}) from other levels and relaxation rates due to absorption (R_{A}), spontaneous emission (R_{E}) and stimulated emission (R_{S}) towards other levels. The explicit expressions of these rates can be found in Landi Degl'Innocenti (1983, 1984, 1985). For example, the transfer rate T_{A} due to absorption from

[2]This frame is similar to the laboratory frame used for the description of the molecular structure, in which the z axis (quantization axis) is oriented parallel to the magnetic field vector

lower levels is:

$$T_{\rm A}(J_l;K_lQ_l\rightarrow J;KQ)=(2J_l+1)B(J_l\rightarrow J)\sum_{K_rQ_r}\sqrt{3(2K+1)(2K_l+1)(2K_r+1)}\times(-1)^{K_l+Q_l}\left\{\begin{array}{ccc}J&J_l&1\\J&J_l&1\\K&K_l&K_r\end{array}\right\}\left(\begin{array}{ccc}K&K_l&K_r\\-Q&Q_l&-Q_r\end{array}\right)\bar{J}^{K_r}_{Q_r}, \tag{5.42}$$

where the object between brackets is the 9-j symbol (e.g., Edmonds 1960) and $B(J_l\rightarrow J)$ is the absorption Einstein coefficient of the transition between levels J_l and J. $\bar{J}^{K_r}_{Q_r}$ with $K_r=0,1,2$ and $Q_r=-K_r,\ldots,K_r$ are radiation field tensors given by integrals over frequency and solid angle of the Stokes parameters, weighted by suitable frequency and angular functions (see their explicit expressions in Landi Degl'Innocenti (1983)). When the radiation field has cylindrical symmetry around the direction chosen to evaluate the $\bar{J}^K_Q$ tensors (e.g., the stellar radius vector through the observed point), only the tensors

$$\bar{J}^0_0 = \int {\rm d}\nu \oint \frac{{\rm d}\mathbf{\Omega}}{4\pi}\phi(\nu)I_\nu(\mathbf{\Omega}) \tag{5.43}$$

$$\bar{J}^2_0 = \frac{1}{2\sqrt{2}}\int {\rm d}\nu \oint \frac{{\rm d}\mathbf{\Omega}}{4\pi}\phi(\nu)\Big[\left(3\cos^2\theta-1\right)I_\nu(\mathbf{\Omega})+3(\cos^2\theta-1)Q_\nu(\mathbf{\Omega})\Big]$$

are nonzero. θ is the angle between the axis of symmetry of the radiation field and the direction of propagation of the radiation given by the unit vector $\mathbf{\Omega}$ and $\phi(\nu)$ is the line profile. $\bar{J}^0_0$ is the well-known line integrated mean intensity and $\bar{J}^2_0$ provides information on the 'degree of anisotropy' of the radiation field. It is dominated by the contribution of Stokes I and becomes zero if I is angle independent. As reviewed by Trujillo Bueno (2001), a fundamental quantity in scattering polarization is the *anisotropy factor* $w=\sqrt{2}\bar{J}^2_0/\bar{J}^0_0$, whose possible values are bounded by the following expression:

$$-\frac{1}{2}\leq w\leq 1. \tag{5.44}$$

Assuming a reference frame with the z axis parallel to the axis of symmetry of the cylindrically symmetric radiation field, the largest value correspond to illumination coming from a purely vertical radiation field while the lowest limit is related to a purely horizontal radiation field without any azimuthal dependence.

As another example, the transfer rate $T_{\rm E}$ due to spontaneous emissions from upper levels can be written as (Landi Degl'Innocenti 1983):

$$T_{\rm E}(J_u;K_uQ_u\rightarrow J;KQ)=\delta_{KK_u}\delta_{QQ_u}(2J_u+1)A(J_u\rightarrow J)\times \\ \times(-1)^{1+J+J_u+K}\left\{\begin{array}{ccc} J_u & J_u & K \\ J & J & 1 \end{array}\right\}, \tag{5.45}$$

where $A(J_u\rightarrow J)$ is the spontaneous emission Einstein coefficient for the $J_u\rightarrow J$ transition. The term between the brackets is the 6-j symbol (see, e.g. Edmonds 1960).

5.4.3 Emission and Absorption Coefficients

The general expressions of the components of the emission vector and the absorption matrix are very involved (see Landi Degl'Innocenti 1983). They are given in terms of the ρ^K_Q elements of the upper and lower levels of a transition and on line profiles whose dependence on the magnetic quantum numbers cannot be neglected when the Zeeman splittings are a significant fraction of the spectral line width. However, for the case of scattering polarization in weakly magnetized atmospheres, we have for the I, Q and U components of the emission vector (Trujillo Bueno 2003c):

$$\epsilon_I=\epsilon_0\rho^0_0(u) \\ +\epsilon_0 w^{(2)}_{J_uJ_l}\Big\{\frac{1}{2\sqrt{2}}(3\mu^2-1)\rho^2_0(u)-\sqrt{3}\mu\sqrt{1-\mu^2}\left(\cos\chi{\rm Re}[\rho^2_1(u)]-\sin\chi{\rm Im}[\rho^2_1(u)]\right) \\ +\frac{\sqrt{3}}{2}(1-\mu^2)\left(\cos 2\chi{\rm Re}[\rho^2_2(u)]-\sin 2\chi{\rm Im}[\rho^2_1(u)]\right)\Big\} \tag{5.46}$$

$$\epsilon_Q=\epsilon_0 w^{(2)}_{J_uJ_l}\Big\{\frac{3}{2\sqrt{2}}(\mu^2-1)\rho^2_0(u)-\sqrt{3}\mu\sqrt{1-\mu^2}\left(\cos\chi{\rm Re}[\rho^2_1(u)]-\sin\chi{\rm Im}[\rho^2_1(u)]\right) \\ -\frac{\sqrt{3}}{2}(1+\mu^2)\left(\cos 2\chi{\rm Re}[\rho^2_2(u)]-\sin 2\chi{\rm Im}[\rho^2_1(u)]\right)\Big\} \tag{5.47}$$

$$\epsilon_U = \epsilon_0 w^{(2)}_{J_u J_l} \sqrt{3} \Big[\sqrt{1-\mu^2} \left(\sin\chi \mathrm{Re}[\rho^2_1(u)] + \cos\chi \mathrm{Im}[\rho^2_1(u)] \right) + \\ + \mu \left(\sin 2\chi \mathrm{Re}[\rho^2_2(u)] + \cos 2\chi \mathrm{Im}[\rho^2_1(u)] \right) \Big], \tag{5.48}$$

where we have explicitly indicated that the ρ^K_Q are those of the upper level. $w^{(2)}_{J_u J_l}$ is the quantity introduced by Landi Degl'Innocenti (1984) which depends only on J_u and J_l and $\epsilon_0 = (h\nu/4\pi) A_{ul} \phi_\nu \mathcal{N} \sqrt{2J_u + 1}$ (with $\mathcal{N}$ the total number of atoms or molecules per unit volume). The orientation of the ray is specified by the polar angle $\mu = \cos\theta$ and the azimuth χ. The η elements of the absorption matrix have identical expressions but with $\eta_0 = (h\nu/4\pi) B_{lu} \phi_\nu \mathcal{N} \sqrt{2J_l + 1}$ instead of ϵ_0, $w^{(2)}_{J_l J_u}$ instead of $w^{(2)}_{J_u J_l}$ and the values of $\rho^K_Q(l)$ of the lower level instead of $\rho^K_Q(u)$ (stimulated emission has been neglected).

6

Observation and modeling of the Zeeman effect in molecular lines

This chapter is devoted to the investigation of the molecular Zeeman effect and how it can be applied to spectro-polarimetric observations in order to obtain information about the magnetic properties of solar magnetic regions. We start in Section §6.2 by showing that the numerical diagonalization of the total molecular Hamiltonian leads to results which are in accordance with the results obtained from the theory of Schadee (1978) when the same molecular constants are used. We also show results in which only the numerical diagonalization technique can be applied since Schadee's (1978) theory is only devoted to doublet states.

As an application of the previous techniques, we investigate in Section §6.3 the anomalous CN linear polarization profiles observed in sunspots. We show that this anomalous behavior can be correctly explained by the especial Zeeman patterns of the CN lines produced by a transition to the Paschen-Back regime for very weak fields. We also describe in Section §6.4 an inversion code of Stokes profiles induced by the molecular Zeeman effect. We apply this code to obtain information about the thermodynamical and magnetic properties of the umbra in which we observed several OH lines and the CN lines showing the anomalous linear polarization profiles.

In Section §6.5, we investigate with detail the polarization properties of the

CH lines in the G-band. We show that Hund's case (b) can be approximately applied for calculating the Landé factors of the rotational levels of the CH molecule. We perform a formal solution of the vector RT equation for the Stokes profile in a typical semi-empirical model of quiet regions in the solar atmosphere for obtaining the emergent Stokes profiles. We discuss several of the most interesting regions in which CH lines not blended with atomic lines can be found. We finally describe recent observations which confirm many of the predicted line profiles.

In Section §6.6 we describe the detection of polarization from the $E^4\Pi - A^4\Pi$ system of FeH in sunspot spectra. Due to the strong polarization signals produced by the rotational lines of this system, we emphasize their potential as diagnostic tools for empirical investigations on the physical conditions in the lower atmosphere of sunspots and on the magnetism of late-type dwarfs. Since nor the rotational constants neither the coupling constants are known for these electronic states of FeH, this diagnostic potential cannot be used yet. However, we have detected lines with negative effective Landé factors, which clearly show that the lines from this system are in an intermediate coupling between Hund's case (a) and (b).

6.1 LTE synthesis of molecular Stokes profiles

The Zeeman patterns and strengths calculated by the numerical diagonalization of the molecular Hamiltonian of Section 5.3 or with Schadee's (1978) theory of the Zeeman effect for diatomic molecules in doublet states can be used to theoretically calculate the emergent Stokes profiles in magnetized stellar atmospheres. To this end, we have developed a very general synthesis code which is able to calculate, either using the 1D plane-parallel or the 1D spherically symmetric approximation, the emergent Stokes profiles induced by the Zeeman effect in atomic and/or molecular lines under the assumption of LTE. In this section we briefly explain our computer program.

We solve the RT Eq. (5.38) by means of the quasi-parabolic DELOPAR method proposed by Trujillo Bueno (2003c), which is a improvement of the DELO method of Rees et al. (1989). The scheme used for a spherically symmetric atmosphere is similar to the one discussed in Chapter 4 for the solution of the RT equation for unpolarized light.

Consider a ray propagating along direction $\vec{\Omega}$ and with frequency ν. The

elements of the propagation matrix with i=I,Q,U,V for a given transition are obtained from:

$$\begin{aligned} \eta_i &= \kappa_l \phi_i(\nu, \vec{\Omega}) \\ \rho_i &= \kappa_l \psi_i(\nu, \vec{\Omega}), \end{aligned} \tag{6.1}$$

where η_i are the absorption coefficients and ρ_i are the magneto-optical coefficients. The profiles ϕ_i and ψ_i are given by (Landi Degl'Innocenti 1992):

$$\begin{aligned} \phi_I(\nu, \vec{\Omega}) &= \frac{1}{2}\left[\phi_0 \sin^2\theta + \frac{\phi_{-1}+\phi_1}{2}(1+\cos^2\theta)\right] \\ \phi_Q(\nu, \vec{\Omega}) &= \frac{1}{2}\left[\phi_0 + \frac{\phi_{-1}+\phi_1}{2}\right]\sin^2\theta\cos 2\chi \\ \phi_U(\nu, \vec{\Omega}) &= \frac{1}{2}\left[\phi_0 + \frac{\phi_{-1}+\phi_1}{2}\right]\sin^2\theta\sin 2\chi \\ \phi_V(\nu, \vec{\Omega}) &= \frac{1}{2}\left[\phi_1 - \phi_{-1}\right]\cos\theta \\ \psi_Q(\nu, \vec{\Omega}) &= \frac{1}{2}\left[\psi_0 + \frac{\psi_{-1}+\psi_1}{2}\right]\sin^2\theta\cos 2\chi \\ \psi_U(\nu, \vec{\Omega}) &= \frac{1}{2}\left[\psi_0 + \frac{\psi_{-1}+\psi_1}{2}\right]\sin^2\theta\sin 2\chi \\ \psi_V(\nu, \vec{\Omega}) &= \frac{1}{2}\left[\psi_1 - \psi_{-1}\right]\cos\theta, \end{aligned} \tag{6.2}$$

where θ and χ describe the relative orientation of the magnetic field vector and the line-of-sight (see, e.g., Landi Degl'Innocenti 1992). ϕ_q and ψ_q (with $q = 0, \pm 1$) are the normalized line profiles, defined as

$$\begin{aligned} \phi_q &= \sum_{M_l M_u} S_q^{J_l J_u}(M_l, M_u)\frac{1}{\sqrt{\pi}}\frac{1}{\Delta\nu_D}H(v - v_A + v_B(g_u M_u - g_l M_l), a) \\ \psi_q &= \sum_{M_l M_u} S_q^{J_l J_u}(M_l, M_u)\frac{1}{\sqrt{\pi}}\frac{1}{\Delta\nu_D}L(v - v_A + v_B(g_u M_u - g_l M_l), a). \end{aligned} \tag{6.3}$$

$S_q(M_l, M_u)$ is the strength of each individual Zeeman component between M_u and M_l, $H(v, a)$ and $L(v, a)$ are the Voigt and anomalous dispersion profiles, respectively, while $v = (\nu_0 - \nu)/\Delta\nu_D$, $v_A = \nu_0\omega_A/c\Delta\nu_D$ and $v_B = \nu_L/\Delta\nu_D$,

being ω_A the projection of the macroscopic velocities in the medium along the line-of-sight and ν_L the Larmor frequency. a is the damping parameter, while g_u and g_l are the Landé factors of the upper and lower levels, respectively, calculated from Hund's coupling cases formulas or from Schadee's (1978) theory or from the numerical diagonalization of the molecular Hamiltonian. $\Delta\nu_D$ is the Doppler width of the line, which includes thermal as well as microturbulent contributions, while ν_0 is the central wavelength of the line. We note that $q = -1, 0, +1$ correspond to the $\sigma_{\rm blue}$, π and $\sigma_{\rm red}$ components, respectively. It is important to note that, for many molecular lines, the $\sigma_{\rm blue}$ and $\sigma_{\rm red}$ are not blue- and red-shifted with respect to the central wavelength of the line, respectively.

A quantity of great importance in Zeeman diagnostics is the effective Landé factor $\bar{g}$, which represents the wavelength shift from the line center of the "center of gravity" of the $\sigma_{\rm red}$ components in units of $\Delta\lambda_B = \lambda^2 eB/4\pi m_e c^2$:

$$\bar{g} = \sum_{M_u M_l} S_1^{J_l J_u}(M_l, M_u)\,(g_u M_u - g_l M_l)\,. \tag{6.4}$$

The line opacity k_l is obtained under the assumption of LTE, so that:

$$k_l = \frac{h\nu_0}{4\pi}\,(N_l B_{lu} - N_u B_{ul}) = \frac{\pi e^2}{m_e c}\frac{N_{\rm mol}}{U_{\rm mol}(T)}\,gf\,e^{-E_l/kT}\left(1 - e^{h\nu_0/kT}\right), \tag{6.5}$$

where $N_{\rm mol}$ is the molecular abundance, $U_{\rm mol}(T)$ is the temperature dependent partition function of the molecule, E_l is the energy of the lower level of the molecular transition, while gf is the oscillator strength of the transition times the degeneracy of the lower level. The line source function S_l is assumed to be the Planck function. Therefore, the emission vector is obtained from the absorption coefficients as:

$$\epsilon_i = \eta_i S_l = \eta_i B_\nu, \qquad\qquad i = I, Q, U, V \tag{6.6}$$

The atomic lines are treated in exactly the same way. We have used the atomic linelist of Kurucz (1993a). Two differences from the molecular lines arise. First, the Landé factors of the levels are taken from the linelist which appear to be calculated not using simplifications like the L−S coupling (although they can be also calculated using the L−S coupling as an option in the program). Second, the atomic abundances and atomic partition functions

are calculated according to the population distribution given by the Saha and Boltzmann equations.

When the absorption and emission properties of each individual line are obtained, we perform the formal solution of the RT equation using the DELOPAR method frequency by frequency. We take into account the contribution at each frequency of all the blended lines, so that we solve the problem including all the blends which can affect the polarization signal of the individual lines. We shall see an example of this massive blending in the CH G-band circular polarization spectrum in Section §6.5. Therefore, for each frequency:

$$\begin{aligned} \bar{\boldsymbol{\eta}}(\nu) &= \sum_k \bar{\boldsymbol{\eta}}^k(\nu) \\ \bar{\boldsymbol{\epsilon}}(\nu) = \sum_k \bar{\boldsymbol{\epsilon}}^k(\nu) &= \sum_k \bar{\boldsymbol{\eta}}^k(\nu)\boldsymbol{B}_v = \bar{\boldsymbol{\eta}}(\nu)\boldsymbol{B}_\nu, \end{aligned} \tag{6.7}$$

where the k runs over all the included transitions (although it effectively runs over all the transitions which produce a non negligible contribution to the frequency ν), $\bar{\boldsymbol{\eta}}$ and $\bar{\boldsymbol{\epsilon}}$ are the propagation matrix and emission vector, respectively, and $\boldsymbol{B}_\nu = (B_\nu, 0, 0, 0)^\dagger$.

6.2 Comparing Schadee's versus the Hamiltonian Diagonalization Approaches

In this section we show that the numerical diagonalization of the total molecular Hamiltonian leads to results which are in accordance with the results obtained from the theory developed by Schadee (1978) when the same molecular constants are used. The strength of the numerical diagonalization approach is that it allows us to handle problems which cannot be treated under the theory developed by Schadee because it is limited to doublet electronic states ($S = 1/2$). Furthermore, we can easily include additional angular momentum coupling by adding the term to the total Hamiltonian. The technique of reordering the Hamiltonian to build a block-diagonal matrix, developed in Section §5.3, leads to a fast numerical diagonalization algorithm which can compete in speed with the analytical formulas of Schadee (1978), with the obvious advantage of the generality.

In order to verify that the results are correct when performing the numerical diagonalization, we have calculated the Zeeman patterns for different values of

Molecule	Transition	Line	N_u	J_u	N_l	J_l	$B_{\rm rot}^{\rm up}$	$B_{\rm rot}^{\rm low}$	$A_{\rm up}/\gamma_{\rm up}$	$A_{\rm low}/\gamma_{\rm low}$
MgH	$A^2\Pi - X^2\Sigma^+$	$P_1(5.5)$	5	5.5	6	6.5	6.09	5.83	34.99 (Λ-S)	0.025 (S-R)
MgH	$A^2\Pi - X^2\Sigma^+$	$P_2(5.5)$	6	5.5	7	6.5	6.09	5.83	34.99 (Λ-S)	0.025 (S-R)
MgH	$A^2\Pi - X^2\Sigma^+$	$Q_1(5.5)$	5	5.5	5	5.5	6.09	5.83	34.99 (Λ-S)	0.025 (S-R)
MgH	$A^2\Pi - X^2\Sigma^+$	$Q_2(5.5)$	6	5.5	6	5.5	6.09	5.83	34.99 (Λ-S)	0.025 (S-R)
OH	$X^2\Pi - X^2\Pi$	$P_1(10.5)$	9	9.5	10	10.5	17.10	18.55	-139.75 (Λ-S)	-139.21 (Λ-S)
OH	$X^2\Pi - X^2\Pi$	$P_2(9.5)$	9	8.5	10	9.5	17.10	18.55	-139.75 (Λ-S)	-139.21 (Λ-S)
OH	$A^2\Sigma^+ - X^2\Pi$	$Q_1(9.5)$	9	9.5	9	9.5	17.36	18.55	0.201 (S-R)	-139.21 (Λ-S)
OH	$A^2\Sigma^+ - X^2\Pi$	$Q_2(9.5)$	10	9.5	10	9.5	17.36	18.55	0.201 (S-R)	-139.21 (Λ-S)
C_2	$d^3\Pi - a^3\Pi$	$P_1(7)$	5	6	6	7	1.75	1.63	-16.90 (Λ-S)	-15.25 (Λ-S)
C_2	$d^3\Pi - a^3\Pi$	$P_2(6)$	5	5	6	6	1.75	1.63	-16.90 (Λ-S)	-15.25 (Λ-S)
C_2	$d^3\Pi - a^3\Pi$	$P_3(5)$	5	4	6	5	1.75	1.63	-16.90 (Λ-S)	-15.25 (Λ-S)

Table 6.1: Spectroscopic data of the transitions for which the Zeeman patterns have been calculated. The data have been compiled from Huber & Herzberg (2003). The last two columns represent the spin-orbit (indicated with (Λ-S)) or spin-rotation (indicated with (R-S)) coupling constants of the upper and lower levels, depending on wether $\Lambda \neq 0$ or $\Lambda = 0$, respectively.

the field strength for a wide range of electronic transitions, including many of the observed molecular transitions in the solar spectrum. Zeeman pattern plots show the splitting in wavelength units of each Zeeman component of a given transition and the relative strength of each component. In the following figures, we separate the transitions depending on the value of $q = M_u - M_l$. $q = -1$ corresponds to the typical $\sigma_{\rm red}$ components, which are plotted in the upper part of the figures. $q = 0$ corresponds to the π components, which are plotted in the lower part of the figures. Finally, $q = 1$ corresponds to the $\sigma_{\rm blue}$ components, which are plotted in the middle part of the figures.

The rotational constants used in all the subsequent calculations have been obtained from Huber & Herzberg (2003) and they are shown in Table 6.2. It constitutes an actualized database of molecular constants of great usefulness.

6.2.1 MgH

We have calculated the Zeeman patterns of some rotational lines of the $A^2\Pi - X^2\Sigma^+$ electronic transition of MgH, whose rotational structure is observed around 5150 Å. The lower level of these transitions has $\Lambda = 0$ so that no coupling between the orbital angular momentum and the rotation is possible. The spin-rotation coupling constant of the lower level has a value of $\gamma = 0.025$ cm^{-1} so that the splitting due to this coupling is extremely small and the magnetic field necessary to produce a magnetic splitting similar to the spin-rotation

splitting is very small (see Berdyugina & Solanki 2002). An estimation of this Paschen-Back transition field can be obtained by equating both the multiplet and Zeeman splitting, thus obtaining the following formula:

$$H \sim \frac{\Delta\sigma}{\mu_0 g_L}, \tag{6.8}$$

where $\mu_0 = 4.6686 \times 10^{-5}$ cm^{-1} G^{-1} is the Bohr's magneton, $\Delta\sigma$ is the level separation in cm^{-1} and g_L is the Landé factor of the level. The transition to the Paschen-Back regime then starts at very small fields for these particular rotational levels, of the order of 300 G.

On the other hand, the upper level has $\Lambda = 1$ and the spin-orbit coupling constant is $A = 34.99$ cm^{-1}. The transition to the Paschen-Back regime for this level occurs at very high fields, of the order of $1.7{\times}10^5$ G, and we only have to take into account that the lowest rotational levels are described in an intermediate (a)-(b) case. For high J, this level can be correctly described under Hund's case (b) coupling in the Zeeman regime.

We show in Figs. 6.1 and 6.2 the Zeeman patterns of the $P_1(5.5)$ and $P_2(5.5)$ lines. On the left panels we have plotted the Zeeman patterns obtained using Schadee's (1978) theory and in the right panel we show the results obtained via the numerical diagonalization of the full Hamiltonian matrix. The quantum numbers of the transitions can be seen in Table 6.2. First of all, note that the Zeeman patterns obtained using the two techniques are extremely similar (provided that we use the same molecular constants), even in the highly asymmetric patterns obtained for 3000 G. For very small magnetic field strengths, the obtained Zeeman pattern is that of a transition in which both levels are in the Zeeman regime, being the upper rotational level in an intermediate state (a)-(b) and the lower in pure Hund's case (b). The σ and π components are completely symmetric with respect to $\Delta\lambda = 0$. Recalling the previous equations for the absorption coefficients in a magnetized atmosphere and, for example, the simple Milne-Eddington solution of the polarized RT equation (Unno 1956; see also Landi Degl'Innocenti & Landi Degl'Innocenti 1973), we can see that Stokes V profile is proportional to η_V, while Stokes Q is proportional to η_Q. Let ϕ_p, ϕ_r and ϕ_b be the absorption profiles centered in the center of gravity of the π, $\sigma_{\rm red}$ and $\sigma_{\rm blue}$ components, respectively. We can assume, for simplicity, that the line profiles are gaussians with a width given by the thermal broadening. Then, we can assume that η_V is roughly proportional to $\phi_r - \phi_b$, while η_Q is

roughly proportional to $\phi_p - (\phi_b + \phi_r)/2$. Following this scheme, the Stokes V signal for the very weak fields (below 100 G) has the typical antisymmetric shape of V with two lobes and the symmetric shape of Q with three lobes. However, it is usually difficult to directly relate the Zeeman patterns to the emergent Stokes profiles because the fine details of the Zeeman patterns are sometimes crucial. This is produced by the dangerous assumption (which we do not make) that η_V and η_Q can be described by means of the line profiles centered at the center of gravity of the σ and π components.

When the field increases to 500 G, the center of gravity of one of the σ components (depending on wether the line is P_1 or P_2) remains in the same relative position, while the other σ component starts to be perturbed. The shape of Stokes V remains antisymmetric as a first approximation, although the amplitude is reduced. Concerning Stokes Q, it slightly becomes asymmetric.

When the field is increased up to 3000 G, the π components of the P_1 line is again symmetric while that of the P_2 is not. Both of them are no more centered at $\Delta\lambda = 0$. The center of gravity of the $\sigma_{\rm red}$ remains almost in the same relative place for the P_1 line (of course, taking into account that the splitting is the larger the larger the magnetic field strength) while all $\sigma_{\rm blue}$ components loose strength except the one centered in $\Delta\lambda = 0$. Therefore, it is expected that the Stokes V signal will be weaker due to the apparent cancelation of the σ components, whose center of gravity are very close to each other. The Stokes Q signal will become completely symmetric with only one important lobe. Concerning the P_2 line, the center of gravity of both σ components are almost at the same location so that a very weak Stokes V signal is expected. On the other hand, a weak one-lobed Stokes Q is also expected.

The P and R branches of MgH are quite weak while the lines from the Q branch are much more important. To this end, we have obtained the Zeeman patterns of some lines of the Q branch. The behavior of the these lines can be seen in Figs. 6.4 and 6.5. A similar discussion can be done with these lines. The general behavior is that, starting from a very symmetric pattern characteristic of an intermediate coupling case between (a) and (b) for very low fields, a quick transition to a Paschen-Back regime occurs for quite low field strengths. This transition leads to very distorted Zeeman patterns for intermediate values of the field, while they gain some symmetry in the limit of high field. We will see later the effect of a very high magnetic field in the Zeeman pattern of CN lines (see Section §6.3.2).

As mentioned above, all these results must be verified with the complete solution of the polarized RT equation. To this end, we have performed formal solutions of the RT equation in the hot umbra model of Collados et al. (1994). We have assumed that the umbra is placed at μ=0.7, in order to be able to see the effect of the Zeeman pattern in the linear polarization spectrum due to the transverse Zeeman effect. We have introduced an ad-hoc magnetic field vector constant with height in the radial direction and pointing upwards. Although the model provides the value of the magnetic field at each height, we find it more interesting to use a constant magnetic field in order to easily verify the effect of the Zeeman pattern in the emerging Stokes profiles. Although the presence of a temperature gradient in the model affects the emergent Stokes profiles, we can compare the emergent Stokes profiles with the Zeeman patterns by making use of the approximation $\eta_V \sim \phi_r - \phi_b$ and $\eta_Q \sim \phi_p - (\phi_b + \phi_r)/2$. The synthetic Stokes V and Q are plotted in Figs. 6.3 and 6.6. Concerning the lines from the P branch, we see that Stokes V for low fields has the typical antisymmetric shape, with an amplitude which is proportional to the field strength. However, when the field is increased, this proportionality is lost, not because we enter into the strong-field regime of the Zeeman effect, but because of the special deformed Zeeman pattern, characteristic of the Paschen-Back regime. The positions of the centers of gravity of the σ components get closer so that the Stokes V signal gets weaker. Note also that the emergent Stokes V for a field of 3000 G for the P_1 line is extremely deformed, turning into an almost symmetric shape with two positive peaks. Concerning Stokes Q, the Zeeman patterns produce the interesting effect of giving an antisymmetric linear polarization signal, similar to the typical Stokes V signal. Furthermore, the linear polarization signal is larger for Stokes Q than for Stokes V for the P_1 line. The Q peak is $\sim$2.5 times larger the V peak. Finally, since the effective Landé factor of the P_1 and P_2 lines have opposite sign, the circular polarization signal has opposite polarity. This effect is common to molecular lines.

Concerning the lines of the Q branch, we find antisymmetric Stokes V and Q profiles, irrespective of the field strength, at least up to 3000 G. An effect similar to the transition to the strong-field regime is also found for these lines. The circular polarization amplitudes are proportional to the magnetic field except for $B = 3000$ G. This is again produced by the characteristics of the Zeeman patterns. We also find, for high field strengths, linear polarization signals which are comparable to the circular polarization signal.

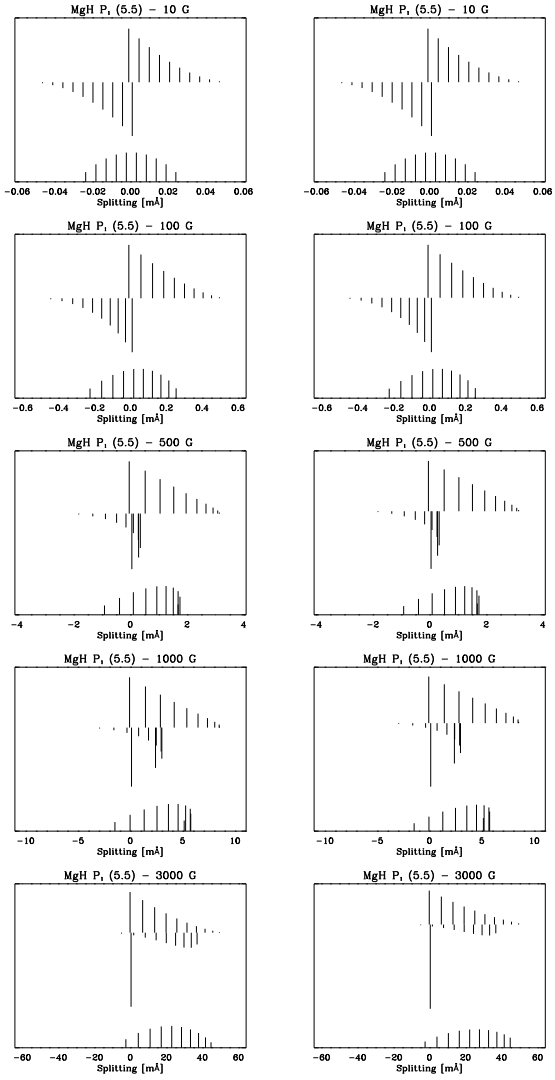

Figure 6.1: Zeeman patterns of the MgH $P_1(5.5)$ rotational transition of the $A^2\Pi - X^2\Sigma^+$ electronic transition. The left panels show the results obtained from Schadee's (1978) theory, while the right panels show the results obtained via our numerical diagonalization of the total Hamiltonian using the very same rotational and coupling constants. The transition to the Paschen-Back regime can be perfectly seen.

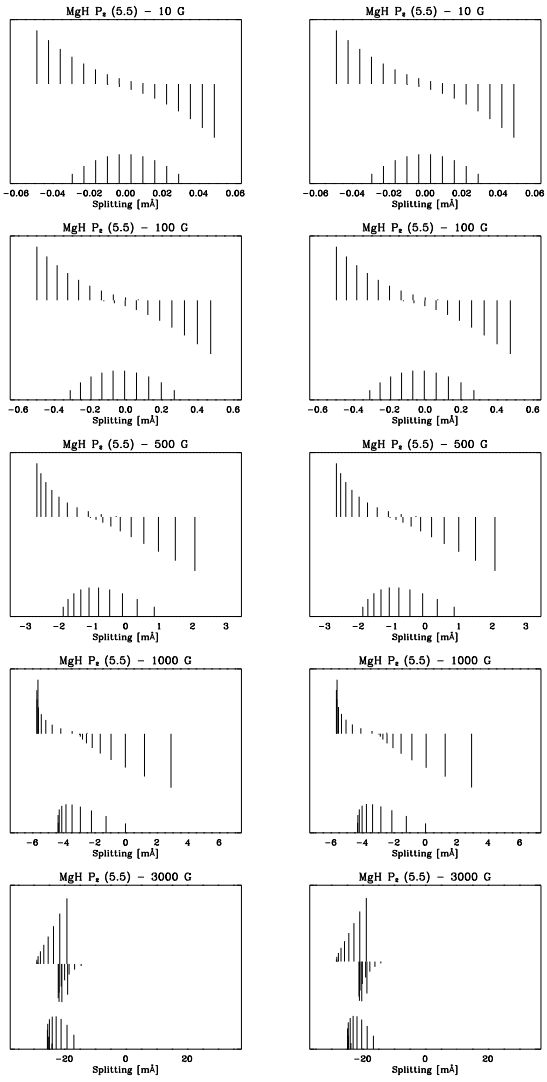

Figure 6.2: Zeeman patterns of the MgH $P_2(5.5)$ rotational transition of the $A^2\Pi - X^2\Sigma^+$ electronic transition. The left panels show the results obtained from Schadee's (1978) theory, while the right panels show the results obtained via our numerical diagonalization of the total Hamiltonian using the very same rotational and coupling constants.

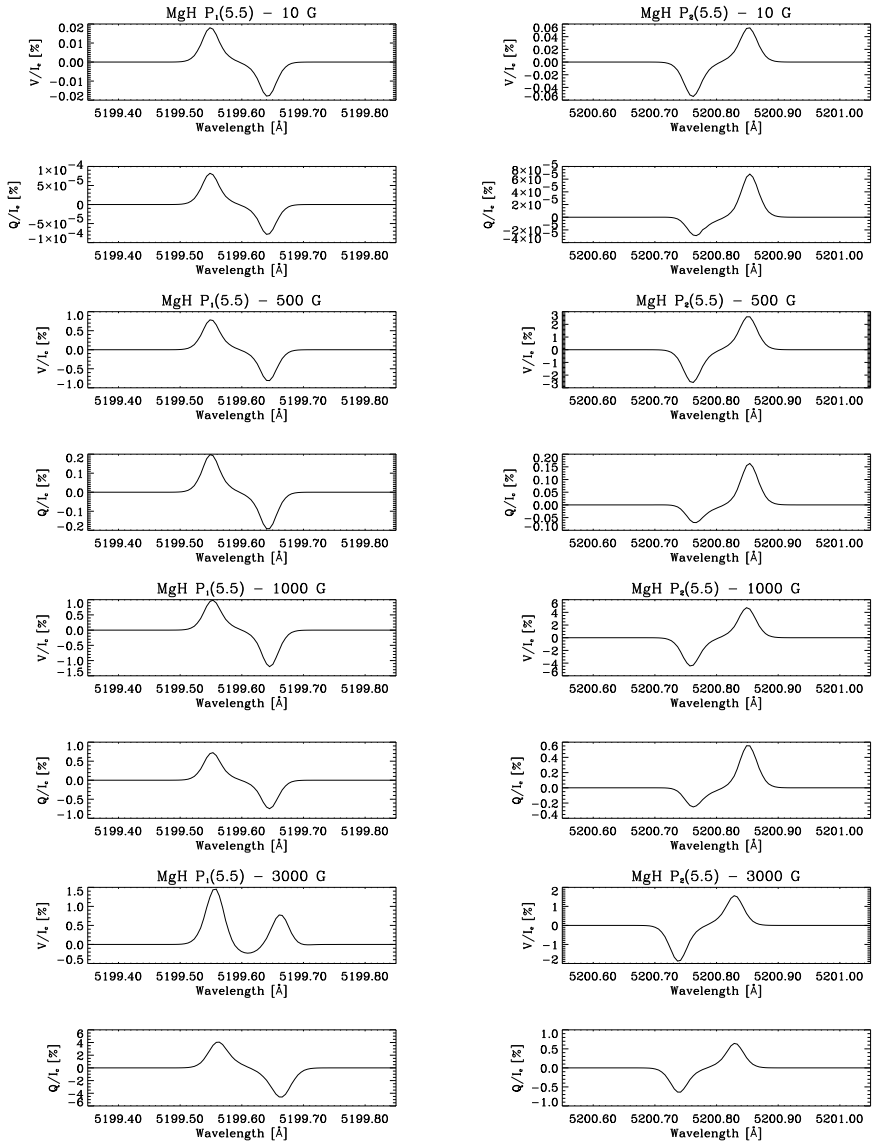

Figure 6.3: Emergent Stokes profiles from the Collados et al. (1994) sunspot atmospheric model at μ=0.7. We show Stokes V and Q for different values of the magnetic field strength. The magnetic field vector is always in the radial direction and pointing outwards. The reference direction for $Q > 0$ is that with $\chi = 0$.

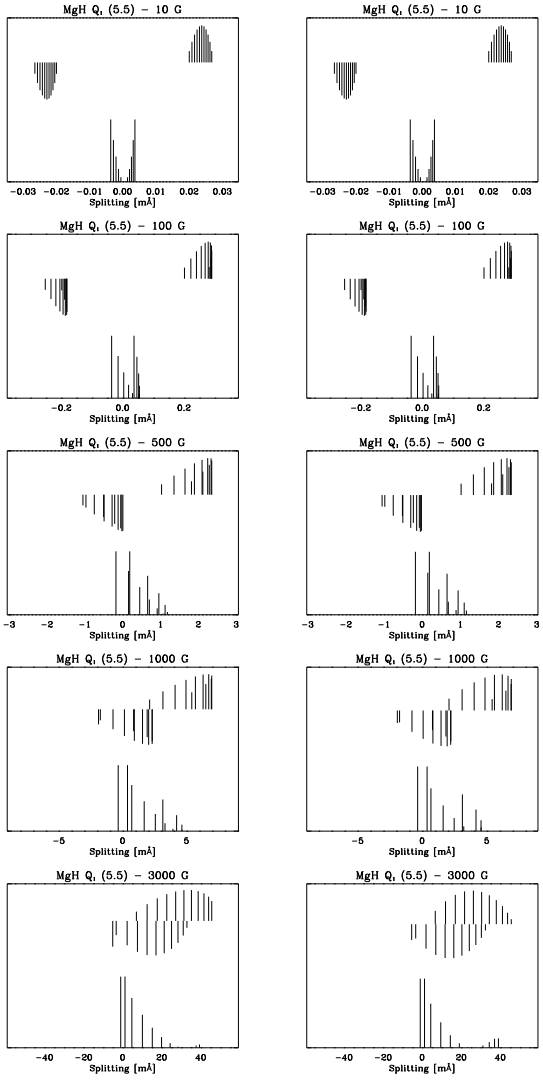

Figure 6.4: Zeeman patterns of the MgH $Q_1(5.5)$ rotational transition of the $A^2\Pi - X^2\Sigma^+$ electronic transition. The left panels show the results obtained from Schadee's (1978) theory, while the right panels show the results obtained via our numerical diagonalization of the total Hamiltonian using the very same rotational and coupling constants. The transition to the Paschen-Back regime can be perfectly seen.

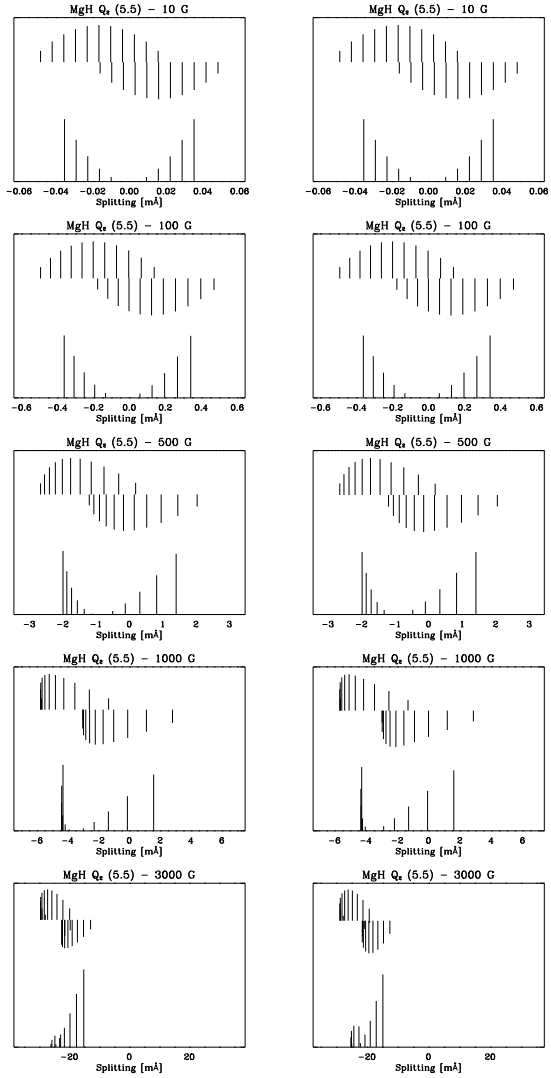

Figure 6.5: Zeeman patterns of the MgH $Q_2(5.5)$ rotational transition of the $A^2\Pi - X^2\Sigma^+$ electronic transition. The left panels show the results obtained from Schadee's (1978) theory, while the right panels show the results obtained via our numerical diagonalization of the total Hamiltonian using the very same rotational and coupling constants.

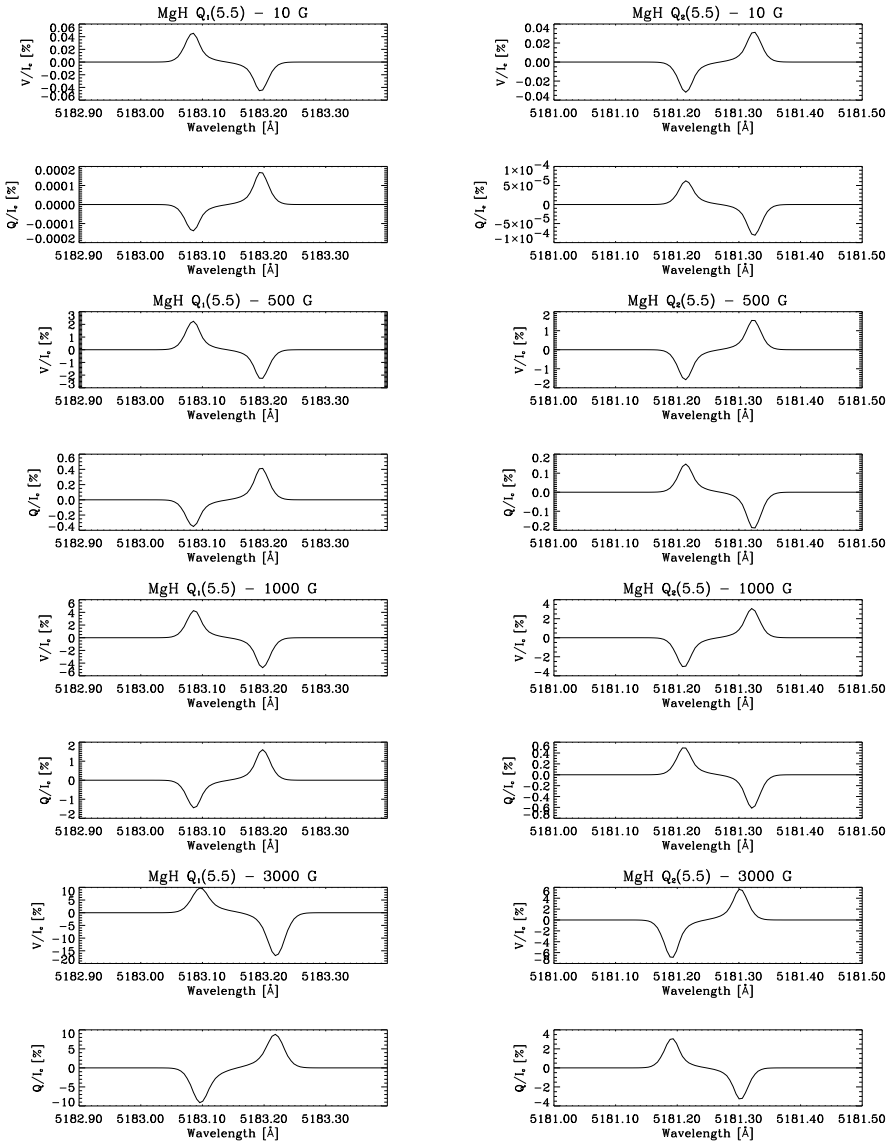

Figure 6.6: Emergent Stokes profiles from the Collados et al. (1994) sunspot atmospheric model at μ=0.7. We show Stokes V and Q for different values of the magnetic field strength. The magnetic field vector is always in the radial direction and pointing outwards. The reference direction for $Q > 0$ is that with $\chi = 0$.

6.2.2 OH

We have calculated the Zeeman patterns of two different bands of OH which are observed in the solar spectrum. The first one are the vibration-rotation transitions inside the fundamental $X^2\Pi$ electronic state observed in the infrared around 1.5 μm. The other one is the electronic transition $A^2\Sigma^+ - X^2\Pi$ observed in the UV. We show in Figs. 6.7 and 6.8 the Zeeman patterns of the $P_1(10.5)$ and $P_2(9.5)$ rotational transitions of the v=2-0 vibrational band. These lines are those observed by Harvey (1985) which present opposite polarity in the polarized spectrum of an umbra. As we will see below, the explanation for this change of polarity is that their respective effective Landé factors have opposite signs (see also Berdyugina & Solanki 2001). The center of gravity of the P_1 line is shifted to $\Delta\lambda > 0$, so that $\bar{g} > 0$, while that of the P_2 lines is shifted to $\Delta\lambda < 0$, so that $\bar{g} < 0$. Since the transition to the Paschen-Back regime occurs for this electronic state at fields larger than 10^6 G, this change of sign is only produced by the specific properties of the pattern in the Zeeman regime. In fact, this change of sign appears also when the levels are described under the Hund's case (b) coupling.

The OH electronic transition in the UV is much more interesting from the point of view of the Zeeman structure since the transition to the Paschen-Back regime occurs at lower fields. It arises from the $A^2\Sigma^+ - X^2\Pi$ transition, which is opposite to the investigated electronic transition of MgH. Those electronic transitions in which the electronic states have $\Lambda = 0$ are interesting because they usually present a transition to the Paschen-Back regime at low fields. This is produced because the spin-rotation coupling is usually much smaller than the spin-orbit coupling thus leading to extremely small multiplet splittings. The magnetic field necessary for obtaining an equivalent Zeeman splitting is unusually weak. This leads to interferences between the rotational levels and the transition from the Zeeman to the Paschen-Back regime occurs. In this case, this transition occurs due to the low spin-coupling constant of the upper level, while the lower level is always in the Zeeman regime. Figs. 6.9 and 6.10 show the Zeeman patterns of the $Q_1(9.5)$ and $Q_2(8.5)$, respectively, for fields up to 3000 G. They all seem symmetric up to fields around 1000 G, showing the typical change of sign of the effective Landé factor for transitions between $J = N + 1/2$ and $J = N - 1/2$ levels, respectively. For higher fields, the asymmetries become important, even leading to a convergence effect similar to

the band-head effect in the molecular bands. When the field increases, there is a return in the σ and π components which is more clearly seen in the $Q_1(9.5)$ line. This leads to an effective Landé factor which changes when the field increases.

6.2.3 C_2

The observed electronic transition of C_2 in the visible around 5100 Å belongs to the $d^3\Pi - a^3\Pi$ transition. Since $S = 1$ in this case, the calculation of the splittings and strengths of the components cannot be accomplished with the theory of Schadee (1978). Berdyugina & Solanki (2002) show that both levels are in the Zeeman regime up to fields as strong as 70000 G, but they are in an intermediate Hund's case between (a) and (b) for lower fields. Because the Zeeman patterns would be very similar independently of the value of the field, we have plotted in Fig. 6.11 the Zeeman pattern for the $P_1(7)$ and $P_2(6)$ lines for a field strength of 3000 G. These patterns clearly show the very symmetric patterns typical of the Zeeman regime and can be used to verify an interesting behavior of these lines. The Landé factor (obtained as the center of gravity of the $\sigma_{\rm red}$ component) of the $J = N$ transitions is much smaller than that of the $J = N \pm 1$. Therefore, the lines between levels $J = N$ have a very reduced magnetic sensitivity with respect to the lines between $J = N \pm 1$ levels. This differential effect between the lines of C_2 can be suitably used for obtaining information about the weak solar magnetic field via the Hanle effect. The lines between $J = N$ levels then become reference lines which are relatively insensitive (at least for moderate fields) to the effect of the magnetic field.

6.2.4 Conclusion

With the previous calculations, we have shown that the transition to the Paschen-Back regime leads to anomalous Stokes profiles induced by the Zeeman effect in molecular lines. We have shown that the most sensitive transitions to this Paschen-Back transition are those where one of the electronic states has $\Lambda = 0$ because the spin-rotation coupling is usually very weak and the ensuing splitting is very small, comparable with the Zeeman splitting for very low fields. Apart from the examples in solar physics, many examples from radio observations can be found in the literature (Bourke & Goodman 2003). However, the transition to the Paschen-Back regime in transitions with other electronic states could, in

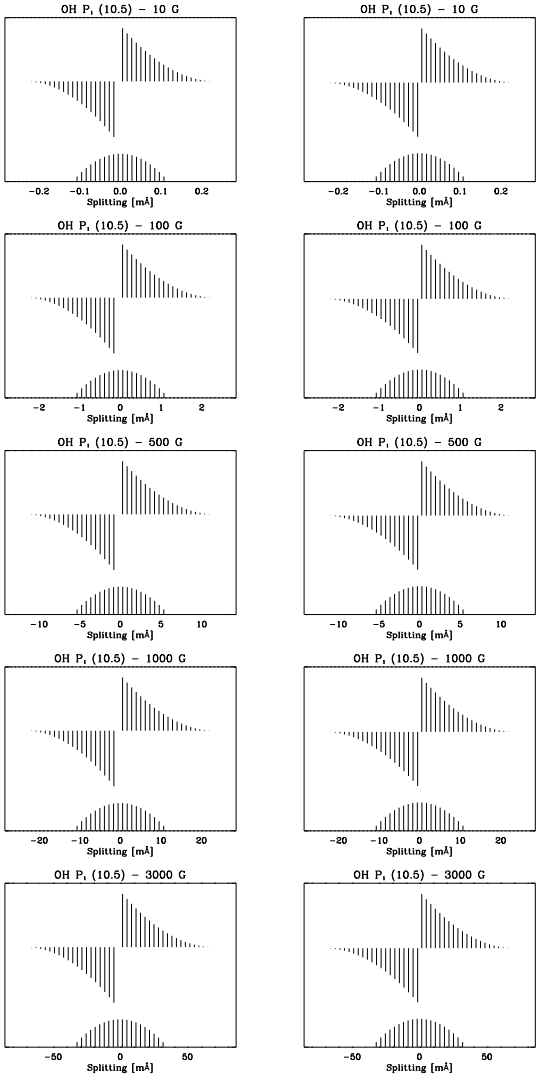

Figure 6.7: Zeeman patterns of the OH $P_1(10.5)$ rotational transition of the v=2-0 vibrational transition. The left panels show the results obtained from Schadee's (1978) theory, while the right panels show the results obtained via our numerical diagonalization of the total Hamiltonian using the very same rotational and coupling constants.

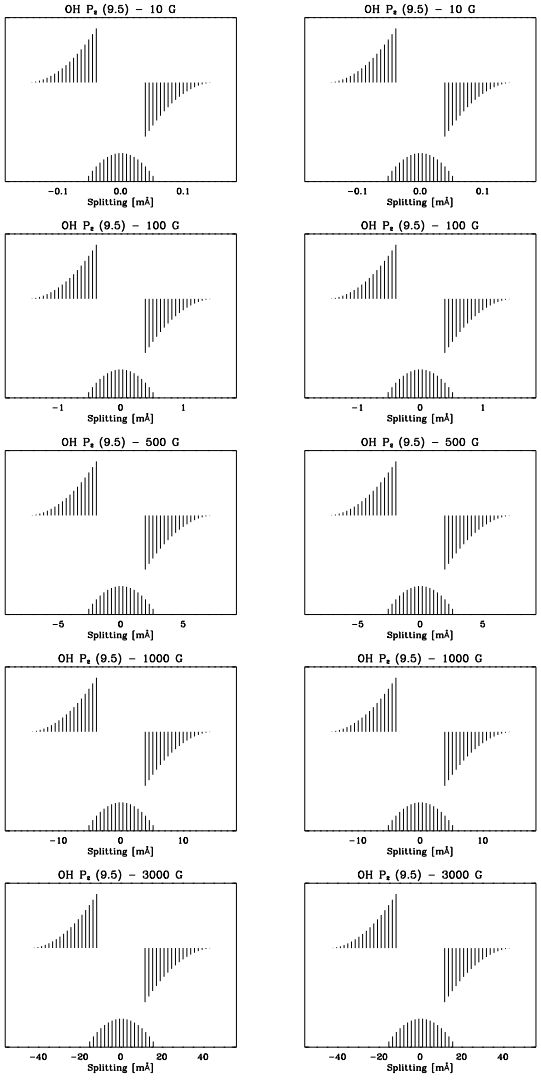

Figure 6.8: Zeeman patterns of the OH $P_2(9.5)$ rotational transition of the v=2-0 vibrational transition. The left panels show the results obtained from Schadee's (1978) theory, while the right panels show the results obtained via our numerical diagonalization of the total Hamiltonian using the very same rotational and coupling constants.

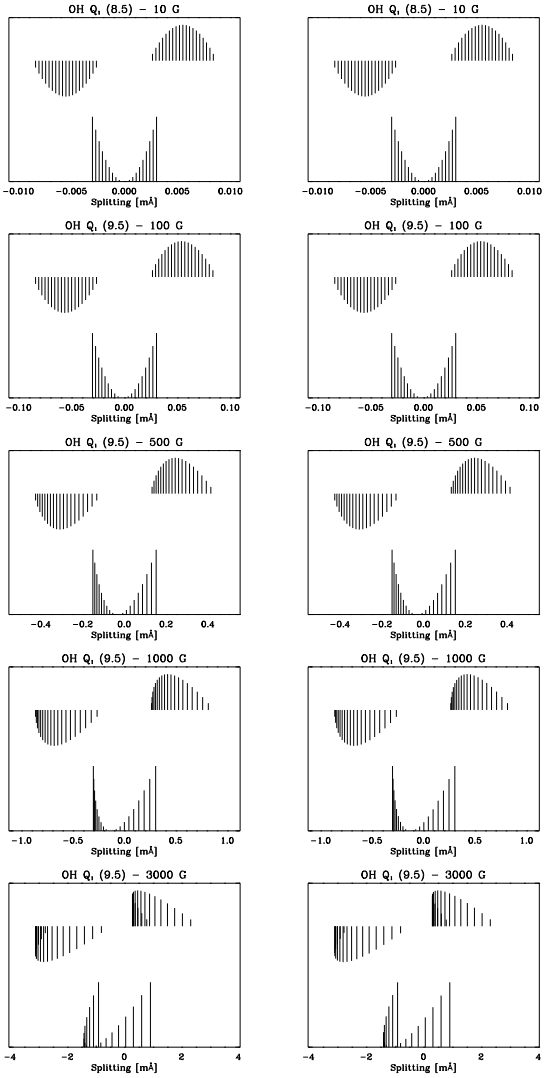

Figure 6.9: Zeeman patterns of the OH $Q_1(9.5)$ rotational transition of the $A^2\Sigma^+ - X^2\Pi$ electronic transition. The left panels show the results obtained from Schadee's (1978) theory, while the right panels show the results obtained via our numerical diagonalization of the total Hamiltonian using the very same rotational and coupling constants.

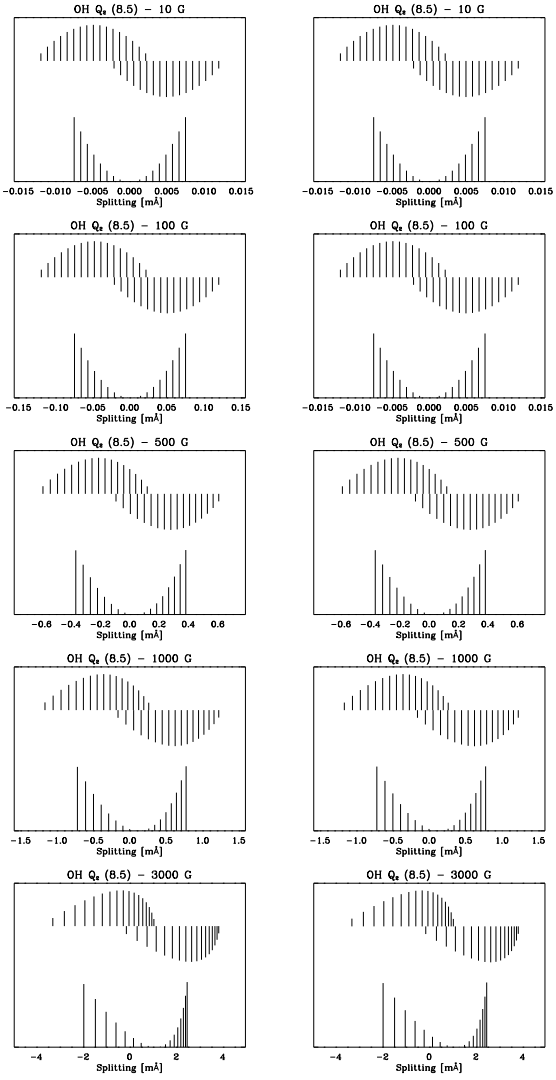

Figure 6.10: Zeeman patterns of the OH $Q_2(8.5)$ rotational transition of the $A^2\Sigma^+ - X^2\Pi$ electronic transition. The left panels show the results obtained from Schadee's (1978), while the right panels show the results obtained via our numerical diagonalization of the total Hamiltonian using the very same rotational and coupling constants.

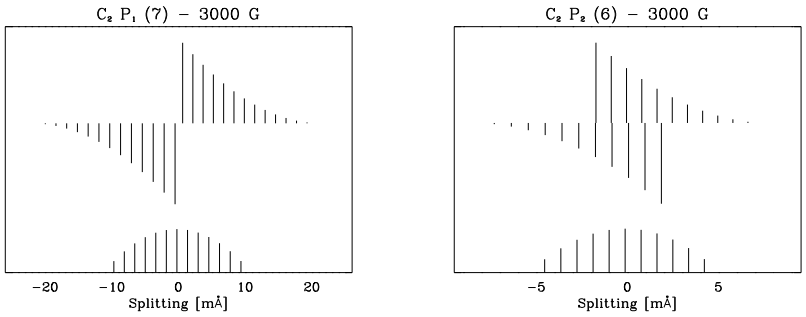

Figure 6.11: Zeeman patterns of the C_2 $P_1(7)$ and $P_2(6)$ rotational transitions of the $d^3\Pi - a^3\Pi$ electronic transition. In this case, since $S = 1$, the theory of Schadee (1978) cannot be applied and these results have been obtained with the numerical diagonalization of the Hamiltonian.

principle, be observed in cool stars with very high magnetic fields.

In the Paschen-Back regime, the effective Landé factor of a transition varies depending on the field strength. We are now investigating the possibility of a change of sign in the value of $\bar{g}$ when the field strength is increased. The previous calculations do not show neither this change of sign nor the possibility of it, since the Zeeman patterns of the $\sigma_{\rm red}$ components always remain in the same positive or negative region of the $\Delta\lambda$ axis. However, this change of sign would lead to a field strength in which there is no Stokes V signal even when the field is pointing towards the observer (at least in a first approximation) due to the longitudinal Zeeman effect, although a strong linear polarization signal can appear if the field is not directly pointing towards the observer.

6.3 Spectro-polarimetric observations with the Tenerife Infrared Polarimeter: discovery of anomalous CN linear polarization profiles

We have performed observations of some spectral regions in the near-IR with the aid of the Tenerife Infrared Polarimeter (TIP) mounted on the German Vacuum Tower Telescope (VTT) at the Observatorio del Teide (Izaña, Spain). We were looking for the Zeeman signal produced by OH in the infrared around 1.5 μm. Many OH lines show prominent circular polarization Stokes V signals in the umbra of sunspots, even showing different polarities in lines which appear

completely similar in the intensity spectrum. Additionally, CN lines are also present in this spectral region showing very weak absorptions in the intensity spectrum. This can be seen from the observed spectra shown in Fig. 6.12. The strong absorptions in the umbra are the OH lines first observed by Harvey (1985). They present conspicuous circular polarization signals which show the opposite polarity found by Harvey (1985). Other lines can be detected in the intensity spectrum showing very weak Stokes V signals and apparently coinciding with the CN weak absorptions in Stokes I. However, some of them present a quite important linear polarization signal, even at the center of the umbra. This turns out to be an enigmatic behavior because the OH lines, having a high value of the Landé factor (as seen from the Stokes V signal) do not show any appreciable Stokes Q or U signal. On the other hand, the linear polarization signal produced by these CN lines extend outside the umbra, well inside the penumbral region.

After comparing the exact wavelength of these lines with the CN linelist of Kurucz (1993b), we have found that these linear polarization signals correspond to rotational transitions of CN. We will indicate the exact quantum numbers of the transitions on Section §6.3.2. We have observationally found that the CN polarization signal is more conspicuous close to the umbra-penumbra transition, while it becomes very small at the center of the umbra. Furthermore, the closer to the disk center the sunspot is, the weaker the polarization signal produced by these CN transitions. On the other hand, the fact that the linear polarization signal is more important than the circular polarization in the CN lines is a common feature to all the observations. Another very interesting property of these CN lines is that the linear polarization signal closely resembles the classical antisymmetric shape of the Stokes V profiles.

6.3.1 Physical Interpretation: OH lines

Obviously, the explanation of the opposite polarity of the OH lines is that the effective Landé factor of both pairs of OH lines have different sign (see Berdyugina & Solanki 2001). Investigating the spectroscopic details of the transitions, we find that two lines are the $P_{1e}(21/2)$ and $P_{1f}(21/2)$ and the other two are the $P_{2e}(19/2)$ and $P_{2f}(19/2)$. Both the upper and lower levels belong to the fundamental electronic state $X^2\Pi$, the transitions belonging to the $\Delta v = 2$ vibrational band. Therefore, they are lines between different spin-

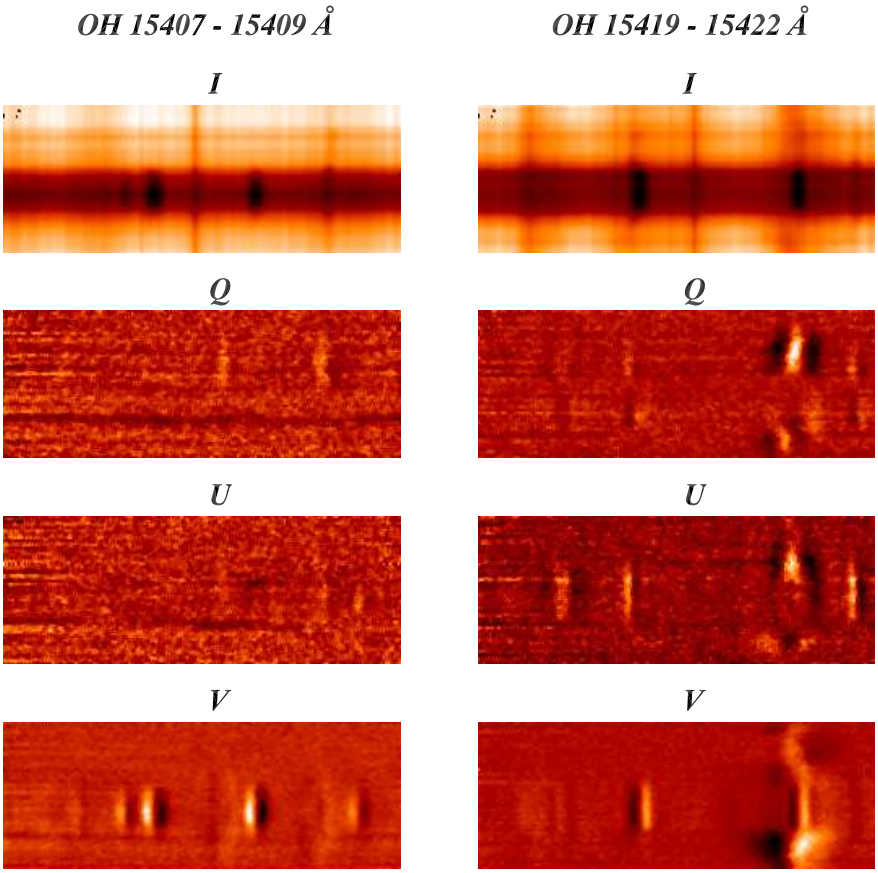

Figure 6.12: Observed Stokes profiles in a sunspot at μ=0.75. The lines showing conspicuous circular polarization Stokes V signals belong to OH. Note that the two most important OH lines at lower wavelengths have opposite polarity as compared with the two most prominent OH lines at longer wavelengths. The lines showing weak antisymmetric linear polarization U-signals belong to CN. These spectropolarimetric observations were carried out in June 2000 by J. Trujillo Bueno and M. Collados.

orbit components of a given rotational level. We have four lines instead of only two because the electronic state, having $\Lambda = 1$ has Λ-doubling. Each transition indicates the parity e or f of the lower level (see Brown et al. 1975 for an explanation of the notation).

Rotational levels of the $X^2\Pi$ electronic state are in the Zeeman regime for fields below 1.2×10^6 G, although they are described in an intermediate coupling scheme between Hund's case (a) and (b). Although the explanation of the change of sign has been pointed out before in Section §6.2.2 with the aid of the Zeeman patterns, we give here a simplified explanation in terms of the Hund's case (b) coupling, which is a very good approximation for levels above $J = 11/2$. By calculating the Landé factor in this coupling using Eq. (5.19), we obtain:

$$\begin{aligned} g_L(J = N + 1/2) &= \frac{2J+3}{J(2J+1)} \\ g_L(J = N - 1/2) &= -\frac{2J-1}{(J+1)(2J+1)}, \end{aligned} \tag{6.9}$$

which have different signs for $J > 1/2$. Using the formula for the effective Landé factor, we end up with a change of sign for transitions between levels with $J = N + 1/2$ (P_1) and those between levels with $J = N - 1/2$ (P_2):

$$\bar{g} = \pm \frac{4J^2 + 8J + 1}{2(J+1)(2J+1)(2J+3)}, \tag{6.10}$$

where + corresponds to transitions between levels $J = N + 1/2$ and − to transitions between levels $J = N - 1/2$. Additional information can be found in Berdyugina & Solanki (2001), although the previous results represent the fundamental explanation of this problem. See also the Zeeman patterns shown in Figs. 6.7 and 6.8 for an explanation of why the effective Landé factor changes its sign using the complete intermediate treatment.

6.3.2 Physical Interpretation: CN lines

More striking is the case of the CN lines. The CN lines observed around 1.54 μm belong to the $A^2\Pi - X^2\Sigma^+$ electronic transition. This transition is the same that will be included in the modeling of the CN scattering polarization in Section §7.3. The rotational levels of the lower electronic state can be correctly described under the Hund's case (b) coupling when we are in the Zeeman regime. Since the transition to the Paschen-Back regime occurs for very weak fields ($\sim$77 G for the lowest J rotational levels), these lines are always in the Paschen-Back regime under the magnetic fields present in sunspots. Concerning the rotational

levels of the upper electronic state, they are always in the Zeeman regime (the field strength at which the transition to Paschen-Back occurs is ∼560000 G), although, being a $^2\Pi$ level, they cannot be described using any simple coupling scheme. The coupling scheme is intermediate between Hund's case (a) and (b). In view of the results shown by Berdyugina & Solanki (2002), no simple coupling case can be used for determining the magnetic properties of the CN lines around 1.54 μm. Therefore, the numerical diagonalization of the Hamiltonian or the theory of Schadee (1978) has to be used.

The observed lines are located at 15418.29 Å and 15423.39 Å surrounding the OH lines discussed in Section §6.3.1. These are CN lines between levels with very high values of the angular momentum J. The first one is the $Q_1(27.5)$ line and the other is the $Q_1(46.5)$. For the first line we have $J_u = J_l = 55/2$ and $N_u = N_l = 27$, while for the second one we have $J_u = J_l = 93/2$ and $N_u = N_l = 46$. Using the molecular constants from Huber & Herzberg (2003), we have obtained the Zeeman patterns for the $Q_1(46.5)$ line for 50 G, 500 G, 2500 G and 30000 G. They are shown in Fig. 6.13. This electronic transition is the opposite to that of the UV band of OH. Although being a different transition (even different values of the angular momentum J), their Zeeman patterns have some common properties. For fields as low as 50 G, the Zeeman patterns are very similar. The main difference is that the two σ components for the case of OH do not overlap (see Fig. 6.9). Although the Zeeman patterns of the CN lines resemble that of the Zeeman regime in which one level is in an intermediate coupling between case (a) and (b), some deviations from the Zeeman regime are already found for such a weak field. On the other hand, the π component has the same structure. When the field is increased, the center of gravity of the σ components converge to the same structure until arriving to the extreme case obtained for 30000 G in which both σ components are in the same place and with the same structure. The deformations of the Zeeman pattern are larger in CN than in OH because the rotational constants and the spin-rotation coupling constant are smaller for CN. The rotational constant and the spin-rotation coupling constant of the CN states are around an order of magnitude smaller than for the OH states, thus leading to multiplet levels very close in energy. Therefore, strong coupling between consecutive rotational levels appear. We have included in the Hamiltonian the coupling between the rotational level J under study and the levels $J \pm 1$ (see Chapter 5 in Section

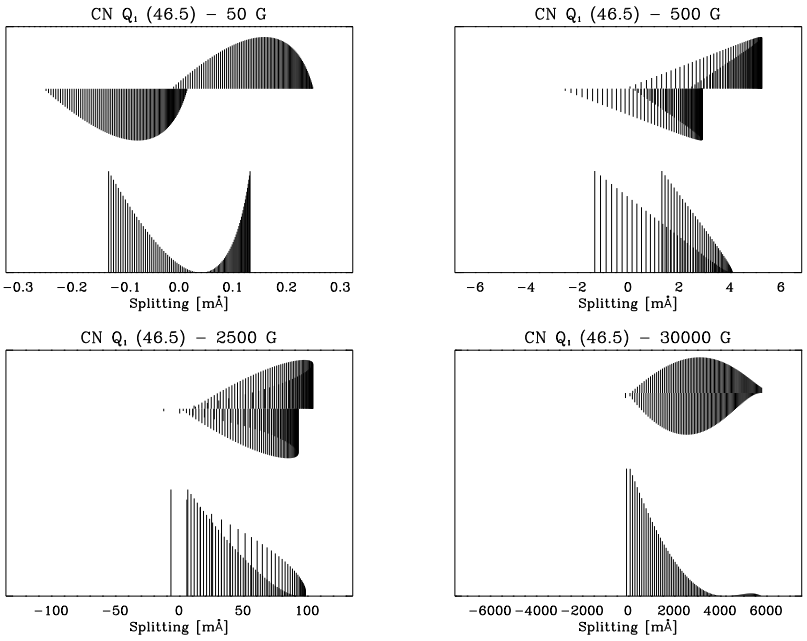

Figure 6.13: Zeeman patterns for 50, 500, 2500 and 30000 G of the $Q_1(46.5)$ CN line. Note that the σ and π components are symmetric for low fields and become deformed due to the transition to the Paschen-Back regime. At very high fields, the symmetry is again recovered.

§5.3). We are now investigating the effect of including a coupling between more separated levels $J \pm 2, 3, \ldots$. In account of Eq. (6.8), the field necessary to obtain any interference between those levels would be as large as ∼80000 G. At least in the solar atmosphere, it is not expected to have such an influence.

The following argument based on the shape of the Zeeman patterns for a field of 2500 G can be used to show why the linear polarization signal can be stronger than the circular polarization one, while also explaining the antisymmetric shape of Q and U in such CN lines. Let us recall the dependence of η_V and η_Q on the the absorption profiles ϕ_r, ϕ_p and ϕ_b. Because the center of gravity of the two σ components are almost at the same position as shown in Fig. 6.13, a cancelation between the profiles is produced in η_V, yielding a very small circular polarization signal. On the other hand, because the center of gravity of the π component is completely displaced from the two σ components, η_Q will

have an antisymmetric shape. To the best of our knowledge, this antisymmetry produced by the structure of the Zeeman pattern itself has not been observed in atomic lines. In fact, this effect cannot be obtained in molecular lines unless the line is in the Paschen-Back regime. If the line is in the Zeeman regime, the Landé factor is well defined and independent on M and the field strength. In this case, the two σ components are symmetric with respect to $\Delta\lambda = 0$ and the π component has its center of gravity at $\Delta\lambda = 0$.

For small field strengths, we recover the typical symmetric shape of Q and U and the antisymmetric shape of V. For higher field strengths, we obtain an even lower V signal than for intermediate fields and Q and U signals which tend to be antisymmetric. If the magnetic field vector lies along the line-of-sight (LOS), the polarization signal in these CN lines is only circular. However, when the magnetic field is inclined with respect to the LOS, the linear polarization signal increases and rapidly becomes more important than the circular polarization signal.

6.4 An inversion code of Stokes profiles induced by the molecular Zeeman effect

6.4.1 Description of the code

In order to obtain as much information as possible from spectropolarimetric observations, we have decided to develop an inversion code for the Stokes profiles induced by the Zeeman effect in atomic and molecular lines. This inversion code makes use of the inversion algorithm of the LILIA inversion code (Socas-Navarro 2001), while the synthesis part is the one developed before in Section §6.1. Our LTE synthesis code allows the synthesis of atomic and molecular lines, so that the inversion code would be able to perform inversions including both kind of lines. Such an inversion code is nothing but a nonlinear minimization of a merit function which takes into account the difference between the observed and the synthesized profiles. The parameters of this function are the parameters which describe the atmospheric model. Consider the Stokes parameters at a given frequency denoted by the four-component vector $\mathbf{I}(\lambda)$. It is usual to choose the

χ^2 as the merit function:

$$\chi^2 = \frac{1}{\nu} \sum_{k=1}^{4} \sum_{i=1}^{N_\lambda} \frac{\left[I_k^{\rm syn}(\lambda_i) - I_k^{\rm obs}(\lambda_i) \right]^2}{\sigma_k(\lambda_i)^2}, \tag{6.11}$$

where N_λ is the number of frequency points, "obs" and "syn" refer to the observed and the synthetic profiles, respectively, while ν is the number of degrees of freedom (difference between the number of observables and the number of free parameters of the model). σ_k are appropriate weights that can be used to fine-tune the inversion.

This minimization is performed using a Levenberg-Marquardt (LM) algorithm (Press et al. 1986). An explanation of the techniques to solve this inversion problem can be found in Ruiz Cobo & del Toro Iniesta (1992). The inversion algorithm of the LILIA code is based on the same approach but the response functions[1] are calculated numerically (see below). We give here a very brief idea on how the inversion algorithm works. The problem is to obtain the depth variation of the physical parameters which define the atmosphere: temperature, density, macroscopic velocity, magnetic field strength, magnetic field orientation and microturbulence. In order to reduce the number of free parameters of the problem, only the parameters at a given amount of nodes along the atmosphere enter the problem, while the physical conditions between these points are interpolated using either linear, parabolic polynomials or cubic splines. This drastically reduces the dimensionality of the problem so that the minimization of the χ^2 function can be correctly performed. It is a fundamental step because the information obtained from the observations is not usually enough to infer the physical conditions at each point in the atmosphere due to the noise. Therefore, the previous procedure is nothing but a regularization technique, usually applied in the general theory of inversion methods. The LM algorithm needs the evaluation of the derivatives of the merit function with respect to the parameters of the model at the nodes. For the moment, our inversion code evaluates the response functions numerically. The main disadvantage of this approach is that many formal solutions have to be performed in order to build the curvature matrix needed in the LM algorithm, thus making it intrinsically slow. Our next step is to study the feasibility of including a

[1] The response functions are the derivatives of χ^2 with respect to the physical parameters that define the atmosphere.

suitable response function technique in our inversion code in order to improve its efficiency, like in the SIR code (Ruiz Cobo & del Toro Iniesta 1992). The main difficulty would be to calculate the response function to the temperature and the density, since the molecular abundances depend highly nonlinearly in these variables through the ICE equations.

6.4.2 Details of the inversion

We have applied this inversion code to the observed molecular lines of OH and CN coming from a point in the sunspot umbra observed at μ=0.76. The four OH lines observed in the umbra (see Section §6.3.1) produce almost the same absorption in the spectrum, thus they are "formed" at equivalent regions. Since we do not obtain more information on the thermodynamical and magnetic properties of the atmosphere by including these four lines in the inversion process, we have decided to include only two of them. More precisely, we have applied the inversion process to the spectral region from 15416.7 to 15423.7 Å, exactly the same range as the observation. In practice, not all the observed spectral region is taken because of the presence of telluric absorptions. We are able to synthesize a complete region with all the blends present in it, so that our inversion code can be applied to highly blended lines also. In this region we have 5 OH lines and 7 CN lines. However, only two OH lines and two CN lines produce measurable signals. We have included all of them in the synthesis process, even though they are very weak. Furthermore, since we are dealing with sunspot observations, we have included the possibility of having stray-light contamination from the surrounding quiet Sun. To this end, we add to the the synthetic spectrum a quantity proportional to the quiet Sun spectrum obtained from the observations.

Our inversion problem is not straightforward, since the molecular lines do not have much information about the upper atmospheric regions. To this end, we have limited the extension of the atmospheric model to the region between continuum optical depth at 5000 Å $\log\tau = 2$ and $\log\tau = -4$. The inversion procedure is initialized with the hot umbra model of Collados et al. (1994) (hereafter HUM from "hot umbra model"). We can see in Fig. 6.14 the observed profiles together with the Stokes profiles emerging from the inferred model. We have performed calculations with different number of nodes as can be seen in Fig. 6.15, but the emergent Stokes profiles are very similar and we have also

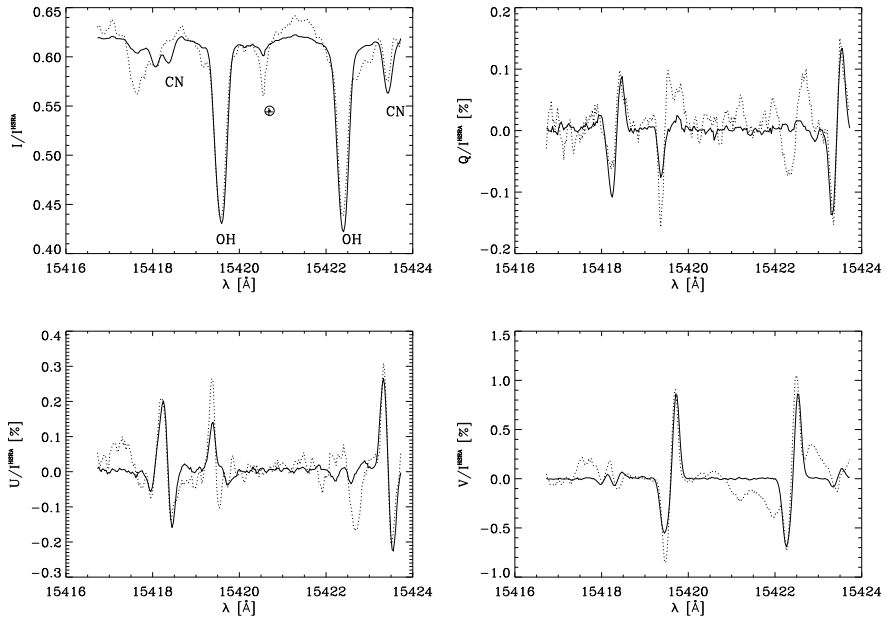

Figure 6.14: Observed profiles (dotted line) and those resulting from the inferred models (solid line), either when the number of nodes in the magnetic field strength, inclination and azimuth are $N_B = 2$, $N_\theta = N_\chi = 3$ or when they are $N_B = 3$, $N_\theta = N_\chi = 2$. Since both give the same indistinguishable profiles, we only plot one of them. The Stokes profiles are normalized to the continuum intensity calculated in the Harvard-Smithsonian Reference Atmosphere (HSRA; Gingerich et al. 1971).

plotted them for one case. The number of nodes used for the magnetic field strength, inclination and azimuth can be obtained from Fig. 6.15 where we show the calculated error at each node. They both share the same 3 nodes in the temperature and macroscopic velocity.

6.4.3 Stokes profiles

Concerning Stokes I, we can recover with good accuracy the depth and width of the OH and CN lines. The stray-light contribution arrives to 14 % in both calculations with different number of nodes in the magnetic field strength, inclination and azimuth. This is the reason why the telluric CO line between the

OH lines appears in the synthetic spectrum. Concerning Stokes V, we obtain a quite good behavior, with slightly asymmetric profiles for OH. The very small Stokes V signal produced by the CN signal is also recovered. The inferred model is such that, when it is used to synthesize the other two OH lines, we obtain a good fit also, including the polarity reversal.

The most interesting results are those corresponding to the linear polarization signals (Stokes Q and U, depending on the azimuth), because they present the strong antisymmetric signals produced by the CN lines. The antisymmetric shapes due to the especial Zeeman patterns are correctly obtained and perfectly fit the observed signals. The feature at 15419.5 Å is produced by the blend between OH and CN. The profile coming from the inferred model does not fit very well the observed profile. In fact, many CN lines are blended with the OH line and the misfit may be produced by not very correct values of the line strength. This is reinforced by the fact that the general shape of the profile seems to be recovered in the synthetic profile. In order to avoid these uncertainties, we have focused on the other two CN lines which appear quite clean. Although clean, they represent the contribution of some weak CN lines surrounding the strong component which produces the main signal.

Fig. 6.14 shows the strikingly good fit of the Stokes Q signal of the 15423.39 Å CN line. This line presents two lobes of about the same strength, which is correctly recovered using the corresponding Zeeman patterns. Stokes U shows again an almost completely antisymmetric profile with two lobes of the same strength. This regularity is produced because of the high value of J for this line. The deviations from the Zeeman regime are less important for high J than for low J levels (the spin-rotation splitting in the $^2\Sigma$ state increases when J increases). Concerning the line at 15418.29 Å we find a good fitting in Stokes U and Q in spite of the fact that the line shows quite asymmetric profiles.

6.4.4 Inferred model

The temperature stratification obtained after the convergence of the inversion procedure is shown in the upper panel of Fig. 6.15, together with the temperature stratification of the HUM model used as initialization. The model recovered in the inner parts of the atmosphere is slightly cooler than the HUM model, perhaps indicating that the observed umbra was slightly larger than that observed by Collados et al. (1994) because of the relation between the

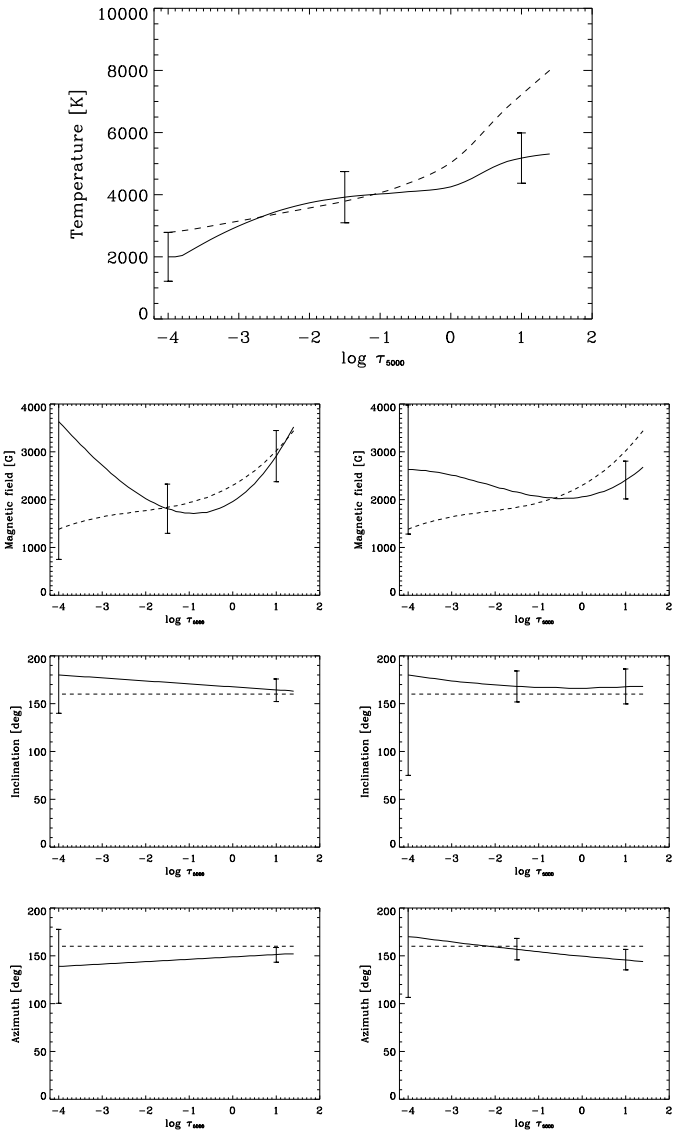

Figure 6.15: Atmospheric model obtained via the application of our inversion code. The upper panel shows the temperature profile. The lower left panel shows the magnetic field strength, inclination and azimuth when $N_B = 3$, $N_\theta = N_\chi = 2$, while the lower right panel shows the case when $N_B = 2$, $N_\theta = N_\chi = 3$. Solid lines represent the inferred model while dotted lines represent the initialization for each property. The vertical bars represent the error bars.

size of the spot and its temperature. However, above $\log\tau = -1$, both models yield approximately the same temperature (at least inside the error bars). The error bars associated with the temperature are slightly large. We have to take into account that the exposure time was only 0.25 seconds. The signal-to-noise ratio is thus not very large and this transforms into the error bars of the inferred model.

The rest of variables shown in Fig. 6.15 are related to the magnetic field and differ in the number of nodes N_i of each variable i. The left panel shows the inferred model when $N_B = 3$, $N_\theta = N_\chi = 2$ while the right panel shows the inferred model when $N_B = 2$, $N_\theta = N_\chi = 3$. The error bars are relatively larger than those of the temperature due to the lower signal-to-noise ratio obtained for Stokes Q, U and V, from where the information for B, θ and χ is obtained. These molecular lines have small effective Landé factors and the polarization signal due to the Zeeman effect is small. For this reason, it is difficult to obtain reliable magnetic information of the umbra only with molecular lines[2]. However, the magnetic field strength, inclination and azimuth obtained from the inversion look quite interesting. The magnetic field is weaker in the deep regions of the atmosphere than that from the HUM model, although the error bars indicate that the HUM model could also give a good representation of the polarized spectrum in this region. Above $\log\tau$ between -1 and -1.5, we get an inversion of the behavior, with a magnetic field larger than that obtained in the HUM model. However, the error bars are so large that this result remains unclear.

The inferred inclination and azimuth present much smaller error bars. In both cases, the inclination is very close to 180°, indicating a field which mainly points downwards in the whole atmosphere. We plan to apply our inversion technique to future 2D spectropolarimetric observations of sunspots in order to obtain a mapping of the magnetic and thermodynamic conditions via the inversion of Stokes profiles in both molecular and atomic lines.

6.4.5 Conclusion

With this experiment, we wanted to show that an inversion with only molecular lines can give us information about the temperature and magnetic structure of

[2]We expect to obtain more reliable information by combining both atomic and molecular lines.

an umbra. Ideally, it would be necessary to jointly use atomic and molecular lines in the inversion procedure. In this way, the thermodynamical and magnetic information obtained via the high effective Landé factor atomic lines will be complemented to the great sensitivity of the molecular lines to the temperature. Furthermore, the strength, inclination and azimuth of the magnetic field inversion would benefit from the additional constraints given by the molecular lines which may serve to reduce the error bars.

6.5 Polarization properties of the CH molecule on the G-band

6.5.1 Introduction

Most of the features observed in the solar surface, except for the granulation produced by convective phenomena, are produced by the presence of magnetic fields. Although magnetic field concentrations are easily observed when they are produced at large scale, small scale magnetic field concentrations are very difficult to observe. Among these small-scale features we can include micropores, network bright points and internetwork fields (Stenflo 1994).

Due to the small size of these small-scale magnetic features, it is extremely difficult to perform good and detailed observations of them The angular resolution of the telescopes is not enough for resolving these structures so that the net magnetic flux which remains when integrating over the resolution element (spatial and temporal) is very small. In spite of that, indirect method have been developed which allow the use of high spatial and temporal resolution techniques. These methods involve obtaining images of the solar surface in wideband filters centered on molecular bands towards the blue and ultraviolet part of the spectrum. As examples, we have the band head at 3883 Å due to $B^2\Sigma - X^2\Sigma$ electronic transitions of CN (Sheeley 1971), and the so-called G band around 4305 Å due to CH (Muller, Hulot, & Roudier 1989; Berger et al. 1995). In these molecular wideband images the magnetic elements appear as bright points with contrasts of typically 30 %, compared to the average photosphere (Berger et al. 1995).

Several efforts have been performed towards understanding why these bright points in these molecular bands are bright. Model calculations of G-band brightness in semi-empirical fluxtube atmospheres provide reasonable values for the bright point contrast (Sánchez Almeida et al. 2001; Rutten et al. 2001;

Steiner et al. 2001). Flux-tube models are hotter than the quiet Sun in the layers producing the observed light. They are evacuated owing to the presence of a magnetic field, thus allowing us to observe deep and therefore hot photospheric layers. For this very reason, Sánchez Almeida et al. (2001) concluded that G-band contrast in the bright points is enhanced compared to the surrounding photosphere because the opacity in the CH lines is less affected by the higher temperatures present in magnetic elements than the continuum opacity, which is mostly due to H^-. In the continuum a rise in temperature leads to a higher formation height of intensity at consequently lower temperatures. On the other hand, in the G band the formation height remains more or less constant (because of the increase in H^- opacity and decrease in CH line opacity through dissociation) so that the emergent intensity reflects the higher temperatures.

6.5.2 Theoretical prediction of the polarization properties of the G-band

The optical band of CH at 4305 Å has been investigated up to now considering only the intensity spectrum. With the theory of Schadee (1978) or the numerical diagonalization of the Hamiltonian presented in this Thesis, we can now predict the polarized spectrum of CH in the solar atmosphere.

The CH band at 4305 Å is produced by the rotational structure of bands between the first four electronic states. These transitions are the $A^2\Delta - X^2\Pi$, $B^2\Sigma^- - X^2\Pi$ and $C^2\Sigma^+ - X^2\Pi$. The G-band is dominated by transitions of the $A^2\Delta - X^2\Pi$ band, representing $\sim$90 % of the total number of lines in the band. According to the coupling constants of each state and using Eq. (6.8), we can estimate the field at which the transition to the Paschen-Back regime occurs. The coupling and rotational constants are again obtained from Huber & Herzberg (2003). The field at which the states of the most abundant transition in the band (the $X^2\Pi$ and $A^2\Delta$ states) enter the Paschen-Back regime is 6×10^5 G and 10^4 G, respectively. Moreover, their rotational levels are extremely well represented using the Hund's case (b) coupling (see Berdyugina & Solanki 2002). For the field strengths present in the quiet Sun or in sunspots, we can safely use the Hund's case (b) for calculating the Zeeman splitting for this band. Concerning the other two states, and since $\Lambda = 0$, spin-rotation coupling becomes important. Using the values $\gamma(B^2\Sigma^-) \approx -0.0285$ cm^{-1} and $\gamma(C^2\Sigma^+) \approx 0.05$ cm^{-1}, we obtain fields for the lowest rotational levels

of 600 G and 1100 G, respectively. Since the Landé factor rapidly decreases with increasing J, we can assume that all the electronic states can be correctly described under the Zeeman regime for the magnetic fields present in the quiet Sun, except for lines with small value of J. In highly magnetized regions, it will be necessary to take into account the transition to the Paschen-Back regime for the few lines of the $B^2\Sigma^- - X^2\Pi$ and $C^2\Sigma^+ - X^2\Pi$ transitions present in the band.

To investigate the intensity and polarization spectra in the G-band we solved the full Stokes radiative transfer equations over a wavelength range of 30 Å centered around 4305 Å through the one-dimensional hydrostatic model of the average quiet solar atmosphere FAL-C with an imposed vertical magnetic field of 1000 G pointing outwards. We have assumed that the inclusion of the magnetic field does not perturb the thermodynamical properties of the model. The synthetic Stokes I and V profiles are shown in Figs. 6.17 , 6.18, 6.19, 6.20, 6.21 and 6.22 for observation at disk-center. We have performed two different calculations: one including only the CH lines and the other including the CH lines and the possible atomic lines in the spectral region. We can then investigate which lines of CH are clean enough to be considered as potentially interesting for investigating the magnetic properties of the bright points. We have also overplotted the Liège disk center spectrum of Delbouille et al. (1973) as reference observed spectrum. The Liège atlas is normalized to its local continuum, which we transform to absolute units by setting the atlas continuum to the synthetic continuum at 4295.5 Å. In this region the observed spectrum shows a quite clean region where the continuum can be correctly obtained.

First, note that the fit between the observation and the synthesis is notable, similar to the one we obtained with the VAL-C model in Sánchez Almeida et al. (2001). Some features are not correctly recovered due to gaps in the atomic and/or molecular linelists, to not very accurate values of the oscillator strengths, to deviations from the LTE approximation or to the assumption of a 1D atmospheric model. The comparison between the spectrum including the atomic and molecular lines and that including only the molecular lines shows that some regions of the spectrum are almost free of atomic lines while CH lines are present. This is the case of the region from 4303.5 to 4304.5 Å. On the other hand, other regions are completely dominated by atomic lines, like the deep absorption at 4308 Å produced by the combined effect of Fe I and Ti II (with a small contribution of CH) and the regions at the extremes of the band,

where the CH lines almost disappear.

Concerning the circular polarization spectrum, the strongest signal in the whole band reaches ∼20 % in V/I_c and is produced by atomic lines. Typical circular polarization signals at the wavelengths where CH lines alone dominate the spectrum are 2-5 % for the 1000 G constant vertical field. The carriers of the stronger signals are discussed below. The rest of CH lines produce very weak V signals, mainly due to the small effective Landé factor of the high J transitions (note that $\bar{g}$ in Hund's case (b) typically varies as J^{-1}). Only the transitions between small J levels produce an important signal in V/I_c.

We have investigated in detail some of the CH lines which produce strong circular polarization signal. None of the regions is dominated by a single CH line, rather the spectrum in each is the result of overlapping lines of varying degrees of magnetic sensitivity. As a result, none of the profiles in Stokes V has a regular double-lobed antisymmetric shape.

- 4298 Å. This region results from the blend of two CH lines and some atomic lines. The Stokes V profile obtained when no atomic lines are included is completely antisymmetric. On the other hand, when atomic opacity is included, the red lobe of the profile completely disappears due to the blend. The CH lines are the $R_{1e}(2.5)$ and the $R_{1f}(2.5)$ of the $v = 0-0$ band, thus representing a Λ-doublet similar to the one observed in OH (see Section §6.3.1). Since the value of J is low, their effective Landé factor ($\bar{g} \approx 0.62$) is high enough to give an important signal. This region may be of interest because it gives a non-zero polarization signal when an integration in wavelength is performed in the surroundings of 4298 Å thus representing, in principle, a candidate for doing filter-polarimetry.

- 4303.3-4304.4 Å. This region has two Stokes V features belonging to CH only. The one at 4303.6 Å is produced by the blend between the lines $Q_{12ef}(1.5)$ and the $Q_{12fe}(1.5)$ of the $v = 0 - 0$ band, forming again a Λ-doublet. The other at 4303.9 Å is produced by the blend between the $R_{1e}(1.5)$ and the $R_{1f}(1.5)$ of the $v = 0 - 0$ band, forming again a Λ-doublet with $\bar{g} = 0.8833$. These lines overlap with lines that are much less magnetically sensitive. This is a particular notable example of a single-lobed Stokes V profile. This blend raises the interesting possibility of recovering the bright point magnetic field with narrowband imaging

in only one polarization, avoiding the difficulties of reconstructing the polarization map from two different exposures (Uitenbroek et al. 2004).

- 4311.9 Å. This region is produced by a massive blend between CH lines. There are many lines contributing in this feature, but the most important are the $P_{12ff}(5.5)$, $R_{21ff}(4.5)$, $Q_{22fe}(4.5)$ and $P_{12ee}(4.5)$ from the $v = 0-0$ band and the $R_{21ff}(1.5)$, $P_{12ff}(4.5)$, $R_{21ee}(1.5)$ and $R_{21ff}(2.5)$ from the $v = 1 - 1$ band. Other weaker lines are also contributing to this profile. Due to the high number of lines in the blend, it may be difficult to obtain any information from this profile.

- 4313.6 Å. This region is produced by the blend of the $Q_{11fe}(3.5)$ and the $Q_{11ef}(3.5)$ lines. The separation of the two lines and the Zeeman patterns produce a V profile which is completely antisymmetric. This profile could be used, in principle, as a diagnostic tool for the field in the line formation region of CH.

Summarizing, all the lines which produce strong signals in the circular polarization spectrum are produced by transitions between levels with small J, in fact, $J < 5.5$ for all these lines. Other CH features present even stronger signals than the previous, but they are blended with atomic lines which highly distort their V profiles. This is the case of the features at 4303.1 Å or 4314.2 Å.

We have shown in Fig. 6.16 the effective Landé factors for the lines of the main and satellite branches. As is well known, the value of $\bar{g}$ for the lines of the main branches fall when increasing J. Interestingly, the value of $\bar{g}$ for the P and R lines of the satellite branches increase when increasing J until reaching the value $\bar{g} = \pm 1$, respectively. It is expected that at least some of the stronger lines of the satellite branches may produce an important V signal. This is the case as we have seen in the massive blend in 4311.9 Å. Note, however, that the satellite lines have much smaller oscillator strengths and they generally are weak lines (between 1 and 2 orders of magnitude lower than for the lines of the main branches).

For a prediction of the amount of Zeeman induced polarization under more realistic conditions in the solar photosphere we solved the Stokes transfer equations in a two-dimensional cross section through a simulation of magneto-convection (Stein et al. 2003). As shown in Uitenbroek et al. (2004), we

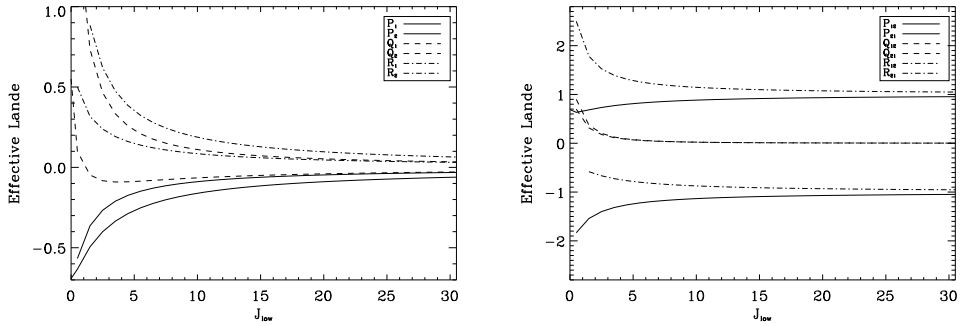

Figure 6.16: Effective Landé factor $\bar{g}$ for the lines of the main branches (left panel) and for the lines of the satellite branches (right panel). Note that the $\bar{g}$ factor for the P and R satellite lines approach unity when J increases, while for the main branch they always go to zero when J increases.

detect several positions along the slit in which the polarization on the CH lines arrives to 1 % of the local continuum intensity. Given that the size of these magnetic elements is ∼100 km, and if the element is isolated without opposite magnetic polarities within the resolution element, they should produce a polarization signal of order at least 10^{-4} even when the seeing induced telescope resolution is only of order 1 Mm (corresponding to slightly more than 1). In any case, it seems to be within the capabilities of current polarimetric instrumentation.

6.5.3 Integrated signal

As the spectro-polarimetric measurement of the CH signals seems to be very difficult, filter-polarimetry turns out to be an option in the quiet Sun. The ideal procedure would be to build a narrow filter centered at one of the three interesting regions and carry out imaging with this filter. To prevent cancelations in an antisymmetric profile, it would be ideal to build the filter centered in one of the one-lobed V profiles, like the lines at 4298 Å (being careful with the blend with the atomic lines) or at 4304 Å. The one-lobed signals do not suffer from this problem since there is never a cancelation when integrating on wavelength. The main advantage of these lines is that, since the Landé factor is relatively small (at least smaller than the highly sensitive lines with $\bar{g} = 2 - 3$),

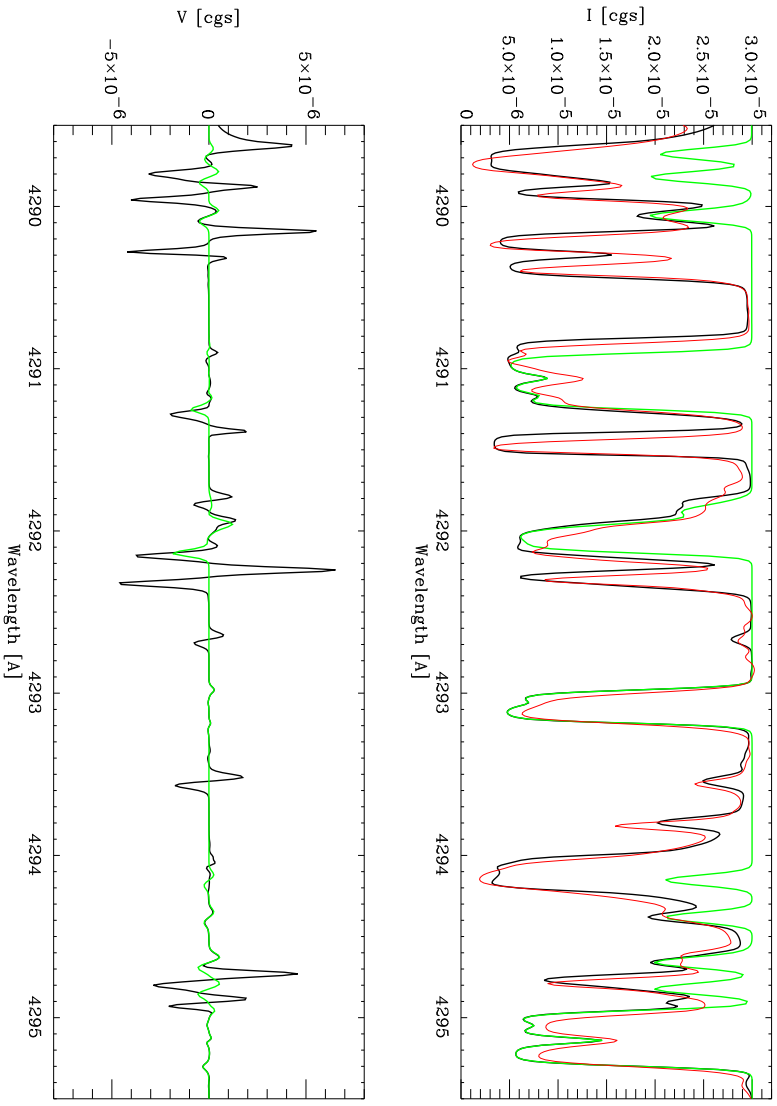

Figure 6.17: Synthetic Stokes I and V profiles of the G-band using the FAL-C model with a constant magnetic field of 1000 G pointing outwards. We show in black the complete spectrum including CH and atomic lines, in green the spectrum produced only by CH and in red the observed Stokes I spectrum from the Liège atlas. Here we show the region between 4290 and 4295 Å.

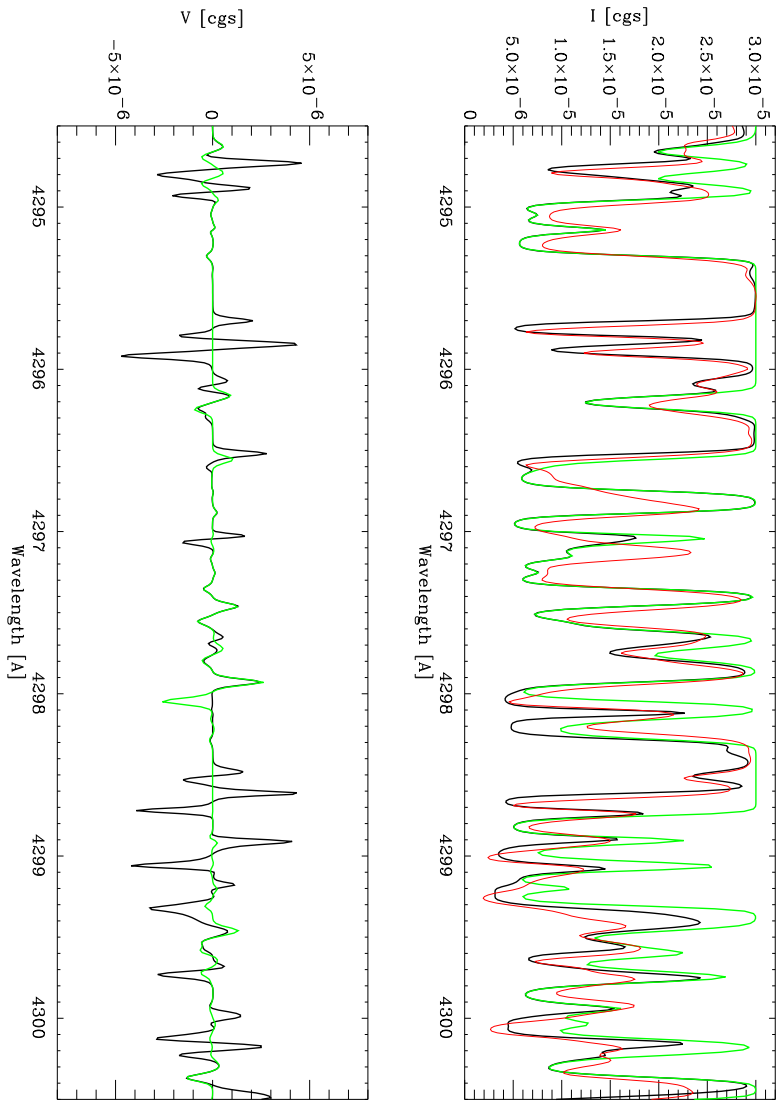

Figure 6.18: Same as Fig. 6.17 but between 4295 and 4300 Å.

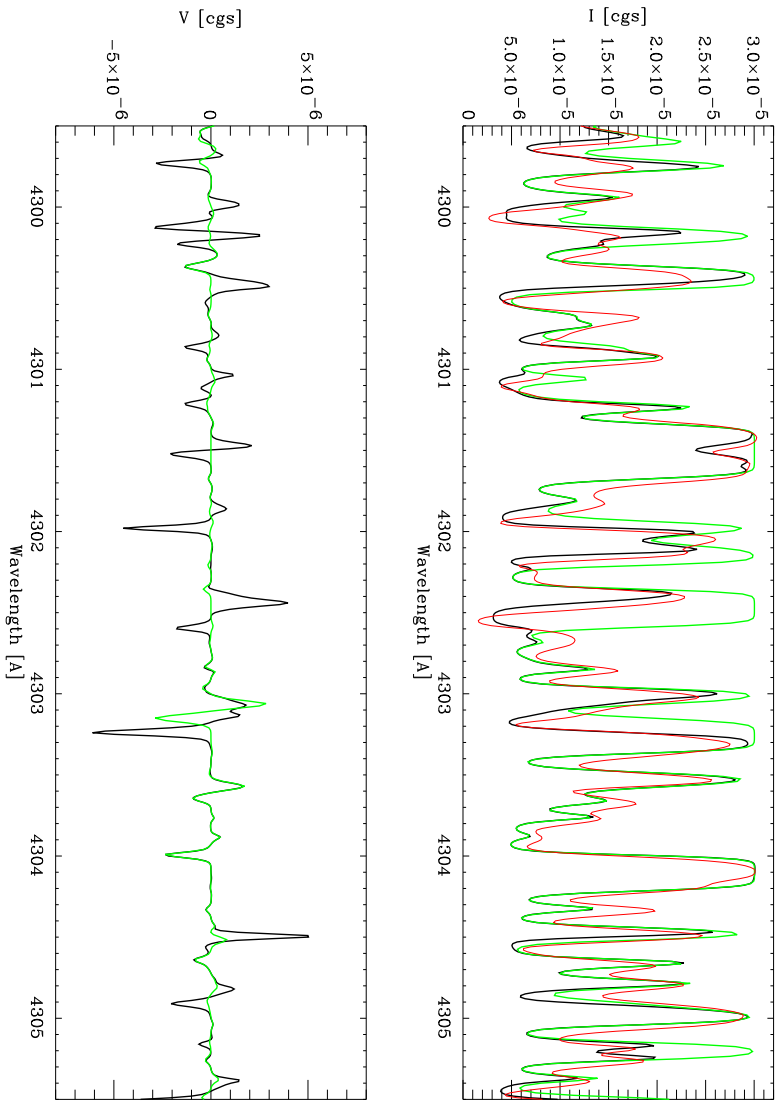

Figure 6.19: Same as Fig. 6.17 but between 4300 and 4305 Å.

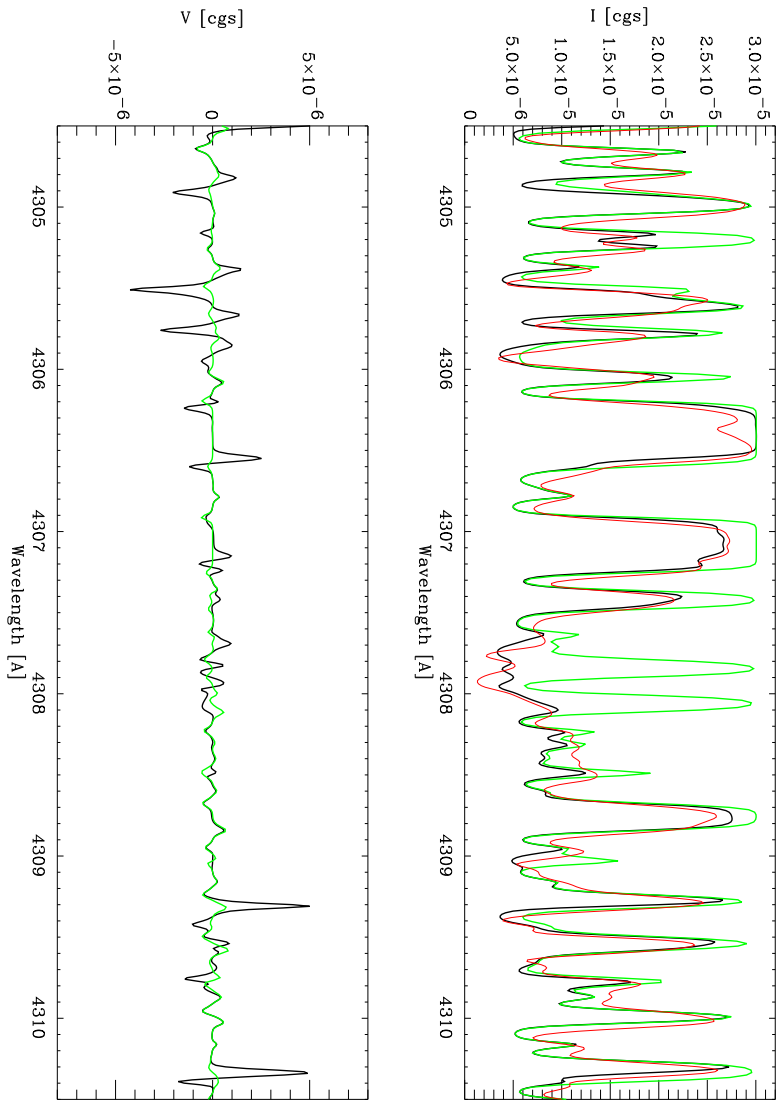

Figure 6.20: Same as Fig. 6.17 but between 4305 and 4310 Å.

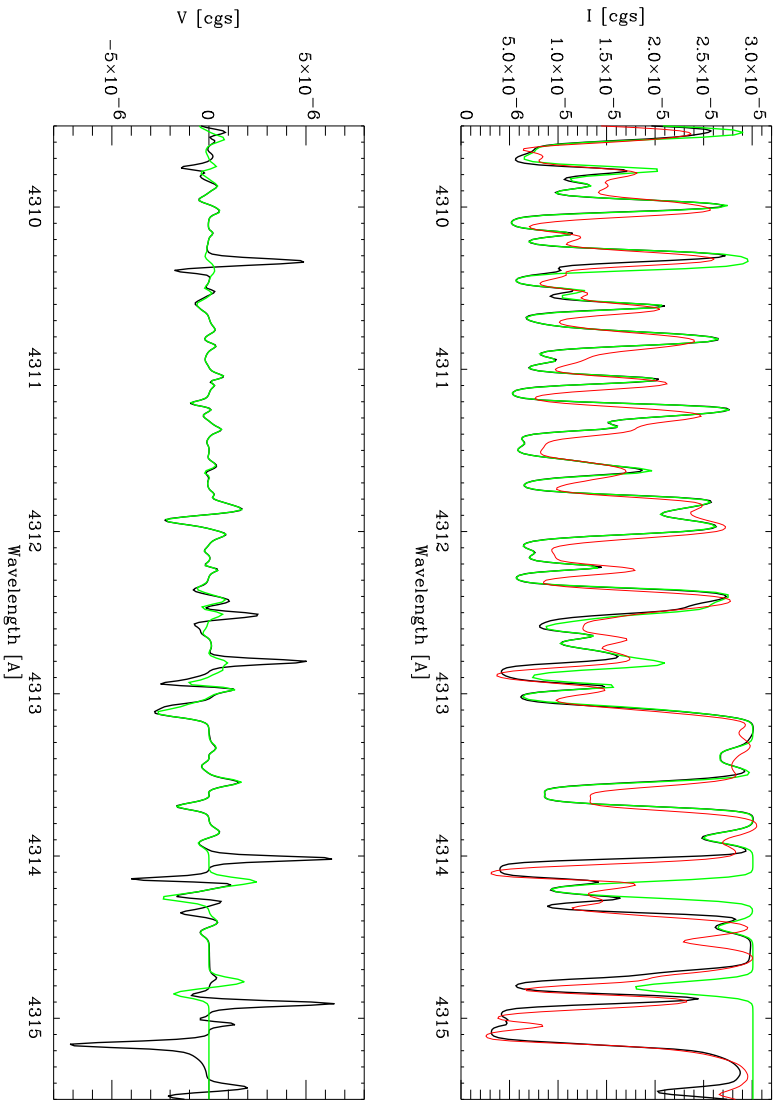

Figure 6.21: Same as Fig. 6.17 but between 4310 and 4315 Å.

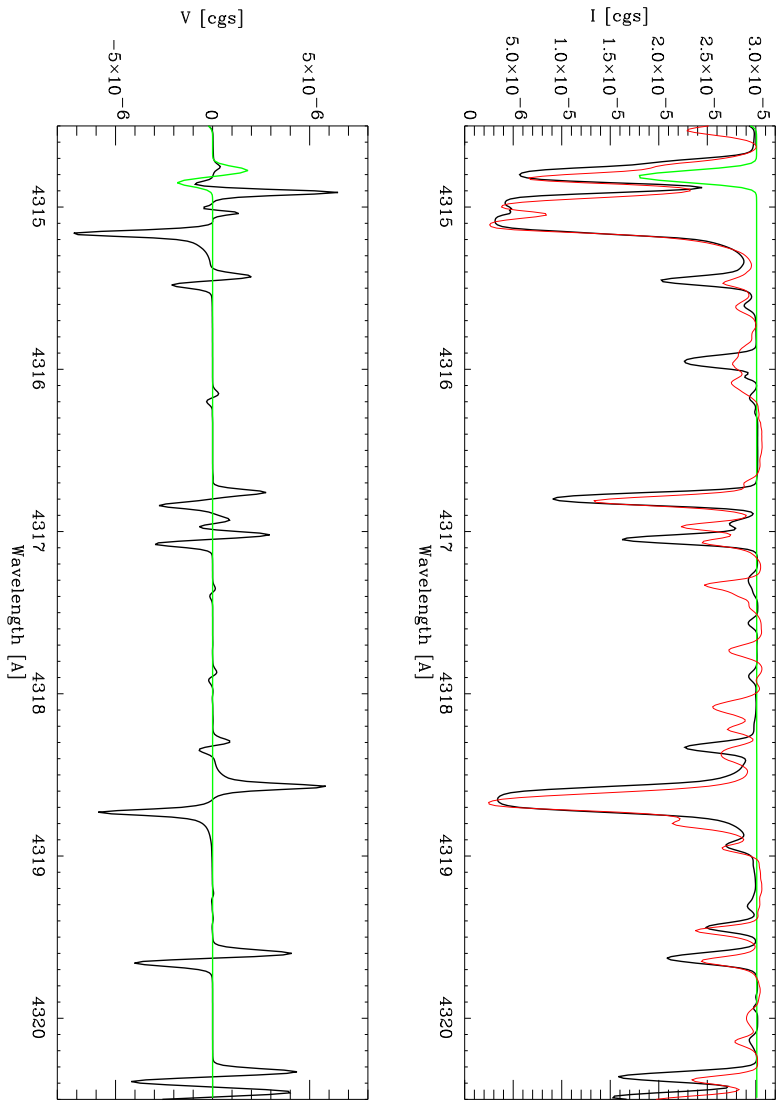

Figure 6.22: Same as Fig. 6.17 but between 4315 and 4320 Å.

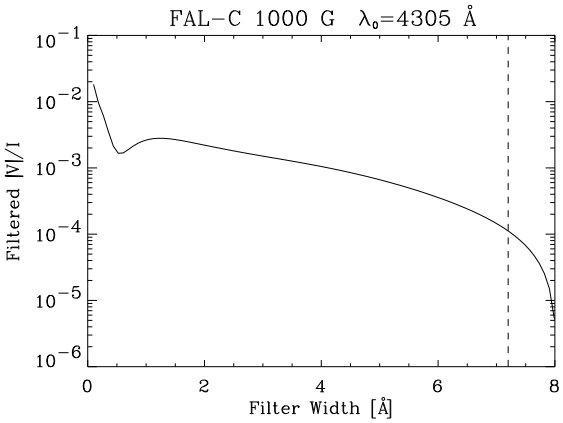

Figure 6.23: Filtered circular polarization signal in the G-band with a filter centered at 4305 Å and with different widths. Note that we show the absolute value of the V/I_c signal.

they are in the weak-field regime of the Zeeman effect up to very high fields. Therefore, the observed signal in the image is directly proportional to the field strength and to the filling factor (size of the magnetic element with respect to the resolution element).

The development of such a narrow filter (of the order of 200 mÅ) may allow the measurement of bright-point line-of-sight magnetic field strength. Such a method would have the full benefit of image quality improving techniques like adaptive optics and phase diversity restoration for optical spatial resolution. Another possibility would be to use the available wideband filters. To this end, we have calculated the integrated circular polarization signal obtained using a filter centered at 4305 Å with different widths. The filter is defined as:

$$f_G(\lambda) = f_0 \exp\left[-(\lambda - \lambda_0)^2/\sigma^2\right], \tag{6.12}$$

where λ_0=4305 Å and f_0 is a normalization constant such that

$$\int_{\lambda_{\rm min}}^{\lambda_{\rm max}} f_G(\lambda) d\lambda = 1. \tag{6.13}$$

$\lambda_{\rm min}$ and $\lambda_{\rm max}$ are 4295 Å and 4315 Å, respectively. In Fig. 6.23 we show the circular polarization integrated signal obtained with different filters, all

centered at 4305 Å, but with different widths σ. We have drawn a vertical line at the position of the G-band filter used by Berger et al. (1995) in their observations and by Sánchez Almeida et al. (2001) in their theoretical modeling. The width is 7.2 Å, equivalent to 12 Å of FWHM. The integrated or filtered circular polarization signal decreases when the filter width increases, except for very narrow filters. In this case, the signal locally increases for widths between 0.5 and 1 Å due to the local variation of the V/I_c signal. More precisely, this enhancement is produced by the atomic line at 4304.5 Å. When the width of the filter is 7.2 Å, the filtered signal is around 10^{-4}, i.e. 0.01 % for a filling factor of 1. The main disadvantage of this technique is that this very weak signal is mainly produced by atomic lines, which may not show the extreme behavior of the CH lines between the magnetic and non-magnetic regions.

6.5.4 Observational confirmation

The main aim of this section is to report on our observational confirmation of the above-mentioned theoretical prediction. To this end, we first show some selected examples of our theoretical modeling of the Zeeman effect in the G band, but considering the predicted fractional polarization in a sunspot model. We then focus on describing our observational confirmation, which we have achieved via sunspot spectropolarimetry in the G band using the Zürich Imaging Polarimeter (ZIMPOL; see Povel 2001) attached to the Gregory Coudé Telescope of IRSOL (Locarno; Switzerland).

Modeling the G band polarization in sunspots

Prior to showing the fractional polarization profiles we have observed in sunspots it is convenient to show some selected examples of our theoretical modeling of the G band polarization in a semi-empirical sunspot model. To this end, we have used the cool semi-empirical model of Collados et al. (1994), but assuming a vertical magnetic field of constant strength. This is sufficient for our demonstrative purposes, that is, for showing that the *shapes* of the computed V/I profiles agree with those we have observed in sunspots. The vector radiative transfer equation for the Stokes profiles is solved using the quasi-parabolic DELO method (Trujillo Bueno 2003b) in a way similar to that described by Uitenbroek et al. (2004).

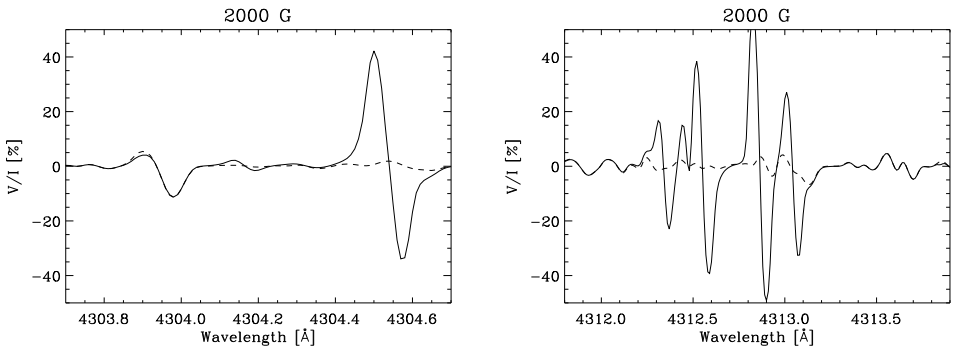

Figure 6.24: Calculated emergent $V(\lambda)/I(\lambda)$ in the cool umbra model of Collados et al. (1994) with a constant vertical magnetic field of 2000 G. The solid line represents the emergent fractional circular polarization taking into account both atomic and CH molecular lines, while the dashed line represents the emergent V/I taking into account only CH lines. The left panel shows the region around 4304 Å in which we find the single-lobed profile produced by CH alone. The other conspicuous signal is produced by an atomic line of Fe I. The right panel shows the region around 4313 Å, where we can find the profiles at 4312 Å and 4313.7 Å which are produced exclusively by CH lines. The signals between both are produced mainly by atomic lines. The strongest signal is due to Ti II.

Fig. 6.24 shows the calculated $V(\lambda)/I(\lambda)$ profiles in two spectral regions of the G band for a vertical magnetic field of 2000 G. The chosen line of sight is given by $\mu = \cos\theta = 0.95$, where θ is the heliocentric angle. The upper and lower panels correspond to the 4304 Å and 4312 Å spectral regions, respectively. The solid line represents the emergent Stokes profiles obtained by including both the atomic and CH lines, while the dashed line represents the emergent Stokes profiles obtained by including only the CH lines. The wavelengths and oscillator strengths for the CH lines have been obtained from the linelist of Jorgensen et al. (1996) while those for the atomic lines have been obtained from CD-ROM 1 by Kurucz[3]. In both instances we have V/I features dominated by CH lines only. For example, the one-lobe V/I profile at 4304 Å results from the blend between the $R_{1e}(1.5)$ and $R_{1f}(1.5)$ lines of the $v = 0 - 0$ band, which gives a Λ-doublet with effective Landé factor $\bar{g} = 0.8833$. The conspicuous V/I profile at 4313.7 Å is produced by the blend of the CH lines $Q_{11fe}(3.5)$ and $Q_{11ef}(3.5)$.

[3] `http://kurucz.harvard.edu`

Finally, the V/I feature at 4312 Å is produced by many overlapping CH lines, but mainly by the $P_{12ff}(5.5)$, $R_{21ff}(4.5)$, $Q_{22fe}(4.5)$ and $P_{12ee}(4.5)$ from the $v = 0 - 0$ band and by the $R_{21ff}(1.5)$, $P_{12ff}(4.5)$, $R_{21ee}(1.5)$ and $R_{21ff}(2.5)$ from the $v = 1-1$ band. As we see, the CH lines that produce clean V/I signals result from transitions between levels with small J-values (i.e., with $J \leq 5.5$).

Spectropolarimetric observations

The spectropolarimetric observations were carried out on 2003 August 30 in collaboration with Drs. Bianda (IRSOL) and Trujillo Bueno (IAC) by using the UV version of the Zürich Imaging Polarimeter (ZIMPOL; see Povel 2001) attached to the Gregory Coudé Telescope of IRSOL (Locarno; Switzerland). In order to facilitate an irrefutable observational proof of the predicted Stokes V/I profiles we selected a bipolar sunspot group (NOAA 0447), which was located at $\mu = 0.95$. We observed simultaneously the two sunspots of opposite magnetic polarity. To this end, a suitable optical device located after the polarimeter allowed us to rotate the solar image in order to get the image of the umbrae of the two main spots on that of the spectrograph slit. The direction of the slit formed an angle of 55° with respect to the closest limb. The slit width was 80 μm corresponding to $0.7''$. The spatial and spectral extensions covered by the ZIMPOL CCD were $160''$and 3.1 Å, respectively.

The ZIMPOL version used for these observations has one piezoelastic modulator (PEM), which allowed us to measure simultaneously Stokes I, Q/I and V/I. Due to the high modulation rate (42 kHz which is much higher than the typical seeing frequencies of the order of hundreds of Hertzs) the seeing-induced crosstalk is insignificant and the noise level in the polarization signals is defined only by the photons Poisson statistics. ZIMPOL is a one beam system and the same pixel of the CCD is used to measure all Stokes components. Therefore, no flatfield technique is needed to correct the polarization images. A calibration was performed by inserting known amounts of polarization in front of the polarimeter (PEM + linear polarizer) The data was also corrected for dark current table. Our measurements were performed adding 60 registrations, each of them taken with a 5 sec integration time. The reduced data are affected by instrumental polarization caused by the two folding mirrors inside the Gregory Coudé Telescope (for details see Gandorfer & Povel 1997). The ensuing effects are quite small and constant over the day and could be easily corrected. In or-

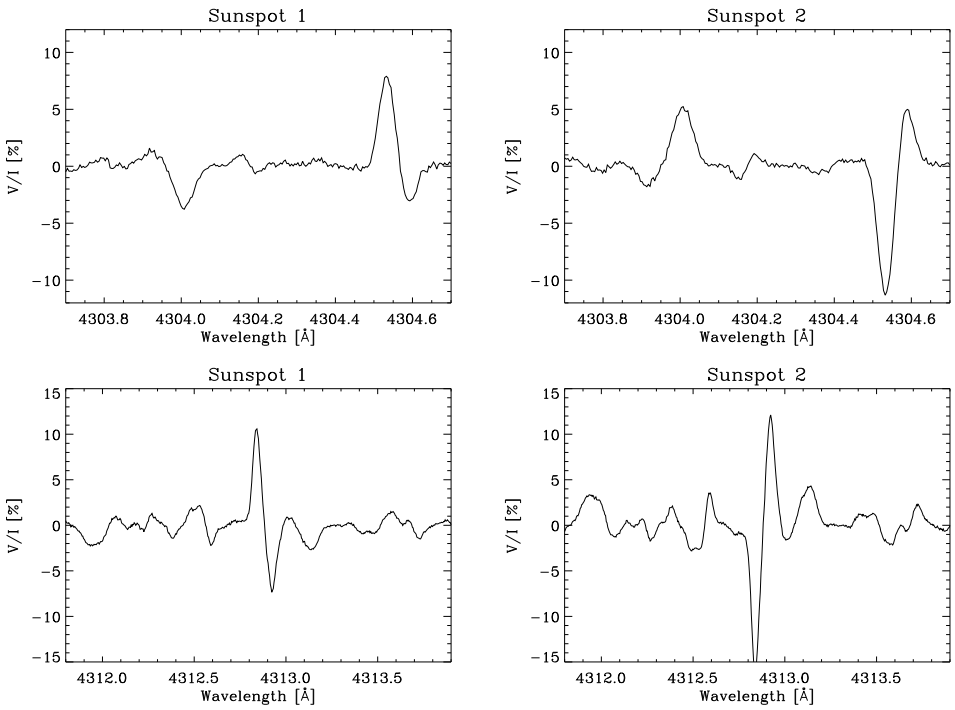

Figure 6.25: Observed V/I in the two spectral regions. The upper panels show the circular polarization profiles in two different sunspots with opposite polarity of the spectral region around 4304 Å. Note the good agreement between the modeling presented in Fig. 6.24 and the observation. The lower panel shows the profiles in the region around 4313 Å. The signatures produced by CH alone are in good agreement with the modeling. On the other hand, the agreement between the modeling and the observation for the atomic lines between 4312.5 Å and 4313.5 Å is not very good.

der to increase the signal-to-noise ratio of the V/I profiles shown in the figures below we averaged over 4 pixel along the spatial direction, which corresponds to 4.5" inside the sunspot umbrae. No other data reduction procedures like smoothing or filtering were applied.

The top panels of Fig. 6.25 show examples of the observed Stokes V profiles around 4304 Å, which is the wavelength position of the CH lines that were predicted to produce a peculiar Stokes V/I profile dominated by its red lobe.

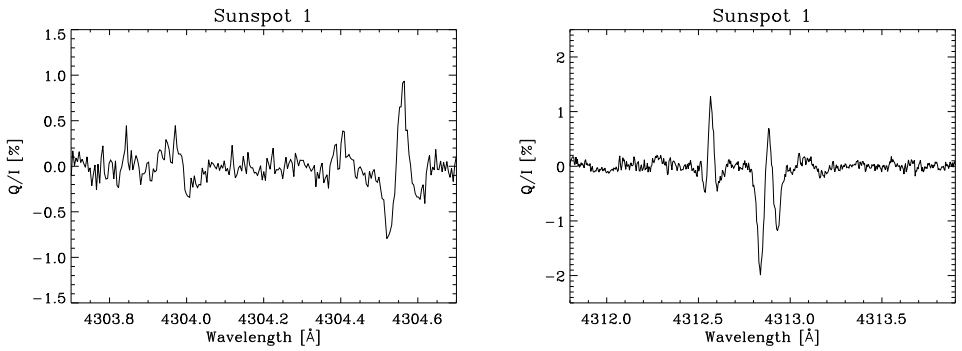

Figure 6.26: Observed Q/I in the two spectral regions for sunspot 1. Note that the conspicuous signals are produced by the atomic lines which also show strong V/I signals.

The left panel corresponds to the sunspot with the positive polarity (i.e., with the magnetic field vector pointing outwards), while the right panel refers to the sunspot with the negative polarity. In full agreement with the theoretical Stokes V/I profiles shown in Fig. 6.24 the observed circular polarization at 4304 Å is dominated by a single-lobed Stokes V profile whose sign changes when going to the sunspot with the other magnetic polarity. The same occurs with the Stokes V/I profile at 4304.6 Å, which is produced by atomic lines alone.

The bottom panels of Fig. 6.25 show the observed V/I profiles for an extra spectral region that also shows profiles dominated by CH lines alone. Note the polarity reversal between the two observed sunspots and the good agreement with the shapes of the theoretical V/I profiles at 4312 Å and 4313.7 Å shown in Fig. 6.24. The Stokes V/I profiles around 4313 Å are mainly due to atomic lines alone.

It is also interesting to mention that the observed linear polarization turns out to be very small at the above-mentioned wavelength locations which show V/I features dominated by CH lines. However, we have detected sizable Q/I signals (of the order of 1%) that are produced by atomic lines alone. We find significant linear polarization in both umbrae and penumbrae, with the signals in the penumbral regions being slightly larger than in the umbral ones. Figure 6.26 shows an example of the observed fractional linear polarization in the penumbra of one of the observed sunspots. We think that the conspicuous Q/I

feature at 4304 Å is produced by the same CH lines that are responsible of the observed V/I profile shown in the left panel of Fig. 6.25.

Conclusions

The polarization profiles we have observed in sunspots confirm our previous theoretical modeling of the Zeeman effect in the G band. There are at least three wavelength locations which show measurable V/I profiles that are produced by CH lines alone. The agreement between the *shapes* of the calculated and observed V/I profiles is remarkable. However, the calculated V/I *amplitudes* in one-dimensional models of sunspot atmospheres are substantially larger than the observed ones when the theoretical modeling is carried out assuming a magnetic filling factor $f = 1$ and a typical magnetic field strength of 2000 G. We consider this as an indication of spatially unresolved magnetic fields in the photospheric regions of sunspot umbrae, with a strong and a weaker field component coexisting within the spatio-temporal resolution element of the observation. The weak field component might be associated with the multitude of umbral dots that are seen in high resolution images of sunspots.

In the sunspot group we have observed (located at $\mu = 0.95$) the observed linear polarization at the wavelength location of such CH lines was very small, but not negligible (see, e.g., the Q/I feature at 4304 Å). However, we have found sizable circular and linear polarization signals in many of the atomic lines that are contained in the spectral region of the G band. Such polarization signals in molecular and atomic lines contain valuable information about the physical conditions in the solar atmosphere. In particular, the theoretical interpretation of the observed polarization in the (*weak*) CH lines we have investigated offers a new diagnostic window for exploring the thermal and magnetic structuring of the solar plasma in relatively deep regions of sunspot photospheres. This type of investigations could help us to choose among competing MHD models on the three-dimensional structure of sunspot umbrae. In a future paper we will address the issue of the inversion of spectropolarimetric observations in the G band, since this promises to be of great interest for improving our knowledge on solar and stellar magnetism.

6.6 Detection of polarization from the $E^4\Pi - A^4\Pi$ system of FeH in sunspot spectra

6.6.1 Introduction

FeH constitutes one of the most important opacity contributors in late-type dwarfs, in the red and near-infrared between 0.7 μm and 1.3 μm. It was however detected in the atmospheres of late M dwarfs much later than many of the other hydrides formed with less abundant atomic species. This is probably due to the fact that the FeH spectrum is very complicated, arising from quartet and sextet terms (Langhoff & Bauschlicher 1990). Although some bands are in the optical and blue part of the spectrum, the crowding of atomic lines makes it difficult to distinguish FeH bands. For this reason, the most studied FeH electronic system is that produced by the transition $F^4\Delta - X^4\Delta$. This band system, widely used in studies of late-type dwarfs, produces a conspicuous absorption near 1 μm. Theoretical analysis of this band system has been performed by Phillips et al. (1987) with the assignation of quantum numbers to many of the observed lines of the $v = 0 - 0$ band.

In a recent study of the infrared intensity spectrum of sunspots, Wallace & Hinkle (2001) identified almost 70 lines between 1.58 μm and 1.755 μm common to both the sunspot spectrum and a furnace laboratory spectrum of FeH . They tentatively associated these lines to the $E^4\Pi - A^4\Pi$ system based on the theoretical work of Langhoff & Bauschlicher (1990). These authors predicted this band system to be around 2 times weaker than the $F^4\Delta - X^4\Delta$ system, even though the $E^4\Pi - A^4\Pi$ is one of the strongest bands of the quartet system in FeH. Later, Cushing et al. (2003) compared the near-infrared spectrum of four late-type dwarfs with the laboratory FeH spectrum, finding 34 features that dominate in the H-band spectra. They associated some of these features to the $v = 0 - 0$ $E^4\Pi - A^4\Pi$ band of FeH. They found a very similar behavior of this band and the other IR bands of FeH when observing stars of different spectral types, thus reinforcing that these features belong to FeH.

There are almost no studies of the polarization properties of FeH lines. A first attempt has been carried out by Berdyugina et al. (2001) and by Berdyugina & Solanki (2002) for lines of the $F^4\Delta - X^4\Delta$ system, assuming that the angular momentum coupling is that given by Hund's case (a) (see Herzberg 1950). These authors were forced to use Hund's case (a) coupling because no

estimation of the spin-orbit coupling constants of the electronic states of the transition are available. In view of the effective Landé factors, they concluded that the $F^4\Delta - X^4\Delta$ band system of FeH might be of interest for the investigation of the magnetic properties of solar and stellar atmospheres.

We present the first full Stokes observations of FeH in the near infrared, showing that the $E^4\Pi - A^4\Pi$ band system must be in intermediate coupling between Hund's cases (a) and (b). To our knowledge, this is the first time polarization signals in FeH are observationally detected in a sunspot (Asensio Ramos et al. 2004).

6.6.2 Observations

The observations were carried out on June 7, 2002 with the Tenerife Infrared Polarimeter (TIP; see Martínez Pillet et al. 1999) mounted on the German Vacuum Tower Telescope (VTT) at the Observatorio del Teide (Spain). The observed sunspot was located out of the solar disk center, at $\mu = 0.68$ (being μ the cosine of the heliocentric angle), so that linear polarization signals may be expected.

The total size of the umbra was $\sim$18". The presence of a light bridge crossing the sunspot umbra led us to select only those points within the umbra whose polarization properties are not contaminated by the presence of the light bridge. Interestingly, the depth of the observed FeH intensity profiles is reduced close to the light bridge, possibly due to the dissociation of the FeH molecules caused by a temperature increase. Similarly, we found a smaller amplitude in the Stokes V spectrum.

The spectral resolution of the observation was $\sim$26 mÅ with a total wavelength coverage of $\sim$7 Å. In order to investigate the polarization properties of FeH lines, we performed three scannings with a step of 0.4" for different spectral regions and three time series with the slit crossing the center of the umbra. The integration time for each position in the scanning was 1 second, while the total integration time for the time series was between 5 and 10 minutes. Although the detection of the FeH features is obtained also in the 1 second integrations, we have used the temporally averaged Stokes profiles which have a much larger signal-to-noise ratio. The typical noise level is $\sim 10^{-4}$ of the continuum intensity.

As shown below in Fig. 6.30, the observed FeH transitions, apart from

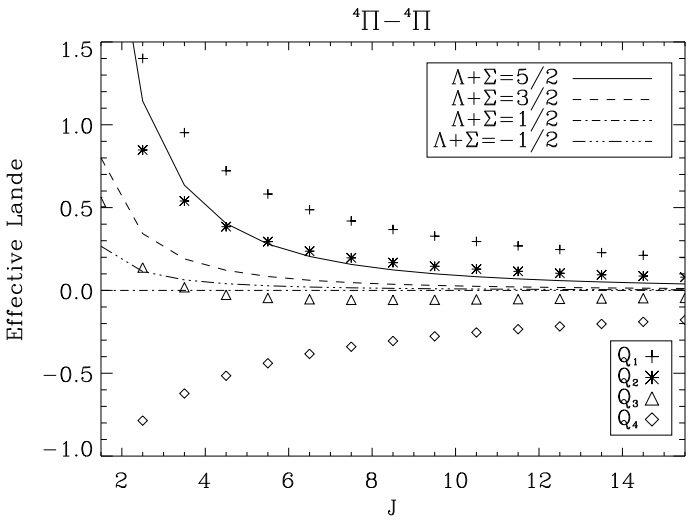

Figure 6.27: Effective Landé factor of the Q branch of the $E^4\Pi - A^4\Pi$ band system of FeH calculated using Hund's case (a) coupling (lines) and Hund's case (b) coupling (symbols). The lines between the $\Lambda + \Sigma = 1/2$ levels are completely insensitive to the magnetic field in Hund's coupling case (a). Note that while the effective Landé factor is always non-negative for Hund's case (a) coupling, it can become negative for Hund's case (b) coupling.

producing conspicuous antisymmetric V signals, also show perfectly detectable symmetric Stokes Q and U profiles. However, we will only focus on Stokes V.

6.6.3 The Zeeman effect in FeH

Since no perturbation analysis has been performed for any of the electronic states of FeH, no spin-orbit coupling constants are available. This makes it necessary to treat the lines of both the $F^4\Delta - X^4\Delta$ and the $E^4\Pi - A^4\Pi$ system in any of the limiting Hund's coupling cases. However, according to Berdyugina & Solanki (2002), the $F^4\Delta - X^4\Delta$ system is known to be in intermediate coupling between (a) and (b) and strong deviations of the effective Landé factor $\bar{g}$ for the lines of the P and R branches are expected from that given by Hund's case (a). In particular, $\bar{g}$ for the lines of the P and R branches will increase as J increases. This increase in the Zeeman sensitivity has been observed by Wallace et al. (1999) in the intensity spectrum of sunspots associated to an increase in

the broadening of the high J lines. A similar behavior is expected for the lines of the $E^4\Pi - A^4\Pi$ band. Wallace & Hinkle (2001) apparently detected such a behavior from the line splitting in the intensity spectrum. They found many FeH lines which appear undoubled but a set of seven lines around 15930 Å which present a splitting, probably caused by the Zeeman effect since it increases with the field strength in sunspots.

For those electronic levels with $\Lambda \neq 0$, the spin-orbit coupling constants are usually large (see Huber & Herzberg 2003). Therefore, the energy separation associated to the multiplet splitting is expected to be large. We also expect the spin-orbit coupling to be large enough so that the field at which the Paschen-Back transition occurs is larger than the typical field strength of sunspots. In fact, this is the case with all the molecules studied by Berdyugina & Solanki (2002) presenting $\Lambda \neq 0$. If the FeH lines that belong to the $E^4\Pi - A^4\Pi$ system are indeed in the Zeeman regime, we expect Stokes profiles similar to those of a normal Zeeman triplet. This is in fact confirmed by the observations.

The value of the effective Landé factor calculated in Hund's case (a) coupling for the lines of the Q branch of the $E^4\Pi - A^4\Pi$ band is shown in Fig. 6.27. Since the lines are between electronic levels of the same quantum numbers, $\bar{g}$ can be written as (Herzberg 1950)

$$\bar{g} = 2\frac{(\Lambda + 2\Sigma)(\Lambda + \Sigma)}{J(J+1)}, \tag{6.14}$$

where $\Lambda = 1$ and $\Sigma = 3/2, 1/2, -1/2, -3/2$. We have not included $\bar{g}$ for the lines of the P and R branches because it is zero. Note that the lines between levels with $\Lambda + \Sigma = 1/2$ are insensitive to the magnetic field. The rest of lines belonging to transitions between low J levels seem to be as sensitive to the magnetic field as those of the $F^4\Delta - X^4\Delta$ system studied by Berdyugina & Solanki (2002). It is very important to note that all the values of $\bar{g}$ are non-negative, contrary to what happens for the $F^4\Delta - X^4\Delta$ system.

Although little magnetic field diagnostics can be done at present with these lines given the lack of precise spectroscopic data, we have used the observed polarization signals in order to get a first insight into the potential diagnostic interest of these FeH lines.

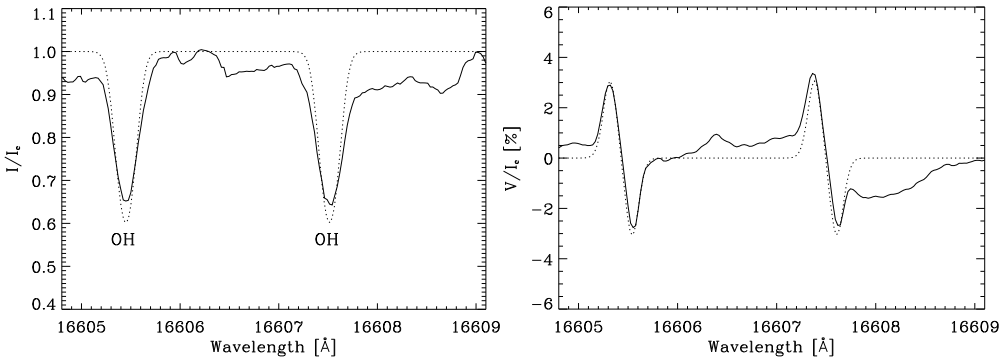

Figure 6.28: Two OH lines close to the studied FeH lines. Since the coupling constants of OH are known, we have calculated the emergent Stokes profiles from the Collados et al. 1994 hot umbra model, finding that a constant magnetic field of 1800 G provides a fairly good fit the observed Stokes profiles. The solid line represents the observation while the dotted line is the modeling.

6.6.4 Discussion

We have observed three spectral regions. A region around 16605 Å, another one around 16110 Å, and a third one around 16575 Å. The observation of the first region was motivated by the presence of two vibration-rotation OH lines of the $X^2\Pi$ level, similar to those observed by Harvey (1985). Because the spectroscopic constants of OH are known, these lines can be used to obtain information about the magnetic field in sunspots. To this end, as shown in Fig. 2, we have performed LTE syntheses in the hot umbra model of Collados et al. (1994) finding that a constant vertical magnetic field of 1800 G pointing radially outwards leads to a fairly good fit to the observed Stokes profiles in the OH lines[4]. The Zeeman patterns for the OH lines have been obtained applying the theory developed by Schadee (1978), thus they do not depend on any assumption about the coupling. We point out that since the OH lines are stronger than the FeH lines, a magnetic strength of 1800 G gives only a lower limit to the strength of the field in the deeper regions of the sunspot umbra where the FeH polarization is originated. Assuming a typical gradient of 4 G km^{-1} (Collados et al. 1994), we estimate that the magnetic field in the

[4]The LTE synthesis in the cool umbra model of Collados et al. (1994) presents OH line absorptions much deeper than the observations.

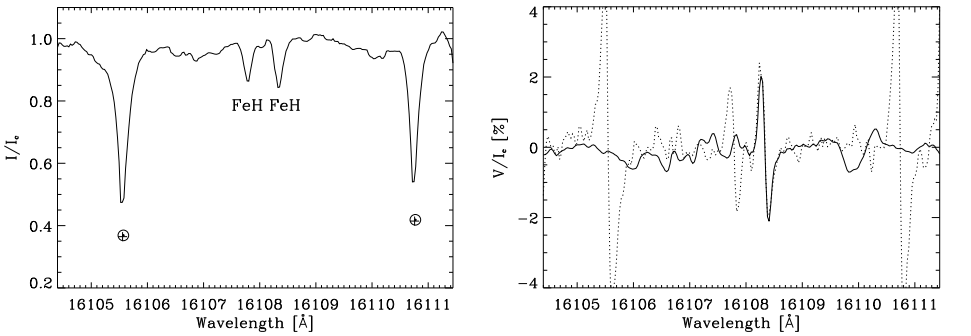

Figure 6.29: Observed FeH lines together with the fit obtained via the weak-field approximation for B =2400 G. The two strong lines in the extremes of the spectral interval are telluric absorption produced by CH_4. The solid line represents the observation while the dotted line the derivative of the intensity spectrum scaled with $\bar{g} = 0.09$ in order to fit the line at 16108.3 Å.

formation region of the FeH lines may be 400-600 G higher than in the OH formation region. For this reason, we have assumed B=2400 G in the following estimations of the effective Landé factors of the observed FeH lines.

In order to obtain information about the approximate value of the effective Landé factor of the FeH lines, we have applied two different techniques. The first one assumes that the line is formed under the weak field (WF) approximation (e.g. Landi Degl'Innocenti 1992). Molecular lines usually have small effective Landé factors except for lines that arise between levels with very small values of J (see Herzberg 1950; Landau & Lifshitz 1982). Since the Zeeman splitting in the IR is relatively large, and assuming typical thermal and microturbulent velocities, the weak field approximation is valid for $\bar{g}B \ll 1000$ G, which is somewhat restrictive for some of our FeH lines. The second one assumes that the line is formed in the strong field (SF) regime so that peak separation in Stokes V is indicative of the separation of the σ components when they are fully split. Since the lines are not in any of these limiting regimes, the correct effective Landé factors will be between both.

Fig. 6.29 shows two FeH lines at 16108 Å, one of which produces a clear circular polarization signal, while the other is apparently insensitive to the Zeeman effect. We show in the same figure the fit obtained to the line at

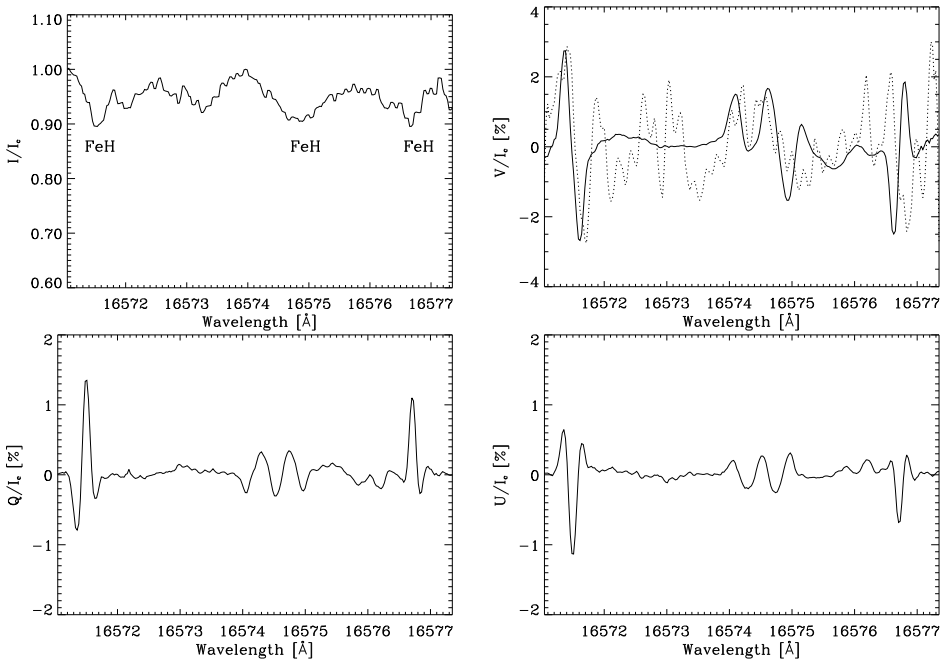

Figure 6.30: Region with several FeH lines producing weak absorptions in the intensity spectrum but very clear features in the circular polarization spectrum. We show also the derivative of the intensity spectrum scaled with $\bar{g} = 0.38$. Note that the line near 16577 Å has negative effective Landé factor. The two lower panels show the observed linear polarization spectrum.

16108.3 Å by plotting the derivative of the intensity spectrum multiplied by the scaling factor using $\bar{g}_{\rm WF} = 0.09$, which represents an approximation to the effective Landé factor of this line. Note that the fit of the magnetic sensitive line is strikingly good for this combination of field strength and $\bar{g}$. From the previous fit, we can infer that the strong field regime has not been reached, since the separation of both Stokes V lobes are correctly obtained with the weak field formula. This is reinforced by the low value obtained for $\bar{g}$. In the strong field regime, we obtain $\bar{g}_{\rm SF} \approx 0.24$.

The FeH line at 16107.8 Å may be assumed to have $\bar{g} \approx 0$, in principle, since at first sight there seems to be no significant signal in Fig. 6.29. However, a closer inspection indicates that a very small V signal with $\bar{g} < 0$ seems to be present in our observations. This may constitute a first indication that

deviations from Hund's case (a) are expected for these lines. Another but much stronger indication will be discussed below.

Fig. 6.30 shows three FeH lines around 16575 Å which have been detected previously in intensity by Wallace & Hinkle (2001). These lines are quite weak in the sunspot intensity spectrum and it has been difficult to apply the weak-field approximation since the derivative of the intensity profile turns out to be very noisy. In any case, we have obtained a value of $\bar{g}_{\rm WF} \approx 0.38$ for the line at 16571.5 Å and a value of $\bar{g}_{\rm WF} \approx -0.38$ for the line at 16576.8 Å. According to the results shown in Fig. 6.27, a negative $\bar{g}$ is not possible in Hund's case (a). This constitutes our strongest proof that this band of FeH is in the intermediate coupling case between Hund's cases (a) and (b). The coupling constants and the line identifications have to be obtained in case the lines of this band are to be used as tools for diagnosing magnetic properties of the coolest regions of sunspot atmospheres or magnetic fields on cool dwarfs. The line at 16575 Å seems to be a blend of some FeH lines at slightly different wavelengths due to the intricate structure of Stokes V with apparent cancelations among them. The linear polarization signal is in the lower panel of Fig. 6.30. Note that all the FeH lines produce conspicuous Stokes Q and U features with an amplitude of around 1%. If we assume that the lines are in the strong field regime, we obtain $\bar{g}_{\rm SF} \approx 0.39$ for the line at 16571.5 Å and $\bar{g}_{\rm SF} \approx -0.28$ for the line at 16576.8 Å from the peak separation in Stokes V.

Our previous results can be compared with the effective Landé factor obtained from the fully split FeH lines in the atlas of the umbral spectrum of Wallace & Livingston (1992). For a field of 3500 G obtained from the fully split V I line at 16570.5 Å whose effective Landé factor is $\bar{g} = 0.7$, one obtains $\bar{g}_{\rm SF} \approx 0.27$ and $\bar{g}_{\rm SF} \approx -0.19$ for the lines at 16571.5 and 16576.8 Å respectively. Comparing with the results obtained directly from our spectropolarimetric observations, we verify that in the sunspot we observed we are in the intermediate field regime.

6.6.5 Conclusions

We have shown observational evidence that the lines of the $E^4\Pi - A^4\Pi$ electronic system of FeH present circular and linear polarization signals that are produced by the Zeeman effect. We have estimated the magnetic field with the aid of two OH lines and inferred the effective Landé factors of the FeH lines using either

the weak-field or the strong-field approximations. We have shown that the $E^4\Pi - A^4\Pi$ band of FeH presents lines with negative effective Landé factors, which is impossible under Hund's case (a) coupling. Therefore, we conclude that this molecular band system must be in intermediate angular momentum coupling between Hund's cases (a) and (b). The FeH lines studied here are potentially interesting for empirical investigations on the physical conditions in the lower atmosphere of sunspots and on the magnetism of late-type dwarfs. To this end, theoretical and/or laboratory investigations of this molecular system are urgently needed.

6.7 Applications to other interesting molecules

Other molecular species may present an observable Zeeman signal in the solar, stellar or interstellar spectrum. We will discuss in this section some examples and their predicted polarization signal. Some of the synthesis have been obtained using the simplified solution of the RT equation of Unno (1956) (see also Landi Degl'Innocenti & Landi Degl'Innocenti 1973). This solution is based on a Milne-Eddington atmosphere. We will use Gaussian profiles with a thermal width equivalent to the typical temperature in each object.

6.7.1 CO

The fundamental electronic state of CO is $X^1\Sigma^+$ and the energy gap between this level and the first excited level is 48686.7 cm^{-1}, high enough to make the fundamental level the most populated. Moreover, the following excited levels are triplets, instead of singlets, so that transitions between these states and the fundamental one are very improbable. The energy difference with the first singlet state is 65075.7 cm^{-1}. The transition between these levels lies in the extreme UV around 1540 Å. The observed transitions in the radio and infrared spectral regions are pure rotation and vibro-rotation transitions inside the fundamental level, respectively. Since the fundamental level has $S = 0$ and $\Lambda = 0$, the Zeeman effect is here produced by the coupling between the rotational angular momentum and the magnetic field. We have included this possibility in the effective Hamiltonian by a term proportional to the scalar product of the rotational angular momentum and the magnetic field vector. The proportionality constant is the rotational g_r factor. The effect of this coupling is

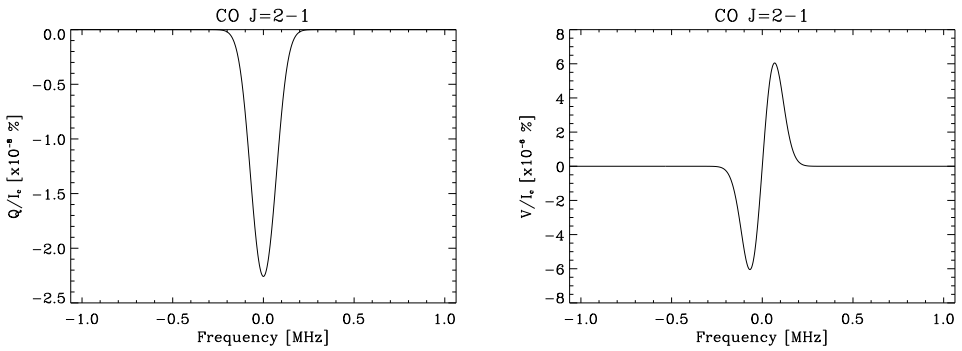

Figure 6.31: Emergent Stokes Q and V in a molecular cloud for the pure rotational $J = 2 - 1$ CO line.

around m_e/m_p times smaller than the electronic coupling. Therefore, we expect a very small splitting for CO and, consequently, an extremely weak V-signal. Due to this small Zeeman splitting and the value of the rotational constants Huber & Herzberg (2003), no transition to the Paschen-Back regime can occur for fields below 10^7-10^8 G.

As an example, we show in Fig. 6.31 the Stokes profiles induced by the Zeeman effect in a molecular cloud for the CO pure rotational line $J = 2-1$. As representative of the physical conditions in the cloud, we select a temperature of 20 K and a magnetic field of 1 mG. The line strength is chosen to be $\eta_0 = 0.1$. We assume observation at $\mu = 1$ while the inclination of the field is 45° and the azimuth is 0°. This pure rotational transition is situated at 230.538 GHz, equivalent to $1.301{\times}10^7$ Å. Note that the signal is extremely small due to the low CO effective Landé factor and the low magnetic field strength. Therefore, the pure rotational CO transitions are not good tracers of the magnetic field present in a molecular cloud. The same can be stated from the vibro-rotational transition of CO. The angular momentum coupling scheme is independent on the vibrational state of the molecule, so that the vibro-rotational band of CO at 4.7 μm and all its overtones at 2.3 μm, 1.15 μm, ... can be assumed to be insensitive to the magnetic field. More sensitive molecules are those having $S \neq 0$ and/or $\Lambda \neq 0$.

6.7.2 SH

The mercapto SH radical has been detected in the solar atmosphere by Berdyugina & Livingston (2002). Chemical equilibrium calculations have shown that SH should be quite abundant in oxygen-rich stellar atmospheres (Tsuji 1973). However, it has been astronomically detected only recently by Yamamura et al. (2000). The $A^2\Sigma^+ - X^2\Pi$ $v = 0 - 0$ electronic transition is found in the UV around 3280 Å. The spin-orbit coupling constant of the lower level is $A = -376.9$ cm^{-1}, while the spin-rotation coupling constant of the upper level is $\gamma = 0.313$ cm^{-1}. Therefore, the transition to the Paschen-Back regime is expected for fields above $\sim$6700 G. Observing polarization signals in this UV region has not been accomplished yet. Apart from the technological problem, and remembering that the Zeeman splitting goes as λ^2, the peak separation in the Stokes V signal is very small, around 20 times smaller than for the IR region of the OH and CN lines. Additionally, the crowding of atomic lines in the UV region becomes impressive and may result difficult to detect the polarization signal.

6.8 Conclusion

We have shown in this Chapter that the Zeeman patterns and component strengths for doublet states obtained with the numerical diagonalization of the rotational effective Hamiltonian leads to the same results as the formulation of the Zeeman effect in diatomic molecules given by Schadee (1978). The advantage of our numerical diagonalization is that it allows to include any additional effect straightforwardly by adding its contribution to the total Hamiltonian. Another advantage is that electronic states with any multiplicity can be tackled.

With the aid of the previous techniques, we have investigated in detail the generation and transfer of polarized radiation induced by the molecular Zeeman effect in the solar atmosphere. We have detected anomalous linear polarization profiles in CN lines. We have shown that these anomalous profiles are produced by the especial Zeeman patterns of the CN lines. In order to obtain as much information as possible from the spectropolarimetric observations, we have developed an inversion code for the Stokes profiles induced by the Zeeman effect in atomic and molecular lines. We have applied this code to OH and CN

profiles observed in a sunspot.

We have investigated in detail the polarization properties of the CH lines in the G band via numerical modeling. We have detected several CH lines which appear to be not blended with other atomic lines. We have also identified a set of CH lines which show single-lobed profiles. This line could be used to obtain high angular resolution images which allow to measure the line-of-sight magnetic field using narrowband filters. We have also shown that these one-lobed profiles are indeed found in the solar spectrum.

We have detected for the first time polarization signals in lines of the $E^4\Pi - A^4\Pi$ system of FeH in sunspot spectra. Since no spectroscopic information is available for this system, we have only been able to obtain approximate values for the effective Landé factors using either the weak-field or the strong-field approximations. The strongest conclusion of this investigation is that the rotational lines of this system are in an intermediate Hund's case between (a) and (b). We show that the FeH lines studied are potentially interesting for empirical investigations on the physical conditions in the lower atmosphere of sunspots and on the magnetism of late-type dwarfs. To this end, theoretical and/or laboratory investigations of this molecular system are urgently needed.

Finally, we have also investigated the polarization signal induced by the Zeeman effect produced by other molecules.

7

Scattering Polarization and the Hanle Effect in Molecular Lines

One of the surprises of the second solar spectrum (the linearly polarized Q/I spectrum produced by scattering processes on the Sun) was the discovery that molecular lines, although typically faint in the intensity spectrum of the quiet Sun, usually show sizable scattering polarization peaks, even dominating the polarized spectrum in some spectral regions. That is the case for MgH, C_2 and CN (see Stenflo & Keller 1997, Gandorfer 2000, Stenflo 2003a, Gandorfer 2003). In this chapter, we focus on the modeling issue of such scattering polarization observations in MgH, C_2 and CN lines and on the influence of the magnetic field in the emerging linear polarization signal through the Hanle effect.

One of the most striking features of the molecular lines is their apparent magnetic immunity. When scattering polarization observations are performed on different moments of the solar cycle, the Q/I signals produced by molecular lines appear to be always the same (compare the Q/I amplitudes reported by Stenflo & Keller 1997 with those of Gandorfer 2000). Furthermore, the observations also show an apparently constant Q/I amplitude along the slit, even when many (strong) atomic lines which produce scattering polarization do present variation along the slit. However, the magnetic fields at which the Hanle effect is expected to start to operate on molecular levels is of the same

order of magnitude of the Hanle field for atomic lines. The molecular levels present much smaller Landé factors, but this is counteracted by their higher lifetimes (Landi Degl'Innocenti 2003; Trujillo Bueno 2003c, 2003b). Therefore, in principle, the molecular lines should be also as sensitive as atomic lines to the Hanle effect. The apparent immunity can be explained by two facts. On the one hand, the linear polarization signal of the molecular lines are coming mainly from the granular regions, where the magnetic fields are expected to be weak (see Trujillo Bueno 2003b). On the other hand, as shown below, the calculated Q/I signal remains practically constant up to the field strength for which the upper level polarization begins to react. The lower level polarization does not produce observable effects if dichroism is taken into account.

7.1 Some details on scattering polarization in molecular lines

The study of scattering polarization in molecular lines has seen very little progress after some pioneering work that dates back to the late 1930's (see e.g. Herzberg 1950 and references therein). These studies were mainly devoted to the interpretation of laboratory experiments and therefore are of reduced interest to the astrophysical case, as noted by Landi Degl'Innocenti (2003). When one considers the scattering polarization problem in molecular lines, one has to take into account that there are two possible situations, depending on whether the pumping transition or the observed transition is selected:

- **The laboratory case**. Consider a molecule in a lower rotational level J_l' which is excited to a rotational level J_u by the absorption of a photon (selective pumping). In the decay process to a lower level J_l, due to the possible selection rules, the molecule may return to the initial rotational level $J_l = J_l'$ (Rayleigh scattering produced in a Q transition) or to a different level $J_l \neq J_l'$ (Raman scattering produced in a R or P transition). The situation is schematized in the left panel of Fig. 7.1. This situation is typical of laboratory conditions in which one excites a given molecule with a photon of a known frequency and is interested in the re-emission (scattering) of the photon.

- **The astrophysical case**. The astrophysical case is somewhat different. One is interested in knowing the polarization properties of a given line

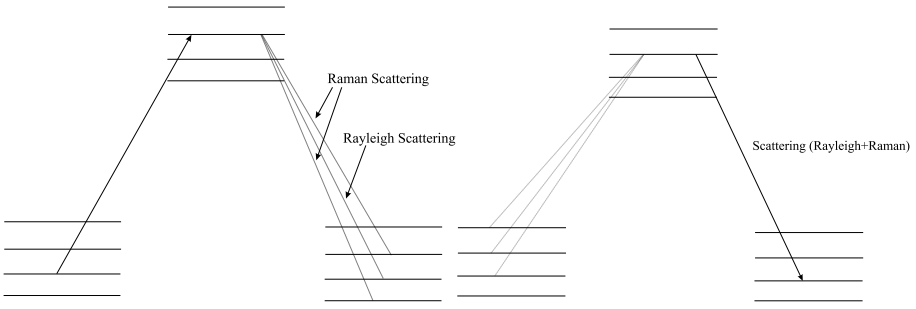

Figure 7.1: Scattering phenomena in molecules. On the left panel we show the typical laboratory experiment in which the molecule is excited by selective pumping. In the decay process, the molecule may return to the initial level (Rayleigh scattering) or to a different level (Raman scattering). On the right panel we show the typical astrophysical situation. A rotational level is pumped from lower states by several transitions following the selection rules. The decay process can be considered as a combination of Rayleigh and Raman scattering (from Landi Degl'Innocenti 2003).

which is produced by the transition between an upper rotational level J_u and a lower rotational level J_l. However, the upper level can be pumped by different transitions (R, P or Q lines) and the spectral line one is interested in is not completely defined by Rayleigh or Raman scattering (the original lower level J_l' is different depending on the branch of the pumping transition). The situation is schematized in the right panel of Fig. 7.1.

The polarizability factor W_2 for the laboratory case can be easily defined (see Landi Degl'Innocenti 1984 for the definition). The formula has been given in terms of 6-j symbols by Landi Degl'Innocenti (2003) and both the Rayleigh and Raman scattering can be described with the following formula, which depends on the values of J_l, J_u and J_l':

$$W_2(J_l', J_u, J_l) = \frac{\left\{ \begin{array}{ccc} 1 & 1 & 2 \\ J_u & J_u & J_l' \end{array} \right\} \left\{ \begin{array}{ccc} 1 & 1 & 2 \\ J_u & J_u & J_l \end{array} \right\}}{\left\{ \begin{array}{ccc} 1 & 1 & 0 \\ J_u & J_u & J_l' \end{array} \right\} \left\{ \begin{array}{ccc} 1 & 1 & 0 \\ J_u & J_u & J_l \end{array} \right\}}. \tag{7.1}$$

If analytical expressions for the 6-j symbols are used, one ends up with analytical expressions of the polarizability factor for Rayleigh and Raman scattering in

the laboratory case. These formulas are equivalent to those used by Berdyugina et al. (2002).

On the other hand, when one is interested in the astrophysical case, the previous polarizability factor has to be generalized. Landi Degl'Innocenti (2003) has defined an *effective polarizability factor* $\mathcal{W}_2$ provided that the following requirements are fulfilled: a) the radiation field has not spectral structure, at least in the wavelength range of the transitions which are pumping the upper level of the transition; b) the lower levels are unpolarized and populated according to their statistical weight; c) stimulated emission can be neglected. Under such assumptions, a closed analytical formula for the effective polarizability factor can be obtained. For the case of a molecule with spin under Hund's case (b) coupling without Λ-doubling it can be written as:

$$\mathcal{W}_2(J_u, N_u; J_l, N_l) = (-1)^{S-J_l-\Lambda_l+2} 3(2N_u+1)(2J_u+1) \times \begin{pmatrix} 1 & 1 & 2 \\ \Delta\Lambda & -\Delta\Lambda & 0 \end{pmatrix} \begin{pmatrix} N_u & N_u & 2 \\ \Lambda_u & -\Lambda_u & 0 \end{pmatrix} \begin{Bmatrix} N_u & N_u & 2 \\ J_u & J_u & S \end{Bmatrix} \begin{Bmatrix} 1 & 1 & 2 \\ J_u & J_u & J_l \end{Bmatrix}, \tag{7.2}$$

where Λ_u and Λ_l are the values of Λ of the upper and lower electronic states, respectively, while $\Delta\Lambda = \Lambda_l - \Lambda_u$. For more details, refer to Landi Degl'Innocenti (2003).

7.2 Scattering polarization in MgH and C_2 lines

The first attempt to theoretically understand the observed molecular scattering polarization for the non-magnetic case was done by Rao & Rangarajan (1999). They did radiative transfer modeling of two Q branch lines of MgH at 5165.92 and 5168.14 Å, by fitting the I and Q/I profiles with the oscillator strength, inelastic collision rate and depolarizing elastic collision rate as free parameters. An intrinsic polarizability factor W_2 of 0.4, derived from the J quantum number was used. W_2 is the fraction of the scattering processes that occur as dipole-type scattering (which produces polarized scattered radiation), while $1 - W_2$ represents isotropic, unpolarized scattering (Stenflo 1994).

Recently, Faurobert & Arnaud (2002) made an empirical determination of the W_2 polarizability factor for nine C_2 and two MgH lines. They measured the

scattering polarization outside the solar limb. Therefore, the radiation is assumed to be coming from an optically thin layer which allows an interpretation without model-dependent radiative transfer. They found values for W_2 between 0.41 and 0.46 for MgH and between 0.13 and 0.26 for C_2. However, these results should be considered as tentative since off-limb observations are extremely sensitive to spurious effects like stray-light and seeing (see, e.g., Keller & Sheeley 1999).

More recently, Berdyugina et al. (2002) have implicitly taken for granted that the above-mentioned "laboratory case" is valid for the description of molecular scattering in stellar atmospheres and have published tables with the intrinsic polarizabilities, line strengths and effective Landé factors for the different transitions of the P, Q and R branches of MgH and C_2 were obtained. They emphasized that, while the intrinsic polarizabilities remain significant, the effective Landé factor of the main branches are very close to zero. This is the reason given by the authors for explaining the apparent magnetic immunity of the molecular lines. However, as we shall show below, molecular lines are sensitive to the Hanle effect and the Q/I observed invariance can give us information about the magnetic field distribution in the solar atmosphere (see also Trujillo Bueno 2003b; Asensio Ramos & Trujillo Bueno 2003b).

7.2.1 MgH molecular model

Band structure

The rotational lines of MgH observed around 5170 Å belong to the $A^2\Pi$-$X^2\Sigma^+$ v=0-0 electronic transition. While a $^2\Sigma$ state always belongs to Hund's case (b), a $^2\Pi$ state may belong either to case (a) or to case (b) or to an intermediate state between both. The transition from one to the other is smooth when the rotation increases. Since the total electronic spin of the molecule is S=1/2, each rotational level splits into two sublevels, which are labeled as F_1 (the one with J=$N+1/2$) and F_2 (the one with J=$N-1/2$). Since the lower level has $\Lambda = 0$, this is the only splitting present in the lower level, while the upper level, having Λ=1, has an additional splitting due to the Λ-doubling. Therefore, each upper level F_i is composed of two sublevels with different parity, with a slightly different energy.

The MgH lines observed in the solar spectrum with significant linear polar-

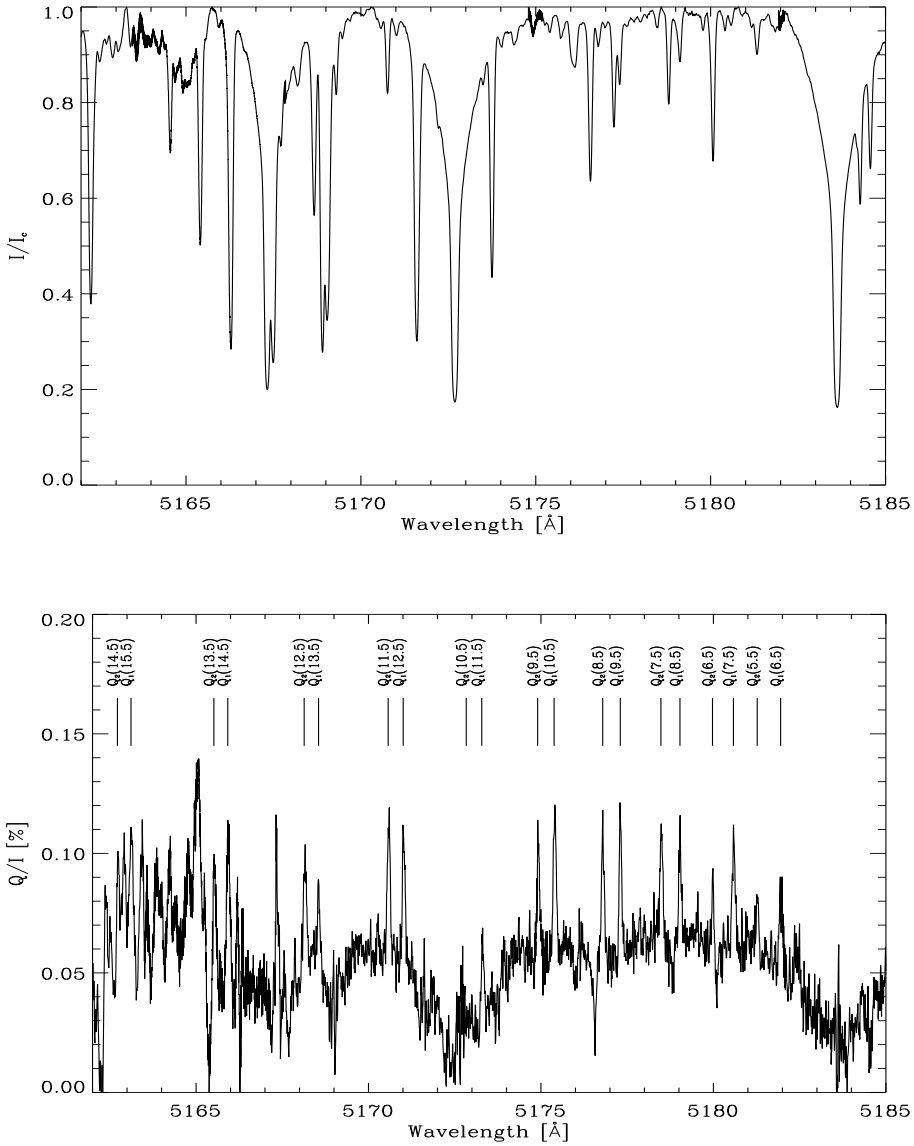

Figure 7.2: Section of 23 Å of the Atlas of the Second Solar Spectrum (Gandorfer 2000) at $\mu = 0.1$. The upper panel shows the intensity spectrum normalized to the continuum intensity. The three strongest absorptions are produced by the Mg b_1, b_2 and b_4 lines. The lower panel shows the fractional linear polarization spectrum Q/I, where the regular sizable signals are produced by the polarizing molecular lines of the Q branch of the $A^2\Pi$-$X^2\Sigma^+$ band of MgH.

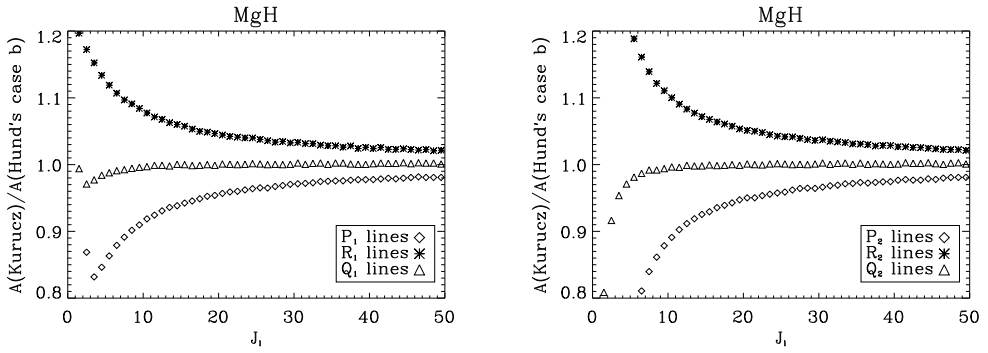

Figure 7.3: Ratio between the Einstein coefficients for MgH lines obtained from the linelist of Kurucz (1993b) and those calculated using Landi Degl'Innocenti (2003) analytical formula for Hund's case (b) adopting the band oscillator strength of Kirby et al. (1979). Note that the ratio is very close to 1 for all the lines belonging to the Q branch, while those of the P and R branches present higher deviations from Hund's case (b). Obviously, the ratio goes asymptotically to 1 when rotation increases.

ization signals are those of intermediate values of J. Following Berdyugina & Solanki (2002), we can consider that the upper level can be well described by Hund's case (b) for values of J higher than $\sim$21/2. If Hund's case (b) applies, the spectrum is composed of a P, R and Q band, the Q branch being the most intense, where each line of the band is split into two components since the spin-doubling splitting is appreciable. This behavior can be verified by looking at the second solar spectrum in the region between 5165 Å and 5185 Å, where all the observed lines belong to the Q branch of MgH. However, as noted by Berdyugina & Solanki (2002), the transition to the Paschen-Back regime is produced at magnetic field strengths as low as 280 G. Therefore, calculations assuming a single Landé factor for each rotational level J is correct only up to this field. For fields larger than $\sim$ 300 G, interferences between the levels appear and the Zeeman splitting is no more proportional to the magnetic quantum number M.

Einstein coefficients

We have built realistic molecular models of the MgH molecule using the linelist of Kurucz (1993b)[1]. We select a minimum and maximum J-value and the model

[1] `http://kurucz.harvard.edu/linelist/linesmol`

molecule is built by reconstructing the energy levels from the linelist using the tabulated Einstein coefficients. In order to verify whether these Einstein coefficients are reliable, we have compared them with theoretically calculated Einstein coefficients. Landi Degl'Innocenti (2003) has given closed analytical formulae for the calculation of the Einstein coefficients for a molecule with spin assuming that the molecule can be described under the Hund's (b) coupling case. Consider a transition between an upper rotational level characterized by the total angular momentum J_u and the rotational angular momentum N_u and a lower level characterized by J_l and N_l. The upper level belongs to a given electronic state characterized by Λ_u and the spin S, while the lower level belongs to another electronic state characterized by Λ_l and the same spin (following the selection rules). The Einstein coefficient for such a transition is given by (Landi Degl'Innocenti 2003):

$$A(J_u,N_u\rightarrow J_l,N_l)=A_0(2J_l+1)(2N_l+1)(2N_u+1) \times \begin{pmatrix} N_u & N_l & 1 \\ \Lambda_u & -\Lambda_l & \Delta\Lambda \end{pmatrix}^2 \begin{Bmatrix} J_l & J_u & 1 \\ N_u & N_l & S \end{Bmatrix}^2, \tag{7.3}$$

where $\Delta\Lambda=\Lambda_l-\Lambda_u$. The constant A_0 is proportional to the Franck-Condon factor which contains information about the strength of the individual vibrational transition. The rest of the terms constitute the rotational dependence of the Einstein coefficient which is usually referred to as the Hönl-London factor. The value of A_0 can be obtained by making use of the band oscillator strength $f_{v_uv_l}$, which has been empirically determined for many important molecular bands:

$$A_0=\frac{8\pi^2e^2}{m_ec}\frac{g_l}{g_u}f_{v_uv_l}\omega^2, \tag{7.4}$$

where ω is the wavenumber of the transition. Note that this formula is completely equivalent to Eq. (3.44) but for the strength of the whole rotational band. For MgH we have used f_{00}(MgH)=0.161 from Kirby et al. (1979). In Fig. 7.3 we show the difference between the analytical Einstein coefficients and the Einstein coefficients tabulated by Kurucz (1993b) for MgH. As seen in the figure, the values of both types of Einstein coefficients are very similar, although differences tend to be higher for lower angular momentum values. This effect is produced because such electronic levels are in an intermediate coupling case. The intermediate coupling case is taken into account in the Einstein coefficients

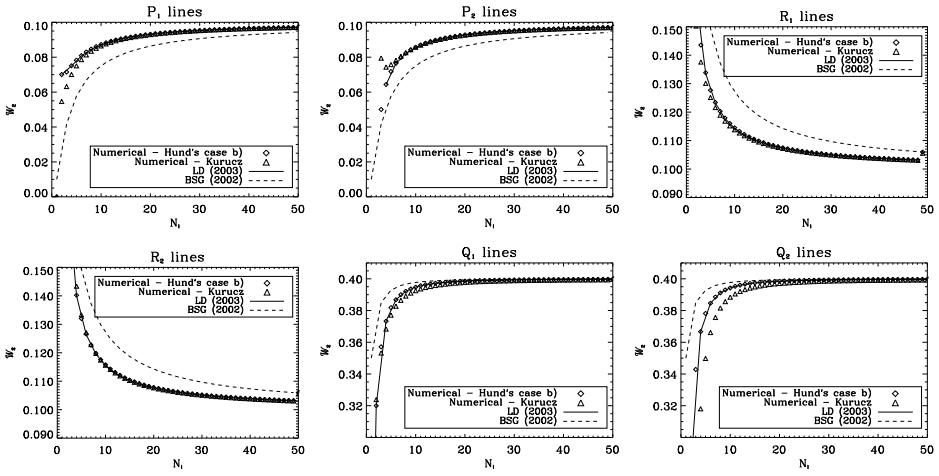

Figure 7.4: Polarizability factors for the P, R and Q branches of MgH. Note the perfect overlap between the $\mathcal{W}_2$ obtained with the analytical formula and that obtained numerically under the same assumptions.

tabulated by Kurucz (1993b), while the analytical ones are calculated assuming Hund's case (b), which leads to accurate results only for high J quantum numbers. Note that the ratio is closer to 1 for the lines belonging to the Q branch, which are those having the highest Einstein coefficients.

Polarizability factors

We have studied the influence of the Einstein coefficients on the polarizability factor. To this end, we have solved the statistical equilibrium equations (SEE) for the irreducible tensor components of the atomic density matrix ρ^K_Q given by Eq. (5.42) (see Landi Degl'Innocenti 1983). We have carried out two different calculations: one using the Einstein coefficients tabulated by Kurucz (1993b) and an extra one using the Einstein coefficients obtained from the analytical formula given by Eq. (7.3) with the band oscillator strength of Kirby et al. (1979). Since the effective polarizability factor has been defined under some assumptions, we have solved the SEE under the very same restrictions in order to be able to compare the results with the analytical formulae: a) the radiation field has no spectral structure; b) the lower levels are unpolarized and populated

according to their statistical weight; c) stimulated emission is neglected.

The molecular model for MgH includes rotational levels of the upper $A^2\Pi$ and the lower $X^2\Sigma^+$ from $J = 1/2$ to $J = 101/2$, all belonging to the fundamental vibrational level. The fine structure due to the spin-coupling and the Λ-doubling is taken into account. The lack of neither pure rotational transitions nor collisional transitions produce an interesting effect in this molecule. Since the parity selection rule $+ \leftrightarrow -$ has to be fulfilled, we end up with two independent subsystems in the MgH molecule which have to be solved independently. Therefore, half of the levels of the upper and lower electronic states belong to one subsystem, while the other half belong to the other subsystem. These subsystems are not radiatively connected. The total number of rotational levels included in the model is 152 for each subsystem, 51 levels belonging to the lower level in which there is no Λ-doubling and 101 levels belonging to the upper level, in which the Λ-doubling is taken into account (this is the reason why there is two times more levels in the upper state than in the lower state). The number of electronic transitions among these levels is 300. We have included lines belonging to main branches and to satellite branches.

In order to completely define the problem, we need to characterize the "degree of anisotropy" of the radiation field. Since we are interested in comparing the results between two possible options of the Einstein coefficients, we do not worry about using a very accurate value of the anisotropy factor w (e.g., by means of 3D calculations). Therefore, we have just calculated the radiation field tensors J^0_0 (mean intensity) and J^2_0 (anisotropy) using the observed center-to-limb variation of the solar continuum intensity from Cox (2000), which completely defines w. The anisotropy in the solar atmosphere is weak, so the weak anisotropy limit holds (i.e., $J^2_0/J^0_0 \ll 1$). Therefore, we have limited the calculations to multipoles of the density matrix with $K \leq 2$, which leads to a reduction in the size of the linear system describing the SEE. However, we have verified that the results do not change in a significant way when using all the multipoles of the density matrix for each level of total angular momentum J. Once the value of the fractional alignment $\sigma^2_0 = \rho^2_0/\rho^0_0$ is known for the upper and lower level of a transition, the fractional linear polarization Q/I for a tangential observation ($\mu = 0$) in a plane-parallel atmosphere including the effect of a background polarized continuum can be obtained by using the

formula (Asensio Ramos & Trujillo Bueno 2003b):

$$Q/I = \frac{r_l \left[\frac{S_l}{S_T} \left(\frac{\epsilon_Q^l}{\epsilon_I^l} \right) - \frac{\eta_Q^l}{\eta_I^l} \right] + \frac{B_\nu}{S_T}(1-r_l) \left(\frac{\epsilon_Q^c}{\epsilon_I^c} \right)}{1 - r_l \left[\frac{S_l}{S_T} \left(\frac{\epsilon_Q^l}{\epsilon_I^l} \right) + \frac{B_\nu}{S_T}(1-r_l) \left(\frac{\epsilon_Q^c}{\epsilon_I^c} \right) \right] \frac{\eta_Q^l}{\eta_I^l}}, \tag{7.5}$$

where $r_l = \eta_I^l/(\eta_I^l + \eta_I^c)$ is the line strength, S_l is the line source function, S_T is the total source function and B_ν is the Planck's function (continuum source function). A more simplified version of this formula has been obtained also by Landi Degl'Innocenti (2003). For the limiting case of a strong line ($r_l \simeq 1$ and $S_T \simeq S_l$), using the definition of the emission coefficients ϵ_I and ϵ_Q, given by Eqs. (5.46) and (5.47), and their corresponding absorption coefficients, one ends up with:

$$Q/I = \frac{\frac{3}{2\sqrt{2}} \left[\omega^{(2)}_{J_u J_l} \sigma_0^2(u) - \omega^{(2)}_{J_l J_u} \sigma_0^2(l) \right]}{1 - \frac{1}{2\sqrt{2}} \left[\omega^{(2)}_{J_l J_u} \sigma_0^2(l) + \omega^{(2)}_{J_u J_l} \sigma_0^2(u) \right] - \omega^{(2)}_{J_u J_l} \omega^{(2)}_{J_l J_u} \sigma_0^2(l) \sigma_0^2(u)}, \tag{7.6}$$

which simplifies to $Q/I \simeq \frac{3}{2\sqrt{2}} \left[\omega^{(2)}_{J_u J_l} \sigma_0^2(u) - \omega^{(2)}_{J_l J_u} \sigma_0^2(l) \right]$ when taking into account that $\sigma_0^2 \ll 1$ in the solar-like atmospheres (Trujillo Bueno 1999, 2001). In these expressions we have chosen our system of reference for $Q > 0$ in the plane formed by the propagation direction and the tangent to the solar limb. $\omega^{(2)}_{J_u J_l}$ is a numerical factor depending on the angular momenta of the levels involved in the transition (see Landi Degl'Innocenti 1984). The polarizability factor can be obtained from:

$$\mathcal{W}_2 = 4 \frac{Q/I}{w\,(3 + Q/I)} \simeq \frac{\sqrt{2}}{w} \omega^{(2)}_{J_u J_l} \left[\sigma_0^2(u) \right]_{\text{u.l.l}}. \tag{7.7}$$

The second equality assumes that the lower level is unpolarized, which is the assumption made in all analytical derivations of the polarizability factor.

This formula can be used to calculate the effective polarizability factor via the numerical solution of the SEE and compare it with that resulting from the analytical formulae. Fig. 7.4 shows the results. Note that there is a perfect overlap between the $\mathcal{W}_2$ obtained with the analytical formula (see Eq. 7.2) and that obtained by solving the SEE under the very same conditions

necessary for the derivation of the formula. This agreement demonstrates the reliability of the codes which solve the SEE numerically. On the other hand, the value of $\mathcal{W}_2$ obtained when using the tabulated Einstein coefficients are also very close to that obtained assuming Hund's case (b), which shows that this quantity is not extremely dependent on the exact value of the Einstein coefficient. We have also plotted the value of $\mathcal{W}_2$ obtained by Berdyugina et al. (2002) using the laboratory formulae for Raman and Rayleigh scattering. Although the asymptotic value of $\mathcal{W}_2$ is correctly obtained with the formulae used by Berdyugina et al. (2002), the behavior for small and intermediate J-values is not correctly obtained due to the mixing of Rayleigh and Raman scattering.

Landé factors

The effect of an external magnetic field on the rotational levels of a given molecule is dictated by the molecular Landé factor, similar to what happens in the atomic case. The Landé factor can be obtained quite easily in extreme coupling cases (Herzberg 1950). Formulae for intermediate coupling cases, valid for both the Zeeman and Paschen-Back regimes, have been obtained by Schadee (1978) for doublet states.

Fig. 7.5 shows the Landé factors and the effective Landé factors for the MgH transitions under study assuming Hund's (b) coupling case. The absolute value of the Landé factor decreases as J increases. Typically, in Hund's case (b) coupling, the Landé factor of a given rotational level goes as $g_J \propto J^{-n}$, with $n = 1, 2$ depending on the value of N. Therefore, the Landé factor of the lines which present a conspicuous linear polarization signal with $10 < J < 40$ is very small. A rough estimation of the magnetic field strength at which the Hanle effect can produce an important effect in the amplitude of the linear polarization signal can be obtained by the formula (see, e.g., Trujillo Bueno 2001):

$$2\pi\nu_L g_J = 8.79 \times 10^6 B_H g_J \approx \frac{1}{\tau}, \tag{7.8}$$

where ν_L is the Larmor frequency, B_H is the critical Hanle field in gauss, while τ and g_J are the lifetime in seconds and the Landé factor of the level under consideration. Berdyugina et al. (2002) concluded that molecular lines are immune to the Hanle effect because the Landé factor of the levels are very small,

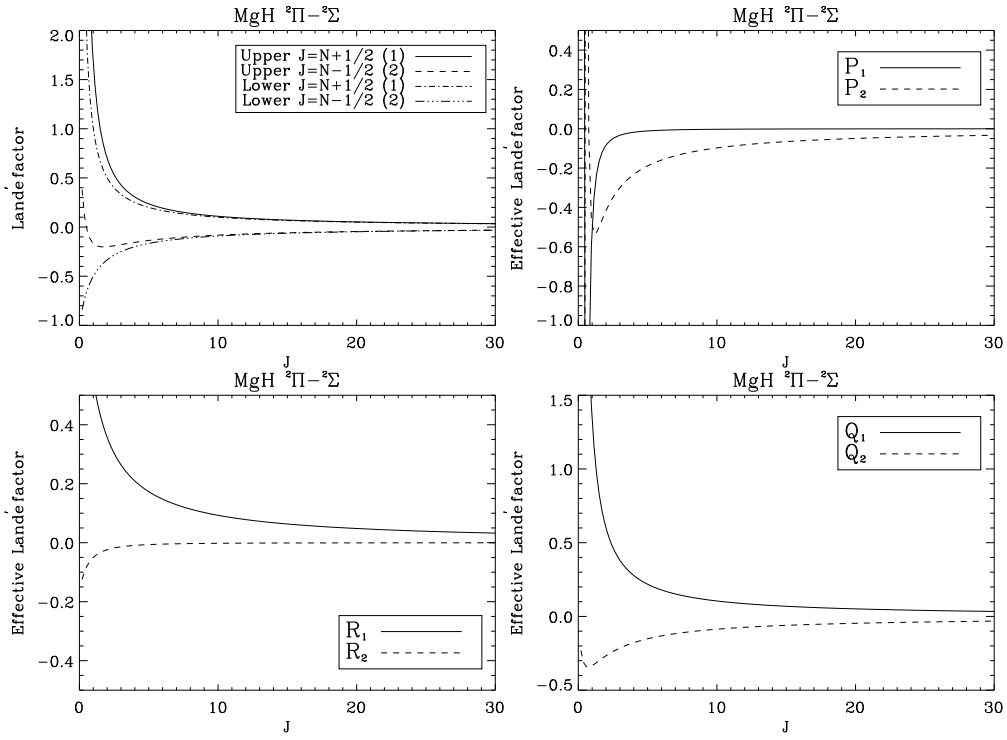

Figure 7.5: Landé factors of the upper and lower levels of the $A^2\Pi$-$X^2\Sigma^+$ transition of MgH and the ensuing effective Landé factors for each of the sub-branches. All the Landé factors have been obtained assuming Hund's case (b) coupling, which gives a good representation of the correct Landé and effective Landé factors for high values of J (typically for $J > 10$).

much smaller than the atomic ones. However, Landi Degl'Innocenti (2003) and Trujillo Bueno (2003b) have pointed out that one has to take into account that the lifetime of the molecular levels is usually higher than for atomic levels. One can prove that the product $g_J\tau$ is essentially the same for molecular lines and for atomic resonance lines. Therefore, molecular lines are sensitive to magnetic fields in the same range as atomic lines are and, as discussed by Trujillo Bueno (2003b), their "apparent" immunity is telling us something new about solar surface magnetism. We will consider this point below.

Finally, since the Landé factors of the $J = N + 1/2$ and $J = N - 1/2$ levels have opposite signs, the value of the emerging U/I has opposite sign for lines

between levels with $J = N + 1/2$ and lines between levels with $J = N - 1/2$.

7.2.2 C_2 molecular model

Band structure

The rotational lines of C_2 observed between 5080 Å and 5160 Å belong to the $d^3\Pi_g$-$a^3\Pi_u$ v=0-0 electronic transition. The magnetic properties of this system of C_2 have been investigated by Berdyugina & Solanki (2002). They concluded that both the upper and lower electronic states belong to intermediate coupling schemes, although they rapidly approach Hund's case (b) for $J \geq 10$. In both levels, the transition to the Paschen-Back regime occurs for magnetic field strengths higher than 70 kG and therefore we can safely treat them in the Zeeman regime. Since the spin of both levels is S=1, each rotational level splits into three sublevels, labeled as F_1 (the one with J=$N+1$), F_2 (the one with J=N) and F_3 (the one with J=$N-1$). Therefore, if both levels belong to Hund's case (b), the structure of the band consists of three sub-bands: $^3\Pi_0 - ^3\Pi_0$, $^3\Pi_1 - ^3\Pi_1$, $^3\Pi_2 - ^3\Pi_2$. Each sub-band has strong P and R branches and a weak Q branch (with the possible exception of the $^3\Pi_0 - ^3\Pi_0$ sub-band), each one splitted into three sub-branches due to the spin-doubling. Λ-doubling is not present in this molecule because it is composed of two identical nuclei. Therefore, since the total wavefunction has to be symmetric under the exchange of the two nuclei, only one of the Λ-doubling levels is possible for each state. The allowed levels have parity $-$ for the lower electronic state and parity $+$ for the upper electronic state.

The C_2 lines observed in the second solar spectrum with non-negligible linear polarization signal show the band structure mentioned before. Each line is splitted into three components belonging to transitions between the different sublevels arising from the spin-orbit coupling. For example, the lines in the P branch are labeled as P_1, P_2 and P_3 (see e.g., Fig. 128 on Herzberg 1950).

Einstein coefficients

The scattering polarization calculations for C_2 have been performed with molecular models built from the linelists of Kurucz (1993b). The band oscillator strength for the v =0-0 band of C_2 has been obtained from Cooper & Nicholls (1976), with a value of $f_{00}(C_2)$=0.0257. As in the case of MgH, we have plotted

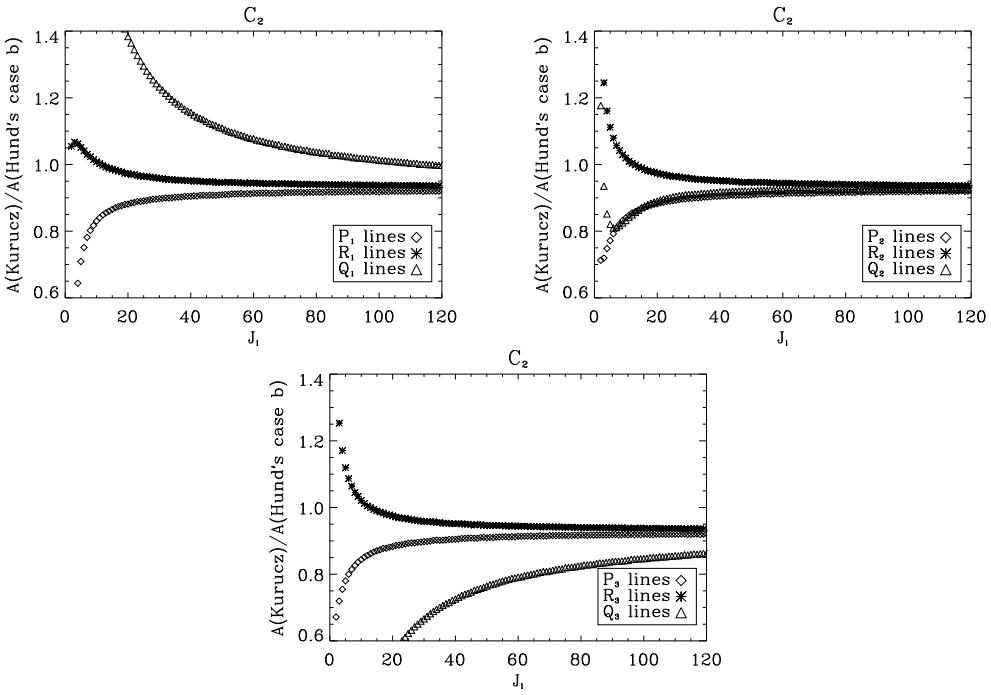

Figure 7.6: Ratio between the Einstein coefficient for C_2 lines obtained from the linelist of Kurucz (1993b) and that calculated using the formula for Hund's case (b) given by Landi Degl'Innocenti (2003) assuming the band oscillator strength of Cooper & Nicholls (1976). Note that for $J_l > 10$ the ratio is close to 1 for all the lines belonging to the P and R branches, while those of the Q branch present higher deviations from Hund's case (b). However, it is clear that the ratio goes asymptotically to 1 when rotation increases.

the tabulated Einstein coefficient versus the analytical one calculated assuming Hund's case (b) coupling (see Fig. 7.6). Note that, contrary to what happens for MgH, the best agreement between the tabulated data and the Hund's case (b) is obtained for the R and P branches, while that for the Q branch has strong variations depending on wether the line is Q_1, Q_2 or Q_3. In this case, the lines with larger Einstein coefficients are the P and R branches. Finally, the ratio becomes close to 1 when the rotation is increased because Hund's case (b) turns out to give a better description.

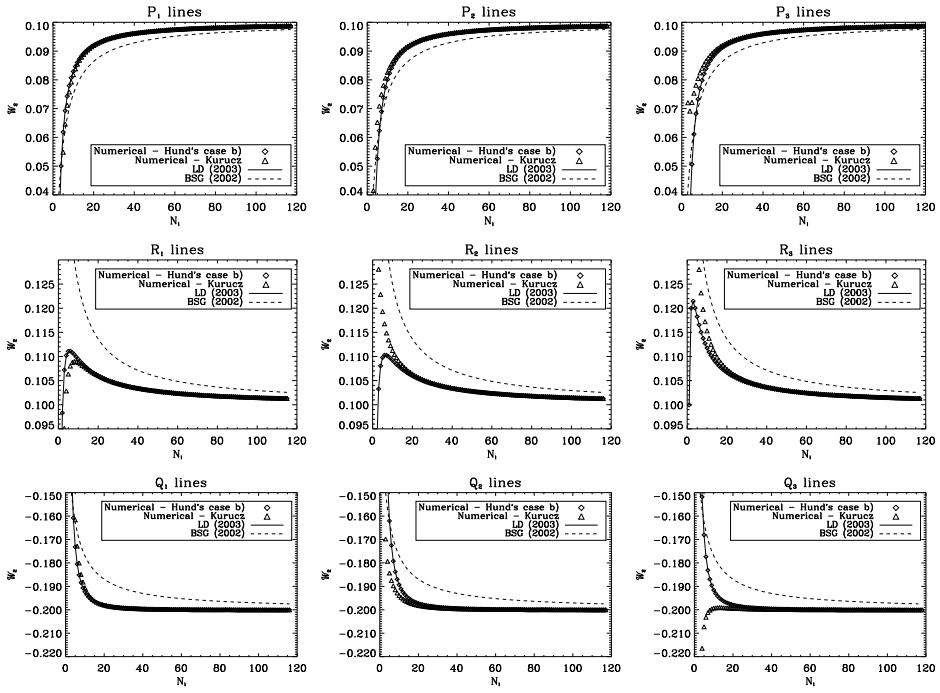

Figure 7.7: Polarizability factors for the P, R and Q branches of C_2. Note the perfect overlap between that given by the analytical formula and that numerically obtained under the same assumptions.

Polarizability factor

We have also calculated the polarizability factors using the same approach as in MgH. Here, the model includes levels from J=0 to J=120 of the fundamental vibrational level of both electronic states, including the fine structure due to the spin coupling. The number of rotational levels is therefore 360 for each level, giving a total of 720 rotational levels. The number of individual rotational transitions is 2657. The increase in the number of levels included in the C_2 model with respect to the number of levels of the MgH model is motivated by the value of the Einstein coefficients. While the stronger lines for MgH are those belonging to the Q branch ($\Delta J = J_u - J_l = 0$), for C_2 the stronger lines are those belonging to the P ($\Delta J = -1$) and R ($\Delta J = 1$) branches.

This particular radiative structure produces very strong *pumping ladders* which couple rotational levels with very different value of J. These ladders introduce another complication to the problem. Those levels close to the boundary of the model (having J close to 0 or to 120) are affected by the finite size of the model. In order to verify the minimum size of the molecular model so that these boundary effects are minimized for rotational levels with $J \lesssim 40$, we have performed calculations with some C_2 models varying the maximum value of J. We have verified that the results remain stationary for molecular models with a maximum value of $J = 120$. Models with a smaller number of rotational levels introduce spurious effects in the density matrix values (ρ^K_Q) obtained from the solution of the SEE. Therefore, and by economy reasons, we have decided to use a model with $J_{\max} = 120$ for all the calculations. This effect does not appear in MgH, because the population and atomic polarization of a given level in MgH is mainly dominated by the coupling with rotational levels with the same value of J. This is the reason why simple models of MgH, such a two-level model, give results very close to those obtained with the full model.

The resulting polarizability factors are shown in Fig. 7.7. Note that we again obtain a perfect overlap between the polarizability factor given by the analytical formula and that obtained numerically using the same restrictive assumptions and the same Einstein coefficients resulting from Hund's case (b) formula. Similarly to what happens with MgH, the polarizability factor is not very sensitive to the exact value of the Einstein coefficient. We have also plotted the value of the polarizability factor obtained with the formulae of Berdyugina et al. (2002). Note that these formulae always underestimate the absolute value of $\mathcal{W}_2$ for the lines of the P and Q branches while they always overestimate the absolute value for the R branch.

Landé factors

Fig. 7.8 shows the Landé factors and effective Landé factors for C_2 assuming Hund's case (b) coupling. Similarly to what happens in MgH, the Landé factors quickly go to zero as J increases. However, the Landé factor of the levels with $J = N$ are much smaller than those for the levels with $J = N \pm 1$. This has two important consequences: first, the lines between levels with $J = N$ need relatively large magnetic field strengths to produce appreciable Zeeman splittings; second, since the Einstein coefficients of the P_1, R_1, P_2, R_2, P_3

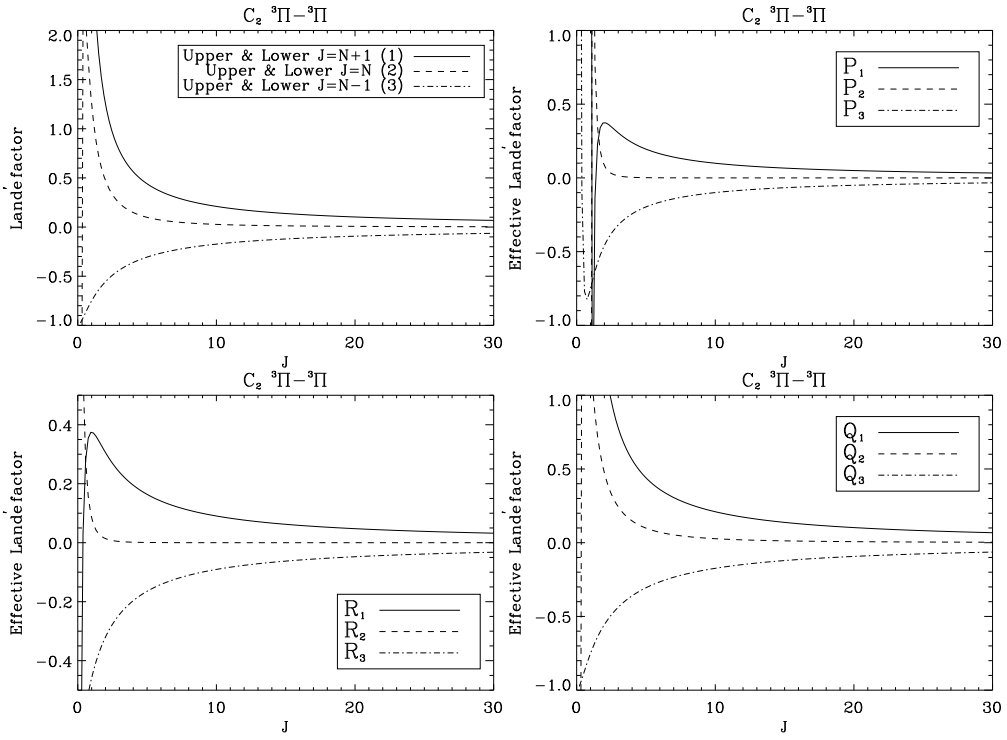

Figure 7.8: Landé factors of the upper and lower levels of the $d^3\Pi_g$-$a^3\Pi_u$ transition of C_2 and the ensuing effective Landé factors for each of the subbranches. All the Landé factors have been obtained assuming Hund's case (b) coupling, which gives a good representation of the correct Landé and effective Landé factors for high values of J (typically for $J > 10$).

and R_3 lines are very similar, the Hanle field for the $J = N$ lines are much higher (typically one order of magnitude higher). This makes these C_2 lines very attractive for the study of weak magnetic fields in the solar atmosphere because they can be used as calibration. Furthermore, the same effect of the change of sign in U/I appears in C_2. The value of the emerging U/I has different sign for transitions between levels with $J = N + 1$ and between levels with $J = N - 1$.

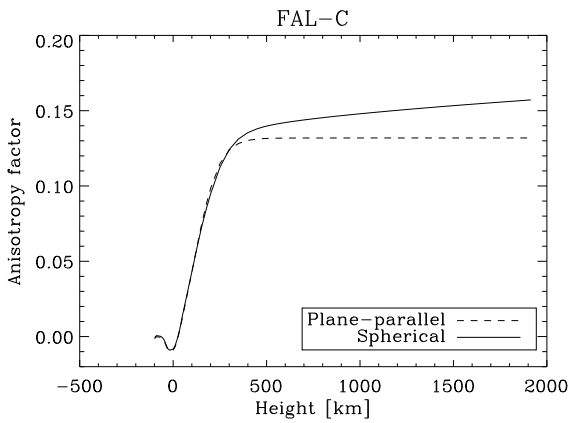

Figure 7.9: Anisotropy factor w of the continuum radiation at 5000 Å for the FAL-C solar atmosphere model calculated for the plane-parallel and spherically symmetric cases.

7.2.3 Anisotropy factor

We have seen that the differential population of the sublevels of a given atomic or molecular J-level is dictated by the anisotropy of the radiation field which induces radiative transitions in the atomic or molecular system. This "anisotropy" can be quantified in terms of the anisotropy factor

$$w = \sqrt{2}J^2_0/J^0_0. \tag{7.9}$$

We have calculated this anisotropy factor in the semi-empirical solar atmospheric model FAL-C using either the assumption of a plane-parallel (PP) atmosphere or a spherically symmetric (SS) atmosphere. Since the molecular lines are very weak, we can assume that the relevant radiation field is the continuum radiation field. We have solved the radiative transfer equation in both PP and SS geometries for the wavelength region of the MgH and C_2 lines. We have calculated the radiation field tensors given by Eq. (5.43) using suitable quadrature formulae. The number of quadrature points has been selected in a trial-and-error scheme. This number was increased until no significant variation is seen in the value of the radiation field tensors at each height in the atmosphere. The results are shown in Fig. 7.9. There are some important properties we can point out from this figure. First, the continuum radiation

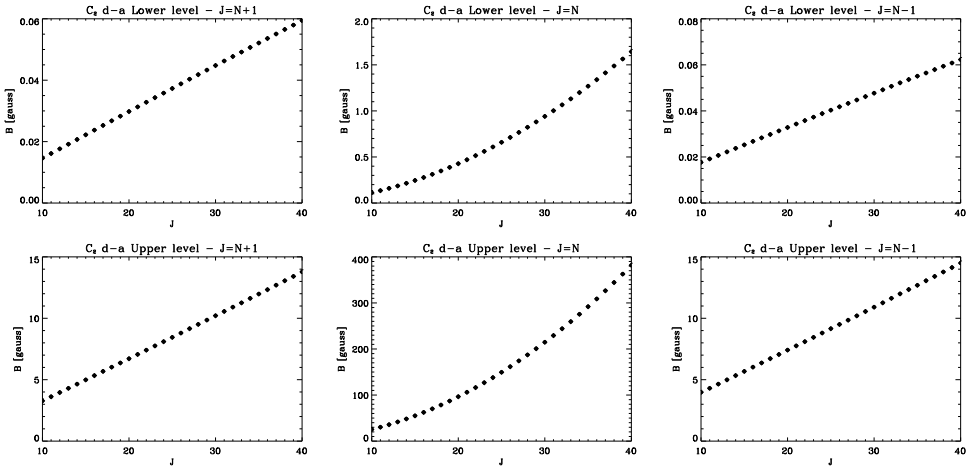

Figure 7.10: Application of the basic formula of the Hanle field (see Eq. 7.8) to the upper and lower levels of C_2 lines that produce scattering polarization on the Sun. Each point refers to upper/lower level of a given spectral line of the P and R branches.

field in the deep regions of the atmosphere is almost completely isotropic and therefore the value of w goes rapidly to 0. Second, sphericity effects for the solar continuum radiation are important only for heights above 300 km. Above this height, the value of w for the PP calculation remains constant at a value of $\sim$0.13, while that obtained using the SS formal solver increases almost linearly with height. This effect is produced because at such heights the influence of the solid angle subtended by the solar atmosphere starts to be important. Third, there is a very small region around $\tau_{5000} = 1$ where the anisotropy factor is negative. Recalling the meaning of the sign of w, the illumination in this region is preferentially horizontal, while it becomes preferentially vertical when going upwards. As shown by Trujillo Bueno (2003c, 2003b), the situation is much more complicated in 3D models of the solar photosphere, since w shows important horizontal fluctuations being larger in the upflowing regions than in the downflowing plasma.

7.2.4 The critical Hanle field

In order to have an idea of the magnetic fields necessary for producing an appreciable Hanle depolarization on the molecular lines, we have used Eq. (7.8) to obtain the critical Hanle field for the upper and lower levels of the rotational transitions of MgH and C_2. The lifetime of each level is calculated taking into account all the transitions which depopulate the level. For the upper levels of the transitions, it is obtained as the inverse of the sum of the spontaneous Einstein coefficients A_{ul} of all the radiatively allowed transitions:

$$t_{\rm life}(u) = \left(\sum_l A_{ul} \right)^{-1} . \tag{7.10}$$

On the other hand, the lifetime of the lower levels is obtained as the inverse of the sum of the absorption Einstein coefficients (B_{lu}) times the mean intensity J^0_0:

$$t_{\rm life}(l) = \left(\sum_u B_{lu} J^0_0 \right)^{-1} . \tag{7.11}$$

Note that the lower level Hanle field is therefore dependent on the radiation field present in the medium. We have used the same radiation field we have used in the calculations, i.e. that obtained from the Cox (2000) tabulation of the observed center-to-limb variation of the solar continuum radiation.

We show in Figs. 7.10 and 7.11 the critical Hanle fields for the upper and lower levels of the MgH and C_2 transitions. The Hanle field for the lower levels is typically two orders of magnitude lower than for the upper level, a direct consequence of the two orders of magnitude difference in the lifetime. Furthermore, the critical Hanle fields for molecular lines are of the same order of magnitude as the Hanle fields of atomic lines. As stated above, this is produced because the quantity $g\, t_{\rm life}$ is similar for both kind of transitions: for atomic lines g is large and $t_{\rm life}$ is small, while for molecular lines g is small and $t_{\rm life}$ is large. When a molecule spends more time in a given rotational level, there is more time for the magnetic field to affect its atomic polarization via the Hanle effect. Concerning C_2, the Hanle field for the R_2 and P_2 lines is much higher than for the rest of line components. This is due to the especial behavior of the Landé factor of the $J = N$ levels which, behaving as $g \propto J^{-2}$,

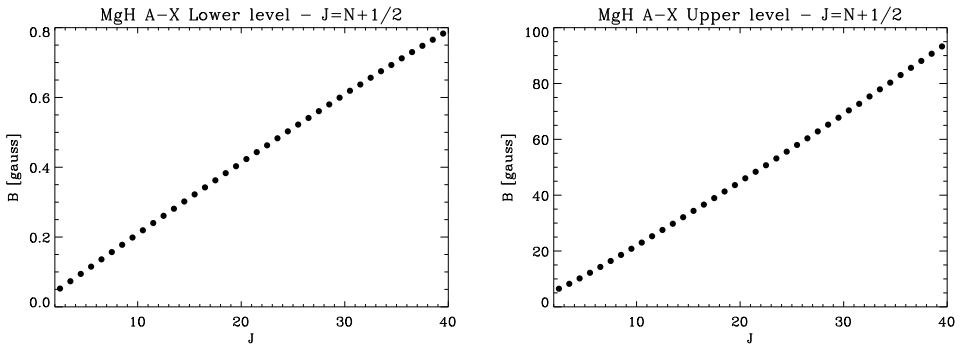

Figure 7.11: Application of the basic formula of the Hanle field to the upper and lower levels of MgH lines that produce scattering polarization on the Sun. Each point refers to the upper/lower level of a given spectral line of the Q branch.

are extremely small in comparison with the Landé factor of the $J = N + 1$ and $J = N - 1$ (which behave as $g \propto J^{-1}$) for a given rotational level J. Since the critical Hanle fields are inversely proportional to the Landé factor, the behavior for transitions between $J = N$ levels is parabolic, while the rest are completely linear. The upper level Hanle field for the observed lines of C_2 are around 10 G for the lines corresponding to levels $J = N + 1$ and $J = N - 1$, while it is around 200 G for the lines corresponding to levels $J = N$. Therefore, we could only expect Hanle depolarization in the weak field regions for the lines with lower Hanle fields. As we shall show below, this curious behavior can be used to extract information on the weak magnetic fields in the granular regions of the quiet Sun.

7.2.5 Non-magnetic case

The diagnostics of magnetic fields via the Hanle effect requires a correct modeling of the scattering polarization amplitudes for the case of zero magnetic field. Instead of solving the full non-linear radiative transfer problem, we will consider the simplified linear problem in which the SEE system given by Eqs. (5.42) are solved assuming that the radiation field tensors J^K_Q are known. Following this approach, the problem is extraordinarily simplified. The SEE for the irreducible spherical components of the density matrix transform then into

a linear system of equations which can be solved using any suitable linear solver. We assume that the radiation field is axially symmetric. Therefore, the only non-zero components of the radiation field tensor are the J^0_0 and J^2_0. The first one is the mean intensity, which we have calculated from the angular integration of the center-to-limb variation of the solar continuum radiation tabulated by Cox (2000). Instead of giving J^0_0, we will work with $\bar{n}$, the solid-angle average of the number of photons per mode at a given frequency ν, related to J^0_0 by:

$$\bar{n} = \frac{c^2}{2h\nu^3} J^0_0. \tag{7.12}$$

The value of the degree of anisotropy J^2_0 is given in terms of the anisotropy factor w. We have verified that the calculated irreducible spherical tensor components of the density matrix (i.e., the ρ^K_Q elements) depend much more strongly on the anisotropy factor w than on the exact value of the mean intensity. As an example, the fractional alignment of the upper level in a two-level atom transition with angular momenta J_u and J_l without lower level polarization and in the absence of depolarizing collisions and of magnetic fields can be written as (Landi Degl'Innocenti 1984):

$$\sigma^2_0 = \frac{w^{(2)}_{J_u J_l}}{\sqrt{2}} w. \tag{7.13}$$

Even more striking is the result of the calculation shown in Fig. 1 of Trujillo Bueno & Manso Sainz (1999) who solved the full polarized radiative problem self-consistently. It shows that, in the absence of depolarization mechanisms (e.g. by elastic collisions and/or magnetic fields), σ^2_0 is approximately equal to J^2_0/J^0_0 for a transition with $J_l = 0$ and $J_u = 1$ at each height in an isothermal atmosphere.

Since the "degree of anisotropy" in the solar atmosphere is weak, we can make the additional assumption of neglecting all the multipole moments of the density matrix with $K > 2$ and retain only those with $K \leq 2$. Because we are here considering the unmagnetized case and the radiation field is axially symmetric, the only non-zero irreducible spherical tensor components of the density matrix are ρ^0_0 and ρ^2_0. We have solved the SEE for a value of $w = 0.145$. We have verified that solving the full problem including all the values of ρ^K_0 with $K = 0, 2, \cdots, 2J$ does not significantly affect the solution because w is

sufficiently small. The SEE are solved for different values of the depolarizing rates $D^{(2)}$. As it becomes obvious from the rate equations given by Eq. (5.42), the multipole moments of the density matrix with $K = 2$ go to zero when $D^{(2)}$ increases and the molecular polarization is destroyed, i.e. all the sublevels of a given level J are equally populated. We have plotted in the upper panels of Fig. 7.12 the value of σ_0^2 for the upper level (solid line) and lower level (dashed lines) of some interesting transitions of MgH. These transitions are the $Q_1(17)$ and $Q_2(16)$ observed by Faurobert & Arnaud (2002) and the additional $Q_1(6)$ as representative of a transition between low J values. Note the extremely similar behavior of σ_0^2 for the different lines. There are small differences in the value of σ_0^2 when the depolarization rates are very small and on the value of $D^{(2)}$ necessary for obtaining a significant variation of the fractional alignment with respect to the case with $D^{(2)} = 0$, which is slightly smaller for the lines with higher values of J. The curves for the lower levels (dashed lines) tend to zero faster than those for the upper levels (solid lines) because the lower level lifetime is usually much longer than that of the upper level. As a result, the depolarizing collisions can act during a longer time and efficiently reduce the lower level atomic polarization. On the other hand, note that there is a feedback effect between the σ_0^2 values of the upper and lower levels. When the value of $\sigma_0^2(\mathrm{low})$ starts to decrease due to the action of collisional processes, $\sigma_0^2(\mathrm{up})$ changes in a very similar way. This effect is produced by the coupling between both levels in the SEE. In fact, it can be shown that the fractional alignment of the upper and lower levels of a $J_u = 1 \rightarrow J_l = 1$ transition can be expressed as (see Trujillo Bueno (2001)):

$$\begin{aligned} \sigma_0^2(\mathrm{up}) &\approx \frac{-1}{2(1+\delta_u)}\left[\frac{\omega}{\sqrt{2}} + \sigma_0^2(\mathrm{low})\right] \\ \sigma_0^2(\mathrm{low}) &\approx \frac{1}{2(1+\delta_l)}\left[\frac{\omega}{\sqrt{2}} - \sigma_0^2(\mathrm{up})\right], \end{aligned} \tag{7.14}$$

where $\delta_u = D^{(2)}/A$ and $\delta_l = D^{(2)}/B\bar{J}_0^0$. Note the inter-relationship between the fractional alignments of the upper and lower levels. Interestingly, the atomic polarization of the upper level of the MgH lines increases in absolute value when the lower level polarization is destroyed by collisions (see upper panels of Fig. 7.12).

The middle panels of Fig. 7.12 show the fractional linear polarization. The formula used to obtain Q/I is that given by Eq. (7.6). The most important

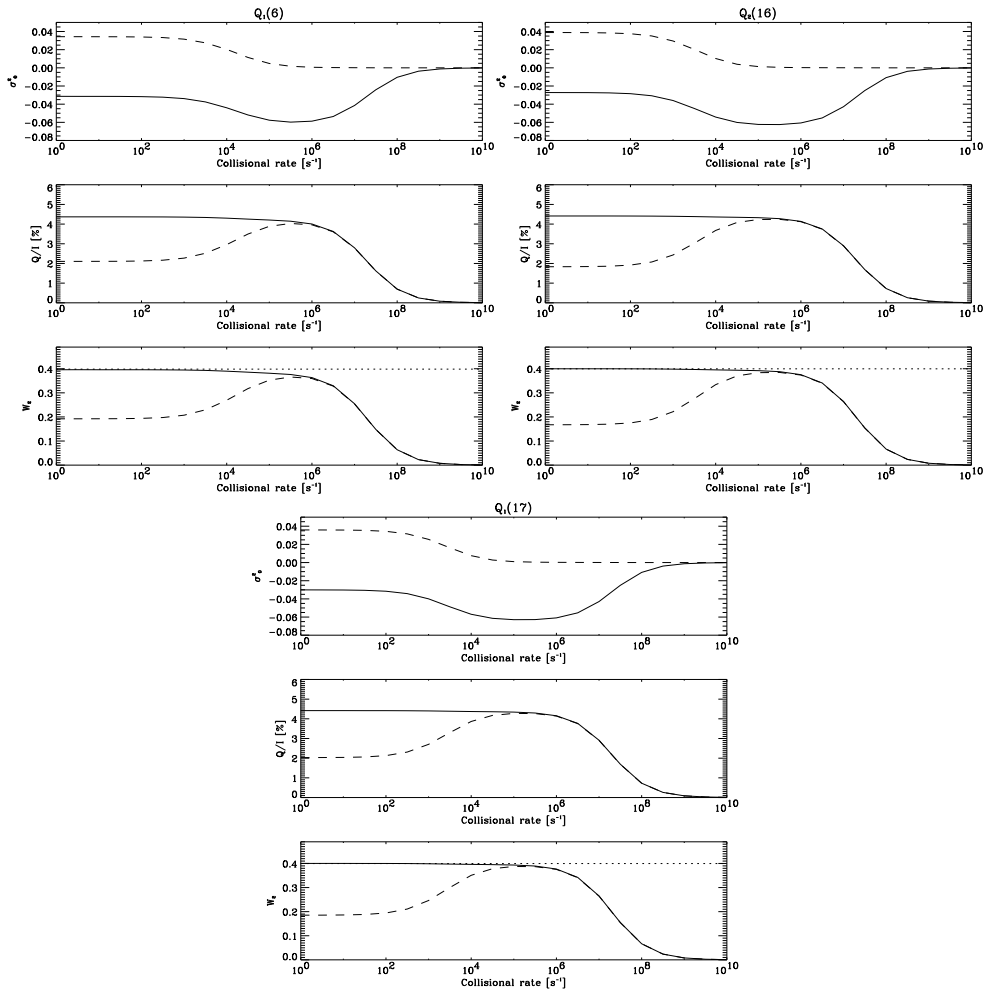

Figure 7.12: Upper panels: fractional alignment σ_0^2 of the upper (solid line) and lower (dashed line) levels of some transitions of the Q branch of MgH for increasing values of the depolarizing collisional rate. Middle panels: the corresponding fractional linear polarization (Q/I) obtained under the assumption of single scattering events. The solid line takes into account the effect of dichroism and the dashed line does not. Lower panels: the corresponding polarizability factor obtained from the calculated Q/I via Eq. (7.7). The dotted line is the $\mathcal{W}_2$-value obtained from the analytical formula given by Landi Degl'Innocenti (2003).

term in this formula is the numerator, while the denominator turns out to be a very small correction due to the small value of the fractional alignment. The numerator is nothing but the Eddington-Barbier expression obtained by Trujillo Bueno (1999, 2001). Therefore, the fractional linear polarization Q/I is given by $Q/I \simeq \frac{3}{2\sqrt{2}}\left[\omega^{(2)}_{J_uJ_l}\sigma^2_0(u) - \omega^{(2)}_{J_lJ_u}\sigma^2_0(l)\right]$, i.e. the difference between the fractional alignment of the upper and the lower levels, where each σ^2_0 value is weighted by factors which depend on the J_l and J_u values of the considered exact transition. However, these numerical factors quickly tend to an asymptotic value when J increases, which are $\omega^{(2)}_{JJ\pm1} = 1/\sqrt{10}$ and $\omega^{(2)}_{JJ} = -\sqrt{2/5}$. The middle panel of Fig. 7.12 shows the value of Q/I taking into account the dichroism effect produced by the lower level polarization. The figure also shows, $Q/I(\mathrm{up})$, i.e. the Q/I signal observed off-limb where no dichroism effect is operative (to this end we simply set $\sigma^2_0(l) = 0$ in Eq. 7.6).

In this case, however, the value of $\sigma^2_0(u)$ contains information on the feed-back effect of the non-zero σ^2_0 value of the lower level. As shown by the solid lines of the Q/I panels in Fig. 7.12 the result is that Q/I remains insensitive to the depolarizing collisions until the upper level polarization begins to be affected. However, $Q/I(\mathrm{up})$ is sensitive to the depolarization of the lower level as well as to the depolarization of the upper level. Therefore, the lower level polarization cannot be observationally detected in MgH lines unless an off-limb observation is made. In an on-disk observation, the feed-back effect produced in the SEE results in a Q/I signal which is completely insensitive to the lower level polarization. Note that this effect is more pronounced when J is increased. A small variation in Q/I is seen for the $\mathrm{Q}_1(6)$ transition when increasing the depolarization rate, indicating the presence of lower level polarization. Landi Degl'Innocenti (2003) has shown that this behavior we had found numerically can be proved analytically as a theorem which states that, *in the absence of depolarizing mechanisms for the upper level of an electronic state of a molecule, the difference between the asymptotic value of the atomic polarization of the rotational levels of the upper electronic state and the corresponding value for the lower electronic state equals the asymptotic value of the atomic polarization of the rotational levels of the upper electronic state corresponding to the case of complete depolarization of the lower levels.* Expressed analytically,

$$\lim_{J_u\to\infty}\sigma^K_Q(J_u) - \lim_{J_l\to\infty}\sigma^K_Q(J_l) = \left[\lim_{J_u\to\infty}\sigma^K_Q(J_u)\right]_{\mathrm{u.l.l}}, \qquad (7.15)$$

where u.l.l means unpolarized lower level.

The calculated values of Q/I(up) are compatible with those observed by Faurobert & Arnaud (2002) only in a very limited range of depolarizing collisional rates. We have to use Q/I(up) for the comparison because the observations were made off-limb, where no dichroism effect is present, although the feed-back effect of σ^2_0(low) on σ^2_0(up) may be present (in principle). Interestingly, the rate of depolarizing collisions needed to fit the off-limb observations is enough to completely destroy the lower level polarization. A severe problem arises here, because no information about how important the depolarizing collisions may be for molecules is available. Therefore, we cannot reject the possibility of having an unpolarized lower level until any suitable value for the order of magnitude of the depolarizing collisions is available.

The lower panels of Fig. 7.12 show the values of the polarizability factor $\mathcal{W}_2$ obtained from Q/I and Q/I(up) using Eq. (7.7). We have also indicated the value of $\mathcal{W}_2$ obtained from the analytical formulae of Landi Degl'Innocenti (2003), showing that the analytical formulae give very good results for the polarizability factor in the limit of zero depolarization collisions. Therefore, and similar to what happens with Q/I, the polarizability factor is completely insensitive to the lower level polarization.

Fig. 7.13 shows the results obtained for C_2 in a similar way as for MgH. We show two lines with high J and one with small J, where J is the total angular momentum of the lower level. The results are similar for lines between levels with $J = N + 1$, $J = N$ or $J = N - 1$ so that we plot the results for the $J = N + 1$ lines as representative of all the lines. In this case, the molecular model for C_2 includes much more levels because the spin is now $S = 1$ and each rotational levels splits into three sublevels with the same value of N and different value of J.

Furthermore, the above-mentioned complication of the radiative ladders appears and the molecular model has to be big enough to avoid boundary effects (i.e. the same problems we had when calculating the polarizability factors). From a computational viewpoint, the fact that we have low anisotropy and the ensuing neglect of the multipoles with $K > 2$ turns out to be fundamental in this case. The upper panels show the fractional alignment of the upper (solid line) and lower (dashed line) levels of the transitions. Note that, contrary to what happens with MgH, the fractional alignment here is always positive. The definition of the spherical statistical tensor components of the density matrix

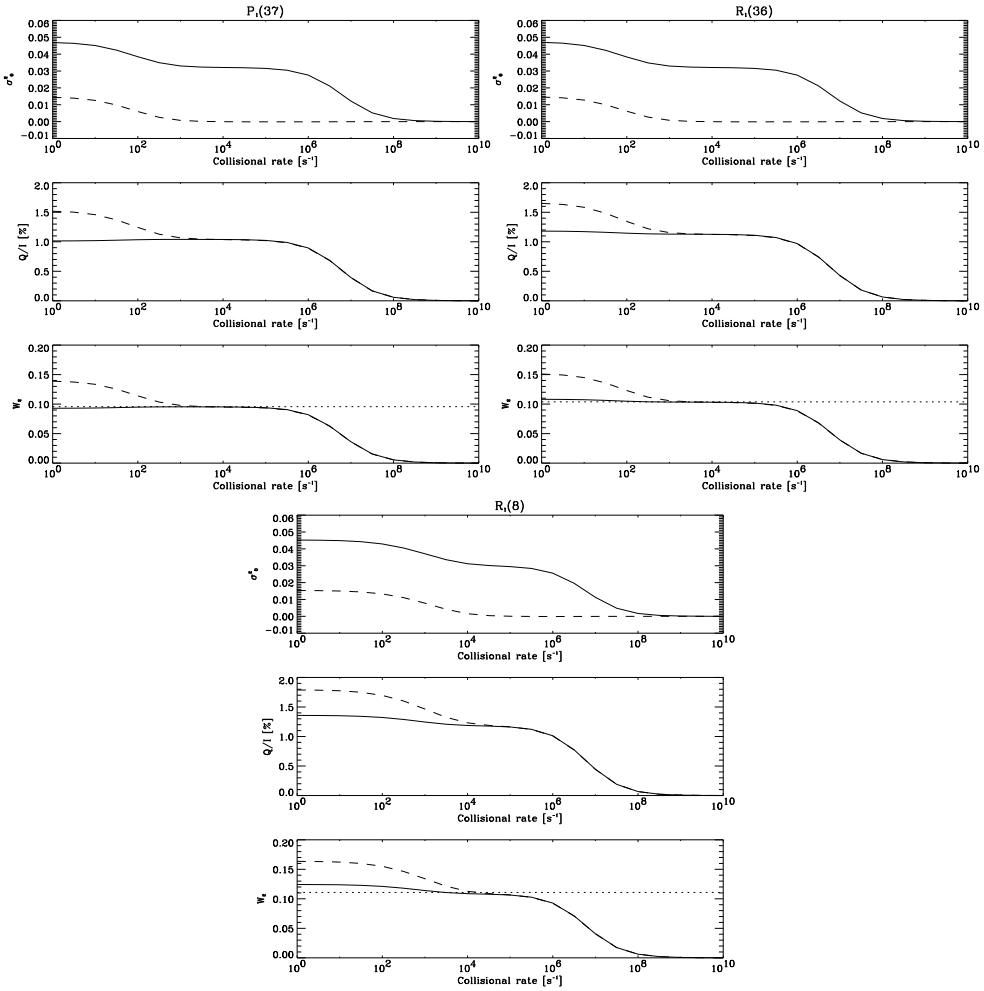

Figure 7.13: Upper panels: fractional alignment σ_0^2 of the upper (solid line) and lower (dashed line) levels of some transitions of the P and R branches of C_2 for increasing values of the depolarizing collisional rate. Middle panels: the corresponding fractional linear polarization (Q/I) obtained under the assumption of single scattering events. The solid line takes into account the effect of dichroism and the dashed line does not. Lower panels: the corresponding polarizability factor obtained from the calculated Q/I via Eq. (7.7). The dotted line is the $\mathcal{W}_2$-value obtained from the analytical formula given by Landi Degl'Innocenti (2003).

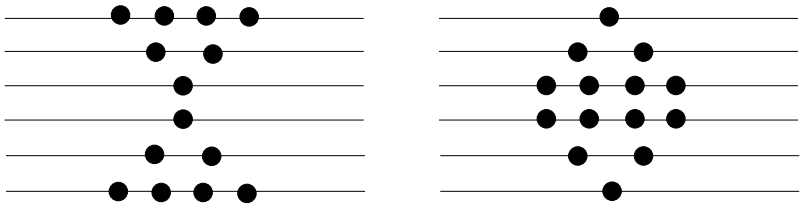

Figure 7.14: Typical population scheme for a given level (in this case $J = 5/2$) depending on the sign of σ_0^2. The left panel shows the population scheme when $\sigma_0^2 > 0$, while the right panel shows the population scheme when $\sigma_0^2 < 0$.

elements:

$$\rho_Q^K(J) = \sum_{MM'} (-1)^{J-M} \sqrt{2K+1} \begin{pmatrix} J & J & K \\ M & -M' & -Q \end{pmatrix} \rho_J(M, M'), \qquad (7.16)$$

can give us some information about which sublevels are more populated. If we are interested in the value of the components with ρ_0^2, we can evaluate the 3-j symbol, perform the summation using the rules of Racah algebra to obtain:

$$\rho_0^2(J) = \sum_M (-1)^{2J-2M+1} \frac{\sqrt{2}\left(J^2 + J - 3M^2\right)}{\sqrt{J(2J-1)(2J+1)(2J+2)(2J+3)}} \rho_J(M, M), \qquad (7.17)$$

where $\rho_J(M, M)$ is the population of the sublevel with magnetic quantum number M. The value of ρ_0^2 is given by a sum of the populations of the sublevels with given weights (except for $J = 0$ and $J = 1/2$, for which $\rho_0^2 = 0$). There is a change of sign in ρ_0^2 which is produced at $J^2 + J - 3M^2 = 0$. Since $(-1)^{2J-2M+1}$ is always equal to -1 for J integer or half-integer, the sublevels which contribute to the sum can be divided into:

$$\begin{aligned} |M| &\leq \frac{1}{3}\sqrt{3J^2 + 3J} \quad &\Rightarrow \quad &\text{contribute positively} \\ |M| &\geq \frac{1}{3}\sqrt{3J^2 + 3J} \quad &\Rightarrow \quad &\text{contribute negatively} \end{aligned} \qquad (7.18)$$

Therefore, we can calculate which levels are more populated depending on the sign of σ_0^2 taking into account that ρ_0^0 is always positive because it is proportional to the total population of a level J. For the case of C_2, we have that

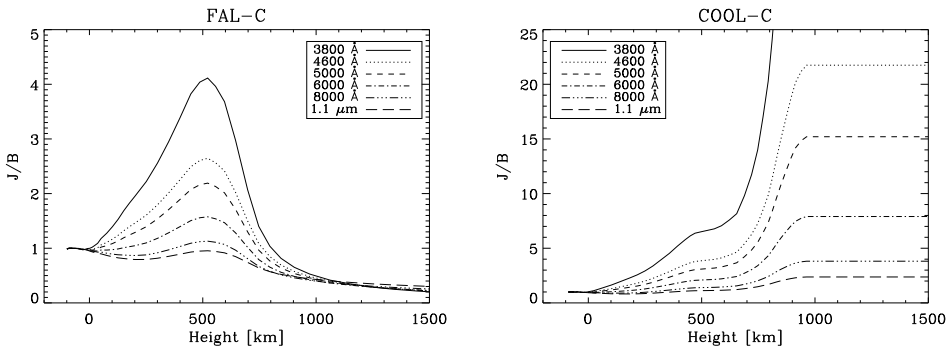

Figure 7.15: Ratio between the continuum mean intensity J^0_0 and the Planck function for different heights of the FAL-C and COOL-C semi-empirical models and for different wavelengths. The ratio increases towards the blue part of the spectrum.

$\sigma^2_0 > 0$ for all the transitions, meaning that the levels with lower absolute value of M are less populated than the levels with higher value of M. For MgH, we have that the upper level has $\sigma^2_0 < 0$, which means that the sublevels with higher absolute value of M are less populated (see Figure 7.14).

We have also carried out a similar investigation for the case of the C_2 line transitions that produce scattering polarization in the Sun. The results are summarized in Fig. 7.13.

7.2.6 Effect of the weakness of the lines

The formulae we have used for calculating Q/I are valid in the limit of an infinitely strong line. But we know that the molecular lines observed in the solar atmosphere are usually weak. Therefore, additional terms like S_l/S_T and r_l may play a role (see Eq. (7.5). In order to get a feeling of the effect of the weakness of the lines on the linear polarization signal, we have calculated the ratio S_l/S_T at different continuum wavelengths for the semi-empirical models FAL-C and COOL-C. The line source function for a two-level atom is given by (e.g., Mihalas 1978)

$$S_l = (1-\epsilon)J^0_0 + \epsilon B_\nu, \tag{7.19}$$

where $\epsilon = C_{ul}/(A_{ul}+C_{ul})$ is the non-LTE parameter. If we assume that $\epsilon \ll 1$, the line source function turns out to be dominated by the mean intensity J^0_0.

On the other hand, the total source function is given by:

$$S_T = \frac{\chi_l S_l + \chi_c B_\nu}{\chi_l + \chi_c} = r_l S_l + (1 - r_l) B_\nu. \tag{7.20}$$

Because the lines are weak, we have $\chi_l \ll \chi_c$, and $S_T \approx B_\nu$. Therefore, $S_l/S_T \approx J^0_0/B_\nu$. We have solved the RT equation including only the background continuum opacity to get the relevant mean intensity J^0_0. The mean intensity is equal to the Planck function at depths where $\tau_c \gg 1$. When going upwards, J^0_0 decreases up to the height where the atmosphere becomes optically thin for the frequency under consideration and J^0_0 becomes constant. The ratio J/B is shown in Fig. 7.15 for a wide range of wavelengths, from the ultraviolet to the near infrared. Note the extremely different behavior between semi-empirical models of the solar atmosphere. This is because FAL-C has a temperature rise above its temperature minimum at ∼500 km, while the temperature stratification for COOL-C is monotonically decreasing and remains constant above ∼900 km. An interesting thing to note is that at any fixed height in the solar atmosphere the J/B ratio is monotonically decreasing as the wavelength is increased, i.e. the ratio S_l/S_T is higher for UV wavelengths than for IR wavelengths. If we focus on what happens around the MgH and C_2 lines (the curve for 5000 Å), we see that the ratio is always between 1 and 2 in the zone where the molecular lines are formed (see Section §7.2.8) for the FAL-C model and between 1 and 3-4 for the COOL-C model. In fact, when this ratio is calculated using a snapshot of the 3D hydrodynamical simulations of Asplund et al. (2000), one finds that its average value is ∼1.3 (see Trujillo Bueno 2003b). If one takes into account that this ratio can be different from 1 and assuming that the continuum is not polarized, the single scattering formula (see Eq. (7.5)) should be transformed into:

$$Q/I = \frac{\frac{3}{2\sqrt{2}} r_l \left[\omega^{(2)}_{J_u J_l} \frac{S_l}{B_\nu} \sigma^2_0(u) - \omega^{(2)}_{J_l J_u} \sigma^2_0(l) + \frac{1}{2\sqrt{2}} \left(1 - \frac{S_l}{B_\nu}\right) \omega^{(2)}_{J_u J_l} \omega^{(2)}_{J_l J_u} \sigma^2_0(l) \sigma^2_0(u) \right]}{1 - r_l^2 \frac{1}{2\sqrt{2}} \left[\omega^{(2)}_{J_l J_u} \sigma^2_0(l) + \omega^{(2)}_{J_u J_l} \sigma^2_0(u) \right] + r_l^2 \frac{1}{8} \left(1 - 9 \frac{S_l}{B_\nu}\right) \omega^{(2)}_{J_u J_l} \omega^{(2)}_{J_l J_u} \sigma^2_0(l) \sigma^2_0(u)}. \tag{7.21}$$

where we have substituted the value of the emission and absorption coefficients in terms of the fractional alignments. If the weak anisotropy limit is recalled, this formula transforms in:

$$Q/I = \frac{3}{2\sqrt{2}} r_l \left[\omega^{(2)}_{J_u J_l} \frac{S_l}{B_\nu} \sigma^2_0(u) - \omega^{(2)}_{J_l J_u} \sigma^2_0(l) \right], \tag{7.22}$$

which represents nothing but the usual Eddington-Barbier relation for Q/I obtained by Trujillo Bueno (1999, 2001) with the modification of multiplying the fractional alignment of the upper level by the ratio S_l/B_ν and a global rescaling factor given by r_l. Therefore, the upper level atomic polarization in a weak transition has more weight than in a strong line. The effect is shown in Fig. 7.16 for the $P_3(28)$ rotational line when a microturbulent magnetic field is included (see §7.2.7). The left panel shows the case with $S_l/B_\nu = 1$, which gives the same results of Fig. 7.21. When the J/B ratio is increased, the value of Q/I increases as can be verified from the previous formula. If we neglect second order terms in the fractional alignment, neglect the contribution of the denominator of the formula and assume that r_l does not vary (in fact, we are assuming that $r_l = 1$ because we are interested in off-limb observations, where there is no continuum), increasing the ratio by a given factor is equivalent to increasing the fractional alignment of the upper level by the same factor. One interesting effect is that the flat behavior of Q/I for a very broad values of the magnetic field is lost and more structure appears, thus leading to an improved diagnostic capability.

7.2.7 Magnetic case

After having investigated the Q/I signal produced by scattering processes in MgH and C_2 lines and how it is modified when depolarizing collisions are included, we now investigate the effect of a magnetic field through the Hanle effect. The effect of a deterministic magnetic field is incorporated into the statistical equilibrium equations (5.42) through the term $-2\pi i \nu_L g_L Q \rho^K_Q(J)$ when they are written in the magnetic field reference frame. When the radiation field has a symmetry axis, it is desirable to write the SEE in a reference system with the quantization axis chosen along this symmetry axis. Taking advantage of the formal invariance of the radiative rates when a change of reference frame is performed, the SEE turn out to be similar to those given by Eq. (5.42) but substituting the magnetic term by $-2\pi i \nu_L g_L \sum_{Q'} \mathcal{K}^K_{QQ'} \rho^K_{Q'}(J)$ (see Landi Degl'Innocenti et al. 1990), where $\mathcal{K}^K_{QQ'}$ is a magnetic kernel which couples the density matrix elements of a given rank K among themselves.

Contrary to what happens in the non-magnetic case in which the only non-zero components of the density matrix are the ρ^K_0, when a magnetic field is present the components with $Q \neq 0$ can be non-zero. If we limit ourselves to

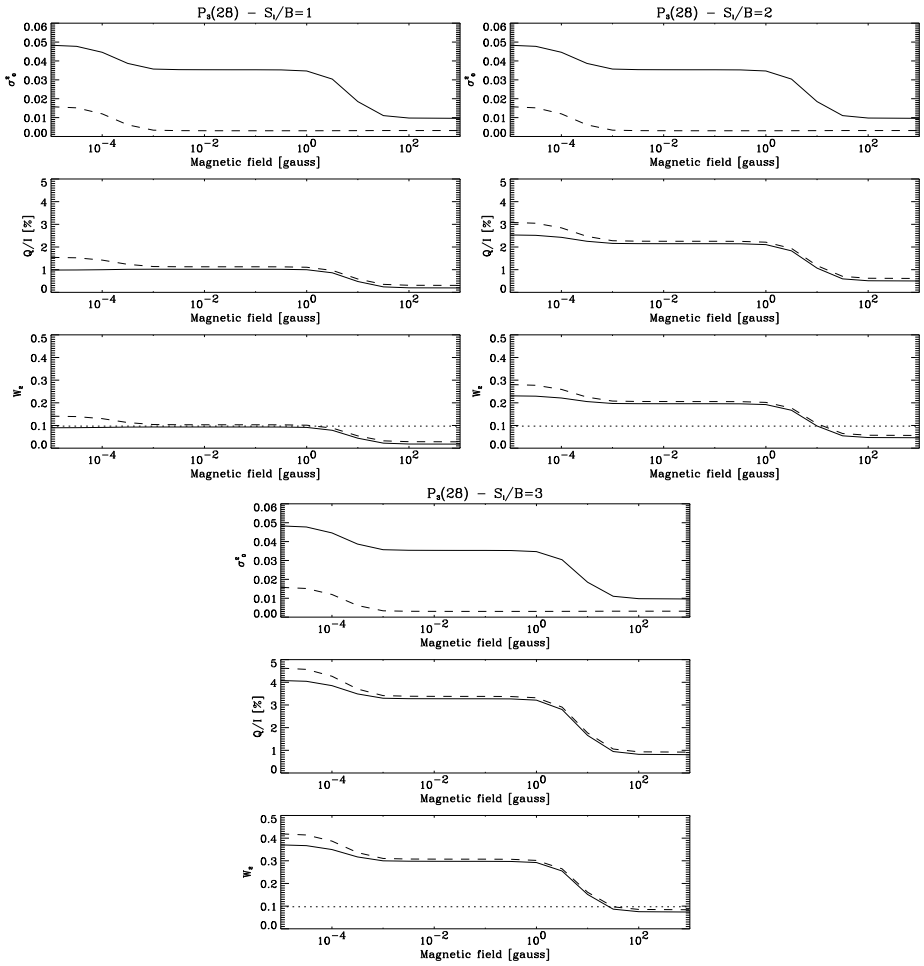

Figure 7.16: Upper panels: fractional alignment σ_0^2 of the upper (solid line) and lower (dashed line) levels of the $P_3(28)$ rotational transition of C_2 for different value of the microturbulent magnetic field. Middle panels: the corresponding fractional linear polarization (Q/I) obtained under the assumption of single scattering events. We show the effect of changing the ratio S_l/B_ν on the value of Q/I. The solid line takes into account the effect of dichroism and the dashed line does not. Lower panels: the corresponding polarizability factor obtained from the calculated Q/I via Eq. (7.7). The dotted line is the $\mathcal{W}_2$-value obtained from the analytical formula given by Landi Degl'Innocenti (2003).

the weak-anisotropy limit so that we only retain ρ^K_Q components with $K \leq 2$, the spherical components of the density matrix which are important for the problem are ρ^0_0, ρ^2_0, ρ^2_1 and ρ^2_2. While the components with $Q = 0$ are real quantities, the components with $Q \neq 0$ are complex in general, and we will need a maximum of 6 components for a given level J when $K \leq 2$ in order to describe its atomic polarization state completely.

The strength of the magnetic field enters the problem through the Larmor frequency (ν_L), while the sensitivity of each level to the magnetic field is controlled by the Landé factor. Because the magnetic fields we are interested in are rather weak, we have assumed that we are always in the Zeeman regime, where the splitting of the magnetic sublevels M of a rotational level J is well represented by a unique and constant Landé factor. In the case in which the magnetic field is strong enough to produce the transition to the Paschen-Back regime, the equations to apply are much more complicated, because quantum interferences between levels having different J-values have to be taken into account. Restricting ourselves to the Zeeman regime, we can easily obtain the Landé factor for each level J. Hund's case (b) is often used to represent the Landé factor for rotational levels with high J. However, the intermediate case between Hund's case (a) and (b) can be used, using either Schadee's (1978) theory or the numerical diagonalization of the total molecular Hamiltonian developed in this Thesis (see Section §5.3). For the case of MgH we have used the intermediate case between Hund's case (a) and (b) formulas given by Schadee (1978) and for C_2 we have decided to use Hund's case (b). The theory developed by Schadee (1978) is not applicable to C_2 since it is limited to doublet states. However, in view of the results obtained by Berdyugina & Solanki (2002) for the Landé factors, the formulas of Hund's case (b) are good enough to represent the Landé factor of the levels of C_2 with $J > 10$.

We consider in this section the effect of a microturbulent and isotropically distributed magnetic field on the linear polarization signal of molecular lines[2]. We obtain the microturbulent magnetic field limit by solving numerically the SEE for many directions of the magnetic field and then averaging the obtained

[2]We note that for the case of a two-level model without lower-level polarization the SEE for the microturbulent limit can be obtained analytically (Trujillo Bueno & Manso Sainz 1999). The case of a two-level atom model with lower-level polarization in the weak-anisotropy limit is developed in Appendix A.

spherical components of the density matrix:

$$\overline{\rho^K_Q}(J) = \frac{1}{4\pi}\int_0^{2\pi} d\chi_B \int_0^{\pi} d\theta_B \sin\theta_B\, \rho^K_Q(J,\theta_B,\chi_B), \tag{7.23}$$

where we have explicitly indicated the dependence of the density matrix components on the angle between the magnetic field and the symmetry axis of the radiation field. This angle is given in terms of the inclination θ_B and the azimuth χ_B. The other Euler angle γ_B which describes the transformation between the magnetic field reference system and the radiation field reference system can be set to 0 without loosing generality. The transformation properties of the ρ^K_Q elements can be investigated by writing how they change when transforming from one frame to the other:

$$\begin{aligned}\left[\rho^K_Q(J)\right]_{\rm rad} &= \sum_{Q'} \mathcal{D}^K_{Q'Q}(0,-\theta_B,-\chi_B)\left[\rho^K_{Q'}(J)\right]_{\rm mag} \\ &= e^{iQ\chi_B}\sum_{Q'} d^K_{Q'Q}(-\theta_B)\left[\rho^K_{Q'}(J)\right]_{\rm mag},\end{aligned} \tag{7.24}$$

where $d^K_{Q'Q}$ is the reduced rotation matrix (Brink & Satchler 1968). Due to the properties of the rotation matrices, one can verify that the multipole moments ρ^0_0 are invariant under the rotation of the magnetic field vector, while the ρ^2_0 depend only on the inclination of the magnetic field and not on the azimuth. Finally, the irreducible components of the density matrix with $Q \neq 0$ have a periodical dependence on the azimuth. Unless $Q = 0$, the irreducible components of the density matrix in the new reference system are periodical in the azimuth and, since $\int_0^{2\pi} d\phi e^{iQ\chi} = 0$, their angle average is zero. The only tensor components which remain not zero are those with $Q = 0$, i.e. ρ^0_0 and ρ^2_0.

We have approximated the integral of Eq. (7.23) using a gaussian quadrature of N points so that it can be written as:

$$\overline{\rho^K_0}(J) = \frac{1}{2}\int_{-1}^{1} d\mu_B\, \rho^K_0(J,\mu_B) \simeq \sum_{i=1}^{N} W_i \rho^K_0(J,\mu_{B_i}), \tag{7.25}$$

where we have made the change $\mu_B = \cos\theta_B$. We have chosen N=12, which results in a very precise quadrature rule, and the weights W_i have been obtained using standard techniques (see, e.g., Press et al. 1986).

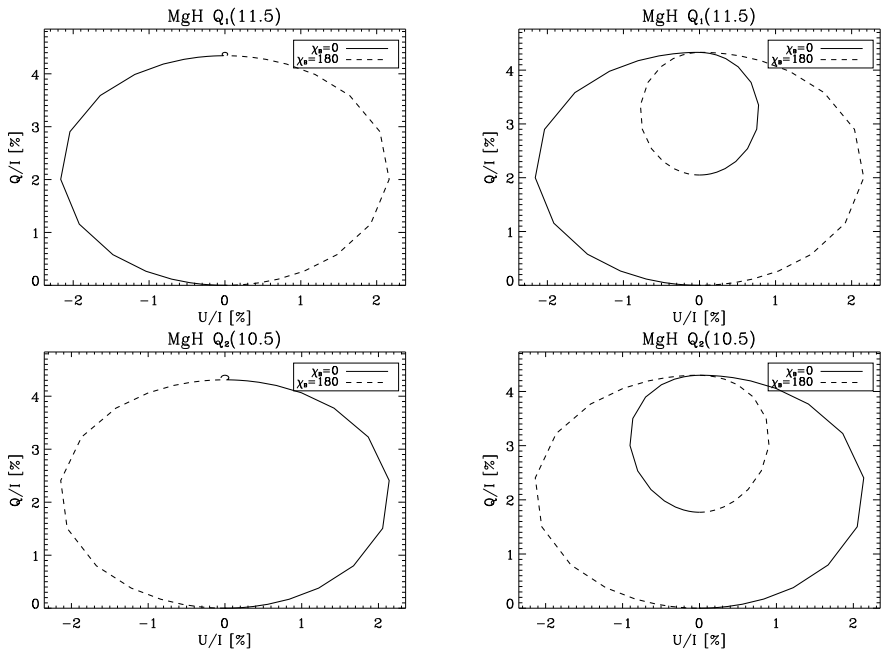

Figure 7.17: Hanle diagrams for the $Q_1(11.5)$ and $Q_2(10.5)$ lines of MgH. In the left panel we show the Hanle diagram when dichroism effects are taken into account and in the right panel we show the Hanle diagram when dichroism effects are neglected.

Before showing the results for a microturbulent field, we first show the effect of a deterministic magnetic field with inclination θ_B=90° (horizontal magnetic field) and two different azimuths, χ_B=0° and χ_B=180°, which correspond to fields pointing along or away the line of sight, respectively. We have solved the SEE for these particular orientations of the magnetic field and we have investigated the influence of an increasing magnetic field strength on the linear polarization signals Q/I and U/I obtained for tangential observation (μ=0) in a plane-parallel atmosphere at the core of the spectral line. The value of Q/I and U/I can be obtained directly from (Manso Sainz 2002):

$$\begin{pmatrix} I \\ Q \\ U \end{pmatrix}_{\mu=0} = \begin{pmatrix} \eta_I & \eta_Q & \eta_U \\ \eta_Q & \eta_I & 0 \\ \eta_U & 0 & \eta_I \end{pmatrix}^{-1} \begin{pmatrix} \epsilon_I \\ \epsilon_Q \\ \epsilon_U \end{pmatrix}, \tag{7.26}$$

where all the coefficients must be evaluated at the atmosphere's surface and for $\mu = 0$. The obtained diagrams, known as *Hanle diagrams*, can be seen in Figs. 7.17 and 7.18 for two lines of MgH and C_2, respectively. We have shown in the left panel the Hanle diagrams when dichroism is taken into account (i.e., η_Q and η_U are used) and in the right panel when dichroism is not included (i.e., η_Q and η_U are neglected). The diagrams show the typical *8-shape*, where the two lobes correspond to the upper- and lower-level Hanle effect.

Concerning the MgH lines, note that the lobe corresponding to the lower level Hanle effect is extremely small when dichroism is taken into account, while it turns out to be significant when it is neglected. This means that the effect of the lower level polarization on the observable linear polarization signal when dichroism is taken into account is extremely small, similar to what happens for the non-magnetic case. On the other hand, when dichroism is neglected, the Q/I signal increases when the magnetic field is increased until the lower level polarization is destroyed by the magnetic field, completely equivalent to what happens for the non-magnetic case when the depolarizing collisions are increased. A very interesting property of the MgH lines is that the value of U/I has different sign for lines with $J = N + 1/2$ and for lines with $J = N - 1/2$, a direct consequence of the change of sign of the Landé factor between the levels with $J = N + 1/2$ and those with $J = N - 1/2$ (see Trujillo Bueno 2003b).

As shown in Fig. 7.18, concerning the C_2 lines, the behavior is similar when dichroism is included, with a very small lobe corresponding to the lower level Hanle effect. In this case, it turns out very difficult to detect the lower level polarization by the observables Q/I and U/I because they do not change until the lower level polarization is completely saturated by the Hanle effect. When dichroism is neglected, the lobe corresponding to the lower level Hanle effect appears. In this case, when the magnetic field is increased so that the lower level polarization is destroyed, the linear polarization signal decreases. Note the curious shape of the lobe corresponding to the lower level Hanle effect in the $P_2(35)$.

Let us now show the effect of a microturbulent magnetic field. Fig. 7.19 shows the results obtained for the fractional alignment, the fractional linear polarization signal Q/I and the polarizability factor for three representative MgH lines and for increasing strengths of the turbulent magnetic field. Since we are not using the SEE appropriate for treating the Paschen-Back regime in which quantum interferences between rotational levels belonging to different

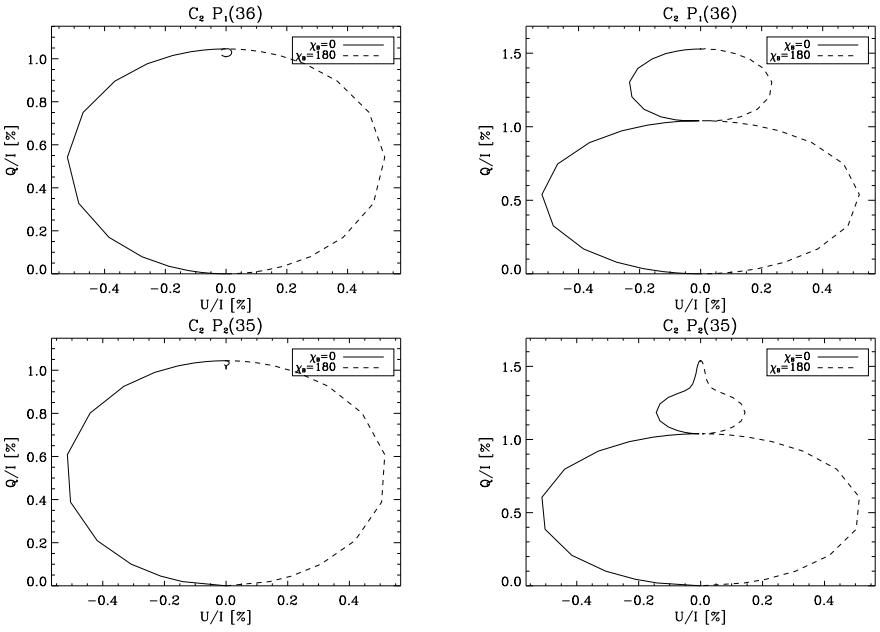

Figure 7.18: Hanle diagrams for the $P_1(36)$ and $P_2(35)$ lines of C_2. In the left panel we show the Hanle diagram when dichroism effects are taken into account and in the right panel we show the Hanle diagram when dichroism effects are neglected.

values of J are taken into account, there is a limit for the magnetic field strength above which the results shown here may not be valid. For MgH, this limit is given by the field necessary to have a Zeeman splitting similar to the multiplet splitting due to the spin-rotation coupling. For the low J levels, this happens for ~ 280 G (Berdyugina & Solanki 2002). However, note that the saturation of the Hanle effect is reached for fields of ~ 100 G, so that the saturation limit is reached before any Paschen-Back complication appears.

As shown in the Figs. 7.19, 7.20, 7.21 and 7.22, the behavior of σ_0^2 when the microturbulent field is increased is extremely similar to that obtained when the depolarizing collisions are increased, although there is a fundamental difference. When the magnetic field is increased, the fractional alignment is not completely destroyed and a residual remains. This residual is equal to 1/5 the value of σ_0^2 for zero-field (Trujillo Bueno & Manso Sainz 1999). As shown by these authors, the value of σ_0^2 for the two-level atom case without lower-level polarization and

for a microturbulent magnetic field is proportional to:

$$\mathcal{H}^{(2)} = \frac{1}{5}\left(1 + \frac{2}{1+\Gamma'^2} + \frac{2}{1+4\Gamma'^2}\right), \tag{7.27}$$

where $\Gamma' \propto \nu_L$. Therefore, in the limit of zero magnetic field ($\Gamma' \to 0$), $\mathcal{H}^{(2)} = 1$, while for very high magnetic field ($\Gamma' \to \infty$), $\mathcal{H}^{(2)} = 1/5$. This result, obtained for the two-level atom case, is also correct for the multilevel case, even for very complicated molecular models. The variation of σ_0^2 when the microturbulent magnetic field strength is increased is very similar to that found for the zero-field case when increasing the rate of depolarizing collisions. In Appendix A we give the expression for σ_0^2 in the microturbulent limit of a two-level atom in the weak-anisotropy limit when both levels are polarized.

In addition to the previous results, Figs. 7.19 and 7.20 also show the effect of using $S_l/B_\nu = 2$ in the formula for calculating the emergent fractional linear polarization. Note in Fig. 7.19 that there appears a sensitivity of Q/I to the lower level polarization Interestingly, for the MgH case (see Fig. 7.19), there is a region between $\sim 10^{-2}$ and $\sim$1 G where the linear polarization signal is magnified with respect to the case with $S_l/B_\nu = 1$.

On the other hand, we have also shown in Fig. 7.20 the results obtained when the lower level of each individual rotational line is assumed to be completely unpolarized. Under such assumption, the fractional alignment of these levels is zero irrespective of the value of the magnetic field. The result is that the fractional linear polarization signal produced by the emission processes from the upper level is almost equal to that obtained when the lower level polarization and dichroism effects are taken into account. This applies to the $S_l/B_\nu = 1$ case.

Similar calculations for some lines of C_2 are shown in Fig. 7.21. Parallel to what happens for MgH, the behavior of σ_0^2 with the turbulent magnetic field strength is similar to the behavior with the depolarizing collisions. The transition to the Paschen-Back regime for C_2 is reached for fields larger than 70000 G and we can therefore consider that we are always in the Zeeman regime. Note that, since the Landé factor of the levels with $J = N$ are around two orders of magnitude smaller than those of the $J = N + 1$ and $J = N - 1$ levels, the field at which the Hanle depolarization occurs tends to be around 2 orders of magnitude larger. This difference in the field regime at which a

change in Q/I occurs will be used later to diagnose weak magnetic field in the solar atmosphere. We have also shown the value of Q/I for the lines of C_2 when the ratio $S_l/B_\nu = 2$. In this case, since the feed-back effect of the lower level polarization on the upper level of the transitions is weaker, the features due to the lower level polarization in the observed Q/I are less important.

Fig. 7.22 shows also the results obtained when the lower level is completely unpolarized. The observed Q/I is completely similar to what is obtained when the lower level polarization and dichroism are taken into account, which applies to the $S_l/B_\nu = 1$ case.

7.2.8 3D models

Spectral synthesis of photospheric lines of atomic species in the recent three-dimensional (3D) radiation hydrodynamics models of Asplund et al. (2000) show a notable agreement with the observed spatially averaged spectrum (Shchukina & Trujillo Bueno 2001). Therefore, it is expected that the thermodynamical conditions in these 3D models may also be able to explain the observations of MgH and C_2 lines. We have seen that the granular regions are hotter than the intergranular plasma only in deep regions, while this trend is reversed for higher photospheric regions. Therefore, we expect that the molecular abundances in the regions of the solar photosphere where the molecular lines are formed are higher above the visible granules than above the intergranular lanes. We have obtained the MgH and C_2 abundances for all the $50\times50\times102$ grid points of the Asplund et al. (2000) 3D simulation. Fig. 7.23 shows the abundances of MgH and C_2 relative to the maximum abundance at two different heights in the 3D model. We have also plotted the contours of zero vertical velocity at h=0 km (see the yellow contour curves), which define the regions where the plasma is moving upwards (the regions inside the contours) and downwards (the regions outside the contours).

The first conclusion is that the abundance of C_2 and MgH is greater in upflowing regions than in the downflowing plasma. On the other hand, Trujillo Bueno (2003b) has shown that the anisotropy factor for the solar continuum radiation is *strongly* correlated with the upflowing regions (i.e., precisely from the same regions where we find the largest molecular concentrations). Therefore, the molecular scattering polarization is coming preferentially from the upflowing regions of the solar photosphere.

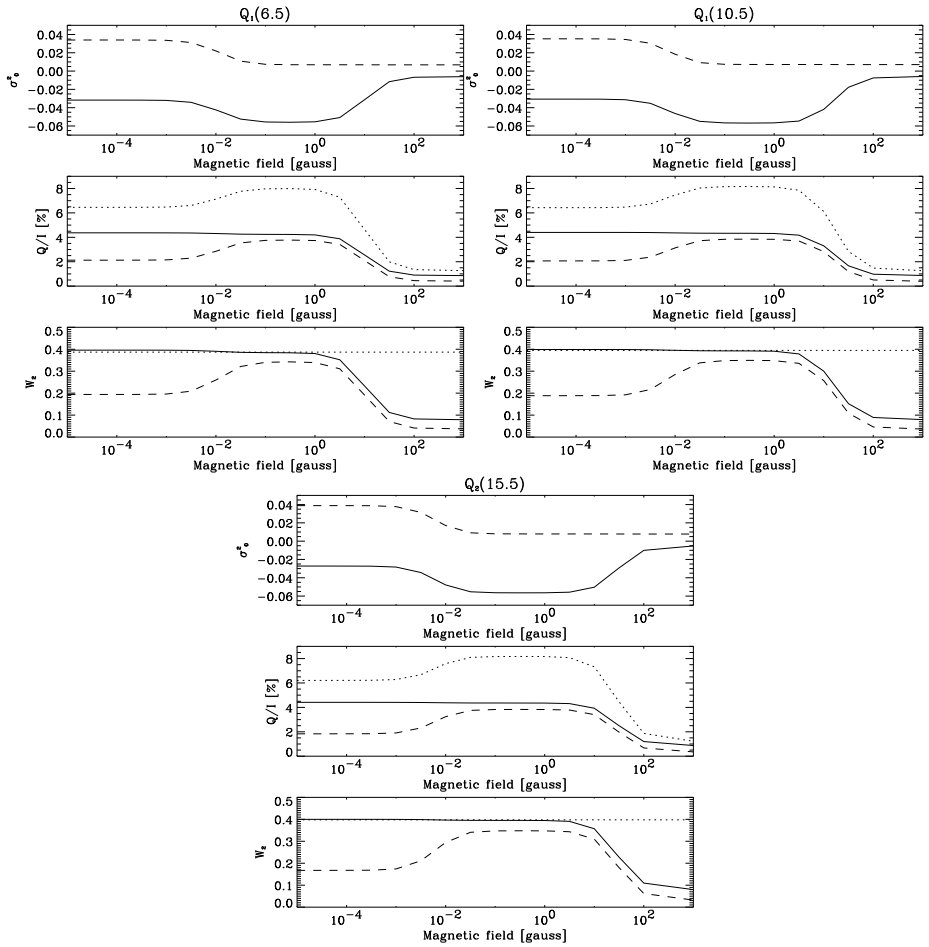

Figure 7.19: Upper panels: fractional alignment σ_0^2 of the upper (solid line) and lower (dashed line) levels of some transitions of the Q branch of MgH for increasing values of the microturbulent magnetic field. Refer to the text for details on how the microturbulent limit has been obtained. Middle panels: the corresponding fractional linear polarization (Q/I) obtained under the assumption of single scattering events. The solid line takes into account the effect of dichroism and the dashed line does not. The dotted line takes dichroism into account, but corresponds to the case $S_l/B_\nu = 2$. Lower panels: the corresponding polarizability factor obtained from the calculated Q/I via Eq. (7.7). The dotted line is the $\mathcal{W}_2$-value obtained from the analytical formula given by Landi Degl'Innocenti (2003).

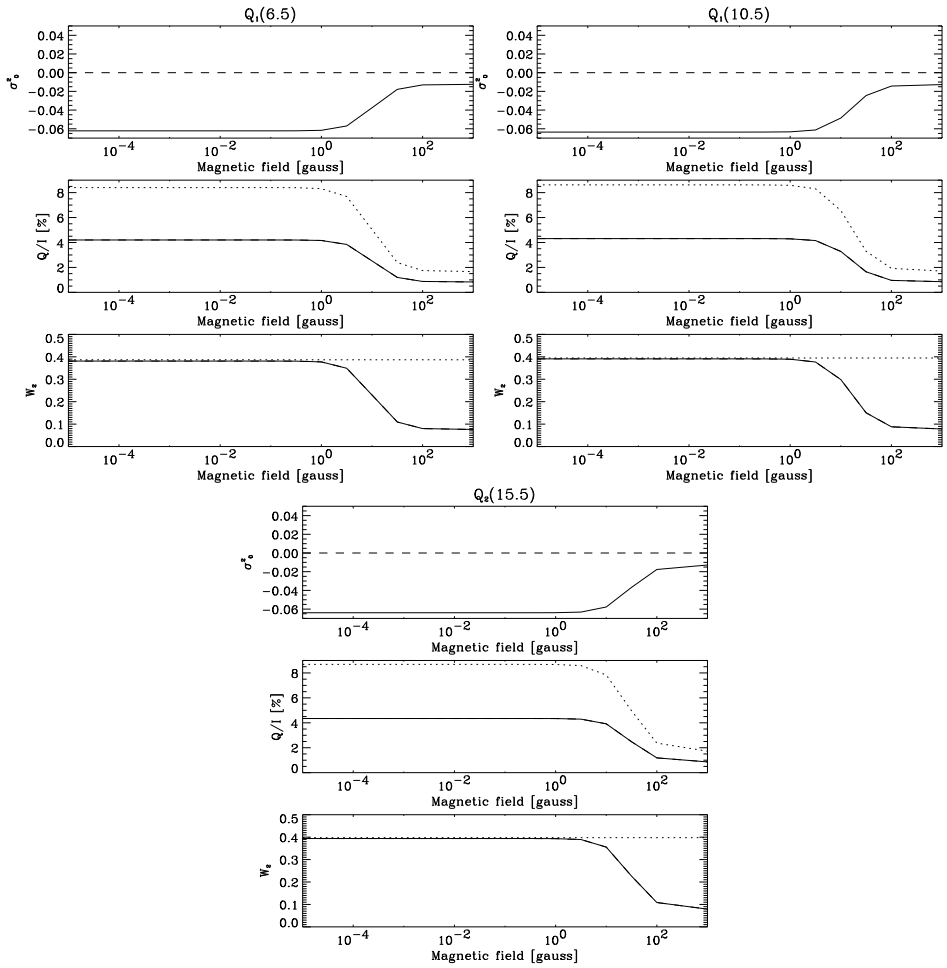

Figure 7.20: Upper panels: fractional alignment σ_0^2 of the upper (solid line) and lower (dashed line) levels of some transitions of the Q branch of MgH for increasing values of the microturbulent magnetic field when the lower level is unpolarized. Middle panels: the corresponding fractional linear polarization (Q/I) obtained under the assumption of single scattering events. Lower panels: the corresponding polarizability factor obtained from the calculated Q/I via Eq. (7.7). The dotted line is the $\mathcal{W}_2$-value obtained from the analytical formula given by Landi Degl'Innocenti (2003).

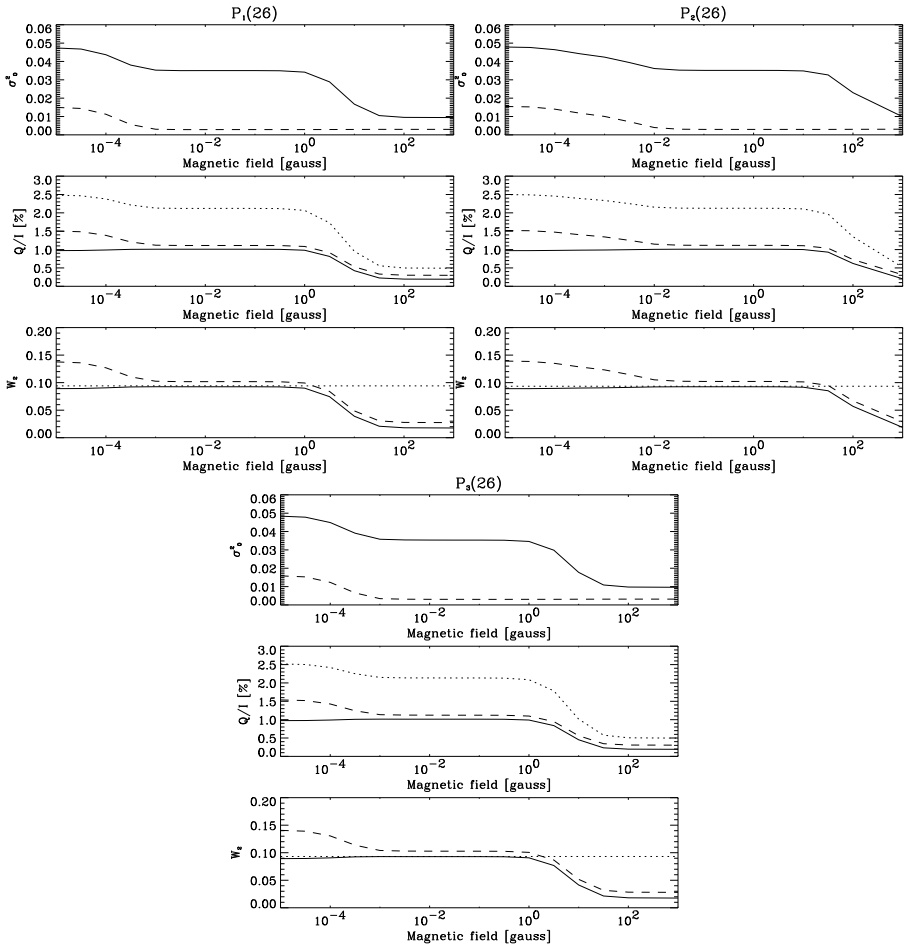

Figure 7.21: Upper panels: fractional alignment σ_0^2 of the upper (solid line) and lower (dashed line) levels of some transitions of the P and R branches of C_2 for increasing values of the microturbulent magnetic field. Refer to the text for details on how the microturbulent limit has been obtained. Middle panels: the corresponding fractional linear polarization (Q/I) obtained under the assumption of single scattering events. The solid line takes into account the effect of dichroism, the dashed line does not and the dotted line is the one obtained taking dichroism into account and $S_l/B_\nu = 2$. Lower panels: the corresponding polarizability factor obtained from the calculated Q/I via Eq. (7.7). The dotted line is the $\mathcal{W}_2$-value obtained from the analytical formula given by Landi Degl'Innocenti (2003).

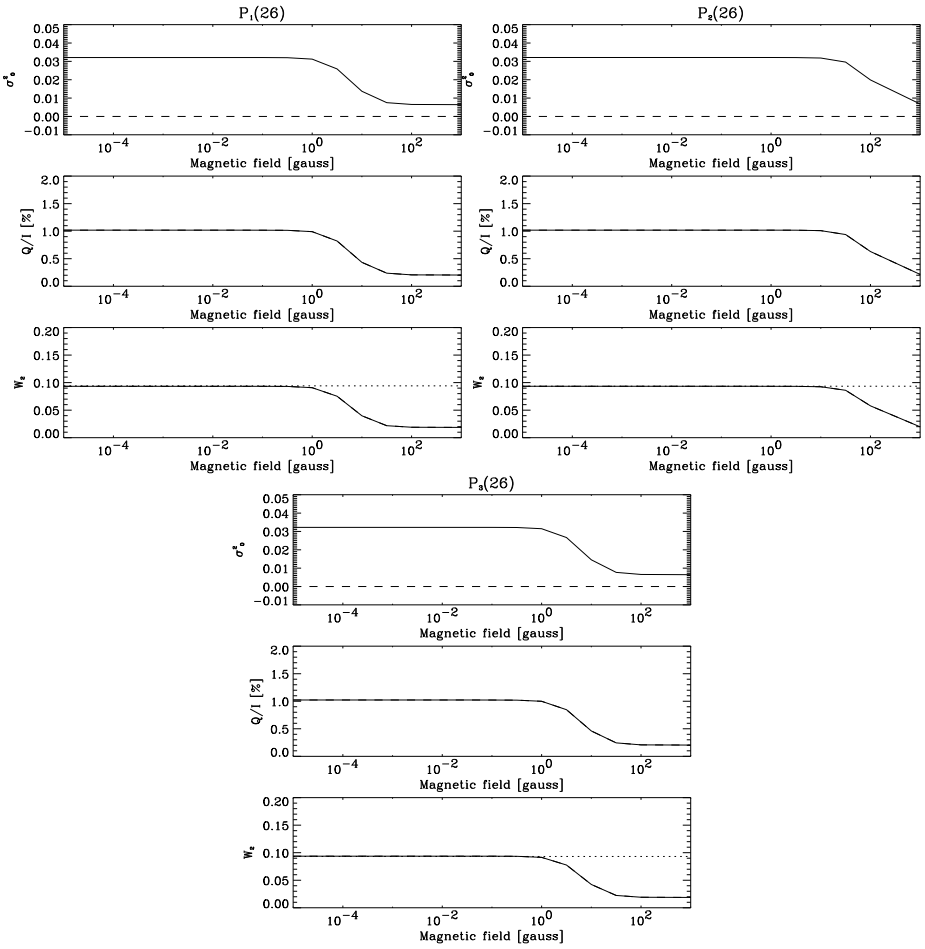

Figure 7.22: Upper panels: fractional alignment σ_0^2 of the upper (solid line) and lower (dashed line) levels of some transitions of the P and R branches of C_2 for increasing values of the microturbulent magnetic field when the lower level is unpolarized. Refer to the text for details on how the microturbulent limit has been obtained. Middle panels: the corresponding fractional linear polarization (Q/I) obtained under the assumption of single scattering events. Lower panels: the corresponding polarizability factor obtained from the calculated Q/I via Eq. (7.7). The dotted line is the $\mathcal{W}_2$-value obtained from the analytical formula given by Landi Degl'Innocenti (2003).

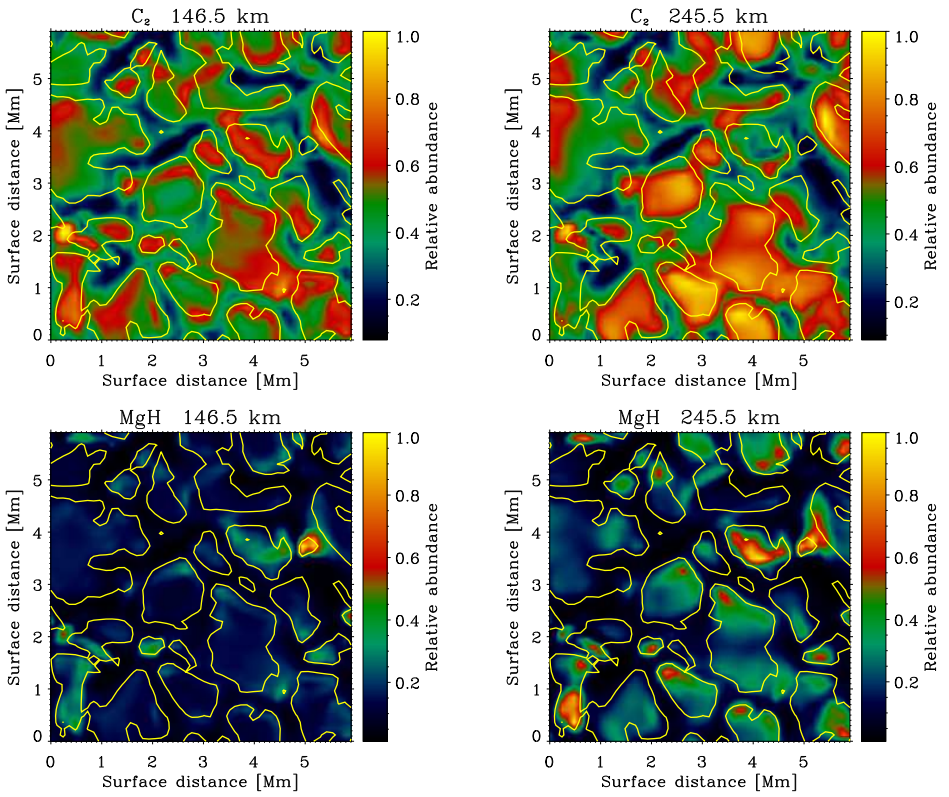

Figure 7.23: Number density of MgH and C_2 relative to the maximum concentration in the 3D snapshot model at heights of 145.5 km and 245.5 km. Note that h=0 km is, as usual, the height where we have optical depth unity in the continuum at 5000 Å for vertical incidence. Note also that the molecular abundance is higher in the upflowing material than in the downflowing plasma.

We have investigated the correlation factor between the MgH and C_2 concentrations and the local temperature and hydrogen number density at each height. The correlation between vectors X and Y can be written as (e.g., Press et al. 1986):

$$r(X,Y) = \frac{1}{N-1} \frac{\sum_{i=1}^{N} (X_i - \bar{X})(Y_i - \bar{Y})}{\sigma_X \sigma_Y}, \tag{7.28}$$

where the sum is extended up to the number N of elements in each vector, while

σ is the standard deviation of each vector. This correlation factor lies in the interval $[-1, 1]$ depending on whether the variables X and Y are completely anticorrelated or completely correlated. The case $r = 0$ means that both variables are not correlated at all. We have obtained the correlation factor for the following four combinations: T-n(MgH), T-$n(C_2)$, n(H)-n(MgH) and n(H)-$n(C_2)$. This factor is obtained independently for every height in the atmosphere, taking into account that the ICE approximation gives molecular abundances which depend only on local values of the thermodynamical conditions. We show in the left panel of Fig. 7.24 the correlation factor for all the heights in the Asplund et al. (2000) 3D model. Intuitively, the molecular abundances are anticorrelated with the local temperature, as can be understood from the ICE equations. On the other hand, they are correlated with the local hydrogen number density. At heights above 200 km, the C_2 abundance is strongly correlated with the hydrogen density, while this coupling is weaker for MgH. The contrary happens for the correlation with the temperature, which is much stronger for MgH than for C_2. In fact, the C_2 number density gets almost completely uncorrelated with the local temperature above 400 km. Interestingly, both molecular abundances get almost completely uncorrelated with the hydrogen number density at heights around 0 km, where the optical depth unity is reached for 5000 Å in vertical incidence.

However, the most conclusive plot is the one shown in the right panel of Fig. 7.24, where the correlation between the molecular abundances and the vertical velocity v_z is plotted for all the heights of the 3D model. Note that we are using the convention that $v_z > 0$ for macroscopic motions going downward, and $v_z < 0$ for macroscopic motions going upward. Therefore, $v_z > 0$ is related to downflows (which coincide with intergranular material in the deep layers) and $v_z < 0$ is related to upflows (which coincide with granular material in the deep layers). The correlation has been obtained between the molecular abundances and the local vertical velocity and between the molecular abundances and the vertical velocity at h=0 km, which is representative of the granular pattern observed in the continuum radiation at 5000 Å. However, note that the general trend of this plot remains equal for both calculations. Deep in the atmosphere, the regions with higher molecular abundances are those corresponding to downflows, since they are positively correlated. Following the same reasoning, at heights $h \lesssim 0$ km the regions with lower molecular abundance are those showing upflows. At regions around 0 km, there is a change of sign of

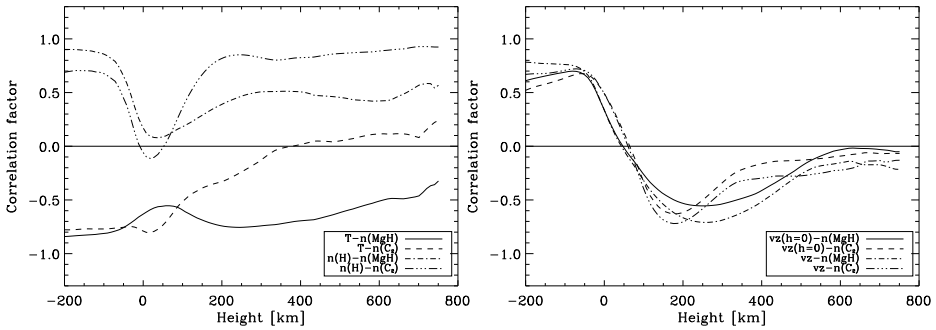

Figure 7.24: Various correlation factors at each height in the three-dimensional radiation hydrodynamical simulation.

the correlation factor r, which indicates that the regions with higher molecular abundance are those corresponding to upflows. This behavior has been also pointed out for the case of CO. Our Fig. 7.24 shows, in a more conclusive way and for all the heights of the 3D model what can be also seen in Fig. 7.23 for two selected heights.

In order to get an estimation of the region where these molecular lines are formed, we have calculated the position of the $\tau = 1$ surfaces at the wavelengths where the C_2 molecular lines are situated. To this end, we have carried out formal solutions of the RT equation in one-dimensional models of the granular and intergranular material extracted from the 3D snapshot of the hydrodynamical simulation. Of course, these 1D models are only representative of what can be observed in the Sun when a synthesis is done at $\mu = 1$. For $\mu < 1$, the emergent ray crosses granular and intergranular regions and the distinction between a granule and intergranule looses its meaning. For an emergent ray at $\mu = 1$, the depth at which $\tau = 1$ is reached for the granular material at continuum wavelengths is $h \approx 50$ km, while for the intergranular model it is $h \approx -100$ km. Since the considered wavelength is close to 5000 Å, we get depths very close to $h = 0$ km. If one performs spectral synthesis at μ=0.1 in such 1D models independently, the continuum optical depth unity is obtained at $h \approx 230$ km for the granular model and at $h \approx 170$ km for the intergranular model. On the other hand, for $\mu = 1$ rays we find that $\tau = 1$ at the line core of the C_2 lines is reached at $h \approx 290$ km for the granule and at $h \approx 200$ km for the intergranule.

Note that the position of $\tau = 1$ at the core of the line is very close to that of the continuum since the lines are weak. Since both models are assumed to be 1D, we find an appreciable difference between the position of the $\tau = 1$ surfaces for the granular and intergranular models. We have also performed LTE spectral synthesis of the C_2 lines at $\mu = 0.1$ in the 3D model. The distinction between granule and intergranule in this calculation looses its meaning because the ray crosses regions with both granular and intergranular physical conditions. The spectra emerging from all the 50 surface points we have synthesized are very similar and the above-mentioned sizable variation on the depth of the line core in the individual granular and intergranular models is lost. In fact, if we compare these results with the individual 1D spectra, one finds that the 3D synthesis is dominated by the granular spectra obtained for the 1D case. This can be easily understood in view of the previous results. We have seen that the $\tau = 1$ surface is deeper in the atmosphere for the intergranule than for the granule. Therefore, if the whole atmosphere would be of intergranular type, the photon is very likely to escape from such deep regions. However, in the real situation, the photon will cross material with granular physical conditions when going upwards. Since the $\tau = 1$ surface for the granular material is almost 100 km higher in the atmosphere, the photon will be absorbed with a large probability and substituted by a photon generated in the granule. Typically, the probability of absorption could be approximated by $P = 1 - e^{-\tau}$, which, for $\tau \gtrsim 1$ gives $P \gtrsim 63$ %. A photon generated in an intergranule has a low probability of escaping to the surface while a photon generated in a granule has a much higher escape probability.

This idea has led us to try to fit the 3D spectra with the individual 1D spectra belonging to the granular and intergranular models. The fit is done with the following formula:

$$I_{3D} = \alpha I_{1D}^{\text{granule}} + (1 - \alpha)\, I_{1D}^{\text{intergranule}}, \tag{7.29}$$

where α plays the role of a filling factor. We get $\alpha = 0.55$ for a $\mu = 0.1$ observation.

If we calculate the area of the 3D snapshot model which is covered by upflowing or downflowing material, we find the results presented in Table 7.1. When going upward in the atmosphere, we find that there is less material going up and more material going down. It is interesting to see that, although the

Table 7.1: Surface covered by the granular and intergranular material at some heights of the 3D simulation by Asplund et al. (2000).

Height (km)	Upflows	Downflows
2	53 %	47 %
100	49 %	51 %
200	44 %	56 %
300	39 %	61 %

area covered by the upflowing regions becomes smaller than the are associated with downflowing regions when moving upwards in the atmosphere (see Table 7.1), the average spectrum in the spectral region where the MgH and C_2 lines originate has a weight of $\sim$55 % from the upflowing regions. Let us make the assumption that the observed Q/I signal can be represented as well with:

$$\left(\frac{Q}{I}\right) \approx \alpha_{\rm g} \left(\frac{Q}{I}\right)_{\rm g} + (1-\alpha_{\rm g}) \left(\frac{Q}{I}\right)_{\rm i} , \tag{7.30}$$

where $\alpha_{\rm g}$ is given by Table 7.1. Now, assume that there is a magnetic field present in the granular and the intergranular material, which produces depolarization via the Hanle effect, reducing in a factor $\beta_{\rm g}$ and $\beta_{\rm i}$ the scattering polarization of the corresponding zero magnetic field reference case, which we will assume that is similar in the granule and the intergranule and equal to $(Q/I)_0$. This last assumption is not correct at all because the anisotropy factor is completely different in both media (see Trujillo Bueno 2003b). We can rewrite Eq. (7.30) as:

$$\left(\frac{Q}{I}\right) \approx [\alpha_{\rm g}\beta_{\rm g} + (1-\alpha_{\rm g})\beta_{\rm i}] \left(\frac{Q}{I}\right)_0 . \tag{7.31}$$

Magnetoconvection simulations (e.g., Stein & Nordlund 2003) show that the magnetic field tends to concentrate in the intergranular lanes. Therefore, we assume now that the linear polarization signal in the intergranular material is in the saturation limit in which it is reduced by a factor 1/5, while the signal in the granular material is not significantly modified via the Hanle effect. Therefore,

$\beta_{\rm g} \sim 1$ and $\beta_{\rm i} \sim 1/5$. If we select the granular-material surface distribution at a height of $\sim$200 km as representative of the formation height of the molecular lines, we end up with:

$$\left(\frac{Q}{I}\right) \approx 0.55 \left(\frac{Q}{I}\right)_0 , \tag{7.32}$$

which states that the observed linear polarization signal emerging from the whole simulation is approximately equivalent to half the signal with no magnetic field. We can now take into account that the anisotropy factor in the granular and intergranular material is not the same. In this case, and making the assumption that the linear polarization signal is proportional to the anisotropy factor w, we can write a formula similar to the previous ones:

$$\left(\frac{Q}{I}\right) \approx \left[\alpha_{\rm g}\beta_{\rm g} + (1-\alpha_{\rm g})\beta_{\rm i}\frac{\omega_{\rm i}}{\omega_{\rm g}}\right] \left(\frac{Q}{I}\right)_0^{\rm g} , \tag{7.33}$$

where now $(Q/I)_0^{\rm g}$ is the one obtained in the granular material. Using the same numbers as before and typical anisotropy factors of $\omega_{\rm i} \sim 0.1$ and $\omega_{\rm g} \sim 0.17$, we end up with:

$$\left(\frac{Q}{I}\right) \approx 0.51 \left(\frac{Q}{I}\right)_0^{\rm g} , \tag{7.34}$$

a result which is very similar to the one presented before because the intergranular material contributes very weakly to the polarization signal due to the Hanle depolarization. Therefore, we expect, after this order-of-magnitude calculation that the observed linear polarization is approximately equal to half the signal produced in the absence of magnetic fields in the granular material. Of course, if the depolarization produced in the intergranular material is not enough to arrive to the saturation limit, this factor will increase.

7.2.9 Formal solution

Consider the radiative transfer equation given by Eq. (5.39). In the case of scattering polarization without the presence of a magnetic field, only Stokes I and Q are relevant and in a weakly anisotropic medium like the solar atmosphere

the RT equation simplifies to (see Trujillo Bueno 2003c):

$$\frac{dI}{ds} = \epsilon_I - \eta_I I - \eta_Q Q$$
$$\frac{dQ}{ds} = \epsilon_Q - \eta_Q I - \eta_I Q. \tag{7.35}$$

Consider now the very simple case of a plane-parallel slab of width $\Delta s_\perp$ with constant physical properties. In this case, the previous equations can be solved analytically. Moreover, we can simplify the problem further by assuming that the Stokes I parameter only suffers absorption when going through the slab while Stokes Q has contributions from both emission and absorption processes inside the slab. Therefore, we can safely neglect the terms ϵ_I and $\eta_Q Q$ in the first equation. In this case, the formal solution can be written as:

$$\begin{aligned} I(s) &= I_{\rm ph} e^{-\eta_I \Delta s} \\ Q(s) &= \frac{\epsilon_Q}{\eta_I}\left(1 - e^{-\eta_I \Delta s}\right) - \Delta s \eta_Q I_{\rm ph} e^{-\eta_I \Delta s}, \end{aligned} \tag{7.36}$$

where Δs is the physical length of the ray propagating in the medium, which is equal to $\Delta s = \Delta s_\perp / \mu$ for observation at angle μ. $I_{\rm ph}$ is the unpolarized photospheric radiation which illuminates the molecules. Note that the factor $\eta_I \Delta s$ is the total optical depth of the slab observed at angle μ. The value of η_I can be obtained from the solution of the SEE. We can factorize the total molecular population N from η_I and put it explicitly in the above expressions. Therefore, $\eta_I \Delta s = N \eta'_I \Delta s$, where η'_I is η_I / N. Therefore, by changing the factor $N\Delta s$, we may try to reproduce the observed absorptions that appear in the observed intensity spectrum of Gandorfer (2000). The value of this product which quite nicely represents the absorption in the C_2 lines is $N\Delta s \approx 6.1 \times 10^{14}$ cm^{-2}. Assuming a slab of 150 km width, this gives a C_2 abundance of $\sim 4 \times 10^6$ cm^{-3}, which is in good accordance with the typical C_2 densities at the heights where the lines are formed.

This approximate formal solution is capable of taking into account the blends between the P_1 and P_2 lines on the C_2 spectrum. Note that, in the case of single scattering, the presence of a blend does not change the amount of fractional linear polarization. In this case, $Q/I = \epsilon_Q / \epsilon_I$.

When magnetic fields are present, sources of Stokes U appear because neither ϵ_U nor η_U are zero. The expression for $U(s)$ is formally identical to the one obtained for $Q(s)$ but substituting η_Q by η_U and ϵ_Q by ϵ_U.

7.2.10 Probability distribution function

It is highly unlikely that the quiet Sun is filled with a "turbulent" magnetic field with only one value of the field strength. A distribution of field strengths results much more reliable. In fact, this possibility is supported by simulations (Cattaneo et al. 2003; Stein & Nordlund 2003) and observations (Lin & Rimmele 1999; Khomenko et al. 2003). C_2 molecular lines can be used to derive some information about the distribution of weak fields. The idea is that, since P_2 and R_2 lines have different sensitivity to the magnetic field than the P_1, P_3, R_1 and R_3 lines, a differential analysis can be performed. In fact, the regime at which the lines between levels with $J = N$ can be affected by the magnetic field through the Hanle effect is around two orders of magnitude larger than the regime of fields for the lines between levels with $J = N \pm 1$. For low fields, we can assume that the atomic polarization of the lines between $J = N$ levels is not affected by the Hanle effect. Therefore, in the absence of blends one can assume that the Q/I amplitudes in P_2 and R_2 lines represent the zero-field reference case. They can be used as reference lines with respect to which relative behaviors can be calculated. However, we have to take into account that for most of the observed C_2 lines, the P_2 (R_2) lines are blended with P_1 (R_1) lines.

The probability distribution function (PDF) is defined such that $P(B)dB$ is the probability that a given magnetic field B is between B and $B + dB$. This distribution is normalized to unity:

$$\int_0^\infty P(B)dB = 1. \tag{7.37}$$

With the aid of this distribution, one can easily calculate the expectation value of any given quantity that depends on the magnetic field. In particular, the expectation value of the observed Stokes I and Q profiles are given by:

$$\langle Q \rangle = \int_0^\infty P(B)Q(B)dB, \qquad \langle I \rangle = \int_0^\infty P(B)I(B)dB. \tag{7.38}$$

Stokes I is almost insensitive to the magnetic field except when the strong field Zeeman regime is reached. Because we are here interested in "quiet" regions dominated by sub-kG fields, we can write the expectation value of the fractional linear polarization as:

$$\left\langle \frac{Q}{I} \right\rangle = \frac{\langle Q \rangle}{\langle I \rangle} = \frac{\int_0^\infty P(B)Q(B)dB}{I} = \int_0^\infty P(B) \left(\frac{Q}{I} \right) (B)dB, \tag{7.39}$$

where Stokes I can be inserted into the integral because it does not significantly depend on the field strength.

The functional form of the PDF is not known and probably its dependence on the magnetic field is not simple. However, both simulations and observations (Cattaneo et al. 2003, Khomenko et al. 2003) show that the PDF of the quiet Sun shows a functional form which decays as the magnetic field strength increases, so the probability of finding weak fields is higher than the probability of finding strong fields when no distinction is made between granular and intergranular regions. We have selected the following three functional forms:

- A Voigt function characterized by two parameters: the damping constant a and the width ΔB_0. The choice of this PDF is motivated by the histograms obtained from magnetograms, like those of Harvey & White (1999) and Stenflo & Holzreuter (2002). The PDF obtained from such magnetograms are well fitted by a Voigt profile whose Gaussian part fits the region of low magnetic fields and its Lorentzian part fits the extended wings. The functional form is:

$$PDF(B) = f_0 H\left(a, \frac{B}{\Delta B_0}\right), \tag{7.40}$$

  where f_0 is chosen so that the normalization condition of the PDF is fulfilled and $H(a, v)$ is the Voigt function.

- An exponential function characterized by only one parameter, which gives an idea of the average field. This PDF has been chosen in view of the recent results concerning observations of the Zeeman effect in near-IR iron lines (Khomenko et al. 2003) and in recent simulations of turbulent dynamos (Cattaneo 1999). The histograms of the Zeeman splittings obtained from IR observations show an exponential decay for fields higher than $\sim$350 G, which suggests the choice of an exponential PDF when no distiction is made between granular and intergranular points. The simulations show a PDF with a narrow core at low fields which is well fitted by an exponential. The functional form is:

$$PDF(B) = f_0 \exp(-B/B_0), \tag{7.41}$$

  where B_0 is the mean value of the magnetic field and $f_0 = 1/B_0$ is the normalization constant.

- A two-exponential profile characterized by two parameters, as that proposed by Socas-Navarro & Sánchez Almeida (2003) in their tentative attempt of reconciling conflicting observations of the Zeeman effect in both IR and visible Fe I lines. The functional form is:

$$PDF(B) = \omega f_1 \exp(-B/B_1) + (1-\omega) f_2 \exp(-B/B_2), \tag{7.42}$$

  where f_1 and f_2 are chosen so that the PDF is normalized, while ω is used to parameterize the relative weight of the two exponentials. We have chosen the constant value $\omega = 0.05$ (Socas-Navarro & Sánchez Almeida 2003) and B_1 and B_2 remain as free parameters. Note here that the mean value of the magnetic field is approximately given by $\omega B_1 + (1-\omega)B_2$.

The filling factor for fields between $B_{\rm min}$ and $B_{\rm max}$ is given by:

$$C(B_{\rm min}, B_{\rm max}) = \int_{B_{\rm min}}^{B_{\rm max}} P(B) dB. \tag{7.43}$$

The filling factor of fields lower than a given field $B_{\rm max}$ is calculated as $C(0, B_{\rm max})$.

In order to get information about the magnetic PDF of the quiet Sun, we will take advantage of the special wavelength position of the C_2 lines. We have realized from the observation of the atlas of the second solar spectrum of Gandorfer (2000) that the lines between levels with $J = N + 1$ and $J = N$ are almost blended for high values of J, while those arising from levels $J = N - 1$ are well isolated. This effect appears in the P as well as in the R branch. As we will see, this apparently fortuitous effect turns out to be an important diagnostic tool. We will focus on the P branch, although it can be extended to the lines of the R branch as well.

Each triplet of P_1, P_2 and P_3 lines which share a similar wavelength have almost the same strength. Since all the C_2 lines of a given spin multiplet have the same Einstein coefficients and the value of the ρ^0_0 and ρ^2_0 of the upper and lower levels of such transitions are very similar, it can verified, by substitution in the RT equation, that for on-disk observations Q/I for the blended lines is approximately twice the value of Q/I for the non-blended lines, at least at first order (with small corrections for higher orders). When a magnetic field is present, the Hanle effect for the P_1 and P_3 lines start to operate at lower fields than for the P_2 lines and ,therefore, a value different from the zero-field case

Table 7.2: Approximate wavelength region of some rotational lines used for the determination of the ratio between the blended and non-blended lines and the effect of a turbulent magnetic field distribution in this ratio.

Wavelength (Å)	Blend	No-blend
5086	$R_1(36)+R_2(35)$	$R_3(34)$
5092	$R_1(34)+R_2(33)$	$R_3(32)$
5098	$R_1(32)+R_2(31)$	$R_3(30)$
5104	$R_1(30)+R_2(29)$	$R_3(28)$

is obtained. In order to account for this behavior, we define the ratio between the blended and the unblended lines as:

$$r = \frac{\left(\frac{Q}{I}\right)_{\rm blend}}{\left(\frac{Q}{I}\right)_{\rm no-blend}}. \tag{7.44}$$

In fact, when a magnetic field starts to depolarize the P_1 and P_3 lines, the ratio has to increase until reaching the field strength at which the P_2 lines start to be affected. At this moment, the ratio decreases until reaching again the zero-field value for extremely high fields, when both levels of the transition are saturated. The procedure which has to be followed to extract some information about the magnetic field distribution on the quiet Sun is the following. One solves the SEE for a given degree of anisotropy w including the Hanle effect of a "turbulent" magnetic field as done before for different values of the magnetic field strength which covers the range from 0 G to a given cutoff strength $B_{\rm max}$ (i.e., calculating the irreducible spherical components ρ^K_Q of the density matrix for different magnetic field vector directions and using a gaussian quadrature to integrate over the whole sphere). Using the ρ^K_Q values from the previous calculation, one can obtain the fractional linear polarization Q/I using one among several options (e.g., single scattering, plane-parallel slab, etc.) and the expression of the emission coefficients given by the Eqs. (5.46), (5.47) and their corresponding absorption coefficients. Once an specific functional form of the magnetic PDF and the values for the parameters that characterize each PDF are fixed, one can obtain via Eq. (7.39) the average value of Q/I

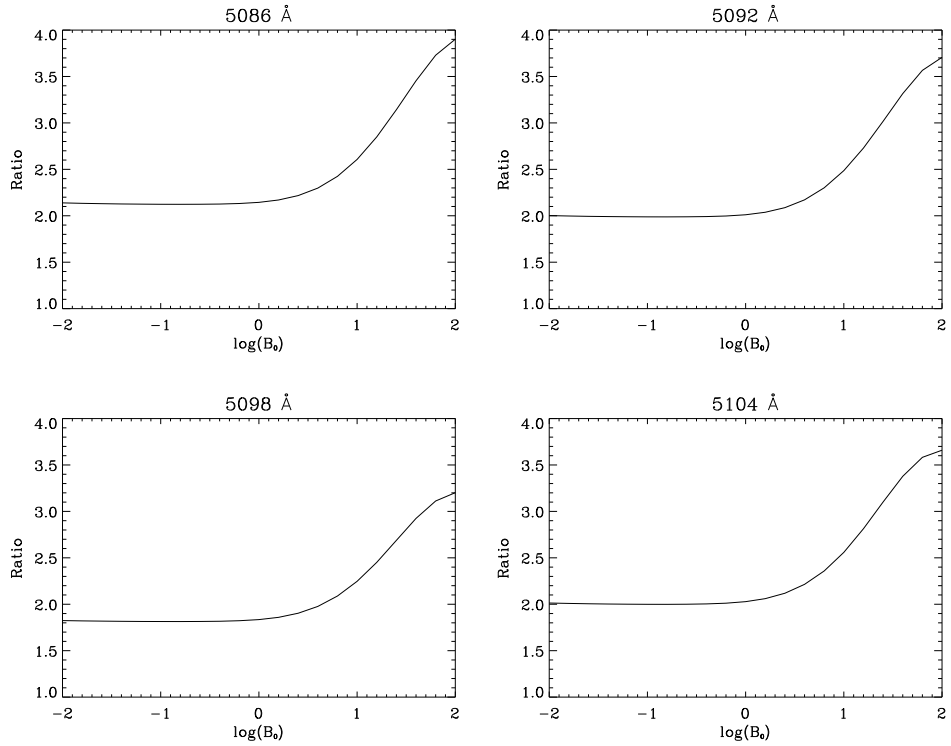

Figure 7.25: Ratio between the blended and the non-blended line when using an exponential PDF. The variation of the ratio is plotted versus the width of the distribution B_0. Note that this ratio monotonically increases for the range of turbulent magnetic fields included in the modeling.

which would emerge from an atmosphere with such a magnetic field distribution. Then, the ratio between the blended and the non-blended lines can be obtained and compared with the zero-field case. These results can be confronted with the observations and information about the parameters that characterize each proposed PDFs can be deduced.

The value of the ratio for four different wavelengths has been obtained using the previous three PDFs and varying the free parameters in a sufficiently wide range. We now describe what information have been obtained:

- **Exponential PDF**. Fig. 7.25 shows the value of the ratio obtained using

the exponential PDF. We can use this plot together with observations of the fractional linear polarization amplitudes in C_2 lines to calculate what can be considered as an upper limit for the width of the magnetic PDF of the stellar region where the molecular lines are being formed. The value of B at which a given filling factor C is reached can be obtained from $B = -B_0 \ln(1 - C)$ by integrating Eq. (7.43). We have not plotted the value of the ratio in the zero-field case, but we can consider that the width $B_0 = 0.01$ G can be effectively considered as the zero-field case since 99% of the fields are below 0.046 G in this case. This value of the magnetic field is low enough to be sure that there is no magnetic depolarization due to the Hanle effect, even in the P_1 and P_3 lines. This can be seen also from the figures, where a significant change in the ratio between the blended and the non-blended lines starts above 1 G. If we consider now that there is a given observational uncertainty in the determination of the ratio, we can give an upper limit for the width of the distribution of magnetic fields, which is different for different values of the uncertainty. We have considered which are the values of the maximum width of the distribution when the observed ratio is 0.5%, 5%, 10% and 15% higher than what is predicted to be for the zero-field reference case. We think that a value 15% higher than the zero-field ratio is high enough to consider it to be compatible with the presence of a magnetic field, instead of being produced by any possible observational spurious effect. If we pick the value of B_0 for which the value of the ratio is 15% higher than the zero-field case, we find that $B_0 \lesssim 10$ G for all the lines in Figure 7.25. For this value of B_0, 50% of the fields are below $\sim$7 G, 90% are below $\sim$23 G and 99% are below $\sim$46 G.

- **Two-exponential PDF**. Fig. 7.26 shows the value of the above-mentioned ratio obtained using the two-exponential PDF. The situation now is less direct than the case of a single exponential because we have the widths of the two exponentials as free parameters. Therefore, the plots of Fig. 7.26 are now surface plots in which we can vary the value of the ratio by changing any of the widths of the exponentials or both at the same time. Note that the ratio increases when increasing the width of the exponentials, while it decreases for very high values of the widths This effect is produced because we are weighting very strong fields which start to de-

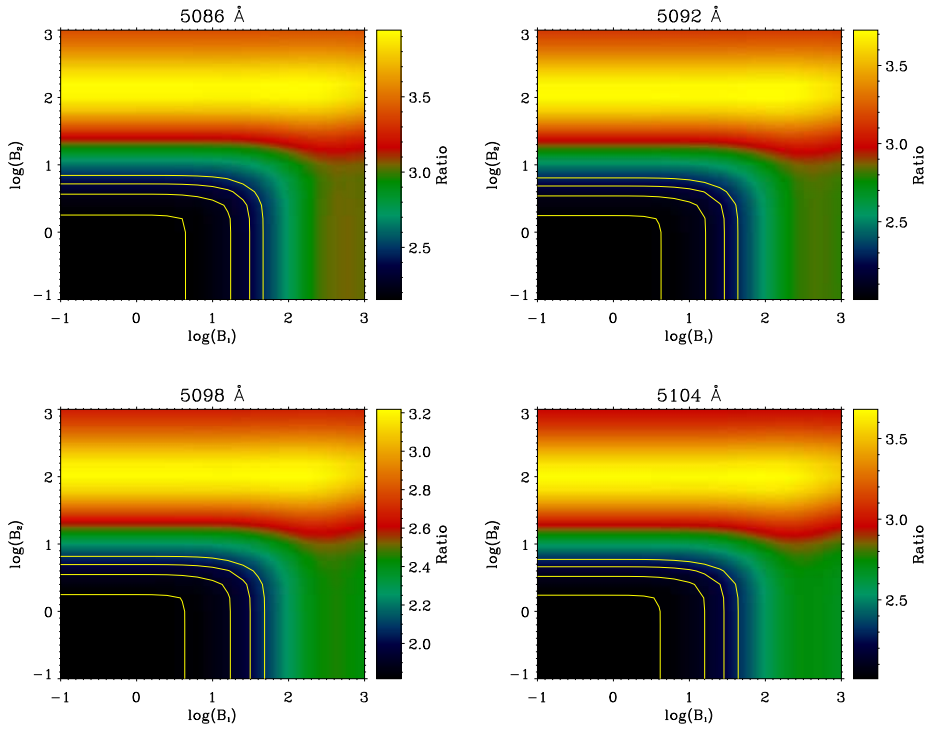

Figure 7.26: Ratio between the blended and the non-blended lines when using the two-exponentials PDF. The variation of the ratio is plotted versus the width of both distributions B_1 and B_2. Note that this ratio monotonically increases up to a certain width and then starts to decrease.

polarize the lines with $J = N$ and the ratio starts to decrease until all the lines are saturated. However, this region can only be taken qualitatively because we are in the strong field regime in which some of the assumptions made initially are not fulfilled (the transition to the Zeeman regime occurs). We have indicated in the figure where the ratio takes values of 0.5%, 5%, 10% and 15% higher than what is predicted to be for the zero-field case. Note that the curve for a ratio 15% higher than the zero-field case implies $B_1 \lesssim 50$ G and $B_2 \lesssim 7$ G. The limiting field for which the filling factor reaches a value C can also be obtained analytically, although a non-linear equation has to be solved. The field is given by $B = -\alpha B_2$,

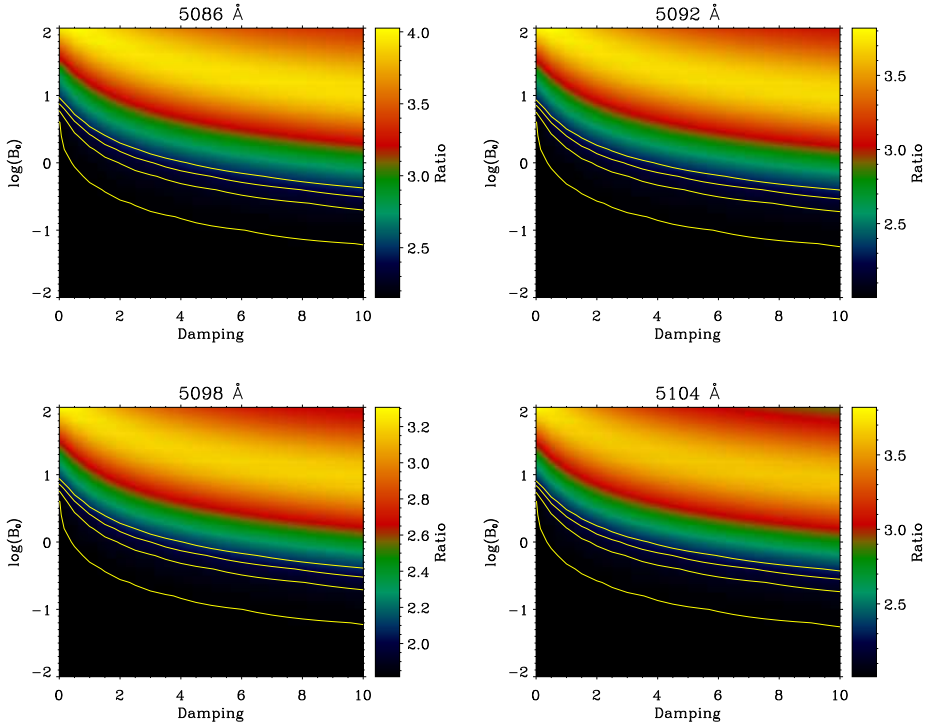

Figure 7.27: Ratio between the blended and the non-blended lines when using a PDF given by a Voigt function. The variation of the ratio is plotted versus the width of the distribution B_0 and the damping parameter a. Note that this ratio monotonically increases, at least for the range of turbulent magnetic fields included in the modeling.

where α is the solution of

$$\omega \left[e^{\left(\frac{\alpha B_2}{B_1}\right)} \right] + e^{\alpha} - 1 + C = 0. \tag{7.45}$$

This equation does not have a general closed solution (unless $B_1 = B_2$) and has to be solved numerically. Solving for the value α with ω=0.05 and the values of B_1 and B_2 obtained from the plots we get that 50% of the fields are below ∼5 G, 90% are below ∼19 G and 99% are below ∼80 G.

- **Voigt PDF**. Fig. 7.27 shows the value of the ratio obtained using the

Voigt function. The situation here is similar to the previous one, where we have a two-dimensional surface when varying the width of the Voigt profile and its damping parameter. We have indicated in the plot where the ratio takes a value 0.5%, 5%, 10% and 15% higher than what is predicted to be for the zero-field case. We point out that the width needed to maintain a given ratio varies when the damping of the Voigt profile is changed. However, we can see that the width is always between 1 and 10 G for $a = 10$ and $a = 0$, respectively, when we are interested in the curve where the ratio takes a value 15 % higher than the zero-field value. It is not easy to obtain the filling factor in a simple way as we did for the previous two PDFs case. Therefore, solving numerically the integral which establishes the filling factor for the case with $a = 0$ and $B_0 = 10$ G we find that 50% of the fields are below ∼5 G, 90% are below ∼ 12 G and 99% are below ∼18 G. For the case $a = 10$ and $B_0 = 1$ G, we find that 50% of the fields are below ∼4 G, 90% are below ∼ 26 G and 99% are below ∼211 G.

In view of the previous results for the three types of magnetic PDFs, the observed change in the ratio between the blended and the non-blended lines implies magnetic fields below ∼100 G in all the regimes (except in the very extreme case of the Voigt function with a damping parameter of $a = 10$). If the observations are obtained in extremely good conditions so that any difference on the ratio can be attributed to physical reasons and not to spurious effects, we can even reduce the uncertainty in the determination of the difference between the ratio in zero-field and the observed ratio and put a more restrictive upper limit for the magnetic field distribution. We have mentioned before that the linear polarization signal of the molecular lines is coming mainly from the upflowing regions (Trujillo Bueno 2003b). Therefore, most of the information about the magnetic PDF we can obtain from the molecular lines is related to the PDF of such regions. The rather low upper limits we have obtained assuming that there is no significant indication of depolarization in the C_2 lines is compatible with the assumption that the magnetic fields in these upflowing regions are quite weak. This assumption needs more exhaustive verification, although recent 3D magneto-convection simulations reproduce this behavior (Stein & Nordlund 2003).

Finally, we show in Fig. 7.28 a scatter plot of the ratio between the blended lines and the non-blended line obtained from Gandorfer's (2000) observations

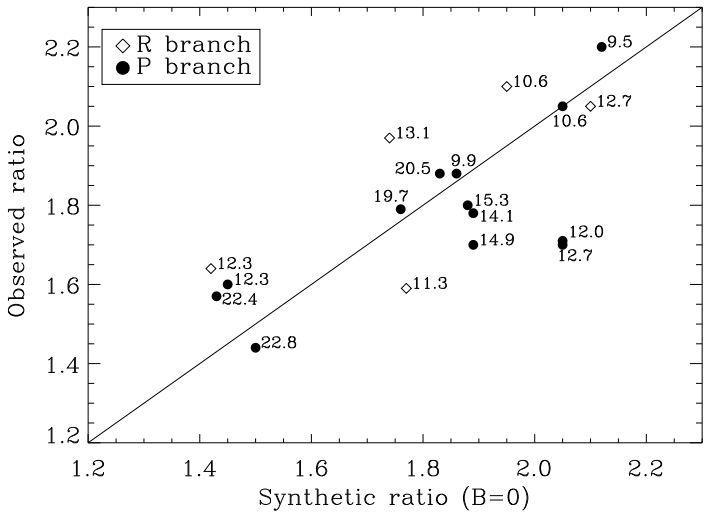

Figure 7.28: Observed ratio between the Q/I signals of the blended lines and the non-blended lines versus the theoretically calculated ratio under the assumption of zero magnetic field. We have plotted the ratio for R and P lines in the C_2 band. Note that there is a fairly good agreement between both. In case any important Hanle depolarization would be present, all the points should be shifted to higher values of the ratio. We have shown the critical Hanle field for each line. Note that there is no indication of a systematic behavior for lines with similar critical Hanle fields.

and those obtained from our modeling for the zero magnetic field case. When the magnetic field is increased, the ratio increases within a range of "sufficiently small" magnetic fields (smaller than the Hanle field of the lines between $J = N$ levels). Note that there is a fairly good correlation between the observed ratio and the synthetic ratio for zero-field. In fact, the linear Pearson correlation factor between both sets is 0.67, high enough to conclude that there is a clear linear trend between them. Furthermore, this linear relation seems to be independent on whether the lines belong to the R or P branches. We consider this result as a clear indication of very weak magnetic fields in the line formation regions of the C_2 lines. Additionally, there is no indication of any systematic behavior of the lines with similar critical Hanle fields.

7.3 Scattering polarization in CN lines

7.3.1 The observation

Fig. 7.29 shows the observations carried out to the blue of the band head of the CN band at 3883 Å (Stenflo 2003a; Gandorfer 2003). This observation was made possible due to advances in instrumentation since the ZIMPOL II polarimeter is now sensitive to the UV part of the spectrum. The upper panel shows the intensity spectrum where some of the lines can be identified with CN lines. The crowding of lines in the UV produces a continuous absorption which forms a pseudo-continuum. The lower panel shows the linear polarization spectrum Q/I. Note the conspicuous profiles produced by CN lines.

7.3.2 Band structure

The rotational lines of CN whose band head is placed at 3883 Å belong to the $B^2\Sigma^+$-$X^2\Sigma^+$ electronic transition. These electronic transitions take place between the second excited state and the fundamental level. The strongest lines belong to the $\Delta v = 0$ vibrational band. Since both levels have zero total electronic angular momentum, Λ-doubling is not present and every level with a given rotational quantum number N is only splitted in two sublevels due to the spin-rotation coupling.

7.3.3 Molecular models

As we have mentioned, the observed CN band in the UV is produced by transitions between the second excited electronic state and the fundamental level. The term energy difference between both levels is $T_e(B^2\Sigma^+) - T_e(X^2\Sigma^+) = 25752\ \mathrm{cm}^{-1}$. The first excited state $A^2\Pi$ is placed at $9245.48\ \mathrm{cm}^{-1}$ above the ground state. There is another strong electronic transition (see, e.g., Herzberg 1950) among the $A^2\Pi$ and $X^2\Sigma^+$ electronic states which is placed around 1.1 μm. The electronic transition which couples the two excited electronic levels lies around 6000 Å, although it is not seen in the solar spectrum. In principle, no selection rule forbids a dipolar transition between these two excited electronic states. It can perhaps have an extremely small electronic oscillator strength.

The electronic oscillator strengths of the UV band is $f_{\mathrm{el}}(\mathrm{UV}) \approx 0.033$ (Huber & Herzberg 2003). That of the IR band is an order of magnitude smaller

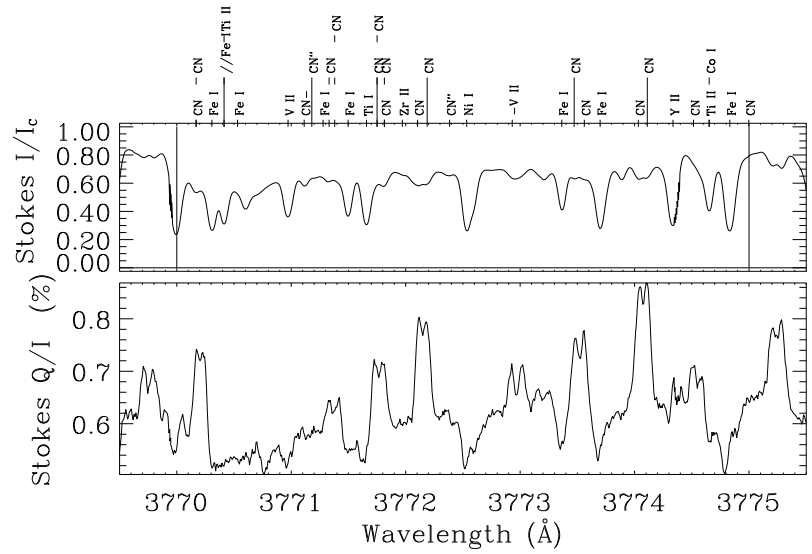

Figure 7.29: Observations of the CN scattering polarization in the ultraviolet. From Gandorfer (2003).

($f_{\rm el}$(IR) $\approx$ 0.0045). However, the huge number of transitions connecting the first excited state with the fundamental state can lead to an efficient transfer of atomic polarization between them. The typical feedback effect produced when lower level polarization is present may lead to an efficient modification of the atomic polarization of the second excited state. The atomic polarization of the vibro-rotational levels of the $B^2\Sigma^+$ state can be affected by the $A^2\Pi$ state, not directly, but through the fundamental level $X^2\Sigma$. If we focus ourselves on the electronic structure of the transition, it is similar to the so-called **V** transition which is mentioned in Trujillo Bueno's (2001) review paper on atomic polarization and the Hanle effect.

In view of the previous description, we have generated molecular models of CN including the first three electronic states and some vibrational levels inside each of these electronic states. Although transitions among all the vibrational levels are included, the strongest transitions are those with $\Delta v = 0$. In order to generate these models, we have used the linelist of Kurucz (1993b). However, there is a problem with the wavelengths of the individual rotational lines of the

UV band of CN in such a linelist. Although the $v = 0-0$ lines have the correct wavelengths (the same as the observed ones), there is a difference between the $v = 1-1$ observed and tabulated wavelengths. The difference increases for $v = 2-2$,..., transitions. This may be the result of an incorrect choice of the vibration-rotation constant of the molecule when Kurucz generated the linelist. In order to solve this problem, we have used the following correction scheme, supported by the fact that our results are not sensibly affected by the shift in wavelength. We have performed a fit between the wavelengths obtained from Kurucz's (1993b) linelist and the CN lines tabulated by Moore et al. (1966). Then, the obtained corrections to the wavenumber of the lines with $v \leq 2$ are:

$$\begin{aligned}
\Delta\omega^{0-0} &= 14919.549 - 1.1492719\omega_{\rm Kur} + 2.2132619 \times 10^{-5}\omega_{\rm Kur}^2 \\
\Delta\omega^{1-1} &= 27419.255 - 2.1179721\omega_{\rm Kur} + 4.0898518 \times 10^{-5}\omega_{\rm Kur}^2 \\
\Delta\omega^{2-2} &= 38294.406 - 3.0089444\omega_{\rm Kur} + 5.9074291 \times 10^{-5}\omega_{\rm Kur}^2, \quad (7.46)
\end{aligned}$$

where $\Delta\omega = \omega_{\rm Kur} - \omega_{\rm Moore}$. On the other hand, the wavelengths of the IR lines correspond to the observed wavelengths, so that no correction is needed for this band. In view of this, perhaps the rotational constants of the second excited electronic state $B^2\Sigma^+$ used by Kurucz (1993b) present some minor error.

Landé factors

Since $\Sigma = 0$ for the upper and lower levels of the $B - X$ ultraviolet transition, these levels can be correctly described under Hund's case (b), at least for magnetic fields below the transition to the Paschen-Back regime. For CN, this transition to the Paschen-Back regime takes place for fields as low as 77 G for the $X^2\Sigma^+$ level and 167 G for the $B^2\Sigma^+$ level (see Berdyugina & Solanki 2002). This is produced because the spin-rotation splitting is very small for this molecule, being $\gamma(B^2\Sigma^+) = 0.00725$ cm^{-1} and even smaller for the $X^2\Sigma^+$ state. However, this transition field strength increases as J increases. In all the subsequent calculations, we have used the Landé factors using Hund's case (b) Eq. (5.19), for simplicity. Therefore, the results for high fields and for low values of J should be considered as preliminary.

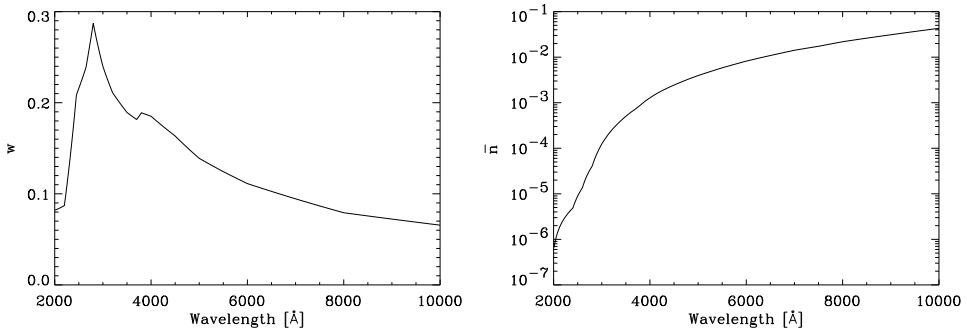

Figure 7.30: Anisotropy factor w and number of photons per mode $\bar{n}$ calculated using the observed center-to-limb variation of the solar continuum radiation tabulated by Cox (2000) as a function of wavelength.

7.3.4 Non-magnetic case

The molecular model we have built includes the electronic states $X^2\Sigma^+$, $A^2\Pi$ and $B^2\Sigma^+$. Inside each electronic state, we have included the first 6 vibrational levels from $v = 0$ to $v = 5$. Inside each vibrational level, we have included rotational levels from $J = 1/2$ to $J = 241/2$. Due to the parity selection rule, we end up with two independent subsystems which are not radiatively linked because we are not including pure rotational lines inside each vibrational level. This effect is similar to the one found in MgH. Therefore we have to solve two completely independent problems. The number of rotational levels included in the model is 2898 for each parity. The number of radiative transitions is 30383, ranging from 3035 Å to 1 μm, with the two bands $B - X$ and $A - X$ well separated in wavelength. In order to be able to solve the problem under different physical conditions (different values

of the depolarizing collisions and magnetic field strengths), we have applied the weak anisotropy limit. When limiting the spherical tensor components ρ^K_Q of the density matrix to $K \leq 2$, we end up with "only" 5848 unknowns in the SEE linear system. On the other hand, if we take into account all the multipole moments of the density matrix for each level J, the total number of unknowns would have raised to 177138!. When dealing with such a big number of variables, special numerical techniques are necessary (Press et al. 1986).

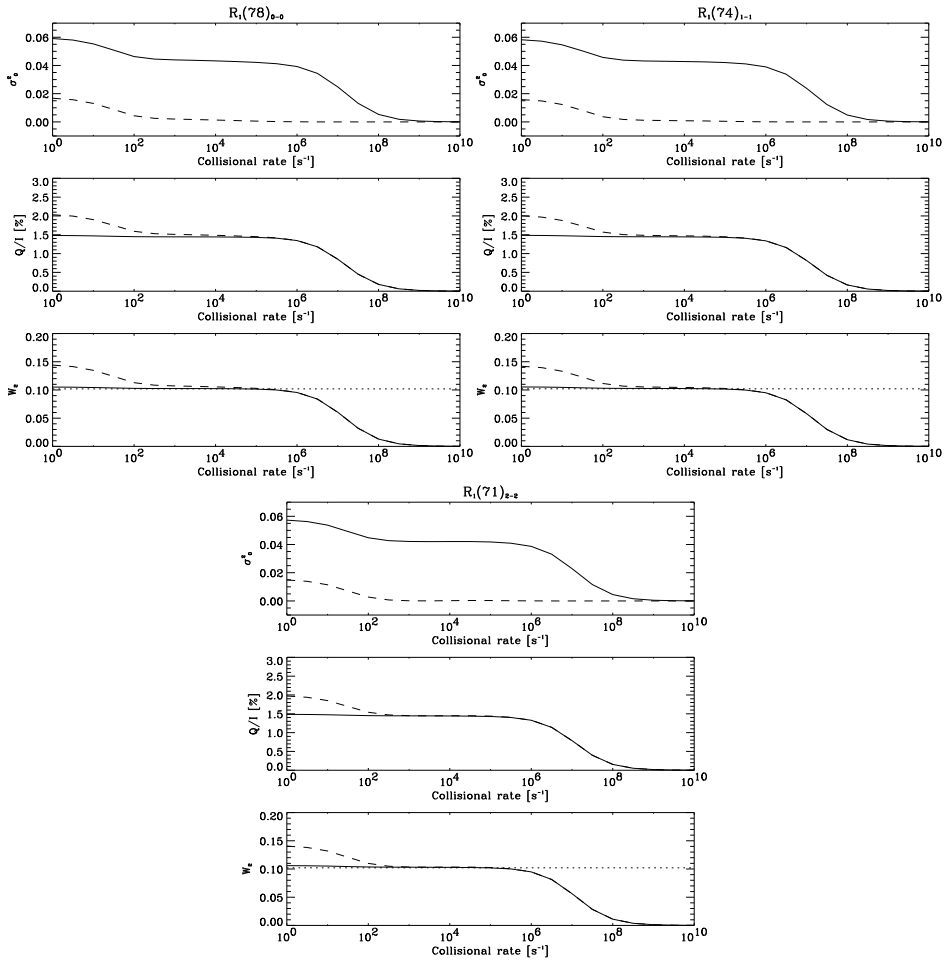

Figure 7.31: Upper panels: fractional alignment σ_0^2 of the upper (solid line) and lower (dashed line) levels of some transitions of the R branch of CN for different vibrational bands and for different values of the depolarizing collisional rate. Middle panels: the corresponding fractional linear polarization (Q/I) obtained under the assumption of single scattering events. The solid line takes into account the effect of dichroism while the dashed line does not include dichroism. Lower panels: the corresponding polarizability factor obtained from the calculated Q/I via Eq. (7.7). The dotted line is the $\mathcal{W}_2$-value obtained from the analytical formula given by Landi Degl'Innocenti (2003).

If one naïvely tries to generate a matrix of this size in double precision, the memory requirements would be ∼230 Gb. In order to avoid this, one can take advantage of the big number of zero entries in the matrix and take advantage of its sparse form (see, e.g., Press et al. 1986). We have found this unnecessary for the non-magnetic case since it is enough with the weak anisotropy limit simplification. However, we will see that it turns out to be fundamental to use such techniques for the magnetic case.

The molecular model we are using includes transitions in the UV and in the IR. The anisotropy factor changes for different wavelengths, being much higher in the blue part of the spectrum than in the red part. This wavelength dependence has to be taken into account because we are including transitions which span over a large range in wavelengths. We have used the observed center-to-limb variation of the solar continuum radiation and its wavelength dependence (Cox 2000) to calculate the anisotropy factor for each wavelength. Fig 7.30 shows the anisotropy factor w and the number of photons per mode $\bar{n}$ (see Eqs. 7.9 and 7.12). Note that the anisotropy factor reaches a maximum at ∼2800 Å, and decreases when going to longer and shorter wavelengths.

The numerical solution of the SEE gives the alignment (ρ^2_0) and the fractional alignment ($\sigma^2_0 = \rho^2_0/\rho^0_0$). when the depolarization collisions are increased. We have plotted the results for three of the rotational lines observed by Gandorfer (2003) whose CN scattering polarization observations we reproduce in Fig. (7.29). Fig. 7.31 shows the fractional alignment of the upper and lower levels, together with the emergent Q/I under the assumption of single scattering events. We also show the value of the polarizability factor $\mathcal{W}_2$ obtained from Eq. (7.7). Note that the behavior is very similar to that obtained for C_2 in Fig. 7.13,

even although the electronic transition is completely different. The main difference comes from the different value of the anisotropy factor which is larger at the UV for the CN transitions than at the visible for the C_2 lines. Furthermore, the different values of the Einstein coefficients produces a slight shift in the position of the collisional depolarization of the upper and lower levels, which is hardly detectable. As in the case of C_2, Q/I and $\mathcal{W}_2$ remain constant for a large range of depolarizing collisions when dichroism effects are taken into account in Q/I.

Fig. 7.32 shows the variation of σ^2_0 with J when depolarization collisions

are not included in the SEE. We have plotted separately σ_0^2 for the upper and lower levels of the $A-X$ IR band and for the $B-X$ UV band. Note that both transitions share the same lower level. The behavior of σ_0^2 does not seem to depend on whether the line is between levels with $J = N+1/2$ or between levels with $J = N-1/2$. Something quite important is that the fractional alignment of the levels in the second excited $B^2\Sigma^+$ state is much higher than in the first excited $A^2\Pi$ state. Since σ_0^2 is roughly proportional to the anisotropy factor (at least, it is higher the higher the value of w), this fact can be easily explained because the anisotropy in the UV is higher than in the IR. There is a factor of $\sim$2 between the value of σ_0^2 for both excited states, which is roughly equivalent to the difference in the anisotropy factor between the regions around 3800 Å and 8000 Å, where both electronic bands are situated.

Note that there is a small spread in the value of σ_0^2 in Figure 7.32. This spread is produced because we are plotting the value of σ_0^2 for all the vibrational levels v with a given value of J. However, the spread is very small, telling us that the atomic polarization is almost independent of the vibrational level we are considering. Concerning the variation of the fractional alignment with the rotational level, we can see that it is almost independent of J. However, in Fig. 7.33 we show the value of σ_0^2 for all the vibro-rotational levels calculated using only the fundamental and the first excited electronic states. By comparing it with Fig. 7.32, we can investigate the effect of including the intermediate electronic state. The obtained fractional alignment is different for intermediate J. On the other hand, for small and high J, the results are in good agreement. Therefore, the inclusion of the $A^2\Pi$ state stabilizes the atomic polarization of the fundamental and the second excited electronic states. In fact, it increases the polarization of the upper and lower levels of the $B-X$ transition. Although σ_0^2 turns out to be different when including the first excited electronic state and when it is not included, the value of Q/I is quite similar for high J, because it is proportional to the difference $\sigma_0^2(\mathrm{up}) - \sigma_0^2(\mathrm{low})$. Therefore, even in the absence of the $A^2\Pi$ state, one could obtain correct values of Q/I, although the atomic polarization would not be calculated correctly. As shown by Asensio Ramos & Trujillo Bueno (2003b), this lack of variation of σ_0^2 leads to a natural explanation of the "ladder" pattern in the $2-2$, $1-1$ and $0-0$ lines of CN observed by Gandorfer (2003). We will show this in more detail below.

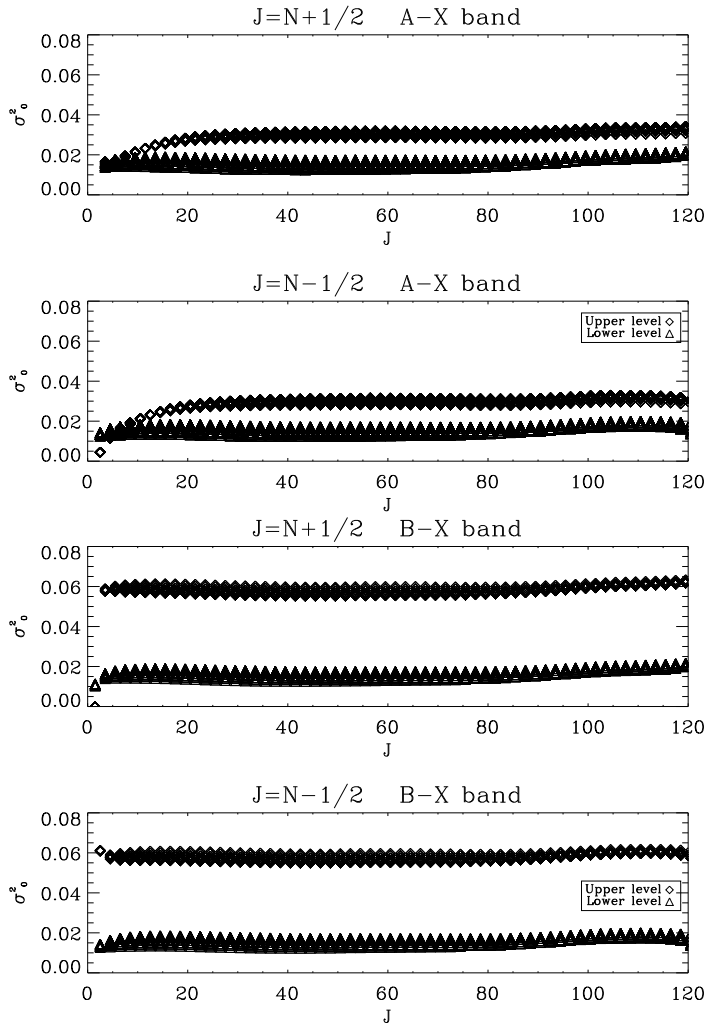

Figure 7.32: Fractional alignment of the upper and lower levels of the vibro-rotational transitions of the $B-X$ and $A-X$ electronic bands of CN. Note that the $X^2\Sigma^+$ state is common to both transitions.

7.3.5 Relative strength of the lines

The intensity spectrum of the spectral region around 3883 Å shows the presence of a rather low pseudo-continuum with a relative absorption I/I_c of $\sim$0.6. The

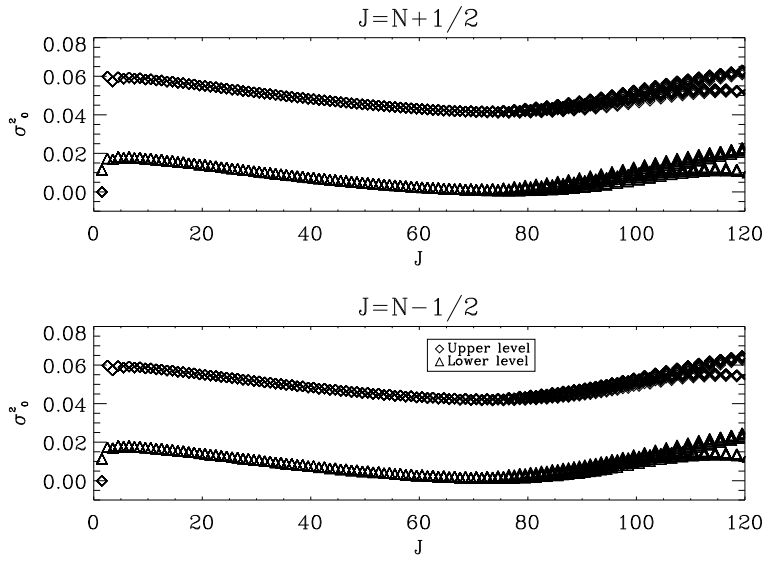

Figure 7.33: Fractional alignment of the upper and lower levels of the vibro-rotational transitions of the $B-X$ electronic band of CN. This calculation has been performed including only the $B^2\Sigma^+$ and the $A^2\Sigma^+$ states.

CN lines, with relative absorptions which rarely arrive to 0.5, can be considered as weak lines. Therefore, the modeling of scattering polarization in such CN lines requires using the formula appropriate for weak lines, i.e. that given by Eq. (7.21). We can consider that we are in the weak anisotropy limit, so that the second order terms in σ_0^2 can be neglected. Furthermore, since the line is weak, we can also neglect second order terms in r_l. The resulting formula is similar to the one obtained by Landi Degl'Innocenti (2003) and reads:

$$Q/I = \frac{3}{2\sqrt{2}} r_l \left[\frac{S_l}{B_\nu} \omega^{(2)}_{J_u J_l} \sigma_0^2(u) - \omega^{(2)}_{J_l J_u} \sigma_0^2(l) \right]. \tag{7.47}$$

Considering now rotational lines with high values of J (so that we can use the asymptotic value of the $\omega^{(2)}_{J_u J_l}$ quantities) and since the most conspicuous observed lines belong to the R branch, we can verify that:

$$\lim_{J\to\infty} \omega^{(2)}_{JJ\pm1} = \frac{1}{\sqrt{10}}. \tag{7.48}$$

We have verified that the value of σ_0^2 is almost independent of the value of the vibrational level, so that the difference in the emergent Q/I between two lines resulting from different vibrational levels must come from the difference on the line strength r_l. We can assume that the continuum opacity is the same for lines belonging to different vibrational levels. This assumption is supported by the fact that the studied CN lines are very close in wavelength and because the intensity profiles have almost similar depths (the CN lines are formed in quite similar heights in the atmosphere). There is a strong line blanketing at these wavelengths and so the value of I/I_c remains at $\sim$0.6 forming an intensity pseudo-continuum. Therefore, the CN lines are formed in a region where there is an additional opacity coming from many lines (probably lines from metallic elements) which can be considered as another contribution to the continuum opacity. We have performed LTE synthesis of this UV region including all the CN lines. If a standard opacity package is used, we get very strong CN lines with relative absorptions as deep as $\sim$0.6. However, as can be verified from the observations of Gandorfer (2003), the CN lines appear as very weak in the intensity spectrum. In order to investigate the order of magnitude of the additional (missing) opacity, we have artificially incremented it by adding a factor $f \geq 0$ to the continuum opacity. Under this assumption, the line strength is given by:

$$r_l = \frac{\eta_I^l}{\eta_I^l + \eta_I^c + \eta_I^{\rm blank}} \approx \frac{\eta_I^l}{\eta_I^l + (1+f)\eta_I^c}. \tag{7.49}$$

We have fitted the value of f via a trial-and-error scheme until reaching a relative absorption of $\sim$0.6. The value of f obtained is $f \sim 4$.

Fig. 7.34 shows the value of the ratio ($r_l(0-0)/r_l(2-2)$, at line center) between the $0-0$ and $2-2$ line strengths and between the $1-1$ and $2-2$ line strengths ($r_l(0-0)/r_l(2-2)$, also at line center) for the CN lines between 3773 and 3774 Å. Such ratios have been obtained for the physical conditions of the FAL-C atmospheric model. The behavior is similar for the rest of CN lines situated in a similar spectral region. We show the ratios for $f = 0$ (no artificial blanketing added to the LTE synthesis) and for $f = 4$ (artificial blanketing added in order to obtain a relative absorption of 0.6 in the pseudo-continuum). The vertical lines indicate the height at which optical depth unity for μ=0.1 is reached for the $0-0$ (the shallowest), $1-1$ and $2-2$ (the deepest) lines. The value of the ratio is very small for $f = 0$. However, we know that this value

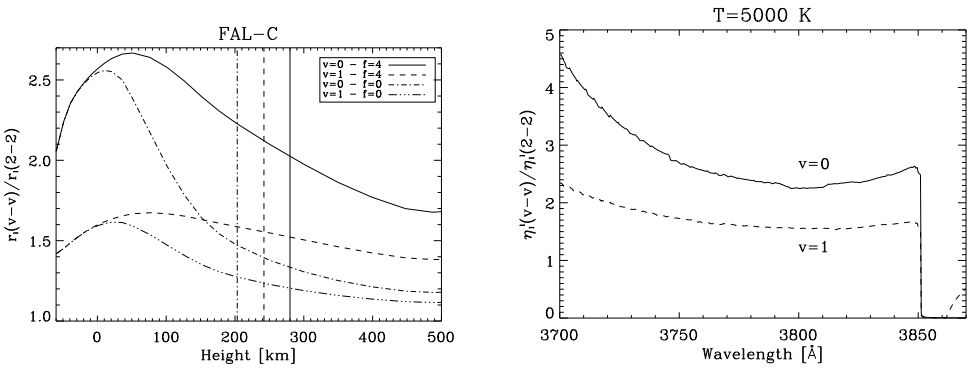

Figure 7.34: Ratio of absorption coefficients between the v=0-0 and the v=2-2 bands and between the v=1-1 and v=2-2 bands in the FAL-C model (*left panel*) for different values of the enhancement factor f of the continuum opacity. We also show the position of optical depth unity for a line of sight at μ=0.1 for the three lines (note that $h(0-0) > h(1-1) > h(2-2)$). The *right panel* shows the same ratios but for a typical temperature of 5000 K. This explains the observed ratios of the CN lines in the UV.

is not correct since the intensity spectrum is not similar to the observed one. The ratio is increased when f increases, becoming similar to the ratio between the line opacities for high values of f. The important idea is that, since η_I^l and η_I^c are of the same order of magnitude, an increase in f leads to an appreciable increase in the line strength ratio.

Table 7.3: Data for three of the rotational lines of CN observed by Gandorfer (2003). We give the wavelength of the transition, the line identification, the oscillator strength and the energy of the lower level. This information is enough to verify that the difference in amplitude is only produced by the differences in the line strength.

Wavelength (Å)	Line	$\log gf$	E_l [cm^{-1}]
3771.4	$R(71)_{2-2}$	0.194	13380
3771.8	$R(74)_{1-1}$	0.290	12245
3772.1	$R(78)_{0-0}$	0.399	11411

If we compare the value of r_l in the atmospheric region where the CN lines are formed (between 200 and 300 km), we find that $r_l(1-1)/r_l(2-2) \simeq 1.5$ and

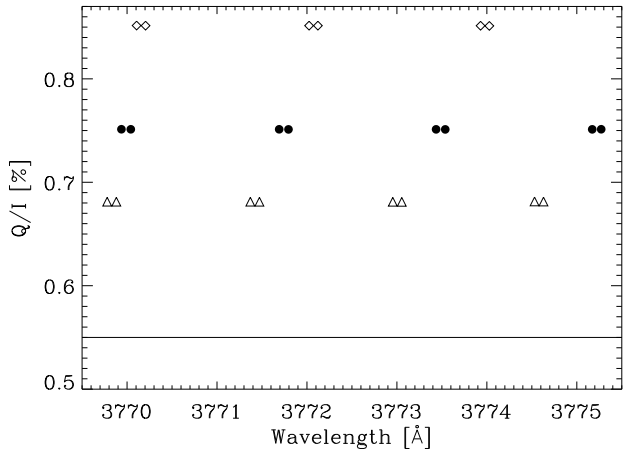

Figure 7.35: Synthetic value of the fractional linear polarization Q/I in the same spectral region observed by Gandorfer (2003). Note the good agreement between theory and observation. The triangles are the $v = 2 - 2$ lines, the black circles are the $v = 1 - 1$ lines and the white circles are the $v = 0 - 0$ lines.

$r_l(0-0)/r_l(2-2) \simeq 2$. The observed ratio can be obtained from the ratio of Q/I values observed by Gandorfer (2003), yielding a value of $[Q/I(1-1)]/[Q/I(2-2)] \simeq 1.6$ and $[Q/I(0-0)]/[Q/I(2-2)] \simeq 2.6$. The fit is quite good, taking into account that we are including the blanketing opacity in an ad-hoc way. We can now go to the limit in which the lines are very weak (they are very weak in the intensity spectrum, similar to what happens with MgH and C_2), and use the line strength given in the limit of very high f. The line opacity is proportional to the Einstein absorption coefficient and to the population of the lower level of the transition. Using the well-known relations between the Einstein coefficients and assuming LTE populations, we can write the ratio between line strengths as:

$$\frac{r_l(v-v)}{r_l(v'-v')} = \frac{\nu^2_{v'-v'}}{\nu^2_{v-v}} \frac{A^{v-v}_{ul}}{A^{v'-v'}_{ul}} e^{-(E^{v-v}_l - E^{v'-v'}_l)/kT}, \tag{7.50}$$

where ν is the frequency of the transition, A_{ul} its spontaneous Einstein coefficient and E_l the energy of the lower level of the transition. T is a temperature representative of the kinetic temperature in the region where the lines are

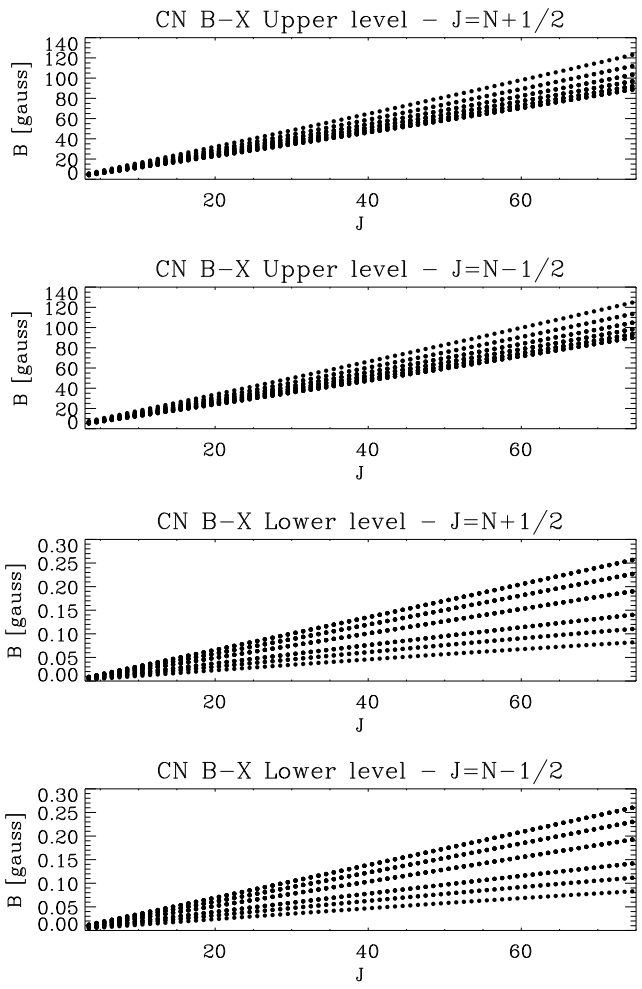

Figure 7.36: Hanle field for the upper and lower levels of the $B - X$ electronic transition of CN.

formed. Using the data of Table 7.3, we obtain, for a temperature of 5000 K, the ratios $r_l(1-1)/r_l(2-2) \simeq 1.7$ and $r_l(0-0)/r_l(2-2) \simeq 2.8$. The theoretically obtained values are in very good agreement with the observed ones. We can extend this calculation to all the wavelengths of the CN band.

The right panel of Fig. 7.34 shows the ratios $r_l(1-1)/r_l(2-2)$ and $r_l(0-0)/r_l(2-2)$ for a temperature of 5000 K. The band-head of the $2-2$ band is clearly seen at ∼3850 Å. The line strength ratio increases towards shorter wavelengths until reaching a value of ~ 4.5 for the $0-0$ versus $2-2$ ratio at wavelength around 3700 Å. In a more realistic modeling effort, one should take into account the UV lines blanketing and calculate the full line strength.

We have plotted in Figure 7.35 the value of Q/I obtained with Equation 7.47. We have applied a scaling factor to all the lines in order to fit the observed amplitude. The calculated relative amplitudes of Q/I are in good accordance with the observations by Gandorfer (2003).

7.3.6 Hanle fields

In order to have information on the magnetic field strength at which the Hanle effect starts to modify the atomic polarization of the levels of the $B-X$ transition of CN, we have calculated the Hanle field obtained with Eq. (7.8). The Landé factors of the rotational levels belonging to the three electronic states have been calculated using Hund's case (b) formula. This assumption is strictly valid for the levels of the B and X states, independently of the value of J, but only for the Zeeman regime. For the A state, the assumption becomes valid for values of J larger than ~ 30. However, we remind that the Zeeman regime in CN applies to magnetic field strengths below ∼100 G for low J, becoming larger for high J levels.

The resulting Hanle fields using such Landé factors are shown in Fig. 7.36 for the upper and lower levels of the CN transitions in the UV. Note that the Hanle field increases when increasing the rotation because the Landé factor in Hund's case (b) varies typically as J^{-1} (this yields the characteristic linear behavior of the Hanle field versus J). The critical Hanle field for the upper levels of the rotational transitions is always smaller than ∼120 G. We emphasize that we cannot trust the results obtained when the magnetic strength is larger than that at which the transition to Paschen-Back regime occurs because quantum interferences between sublevels pertaining to different J-levels can occur. The Hanle field for the lower levels is between 2 and 3 orders of magnitude lower, mainly representative of the difference in the lifetime of the upper and lower levels at these wavelengths. Furthermore, we can see that the value of the Hanle field is slightly different depending on the vibrational level. This is produced

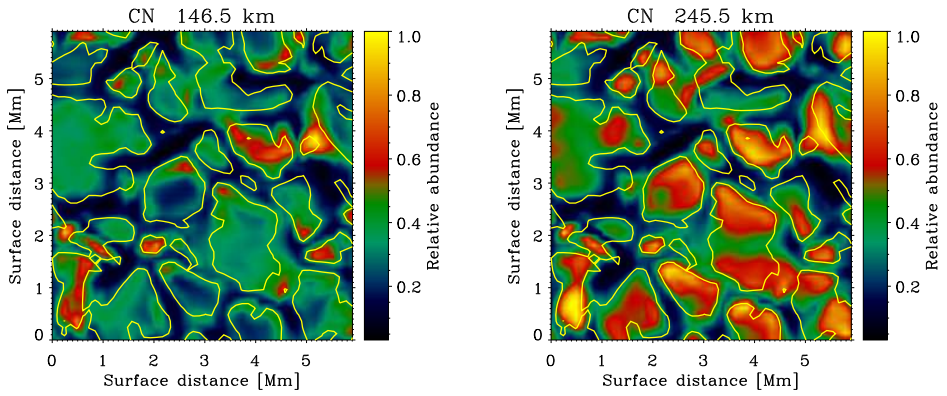

Figure 7.37: CN abundance relative to the maximum abundance. Note that the CN abundance is higher in the upflowing regions than in the downflowing regions.

by the difference in the lifetime of each level. The Einstein coefficients of the vibro-rotational transitions with $\Delta v = 0$ decrease when v increases, so that, the lifetime of a level is the higher the higher the value of v. This can lead to interesting behaviors in the polarization signal of the CN lines. Assume that the lines are formed in a region where there is a magnetic field of strength B. The lines with high J and high v would be depolarized if the field is large enough. On the other hand, the lines with small J and small v would be depolarized for much smaller fields. Therefore, there is a clear differential behavior between the CN lines of the band which could (in principle) be used to constrain the value of the field strength in the line formation region.

7.3.7 3D models

We have also calculated the CN abundance in a snapshot of the 3D hydrodynamical simulation of Asplund et al. (2000). The CN relative abundances for the same two heights investigated for MgH and C_2 are shown in Fig. 7.37. We see that the CN abundance is much higher in the upflowing regions. Therefore, similarly to what happens with the other molecular species, the CN spectrum is coming mainly from the upflowing regions. The polarized spectrum is then a tracer of the physical conditions in such regions, where the magnetic field is expected to be weaker.

Table 7.4: Sizes of the matrices, number of non-zero elements and computing time to solve some selected problems with an INTEL® XEON™ processor at 2.4 GHz.

Matrix Size	Number of non-zero elements	Gain factor	Time [s]
902×902	9248	88	1.5
3554×3554	53154	238	15.14
6489×6489	135456	311	82.01
17298×17298	570120	525	1594.96

7.3.8 Magnetic case

We have seen that a large molecular model is needed for obtaining reliable results for CN. The problem of calculating the effect of the magnetic field in the atomic polarization of the CN rotational levels is that the number of unknowns increases dramatically. If we invoke the weak anisotropy limit (which implies that we retain only the ρ^K_Q with $K \leq 2$), the tensor components with $Q \neq 0$ are different from zero, in general, and the number of unknowns is now 3 times larger than for the non-magnetic case. In the non-magnetic case we had ∼6000 unknowns, so that in the magnetic case, the number of unknowns is ∼18000. Such a linear system arising from the SEE is too big to be solved using standard techniques. A linear solver in which only the non-zero elements of the matrix are stored has to be used (sparse solvers).

The technique we have applied uses three vectors to build the matrix. One of them has the value of all the non-zero elements of the matrix, while the other two have the index in the "virtual" full matrix of each element of the first vector. The SEE matrix of size $N \times N$ has typically αN non-zero elements. Being α typically much smaller than N, the storage needs are reduced in a factor $N/\alpha \gg 1$. As an example, the SEE matrix for a CN molecular model including vibrational levels from $v = 0$ to $v = 5$ of the first three electronic states and including rotational levels from $J = 1/2$ to $J = 241/2$ when a magnetic field is included (limiting the multipoles to $K \leq 2$) has dimension 17298×17298. The number of non-zero elements is 570120, thus the gain in size is ∼525. Other examples are shown in Table 7.4.

An efficient algorithm has to be developed to fill the three vectors appro-

priately. The main disadvantage is that searches in these vectors have to be performed, which obviously take more time the longer they are. In order to obtain some information about the execution time of the code, we have modeled the time to fill the vector at element i as:

$$t_i = t_0 + \lambda i, \tag{7.51}$$

where we have included all the additional operations (solution of the linear system of equations, mathematical calculations, additional loops,$\cdots$) in a common time t_0. The previous equation states that the time to fill an element of the vector is proportional to the size of the vector, which is a direct consequence of the applied search algorithm. λ is a factor with units of time and which gives the proportionality between the time and the size of the vector. The total time to fill the n non-zero elements of the SEE matrix can be obtained by simply summing the previous equation:

$$T = \sum_{i=1}^{n} t_i = \frac{1}{2}\lambda n^2 + \left(\frac{1}{2}\lambda + t_0\right) n. \tag{7.52}$$

With the aid of this formula and considering the execution times shown in Table 7.4, we can obtain an approximate value of λ and t_0 by performing a fit, so that we can extrapolate the results to other problems and predict the execution time. The fit gives values of $\lambda = 10^{-8}$ and $t_0 = -5.8 \times 10^{-5}$. Note that the fit gives a negative value for t_0 which is not physical. This value is perhaps produced by limitations on the assumptions in writing formula 7.51. However, we have also performed a fit by applying the constraints $\lambda > 0$ and $t_0 > 0$ and we have obtained the values $\lambda = 9.81 \times 10^{-9}$ and $t_0 = 3.1 \times 10^{-8}$. These values are in accordance with the typical speeds of the computer in which these tests were performed (INTEL® XEON™ processor at 2.4 GHz). The formula gives a very good approximation to the total calculation time. If we go one step forward and perform a parabolic fit between the matrix size s and the number of non-zero elements in the matrix n (which turns out to be a quite good approximation), we can give the calculation time in terms of the size of the matrix. The final formulas are:

$$\begin{aligned} T &\approx 4.91 \times 10^{-9} n^2 + 3.56 \times 10^{-8} n \\ n &\approx 1.1 \times 10^{-3} s^2 + 14.31 s - 6707.78. \end{aligned} \tag{7.53}$$

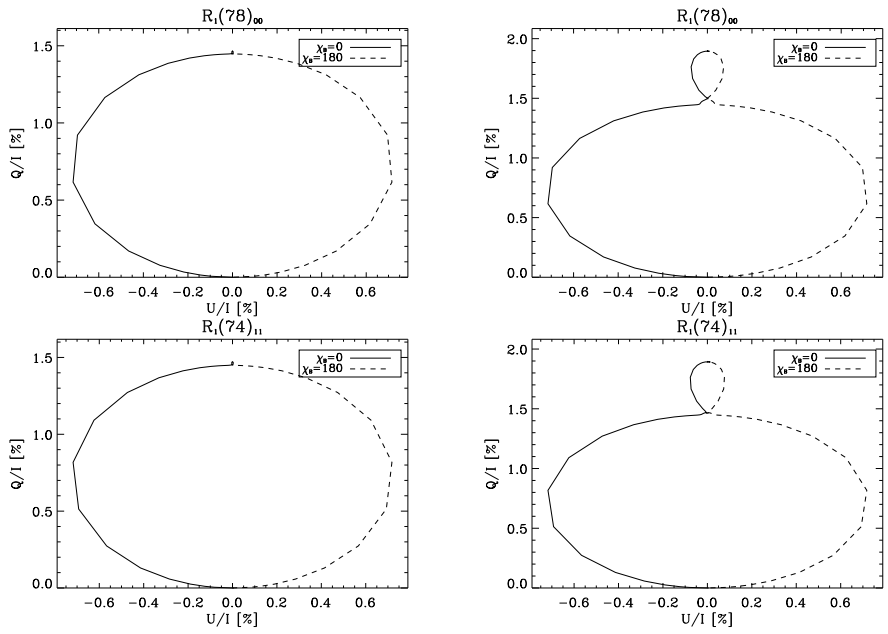

Figure 7.38: Hanle diagrams for the $R_1(78)_{00}$ and $R_1(74)_{11}$ lines of CN. The left panel shows the Hanle diagram when dichroism is taken into account, while the right panel shows the Hanle diagram when dichroism is neglected.

By inverting these equations, we can obtain the size of a matrix which can be solved in a given amount of time. The result is a fourth order polynomial so that we take the positive real root. This way, a problem of size ∼56000 can be solved in 24 hours, one of size ∼94200 can be solved in one week and one of size ∼230000 can be solved in one month.

With the previous modification, the computer program can now be used to calculate more complicated models including the effect of the magnetic field in the atomic polarization. We have calculated the effect of a deterministic magnetic field on the emergent linear polarization signal in a model which is simpler than the one used in the non-magnetic calculations. We include the three electronic states $X^2\Sigma^+$, $A^2\Pi$ and $B^2\Sigma^+$, vibrational levels from $v = 0$ to $v = 2$ in each state and rotational levels from $J = 1/2$ to $J = 181/2$. The Hanle diagrams for two of the observed lines in the region around 3772 Å are

shown in Fig. 7.38. The behavior is very similar to that obtained for the other molecules, with a lower level lobe which appears only when dichroism is neglected, the contribution of the upper level lobe being much more important.

We have also calculated the influence of a microturbulent magnetic field on the emergent linear polarization for the same simplified CN model. The results for three R lines corresponding to $\Delta v = 0$ transitions of the $B - X$ system are shown in Fig. 7.39. By comparing the value of the fractional alignment for weak magnetic fields with the results obtained for small collisional rates (see Fig. 7.31) we can see that the reduced model gives results similar to the big model. The small differences are due to the limitations of the small molecular model. These variations of σ_0^2 with the size of the molecular model are the smaller the bigger the molecular model.

The general behavior of the fractional alignment is similar to that obtained for the C_2 lines. The linear polarization signal is maximum for zero magnetic field, it decreases due to the lower level Hanle effect and decreases again due to the upper level Hanle effect. The lower level of these transitions is saturated for fields lower than 10^{-3} gauss, while the upper level starts its depolarization for fields larger than 10 G. The upper level Hanle depolarization is consistent with the critical Hanle field shown in Fig. 7.36 while the lower level is depolarized for magnetic field strengths lower than expected from the direct application of Eq. (7.8). This might be produced because the lower levels are also radiatively linked with the first excited electronic state, which produces higher values of the lower-level lifetime.

Similarly to what happens with other molecules, the Q/I signal when dichroism is taken into account is completely insensitive to the lower level atomic polarization. For this reason, Q/I remains constant until the lower level starts to depolarize. However, we have plotted in the same figure the value of Q/I obtained for a value of the ratio $S_l/B_\nu = 3$. This turns out to be the average value of this ratio at the heights where the CN lines are formed in the snapshot model taken from the 3D simulation of Asplund et al. (2000). This is also the value obtained for the FAL-C and COOL-C semi-empirical models, as can be seen from Fig. 7.15. In this case, the Q/I signal is essentially proportional to the upper level fractional alignment (the upper level contribution is now $\sim$3 times larger). The feedback effect in the upper level produced by the Hanle depolarization of the lower level produces then a value of Q/I which present a feature that is associated to the lower level atomic polarization. In this case,

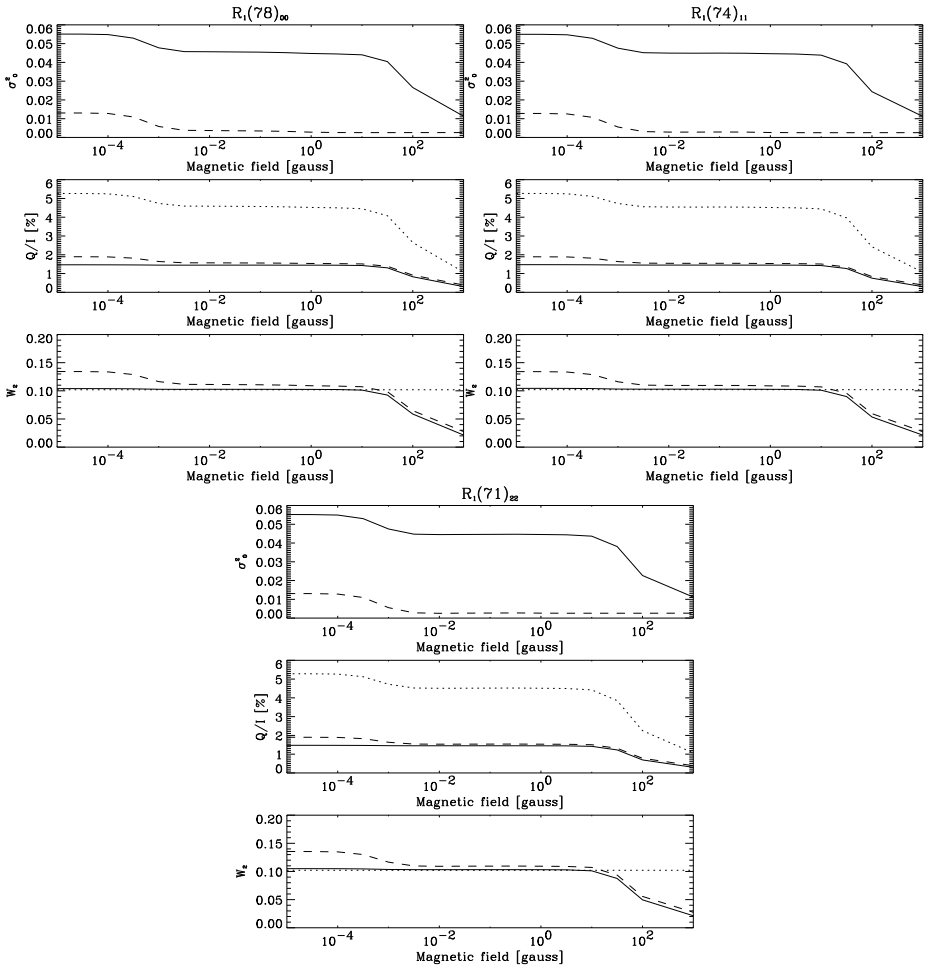

Figure 7.39: Upper panels: fractional alignment σ_0^2 of the upper (solid line) and lower (dashed line) levels of some transitions of the R branch of CN for different vibrational bands and for different values of the microturbulent magnetic field. Middle panels: the corresponding fractional linear polarization (Q/I) obtained under the assumption of single scattering events. The solid line takes into account the effect of dichroism, the dashed line does not and the dotted line is the one obtained when $S_l/B_\nu = 3$. Lower panels: the corresponding polarizability factor obtained from the calculated Q/I via Eq. (7.7). The dotted line is the $\mathcal{W}_2$-value obtained from the analytical formula given by Landi Degl'Innocenti (2003).

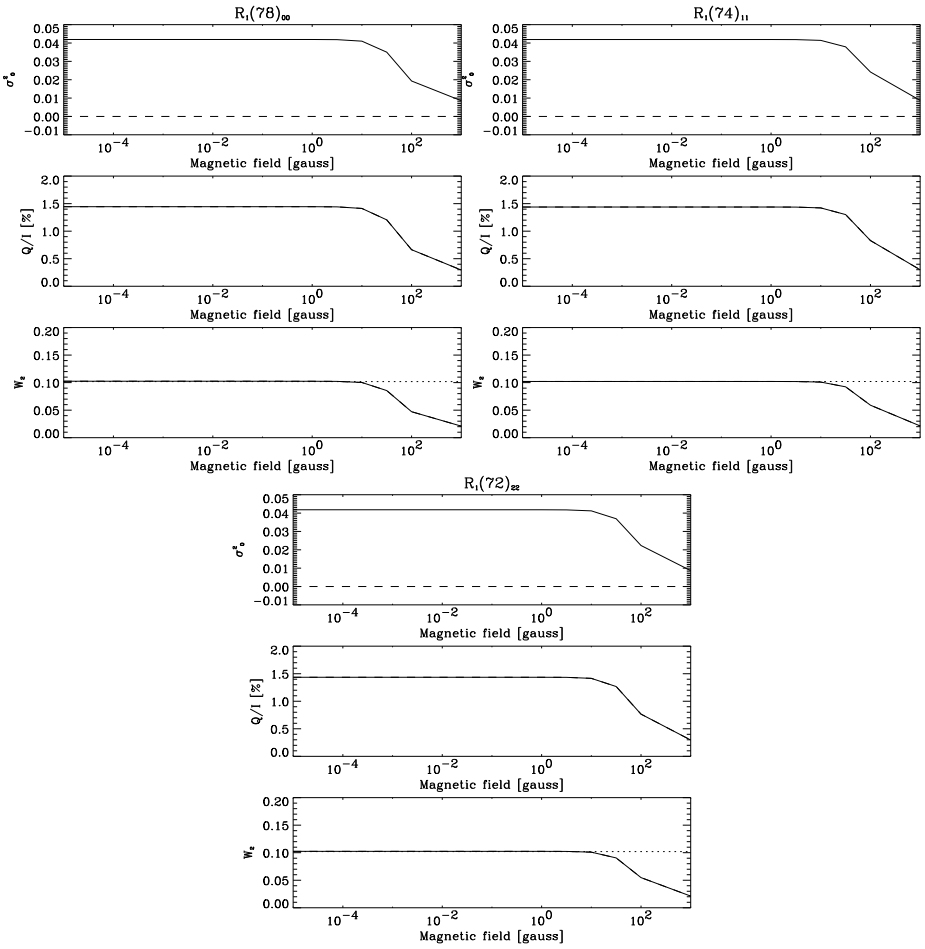

Figure 7.40: Upper panels: fractional alignment σ_0^2 of the upper (solid line) and lower (dashed line) levels of some transitions of the R branch of CN for different vibrational bands and for different values of the microturbulent magnetic field. The lower level is completely depolarized. Middle panels: the corresponding fractional linear polarization (Q/I) obtained under the assumption of single scattering events. The solid line takes into account the effect of dichroism while the dashed line does not include dichroism. Lower panels: the corresponding polarizability factor obtained from the calculated Q/I via Eq. (7.7). The dotted line is the $\mathcal{W}_2$-value obtained from the analytical formula given by Landi Degl'Innocenti (2003).

it is possible, in principle, to detect the influence of lower level polarization in the observed value of the linear polarization. However, it turns out to be not so direct to find a clear diagnostic application of the CN lines as we did for C_2. All the lines belonging to different vibrational bands with $\Delta v = 0$ present the same amount of linear polarization and no differential study can be done with these lines as was done in C_2. We are now studying whether or not the comparison of high J lines with low J lines can be considered as a diagnostic tool. However, we note that the difference between the Hanle field for high J and low J lines is very reduced.

We have shown in Fig. 7.40 the same type of information but when the lower level is totally depolarized. Note that the result for the observed Q/I is equal to that obtained when the lower level polarized but dichroism is included in Q/I. If the lower level atomic polarization is totally destroyed by collisions, we predict that the emerging linear polarization is totally independent of the magnetic field up to ∼10 G. If $S_l/B_\nu \approx 3$, this fact could be used to distinguish if the depolarization collisions are efficient in destroying the lower level polarization. If they are, the Q/I signal would be completely independent on the observed region, at least for weak magnetic regions. If not, the Q/I signal would vary between differently magnetized regions. The observations show an apparent immunity of the CN molecular lines to the Hanle effect along the slit (Stenflo 2003b). This could be explained in view of the previous results, because the variation of Q/I for fields below 10^2 gauss is very small, even for the ratio $S_l/B_\nu = 3$.

7.4 Conclusion

In this Chapter we have investigated in detail the scattering polarization and the Hanle effect in molecular lines. After emphasizing the fundamental difference that exists between the laboratory case and the astrophysical case, we have carried out a detailed investigation of the band structure, Einstein coefficients, polarizability factors and Landé factors for the MgH and C_2 molecules. The fractional alignment, fractional linear polarization (Q/I) and polarizability factors for the non-magnetic case have been discussed. We have shown how the molecular polarization varies when increasing the depolarizing collisions. On the other hand, we have also calculated how the molecular level polarization changes when a microturbulent magnetic field is applied. In order

to understand the observed linear polarization signals and their apparent immunity to the magnetic field, we have made an investigation of the observed molecular bands in the 3D models of Asplund et al. (2000), emphasizing that the polarization signals produced by molecular lines are indeed coming from the upflowing material, as a result of both a larger abundance and a larger anisotropy of the radiation field.

Following the idea that the magnetic field in the "quiet" solar atmosphere is described by a magnetic PDF, we have investigated the molecular Hanle effect for several functional forms of the PDFs. In this way, we have obtained some constraints to their parameters making use of a line ratio technique between the $P_1 + P_2$ lines and the P_3 lines or between the $R_1 + R_2$ and R_3 lines. We have concluded that the PDF in the granular upflowing regions must be quite narrow in order to be able to explain the observed line ratios.

We have considered the scattering polarization in CN lines, concluding also that the CN polarization signals are coming predominantly from the upflowing regions. We have investigated the variation of the molecular polarization when the depolarizing collisions and the magnetic field strength are increased. We have also solved some technical problems which arise when very big molecular models are used.

8

Conclusions

The main aim of this Thesis has been to provide a novel contribution to the development and application of different numerical techniques that are needed for investigating key problems in Molecular Astrophysics. In particular, accurate and fast radiative transfer diagnostic tools are of fundamental importance for a rigorous interpretation of spectroscopic and spectropolarimetric observations of molecular lines.

Chapter 2 has reviewed the theoretical foundations of molecular spectroscopy for diatomic molecules. It gives a brief introduction to the vibrational and rotational motions of molecules, showing how the energies of molecular energy levels can be obtained. We have also described the electronic motions in diatomic molecules, presenting the most usual angular momentum couplings cases. For a quick reference, we have presented useful tables which summarize the fundamentals of diatomic molecular spectroscopy.

Prior to solving any radiative transfer problem in molecular astrophysics, it is necessary to obtain the molecular abundances at each point of the astrophysical plasma under consideration. To this end, in Chapter 3 we have developed a code which calculates the molecular number densities assuming instantaneous chemical equilibrium (the ICE approximation). The non-linear dependence of the molecular abundances on temperature and density allow molecular lines to be used as good tracers of the thermodynamical conditions in stellar atmospheres. We have thus calculated the abundances of many diatomic molecules

in several models of the solar atmosphere. In a second step, we have taken into account the finite molecular formation and destruction times, which has led us to develop a computer program to simulate the time evolution of the molecular number densities when the physical conditions of the medium under investigation are time-dependent. Our first application aimed at solving the enigma of the CO-cooled 'clouds' in the solar chromosphere. To this end, we have calculated the temporal variability of the CO concentration in one-dimensional radiation hydrodynamical models of the solar atmosphere. Our results indicate that the CO line radiation observed close to the edge of the solar disk comes from atmospheric heights not greater than $\sim$700 km, and that the gas in these regions of the low chromosphere must be much cooler than indicated by the cool phases of the Carlsson & Stein (1997) hydrodynamical simulations. We have pointed out that lower temperatures tend to increase the relaxation times needed to reach the molecular equilibrium concentrations. We have also investigated the formation of the infrared CO lines in three-dimensional hydrodynamical simulations of the solar photosphere, comparing our spectral synthesis with spectroscopic observations. Moreover, we have investigated the influence of photodissociation processes on the abundance of CH on the solar atmosphere. Our conclusion is that such photodissociation processes produce a negligible contribution, at least concerning the G-band spectral lines.

In Chapter 4 we have presented our generalization of the accelerated Λ-iteration (ALI) method of Olson et al. (1986) and of the highly-convergent radiative transfer methods of Trujillo Bueno & Fabiani Bendicho (1995) to spherical symmetry, for both atomic and molecular line transfer. We find that the radiative transfer method of Trujillo Bueno & Fabiani Bendicho (1995) based on the Gauss-Seidel scheme is at least 2 times faster than the ALI method, while their SOR method gives an improvement of an order of magnitude. With these fast methods of solution the computing time per iteration is similar to that of the simple Λ-iteration, because the very high convergence rate is achieved via a novel strategy which does not require neither the actual construction nor the inversion of any non-local Λ-operator. After illustrating the convergence properties of our multilevel radiative transfer code for molecular lines, we have applied it to investigate the reliability of the results obtained via the Large Velocity Gradient (LVG) or escape probability method. We emphasize that one should be very careful when using the LVG approximation to obtain the molecular level populations. Our NLTE code for molecular lines has also been

applied to investigate two problems of interest in today's molecular astrophysics: the formation of the warm water spectrum in Sgr B2 and the formation of the CO fundamental vibration-rotation spectrum in the circumstellar envelope of VYCMa.

Besides considering the intensity spectrum, we have also investigated some aspects of the light polarization emitted/absorbed by molecules. For this reason, Chapter 5 has reviewed the fundamentals of the angular momentum theory, as is needed for a rigorous investigation of polarization phenomena in diatomic molecules. We have developed a very general method which allows us to calculate the Zeeman patterns for rotational transitions of diatomic molecules. It is based on the direct numerical diagonalization of the effective molecular hamiltonian. This technique allows the inclusion of any additional refinement into the description of the molecular motion to obtain its influence on the Zeeman patterns. The second part of Chapter 5 provides a brief discussion on the formulation of the scattering polarization and the Hanle effect in molecular lines within the framework of the quantum theory for the generation and transfer of polarized radiation.

We have successfully compared the results obtained via our numerical approach to the molecular Zeeman effect to those we have obtained via the application of the more restricted formulae of Schadee (1978). Thanks to these developments we have investigated in Chapter 6 the polarization signatures induced by the Zeeman effect in molecular lines of different species. The first application has been the investigation of the polarization signals produced in sunspots by OH and CN in the near infrared. To this end, we performed observations with the Tenerife Infrared Polarimeter (TIP) attached to the Vacuum Tower Telescope (VTT) of the Observatorio del Teide. We have theoretically explained the 'anomalous' Stokes profiles of CN we have discovered in sunspots. This has led us to the development of an inversion code of Stokes profiles induced by the Zeeman effect in both atomic and/or molecular lines. Its application to spectropolarimetric observations has allowed us to obtain some preliminary information on the thermodynamical and magnetic properties in relatively deep regions of sunspot umbrae.

We have also investigated in detail, both theoretically and observationally, the Zeeman effect in the G-band. This was motivated by the interest of detecting CH spectral lines which may be useful for obtaining information about the magnetic properties of the so-called G-band bright points observed on the

solar 'surface'. We have also investigated polarization signals produced by the Zeeman effect in many other molecular transitions. A particularly interesting molecule for diagnostic purposes seems to be FeH. To this end, we have observed with TIP spectral lines of the $E^4\Pi - A^4\Pi$ system of FeH which show indeed interesting polarization signals. We have investigated the Zeeman effect in these molecular transitions pointing out that in Hund's case (a) coupling the effective Landé factors are never negative. For this reason, the fact that our spectropolarimetric observations indicate that the Landé factors of pairs of FeH lines have opposite signs, prompt us to conclude that the $E^4\Pi - A^4\Pi$ system must be in intermediate angular momentum coupling between Hund's cases (a) and (b). We emphasized that theoretical and/or laboratory investigations of this molecular system are urgently needed for exploiting its promising diagnostic capabilities.

In Chapter 7 we have investigated in detail the scattering polarization and the Hanle effect in molecular lines within the framework of the quantum theory of polarization, presenting a detailed discussion on the Einstein coefficients, Landé factors and polarizability factors. We have solved the statistical equilibrium equations in order to model the amplitudes of the linear polarization signals produced by scattering processes in molecular lines of C_2 and MgH, and their modification due to the possible presence of 'turbulent' magnetic fields. This has allowed us to show that the magnetic fields in the granular regions of solar surface convection have to be very weak.

Finally, we have also investigated the linear polarization signals produced by scattering processes in CN lines in the near-UV spectral region. Due to the enormous size of the ensuing mathematical problem, we had to solve first several technical issues concerning the resolution of the statistical equilibrium equations. As a result, we have now at our disposal a very powerful tool for investigating astrophysical magnetic fields via the Hanle effect in molecular lines.

A

Appendix A

In this appendix we derive the expression for the fractional alignment of a two-level atom in the weak-anisotropy limit when a microturbulent magnetic field is present and we let both levels to be polarized. In the weak-anisotropy limit, we consider that the only non-zero multipole components of the density matrix are those with $K \leq 2$. Consider a two-level atom in which the upper level has a total angular momentum J_u and the lower level has a total angular momentum J_l. Consider that both levels are affected by inelastic and elastic collisions and that there is a deterministic magnetic field with a direction given by the angles θ_B and χ_B. In this case, the fractional alignment for the upper and lower levels in the magnetic reference frame whose z axis is oriented in the direction of the magnetic field can be written as (Landi Degl'Innocenti & Landolfi 2004):

$$
\begin{aligned}
\sigma_Q^K(J_u) &= \frac{\bar{n}\left[1+\epsilon-\epsilon b(T_c)\right]}{\bar{n}+\epsilon b(T_c)}\frac{1}{\Delta}(-1)^Q\frac{J_{-Q}^K(\nu_0)}{J_0^0(\nu_0)} \\
&\times \left\{ w_{J_uJ_l}^{(K)}\left[\bar{n}\left(1+\delta_l^{(K)}+iH_lQ\right)+\epsilon b(T_c)\right]\right. \qquad \text{(A.1)} \\
&- \left.(-1)^K w_{J_lJ_u}^{(K)}\bar{n}\left[y_{J_uJ_l}^{(K)}+\epsilon_l^{(K)}\right]\right\} \\
\sigma_Q^K(J_l) &= \frac{\bar{n}\left[1+\epsilon-\epsilon b(T_c)\right]}{1+\bar{n}+\epsilon}\frac{1}{\Delta}(-1)^Q\frac{J_{-Q}^K(\nu_0)}{J_0^0(\nu_0)} \\
&\times \left\{ w_{J_uJ_l}^{(K)}\left[y_{J_uJ_l}^{(K)}\left(1+\bar{n}\right)+\epsilon_u^{(K)}\right]\right. \\
&- \left.(-1)^K w_{J_lJ_u}^{(K)}\left[1+\bar{n}+\epsilon+\delta_u^{(K)}+iH_uQ\right]\right\}, \qquad \text{(A.2)}
\end{aligned}
$$

where

$$
\begin{aligned}
\Delta &= \left[1+\bar{n}+\epsilon+\delta_u^{(K)}+iH_uQ\right]\left[\bar{n}\left(1+\delta_l^{(K)}+iH_lQ\right)+\epsilon b(T_c)\right] \\
&- \bar{n}\left[y_{J_uJ_l}^{(K)}\left(1+\bar{n}\right)+\epsilon_u^{(K)}\right]\left[y_{J_uJ_l}^{(K)}+\epsilon_l^{(K)}\right]. \qquad \text{(A.3)}
\end{aligned}
$$

The previous equations are valid for $K \leq 2$ and $|Q| \leq K$. They include all the possible complications which may arise in a two-level atom: elastic and inelastic collisions, radiative pumping, stimulated emission and deterministic magnetic field.

The symbols which appear in the previous equations are related to the

fundamental properties of the two-level atom by:

$$\epsilon = \frac{C_{ul}^{(0)}}{A_{ul}}, \qquad \bar{n} = \frac{c^2}{2h\nu^3} J_0^0 = \frac{2J_l+1}{2J_u+1}\frac{B_{lu}}{A_{ul}} J_0^0, \tag{A.4}$$

$$H_l = \frac{2\pi\nu_L g_l}{B_{lu} J_0^0}, \qquad H_u = \frac{2\pi\nu_L g_u}{A_{ul}}, \qquad b(T_c) = \exp\left(-h\nu_0/kT_c\right), \tag{A.5}$$

$$\delta_u^{(K)} = \frac{D^{(K)}(J_u)}{A_{ul}}, \qquad \delta_l^{(K)} = \frac{D^{(K)}(J_l)}{B_{lu} J_0^0} \tag{A.6}$$

$$\epsilon_u^{(K)} = \frac{C_{ul}^{(K)}}{C_{ul}^{(0)}}\epsilon, \qquad \epsilon_l^{(K)} = \frac{C_{lu}^{(K)}}{C_{lu}^{(0)}}\frac{b(T_c)}{\bar{n}}\epsilon \tag{A.7}$$

$$w_{J_u J_l}^{(K)} = \frac{\left\{ \begin{array}{ccc} 1 & 1 & K \\ J_u & J_u & J_l \end{array} \right\}}{\left\{ \begin{array}{ccc} 1 & 1 & 0 \\ J_u & J_u & J_l \end{array} \right\}}, \qquad y_{J_u J_l}^{(K)} = (-1)^K \frac{\left\{ \begin{array}{ccc} J_l & J_l & K \\ J_u & J_u & 1 \end{array} \right\}}{\left\{ \begin{array}{ccc} J_l & J_l & 0 \\ J_u & J_u & 1 \end{array} \right\}}. \tag{A.8}$$

In order to express the previous Eqs. (A.2) in a *new* reference system which is obtained from the magnetic reference system by the rotation R_B, the spherical components of the tensors transform according to the usual rules (Landi Degl'Innocenti et al. 1990):

$$\begin{aligned} \left[\rho_Q^K\right]_{\rm new} &= \sum_{Q'} \left[\rho_{Q'}^K\right]_{\rm old} \mathcal{D}_{Q'Q}^K{}^*(R_B) \\ \left[J_Q^K\right]_{\rm new} &= \sum_{Q'} \left[J_{Q'}^K\right]_{\rm old} \mathcal{D}_{Q'Q}^K{}^*(R_B), \end{aligned} \tag{A.9}$$

where $\mathcal{D}_{Q'Q}^K{}^*(R_B)$ are the ordinary rotation matrices (Edmonds 1960). Consider now a reference system in which the z direction is along the vertical of the atmosphere which is the symmetry axis of the radiation field. In order to go from the magnetic reference system to this new system, we have to carry out a rotation of:

$$R_B = (\alpha, -\theta_B, -\chi_B), \tag{A.10}$$

where α is an angle which can be arbitrarily set to zero (it is related to the relative orientation of the x and y axis in both reference systems). In this new reference system, the magnetic field vector has polar and azimuthal angles θ_B and χ_B.

Since we are interested in the limit of a microturbulent magnetic field with random orientations, which is considered as turbulent below the photon mean free path, we must do an angle averaging over the whole sphere. Therefore, performing the previous transformation and averaging over the whole sphere making use of the property given by Eq. (5.5), we get:

$$\overline{\sigma^K_Q(J_u)} = \mathcal{H}^{(K)}_{J_uJ_l}(J_u)(-1)^Q \frac{J^K_{-Q}}{J^0_0}$$
$$\overline{\sigma^K_Q(J_l)} = \mathcal{H}^{(K)}_{J_uJ_l}(J_l)(-1)^Q \frac{J^K_{-Q}}{J^0_0}, \tag{A.11}$$

where the bar above σ^K_Q indicates that this is a quantity averaged over a distribution of microturbulent magnetic fields with random orientations. The quantities $\mathcal{H}^{(K)}_{J_uJ_l}(J)$ play the role of the $\mathcal{H}^{(K)}$ quantity in Trujillo Bueno & Manso Sainz (1999) as a Hanle depolarization factor. The explicit expression for these factors is:

$$\begin{aligned}
\mathcal{H}^{(K)}_{J_uJ_l}(J_u) &= \frac{1}{2K+1}\sum_{Q'} \frac{\bar{n}\left[1+\epsilon-\epsilon b(T_c)\right]}{\bar{n}+\epsilon b(T_c)} \frac{1}{\Delta'} \\
&\times \left\{ w^{(K)}_{J_uJ_l}\left[\bar{n}\left(1+\delta^{(K)}_l + iH_lQ'\right)+\epsilon b(T_c)\right]\right. \\
&- \left. (-1)^K w^{(K)}_{J_lJ_u}\bar{n}\left[y^{(K)}_{J_uJ_l}+\epsilon^{(K)}_l\right]\right\} \qquad \text{(A.12)} \\
\mathcal{H}^{(K)}_{J_uJ_l}(J_l) &= \frac{1}{2K+1}\sum_{Q'} \frac{\bar{n}\left[1+\epsilon-\epsilon b(T_c)\right]}{1+\bar{n}+\epsilon} \frac{1}{\Delta'} \\
&\times \left\{ w^{(K)}_{J_uJ_l}\left[y^{(K)}_{J_uJ_l}(1+\bar{n})+\epsilon^{(K)}_u\right]\right. \\
&- \left. (-1)^K w^{(K)}_{J_lJ_u}\left[1+\bar{n}+\epsilon+\delta^{(K)}_u + iH_uQ'\right]\right\}, \qquad \text{(A.13)}
\end{aligned}$$

where

$$\begin{aligned}
\Delta' &= \left[1+\bar{n}+\epsilon+\delta^{(K)}_u + iH_uQ'\right]\left[\bar{n}\left(1+\delta^{(K)}_l + iH_lQ'\right)+\epsilon b(T_c)\right] \\
&- \bar{n}\left[y^{(K)}_{J_uJ_l}(1+\bar{n})+\epsilon^{(K)}_u\right]\left[y^{(K)}_{J_uJ_l}+\epsilon^{(K)}_l\right]. \qquad \text{(A.14)}
\end{aligned}$$

Note that the sums are extended over all the possible values of Q for a given K. Also note that the previous expressions reduce to those derived by Trujillo Bueno & Manso Sainz (1999) when the lower level is depolarized and stimulated emission is neglected. In fact, when $\delta_l^(K) \rightarrow \infty$ and $\bar{n} = 0$,Additionally, in the limit of very large magnetic field, large enough to produce Hanle saturation in both the upper and lower levels, we get:

$$\lim_{B\rightarrow\infty} \mathcal{H}^{(K)}_{J_u J_l}(J_u) = \frac{1}{5} \lim_{B\rightarrow 0} \mathcal{H}^{(K)}_{J_u J_l}(J_u) \tag{A.15}$$

$$\lim_{B\rightarrow\infty} \mathcal{H}^{(K)}_{J_u J_l}(J_l) = \frac{1}{5} \lim_{B\rightarrow 0} \mathcal{H}^{(K)}_{J_u J_l}(J_l) \tag{A.16}$$

References

Asensio Ramos, A., & Trujillo Bueno, J. 2003a, in Stellar Atmosphere Modeling, ed. I. Hubeny, D. Mihalas, & K. Werner, ASP Conf. Ser. 288 (San Francisco: ASP), 335

Asensio Ramos, A., & Trujillo Bueno, J. 2003b, in Solar Polarization 3, ed. J. Trujillo Bueno & J. Sánchez Almeida, ASP Conf. Ser. Vol 307, 195

Asensio Ramos, A., Trujillo Bueno, J., & Cernicharo, J. 2001, in The Promise of the Herschel Space Observatory, ed. G. L. Pilbratt, J. Cernicharo, A. M. Heras, T. Prusti, & R. Harris, ESA-SP 460, San Francisco, 265

Asensio Ramos, A., Trujillo Bueno, J., & Collados, M. 2004, ApJ, 603, L125

Asplund, M. 2004, A&A, in press

Asplund, M., Carlsson, M., & Botnen, A. V. 2003, A&A, 399, 31

Asplund, M., & García Pérez, A. E. 2001, A&A, 372, 601

Asplund, M., Grevesse, N., Sauval, A. J., Allende Prieto, C., & Kiselman, D. 2004, A&A, in press

Asplund, M., Ludwig, H. G., Nordlund, A., & Stein, R. F. 2000, A&A, 359, 669

Auer, L. 2003, in Stellar Atmosphere Modeling, ed. I. Hubeny, D. Mihalas, & K. Werner, ASP Conf. Ser. 288 (San Francisco: ASP), 3

Auer, L., & Mihalas, D. 1969, ApJ, 158, 641

Auer, L. H. 1987, 101

Auer, L. H. 1991, in Stellar Atmospheres: Beyond Classical Models, ed. L. Crivellari, I. Hubeny, & D. G. Hummer, 9

Auer, L. H., Fabiani Bendicho, P., & Trujillo Bueno, J. 1994, A&A, 292, 599

Auer, L. H., & Paletou, F. 1994, A&A, 285, 675

Avrett, E. H. 2003, in Current Theoretical Models and Future High-Resolution Solar Observations: Preparing for ATST, ed. A. A. Pevtsov & H. Uitenbroek, ASP Conf. Ser. 286 (San Francisco: ASP), 105

Avrett, E. H., Höflich, P., Uitenbroek, H., & Ulmschneider, P. 1996, in Cool Stars, Stellar Systems, and the Sun, 9th Cambridge Workshop, ed. R. Pallavicini & A. Dupree, ASP Conf. Ser. 109 (San Francisco: ASP), 105

Avrett, E. H., & Loeser, R. 1987, Numerical Radiative Transfer, 135

Ayres, J. M., Testerman, L., & Brault, J. W. 1986, ApJ, 304, 542

Ayres, T. R. 1981, ApJ, 244, 1064

—. 2002, ApJ, 575, 1104

Ayres, T. R., & Rabin, D. 1996, ApJ, 460, 1042

Ayres, T. R., & Testerman, L. 1981, ApJ, 245, 1124

Ayres, T. R., & Wiedemann, G. R. 1989, ApJ, 338, 1033

Baron, E., Hauschildt, P. H., & Lowenthal, D. 2003, in Stellar Atmosphere Modeling, ed. I. Hubeny, D. Mihalas, & K. Werner, ASP Conf. Ser. 288 (San Francisco: ASP), 385

Bates, D. R., & Spitzer, L. 1951, ApJ, 113, 441

Bennett, A. 1988, in Rate Coefficients in Astrochemistry, ed. T. Millar & W. D.A., 339

Benson, J. M., & Mutel, R. L. 1992, ApJ, 253, 199

Berdyugina, S. V., & Livingston, W. C. 2002, A&A, 387, L6

Berdyugina, S. V., & Solanki, S. K. 2001, A&A, 380, L5

—. 2002, A&A, 385, 701

Berdyugina, S. V., Solanki, S. K., & Frutiger, C. 2001, in Magnetic Field across the Herzsprung-Russel Diagram, ed. G. Mathys, S. K. Solanki, & D. T. Wickramasinghe, ASP Conf. Ser., 99

Berdyugina, S. V., Stenflo, J. O., & Gandorfer, A. 2002, A&A, 388, 1062

Berger, T. E., Schrijver, C. J., Shine, R. A., Tarbell, T. D., Title, A. M., & Scharmer, G. 1995, ApJ, 454, 531

Bernes, C. 1979, A&A, 73, 67

Bieniek, R. J., & Green, S. 1983a, ApJ, 265, L29

—. 1983b, ApJ, 270, L101

Born, M., & Wolf, E. 1980, Principles of Optics: Electromagnetic Theory of Propagation of Light (Oxford: Pergamon Press)

Bourke, T. L., & Goodman, A. A. 2003, in Star Formation at High Angular Resolution, ed. M. G. Burton, R. Jayawardhana, & T. L. Bourke, ASP Conference Series, Vol. S-221, 83

Brink, D. M., & Satchler, G. R. 1968, Angular Momentum (Oxford University Press)

Brown, J. M., & Carrington, A. 2003, Rotational Spectroscopy of Diatomic Molecules (Cambridge: Cambridge University Press)

Brown, J. M., Hougen, J. T., Huber, K.-P., Johns, J. W. C., Kopf, I., Lefebvre-Brion, H., Merer, A. J., Ramsay, D. A., Rostas, J., & Zare, R. N. 1975, J. Mol. Spec., 55, 500

Brown, J. M., Kaise, M., Kerr, C. M. L., & Milton, D. J. 1978, Molec. Phys., 36, 553

Brunish, W. M., & Truran, J. W. 1992, ApJ, 256, 247

Cannon, C. J. 1973, ApJ, 185, 577

Carlsson, M., Judge, P. G., & Wilhem, K. 1997, ApJ, 486, L63

Carlsson, M., & Stein, R. F. 1995, ApJ, 440, L29

—. 1997, ApJ, 481, 500

Carlsson, M., & Stein, R. F. 2002, in *SOHO*-11: From Solar Minimum to Maximum, ed. A. Wilson (ESA SP-508; Noordwijk: ESA), in press

Castor, J. I. 1970, MNRAS, 149, 111

Cattaneo, F. 1999, ApJ, 515, L39

Cattaneo, F., Emonet, T., & Weiss, N. 2003, ApJ, 588, 1183

Ceccarelli, C., Baluteau, J.-P., Walmsley, M., Swinyard, B. M., Caux, E., Sidher, S. D., Cox, P., Gry, C., Kessler, M., & Prusti, T. 2002, A&A, 383, 603

Cernicharo, J., Bujarrabal, V., & Satarén, J. L. 1993, ApJ, 407, L33

Cernicharo, J., Goicochea, J. R., & Caux, E. 2000, ApJ, 534, L199

Cernicharo, J., Goicoechea, J., Pardo, J. R., Asensio Ramos, A., & Ceccarelli, C. 2004, ApJ, submitted

Cernicharo, J., Heras, A. M., Tielens, A. G. G. M., Pardo, J. R., Herpin, F., Guélin, M., & Waters, L. B. F. M. 2001, ApJ, 546, L123

Cernicharo, J., Lim, T., Cox, P., & et al. 1997, A&A, 323, L25

Chandra, D. A., Varshalovich, D. A., & Kegel, W. H. 1984, A&AS, 55, 51

Cheung, A. C., Rank, D. M., Townes, C. H., & Welch, W. J. 1969, Nature, 221, 917

Clark, T. A., Lindsey, C. A., Rabin, D. M., & Livingston, W. C. 1995, in Infrared Tools for Solar Astrophysics: What's Next?, ed. J. Kuhn & M. Penn (Singapore: World Scientific), 133

Collados, M., Martínez Pillet, V., Ruiz Cobo, B., del Toro Iniesta, J. C., & Vázquez, M. 1994, A&A, 291, 622

Cooper, D. M., & Nicholls, R. W. 1976, Spec. Lett., 9(3), 139

Cox, A. N. 2000, Allen's Astrophysical Quantities, 4th ed. (New York: Springer Verlag and AIP Press)

Cushing, M. C., Rayner, J. T., Davis, S. P., & Vacca, W. D. 2003, ApJ, 582, 1066

Danchi, W. C., Bester, M., Degiacomi, C. G., Greenhill, L. J., & Townes, C. H. 1994, AJ, 107, 1469

de Graauw, T., Haser, L. N., & Beintema, D. A. 1996, A&A, 315, L49

Delbouille, L., Roland, G., & Neven, L. 1973, Photometric Atlas of the Solar Spectrum (Liège: Univ. Liège, Inst. d'Astrophysique)

Dickel, H. R., & Auer, L. H. 1994, ApJ, 437, 222

Donati, J. F. 2003, in Solar Polarization 3, ed. J. Trujillo Bueno & J. Sánchez Almeida, ASP Conf. Ser. Vol 307, 41

Draine, B. T. 1978, ApJS, 36, 595

Dunham, T. J., & Adams, W. S. 1937a, Publ. Am. Astr. Soc., 9, 5

—. 1937b, PASP, 49, 26

Edmonds, A. R. 1960, Angular Momentum in Quantum Mechanics (Princeton University Press)

Elitzur, M. 1992, Astronomical Masers (Dordrecht: Kluwer Academic Publishers)

Elitzur, M. 2002, in Astrophysical Spectropolarimetry, ed. J. Trujillo Bueno, F. Moreno-Insertis, & F. Sánchez, Proceedings of the XII Canary Islands Winter School of Astrophysics (Cambridge: Cambridge University Press), 225

Emerson, D. 1996, Interpreting Astronomical Spectra (England: John Wiley & Sons)

Estalella, R., & Anglada, G. 1999, Introducción a la Física del Medio Interestelar (Barcelona: Edicions Universitat de Barcelona)

Fabiani Bendicho, P., Trujillo Bueno, J., & Auer, L. H. 1997, A&A, 324, 161

Fano, U. 1957, Rev. Mod. Phys., 29, 74

Farmer, C. B., Norton, R. H., & Geller, M. 1989, A High-Resolution Atlas of the Infrared Spectrum of the Sun and the Earth Atmosphere from Space, Vol. 1 (NASA Ref. Publ. 1224; Washington, DC: NASA)

Faurobert, M., & Arnaud, J. 2002, A&A, 382, L17

Feuchtgruber, H., Helmich, F. P., van Dishoeck, E. F., & Wright, C. M. 2000, ApJ, 535, L111

Fontenla, J. M., Avrett, E. H., & Loeser, R. 1993, ApJ, 406, 319

Gandorfer, A. 2000, The Second Solar Spectrum, Vol. I: 4625 Å to 6995 Å (Zurich: vdf)

Gandorfer, A. 2003, in Solar Polarization 3, ed. J. Trujillo Bueno & J. Sánchez Almeida, ASP Conf. Ser. Vol 307, 399

Gandorfer, A. H., & Povel, H. P. 1997, A&A, 328, 381

Gear, C. N. 1971, Numerical Initial Value Problems in Ordinary Differential Equations (Englewood Cliffs: Prentice-Hall)

Gingerich, O., Noyes, R. W., Kalkofen, W., & Cuny, Y. 1971, Sol. Phys., 18, 347

Goicochea, J. R., & Cernicharo, J. 2001, ApJ, 554, L213

—. 2002, ApJ, 576, L77

Goicoechea, J. 2003, PhD thesis

Goldreich, P., & Scoville, N. 1976, ApJ, 205, 144

González-Alfonso, E., & Cernicharo, J. 1999, ApJ, 525, 845

Goorvitch, D. 1994, ApJS, 95, 535

Green, S., Maluendes, S., & McLean, A. D. 1993, ApJS, 85, 181

Green, S., & Thaddeus, P. 1976, ApJ, 205, 766

Grevesse, N. 1984, Phys. Scr, 8, 49

Hageman, L. A., & Young, D. M. 1981, Applied Iterative Methods (New York: Academic)

Hanle, W. 1924, Z. Phys., 30, 93, [An english version exists in Moruzzi & Strumia (1991).]

Harvey, J. W. 1985, in Measurements of Solar Vector Magnetic Fields, ed. M. J. Hagyard, NASA CP-2374, 109

Harvey, K. L., & White, O. R. 1999, ApJ, 515, 812

Herzberg, G. 1950, Molecular Spectra and Molecular Structure. I. Spectra of Diatomic Molecules (New York: Van Nostrand Company)

Hill, E. L. 1929, Phys. Rev., 34, 1507

Höflich, P. 2003, in Stellar Atmosphere Modeling, ed. I. Hubeny, D. Mihalas, & K. Werner, ASP Conf. Ser. 288 (San Francisco: ASP), 371

Huber, K. P., & Herzberg, G. 1979, Constants of Diatomic Molecules (New York: Van Nostrand)

Huber, K. P., & Herzberg, G. 2003, in Constants of Diatomic Molecules (data prepared by J. W. Gallagher and R.D. Johnson, III), ed. P. J. Linstrom & W. G. Mallard, NIST Chemistry WebBook, NIST Standard Reference Database Number 69 (Gaithersburg MD: National Institute of Standards and Technology)

Hund, F. 1926, Z. Phys., 36, 657

—. 1927, Z. Phys., 42, 93

Jorgensen, U. G., Larsson, M., Iwamae, A., & Yu, B. 1996, A&A, 315, 204

Judd, B. R. 1975, Angular Momentum Theory for Diatomic Molecules (New York: Academic Press)

Kalkofen, W. 2001, ApJ, 557, 376

Keller, C. 2002, in Astrophysical Spectropolarimetry, ed. J. Trujillo Bueno, F. Moreno-Insertis, & F. Sánchez, Proceedings of the XII Canary Islands Winter School of Astrophysics (Cambridge, UK: Cambridge University Press), 303

Keller, C. U., & Sheeley, N. R. 1999, in Solar Polarization 2, ed. K. N. Nagendra & J. O. Stenflo (Dordrecht: Kluwer), 17

Khomenko, E. V., Collados, M., Solanki, S. K., Lagg, A., & Trujillo Bueno, J. 2003, A&A, in press

Kirby, K., Saxon, R. P., & Liu, B. 1979, ApJ, 231, 637

Knowles, S. H., Mayer, C. H., Cheung, A. C., Rank, D. M., & Townes, C. H. 1969, Science, 163, 1055

Konnov, A. A. 2000, Detailed Reaction Mechanism for Small Hydrocarbon Combustion, release 0.5, `http://homepages.vub.ac.be/~akonnov/`

Kunasz, P., & Auer, L. H. 1988, J. Quant. Spec. Radiat. Transf., 39, 67

Kurucz, R. 1993a, Atomic data for opacity calculations (Kurucz CD-ROM No.1)

—. 1993b, Molecular Data for Opacity Calculations (Kurucz CD-ROM No. 15)

Kurucz, R. L. 1985, CfA preprint series (2162)

Kurucz, R. L., van Dishoeck, E. F., & Tarafdar, S. P. 1987, ApJ, 322, 992

Lada, C. J., & Reid, M. J. 1978, ApJ, 219, L95

Landau, L., & Lifshitz, E. 1982, Quantum Mechanics (Oxford: Pergamon)

Landi Degl'Innocenti, E. 1983, Sol. Phys., 85, 3

—. 1984, Sol. Phys., 91, 1

—. 1985, Sol. Phys., 102, 1

Landi Degl'Innocenti, E. 1992, in Solar Observations: Techniques and Interpretation, ed. F. Sánchez, M. Collados, & M. Vázquez (Cambridge: Cambridge University Press), 73

Landi Degl'Innocenti, E. 2002, in Astrophysical Spectropolarimetry, ed. J. Trujillo Bueno, F. Moreno-Insertis, & F. Sánchez, Proceedings of the XII Canary Islands Winter School of Astrophysics (Cambridge, UK: Cambridge University Press), 1

Landi Degl'Innocenti, E. 2003, in Solar Polarization 3, ed. J. Trujillo Bueno & J. Sánchez Almeida, ASP Conf. Ser. Vol 307, 164

Landi Degl'Innocenti, E., Bommier, V., & Sahal Bréchot, S. 1990, A&A, 235, 459

Landi Degl'Innocenti, E., & Landi Degl'Innocenti, M. 1973, Sol. Phys., 31, 319

Landi Degl'Innocenti, E., & Landolfi, M. 2004, Polarization in Spectral Lines (Kluwer Academic Publishers), in press

Langer, S. H., & Watson, W. D. 1984, ApJ, 284, 751

Langhoff, S. R., & Bauschlicher, C. W. 1990, J. Mol. Spec., 141, 243

Le Teuff, Y. H., Millar, T. J., & Markwick, A. J. 2000, A&AS, 146, 157

Lin, H., & Rimmele, T. 1999, ApJ, 514, 448

Lucy, L. B. 1971, ApJ, 163, 95

Mamon, G. A., Glassgold, A. E., & Huggins, P. J. 1988, ApJ, 328, 797

Manso Sainz, R. 2002, PhD thesis, Universidad de La Laguna, La Laguna

Manso Sainz, R., & Trujillo Bueno, J. 2003, Phys. Rev. Lett., 91, 111102

Martínez Pillet, V., Collados, M., Bellot Rubio, L. R., Rodríguez Hidalgo, I., Ruiz Cobo, B., & Soltau, D. 1999, in Astronomische Gesselschaft Meeting Abstracts, vol. 15

McCabe, E. M., Connon Smith, R., & Clegg, R. E. S. 1979, Nature, 281, 263

Mihalas, D. 1978, in Stellar Atmospheres, Vol. 455

Moneti, A., Cernicharo, J., & Pardo, J. R. 2001, ApJ, 549, L203

Monnier, J. D., Tuthill, P. G., Lopez, B., Cruzalebes, P., Danchi, W. C., & Haniff, C. A. 1999, ApJ, 512, 351

Moore, C. E., Minnaert, M. G. J., & Houtgast, J. 1966, The Solar Spectrum 2935 Å to 8770 Å (Washington: National Bureau of Standards Monograph 61)

Moruzzi, G., & Strumia, F. 1991, The Hanle Effect and Level-Crossing Spectroscopy (New York: Plenum Press)

Muller, R., Hulot, J. C., & Roudier, T. 1989, Sol. Phys., 119, 229

Neufeld, D. A., Feuchtgruber, H., Harwit, M., & Melnick, G. J. 1999, ApJ, 517, L147

Neufeld, D. A., Zmuidzinas, J., Schilke, P., & Phillips, T. G. 1997, ApJ, 488, L141

Ng, K. C. 1974, J. Chem. Phys., 61, 2680

Noyes, R. W., & Hall, D. N. B. 1972, BAAS, 4, 389

Olson, G. L., Auer, L. H., & Buchler, J. R. 1986, J. Quant. Spec. Radiat. Transf., 35, 431

Olson, G. L., & Kunasz, P. B. 1987, J. Quant. Spec. Radiat. Transf., 38, 325

Palmer, P., Zuckerman, B., Buhl, D., & Snyder, L. E. 1969, ApJ, 156, L147

Penzias, A. A., & Wilson, R. W. 1965, ApJ, 142, 419

Phillips, J. G., Davis, S. P., Lindgren, B., & Balfour, W. J. 1987, ApJS, 65, 721

Povel, H. P. 2001, in Magnetic Fields across the Hertzsprung-Russel Diagram, ed. G. Mathys, S. K. Solanki, & D. T. Wickramasinghe, ASP Conf. Ser. Vol 248, 543

Prasad, S. S., & Tarafdar, S. P. 1982, ApJ, 267, 603

Press, W. H., Teukolsky, S. A., Vetterling, W. T., & Flannery, B. P. 1986, Numerical Recipes (Cambridge: Cambridge University Press)

Racah, G. 1942, Phys. Rev., 62, 438

Rao, D. M., & Rangarajan, K. E. 1999, ApJ, 524, L139

Rees, D. E., Durrant, C. J., & Murphy, G. A. 1989, ApJ, 339, 1093

Richards, A. M. S., Yates, J. A., & Cohen, R. J. 1998, MNRAS, 299, 319

Ruiz Cobo, B., & del Toro Iniesta, J. C. 1992, ApJ, 398, 375

Russell, H. N. 1934, ApJ, 79, 281

Rutten, R. J., Kiselman, D., Rouppe van der Voort, L., & Plez, B. 2001, in Advanced Solar Polarimetry: Theory, Observation and Instrumentation, ed. K. N. Nagendra & J. O. Stenflo, ASP Conf. Series, Vol. 236, Kluwer Academic Publishers, 445

Rybicki, G. B., & Hummer, D. G. 1991, A&A, 249, 720

—. 1992, A&A, 262, 209

Sánchez Almeida, J., Asensio Ramos, A., Trujillo Bueno, J., & Cernicharo, J. 2001, ApJ, 555, 978

Sauval, A. J., & Tatum, J. B. 1984, ApJS, 56, 193

Schadee, A. 1978, J. Quant. Spec. Radiat. Transf., 19, 517

Scharmer, G. B., & Carlsson, M. 1985, J. Comput. Phys., 50, 56

Shchukina, N., & Trujillo Bueno, J. 2001, ApJ, 550, 970

Sheeley, N. R. 1971, Sol. Phys., 20, 19

Shu, F. H. 1977, ApJ, 214, 488

Sobolev, V. V. 1958, Theoretical Astrophysics, ed. V. A. Ambartsumyan (London: Pergamon Press Ltd.)

—. 1960, Moving Envelopes of stars (Harvard University Press)

Socas-Navarro, H. 2001, in Advanced Solar Polarimetry: Theory, Observation and Instrumentation, ed. K. N. Nagendra & J. O. Stenflo, ASP Conf. Series, Kluwer Academic Publishers, Vol. 236, 487

Socas-Navarro, H., & Sánchez Almeida, J. 2003, ApJ, 593, 581

Socas-Navarro, H., & Trujillo Bueno, J. 1997, ApJ, 490, 383

Solanki, S. K., Livingston, W., & Ayres, T. 1994, Science, 263, 64

Stein, R. F., Bercik, D., & Nordlund, A. 2003, in Current Theoretical Models and High Resolution Solar Observations: Preparing for ATST, ed. A. A. Pevtsov & H. Uitenbroek, ASP Conf. Series, Vol. 286 (San Francisco, CA: The Astronomical Society of the Pacific), 121

Stein, R. F., & Nordlund, A. 1989, ApJ, 342, L95

—. 2000, Sol. Phys., 192, 91

Stein, R. F., & Nordlund, A. 2003, in Stellar Atmosphere Modeling, ed. I. Hubeny, D. Mihalas, & K. Werner, ASP Conf. Ser. 288 (San Francisco: ASP), 519

Steiner, O. 1991, A&A, 242, 290

Steiner, O., Bruls, J., & Hauschildt, P. 2001, in Advanced Solar Polarimetry: Theory, Observation and Instrumentation, ed. K. N. Nagendra & J. O. Stenflo, ASP Conf. Series, Vol. 236, Kluwer Academic Publishers, 453

Stenflo, J. O. 1994, Solar Magnetic Fields. Polarized Radiation Diagnostics (Dordrecht: Kluwer Academic Publishers)

Stenflo, J. O. 2003a, in Polarimetry in Astronomy, ed. S. Fineschi, Proceedings of the SPIE Vol. 4843 (SPIE), 76

Stenflo, J. O. 2003b, in Solar Polarization 3, ed. J. Trujillo Bueno & J. Sánchez Almeida, ASP Conf. Ser. Vol 307, 385

Stenflo, J. O., & Holzreuter, R. 2002, in Proceedings of the Magnetic Coupling of the Solar Atmosphere Euroconference, ESA SP-505: SOLMAG 2002, 101

Stenflo, J. O., & Keller, C. U. 1997, A&A, 321, 927

Sternberg, A., Dalgarno, A., & Lepp, S. 1987, ApJ, 320, 676

Tejero Ordoñez, J., & Cernicharo, J. 1991, Modelos de Equilibrio Termodinámico Aplicados a Envolturas Circunestelares de Estrellas Evolucionadas (Madrid: IGN)

Trujillo Bueno, J. 1999, in Solar Polarization, ed. K. N. Nagendra & J. O. Stenflo, Kluwer Academic Publishers, 73–96

Trujillo Bueno, J. 2001, in Advanced Solar Polarimetry: Theory, Observation and Instrumentation, ed. K. N. Nagendra & J. O. Stenflo, ASP Conf. Series, Kluwer Academic Publishers, Vol. 236, 161–195

Trujillo Bueno, J. 2003a, in Modeling of Stellar Atmospheres, ed. N. E. Piskunov, W. W. Weiss, & D. F. Gray, IAU Symposium 210 (ASP Conf. Ser.), 243

Trujillo Bueno, J. 2003b, in Solar Polarization 3, ed. J. Trujillo Bueno & J. Sánchez Almeida, ASP Conf. Ser. Vol 307, 407

Trujillo Bueno, J. 2003c, in Stellar Atmosphere Modeling, ed. I. Hubeny, D. Mihalas, & K. Werner, ASP Conf. Ser. 288 (San Francisco: ASP), 551

Trujillo Bueno, J., & Fabiani Bendicho, P. 1995, ApJ, 455, 646

Trujillo Bueno, J., & Manso Sainz, R. 1999, ApJ, 516, 436

Tsuji, T. 1964, Ann. Tokio. Astron. Obs., 2nd ser. 9, 1

—. 1971, Ann. Tokio Astron. Obs. 2nd ser., 9, 1

—. 1973, A&A, 23, 411

Uitenbroek, H. 2000a, ApJ, 536, 481

—. 2000b, ApJ, 531, 571

Uitenbroek, H., Miller-Ricci, E., Asensio Ramos, A., & Trujillo Bueno, J. 2004, ApJ, in press

Uitenbroek, H., Noyes, R. W., & Rabin, D. 1994, ApJ, 432, L67

Unno, W. 1956, Pub. Astr. Soc. Japan, 8, 108

Valenti, J. A., & Jonhs-Krull, C. 2001, in Magnetic Field across the Herzsprung-Russel Diagram, ed. G. Mathys, S. K. Solanki, & D. T. Wickramasinghe, ASP Conf. Ser., 179

van Dishoeck, E., & Blake, G. A. 1998, ARA&A, 36, 317

van Dishoeck, E. F. 1987a, in Astrochemistry, ed. M. S. Vardya & S. P. Tarafdar, IAU Symposium 120 (Dordrecht: Reidel), 51

van Dishoeck, E. F. 1987b, J. Chem. Phys., 86, 196

van Zadelhoff, G. J., Dullemond, C. P., van der Tak, F. F. S., Yates, J. A., Doty, S. D., Ossenkopf, V., Hogerheijde, M. R., Juvela, M., Wiesemeyer, H., & Schöier, F. 2002, A&A, 395, 373

Vernazza, J. E., Avrett, E. H., & Loeser, R. 1981, ApJS, 45, 635

Wallace, L., Bernath, P., Livingston, W., Hinkle, K., Busler, J., Guo, B., & Zhang, K. 1995, Science, 268, 1155

Wallace, L., & Hinkle, K. 2001, ApJ, 559, 424

Wallace, L., & Livingston, W. 1992, An Atlas of a Dark Sunspot Umbra Spectrum from 1970 to 8640 cm^{-1}, Vol. NOAO (Tucson: NSO)

Wallace, L., Livingston, W., Bernath, P. F., & Ram, R. S. 1999, An Atlas of the Sunspot Umbra Spectrum in the Red and Infrared from 8900 to 15050 cm^{-1}, rev., Tech. Repl. 99-001 (Tucson: NSO)

Watson, W. D., Eliztur, M., & Bieniek, R. J. 1980, ApJ, 240, 547

Weinreb, S., Barret, A. H., Meeks, M. L., & Henry, J. C. 1963, Nature, 200, 829

Wilson, R. W., Jefferts, K. B., & Penzias, A. A. 1970, ApJ, 161, L43

Wu Zheng, X., Scalise, E., & Han, F. 1998, ApJ, 507, 384

Yamamura, I., Kawaguchi, K., & Ridgway, S. T. 2000, ApJ, 528, L33